ELECTROHYDRODYNAMIC PROCESSING AND CHARACTERISATION OF TITANIUM DIOXIDE FILMS

A thesis submitted in the partial fulfilment of the requirements for the degree of

Doctor of Philosophy

September, 2008

By

Suntharavathanan Mahalingam

Department of Mechanical Engineering

University College London

Torrington Place

London WC1E 7JE, UK

ProQuest LLC
789 East Eisenhower Parkway
P.O. Box 1346
Ann Arbor, MI 48106-1346

DECLARATION

I, Suntharavathanan Mahalingam, confirm that the work presented in this thesis is my own. Where information has been derived from other sources, I confirm that this has been indicated in the thesis.

Yours Sincerely,

Suntharavathanan Mahalingam

ABSTRACT

The research in this thesis demonstrates a novel electrohydrodynamic preparation of titanium dioxide (TiO_2) films. In this process, a liquid breaks up into spray droplets under influence of an electric field. This process is influenced by many factors; properties of the liquid – surface tension, electrical conductivity, relative permittivity, viscosity, density and liquid flow rate and applied voltage. This technique has unique advantage like simple set-up and economical way to formulate the films.

Many modes of processing were identified by drawing the mode-selection map for various applied voltage and flow rate using a titania sol. For a fixed flow rate, changing the applied voltage changed the processing mode. For a fixed applied voltage, changing the flow rate changed the shape of the liquid filament at the end of the needle. The stable cone-jet mode processing produced a near mono-disperse of droplets. The stable cone-jet processing of TiO_2 films showed anatase phase and converted to rutile phase at higher annealing temperature. The morphological characterisation revealed the dense and crack free surfaces of the TiO_2 films.

The dielectric constant of the electrohydrodynamically processed TiO_2 films was ~7. The increase in annealing temperature reduced the dielectric constant of the films. The leakage current density of the films was improved by post deposition annealing. The optical characterisation of the films showed a good transparency in the visible light region. The transmission in the visible range varied between 70-90%. The annealing temperature influenced the transmittance of the films. The energy bandgap is ~3.50 eV for indirect transition.

The larger coverage area nitrogen doped titanium dioxide films were obtained by using a metal clamped needle – ground electrode set-up for the first time. Metal clamping the needle lowered the stable cone-jet operating voltage window. The nitrogen doping in TiO_2 films retarded the phase formation; however, showed anatase phase even at higher doping concentration. The absorption in doped films is higher than that of undoped ones by 8-15%.

PUBLICATIONS AND PRESENTATIONS

1. Characteristics of electrohydrodynamically prepared titanium dioxide films
   S.Mahalingam and M.J.Edirisinghe, Applied Physics A: Material Science & Processing, **89** (2007) 987

2. Novel preparation of nitrogen-doped titanium dioxide films
   S.Mahalingam and M.J.Edirisinghe (Submitted to Journal of Physics D: Applied Physics)

3. Poster presentation at UCL annual poster event (2006) and presentation at departmental PhD forum (2007)
   Title: Electrohydrodynamic processing of titanium dioxide films

ACKNOWLEDGEMENTS

I take this golden opportunity to thank my supervisor, adviser and my inspirator Professor. Mohan Edirisinghe for his enormous support and encouragements throughout my PhD. He has helped me to develop as a good researcher during this period. As everyone knows, he is one of the renowned material scientists in the world and I am so lucky to get him as my PhD supervisor. His guidance and timely advice allowed me to develop as a good material scientist during this period and he has helped me to improve my English from the first day. He always says ''past is history'' that you can not change; now I realise how true that is, for me the past times with him taught me various lessons for my life.

I wholeheartedly thank University College London and Queen Mary University of London for providing me a scholarship to complete this PhD work.

I would like to thank my research colleagues for their help and invaluable suggestions throughout my research. It was a great pleasure to be with you guys not only in the research work but also the fun times we had never forgettable.

I would like to express my thanks to Mr. Terry Dyer at Mechanical Engineering workshop in UCL for his assistance in preparing materials for my work. I would also like to thank many people who helped in the analytical techniques used and the acquisition of data presented in this thesis.

Thanks to Kevin Reeves at Archaeology Department in UCL, for his assistance in obtaining the SEM images and the FTIR measurements. I would also thank Dr.

Steve Firth from Department of Chemistry at UCL the time he took to train me in TGA and Raman spectroscopy. Thanks to Dr. Jeff for the XRD measurements; Mr. Phil Hayes for the uv-vis spectroscopy data acquisition. My many thanks go to Dr. D.J. Morgan from Department of Chemistry at Cardiff University for the XPS measurements.

I would like to express my gratitude to my landlord Selvaraja and my landlady Chandra for providing me the shelter and the food. The understanding they had with me during my stay is very much appreciated.

I take this special occasion to thank my wonderful family members, my dad Mahalingam who supported my studies during this whole period. Dad! I hope finally your dream is coming true; my mum Selvarani who showed unconditional love and affection for me, my brother Sarevanen and my sister Mahaluckshme who gave timely encouragements to me over the telephone in the weekends. I would like to recall the memories of my grandma late Mrs. Meenachiamma who is so much influential in bringing me up at this level. Ammamma! I miss you so much at this special moment.

Last but not least I would like to thank my teachers who taught me various subjects in my life especially my school chemistry teacher Miss. Shanthi Vellupillai who sowed basic chemistry in me and my supervisor Professor. Mohan Edirisinghe who shaped and carved me as a material scientist. They always believed in me, even when I didn't. They will be remained in my heart for rest of my life.

Words would always fall short while describing all of your contributions to me.

Thank you all,

Sincerely,

Suntharavathanan Mahalingam

DEDICATIONS

TO

MY PARENTS, MY TEACHERS, AND MY GOD

TABLE OF CONTENTS

DECLARATION **2**

ABSTRACT **3**

PUBLICATIONS AND PRESENTATIONS **4**

ACKNOWLEDGEMENTS **5**

DEDICATIONS **8**

LIST OF TABLES **16**

LIST OF FIGURES **17**

CHAPTER 1 ..... **21**

Introduction **21**

1.1 Fundamentals of electrohydrodynamic processing 21

1.2 Contents of this thesis 24

1.3 Aims and objectives of the research 27

1.4 Scope of this research 30

CHAPTER 2 ..... **32**

Literature Review **32**

2.1 Electrohydrodynamic processing 32

2.2 Main modes of electrohydrodynamic processing 37

2.2.1 Cone-jet mode 38

2.2.2 Dripping, micro-dripping, spindle mode and intermittent cone-jet mode.. 41

2.2.3 Multiple-jet mode and rim-emission mode 43

2.2.4 Simple-jet mode and ramified mode 44

2.2.5 Oscillating-jet mode 44

2.2.6 Precession mode 45
2.2.7 Corona discharge 45
2.3 Processes involved in electrohydrodynamic processing in cone-jet mode 46
2.3.1 Spray production 46
2.3.2 Aerosol transport 47
2.3.3 Solvent evaporation and droplet disruption 47
2.3.4 Preferential landing of droplets on the substrate 48
2.3.5 Discharge, spreading and penetration of solution droplets on the surface. 49
2.3.6 Decomposition, reaction and surface diffusion of the solute(s) 50
2.4 Properties influencing electrohydrodynamic processing 50
2.4.1 Process parameters 51
2.4.1.1 Effect of applied voltage 51
2.4.1.2 Effect of flow rate 53
2.4.1.3 Needle size and electrode configuration 55
2.4.2 Influence of liquid physical properties 56
2.4.2.1 Influence of electrical conductivity 56
2.4.2.2 Influence of viscosity 58
2.4.2.3 Influence of surface tension 59
2.4.2.4 Influence of dielectric constant 59
2.4.2.5 Influence of density 60
2.5 Scaling laws 60
2.6 Classification of other deposition methods 63
2.6.1 Evaporative technologies 64
2.6.2 Sputtering technique 65
2.6.3 Chemical vapour deposition 67

2.7 Titanium dioxide (TiO_2) 70

2.7.1 Structure and properties of TiO_2 71

2.7.2 TiO_2 in microelectronic applications 73

2.7.3 TiO_2 in photocatalytic and photoelectric applications 74

2.7.4 Doping of TiO_2 and improvement its optical property 76

2.7.5 Nitrogen as a dopant in TiO_2 76

CHAPTER 3 98

Experimental Details 98

3.1 Materials 98

3.1.1 Titania sol 98

3.1.2 N-doped titania sol 98

3.2 Preparation of sols 99

3.2.1 Preparation of titania sol 99

3.2.2 Preparation of N-doped titania sol 99

3.3 Characterisation of sols 100

3.3.1 Electrical conductivity 100

3.3.2 Surface tension 100

3.3.3 Viscosity 101

3.3.4 Relative permittivity 102

3.3.5 Density 102

3.3.6 Thermo gravimetric analysis (TGA) 103

3.4 Equipment used for electrohydrodynamic processing 103

3.4.1 Needle set-up 103

3.4.2 Metal clamped needle set-up 104

3.4.3 Syringe pump 104
3.4.4 High voltage power supply 104
3.4.5 Data recording 105
3.5 Measurement of droplet and relic sizes 105
3.5.1 Sympatec laser diffraction 105
3.5.2 Optical microscopy 106
3.6 Film and MOS capacitor preparation 106
3.6.1 Substrates 106
3.6.2 Heat treatment 107
3.6.3 MOS capacitor 108
3.7 Characterisation of films 108
3.7.1 Raman spectroscopy 108
3.7.2 X-ray diffraction (XRD) 109
3.7.3 Fourier transform infrared (FTIR) spectroscopy 110
3.7.4 Scanning electron microscopy (SEM) 111
3.7.5 Atomic force microscopy (AFM) 112
3.7.6 Electrical characterisation 113
3.7.7 UV/Vis spectroscopy 113
3.7.8 X-ray photoelectron spectroscopy (XPS) 114

CHAPTER 4 120

TiO_2 Film Preparation and Microstructural Characterisation 120

4.1 Titania sol 121
4.1.1 Sol physical properties 121
4.1.2 TGA of titania sol 122

4.2 Electrohydrodynamic processing of TiO_2 films 123

4.2.1 Mode-selection map 124

4.2.2 Effect of applied voltage 125

4.2.2.1 Operating mode and cone-shape 125

4.2.3 Effect of flow rate 126

4.2.3.1 Operating mode and cone-shape 126

4.2.4 Cone-jet and droplet characterisation 127

4.2.4.1 Jet characterisation 128

4.2.4.2 Droplet characterisation 128

4.3 Film preparation 129

4.3.1 Characterisation of TiO_2 films 129

4.3.1.1 Raman spectroscopy of TiO_2 films 130

4.3.1.2 XRD study of TiO_2 films 131

4.3.1.3 Morphological study of TiO_2 films 132

CHAPTER 5 148

Electrical and Optical Characterisation of Electrohydrodynamically processed TiO_2 films 148

5.1 MOS capacitors 149

5.2 FTIR study of TiO_2 films 149

5.3 C-V characteristics of MOS capacitors 150

5.3.1 Low frequency (100 kHz) C-V plots 151

5.3.2 High frequency (500 kHz) C-V plots 152

5.4 Dielectric constant of TiO_2 films 153

5.4.1 Effect of annealing temperature on dielectric constant 153

5.5 I-V characteristics of MOS capacitors 154

5.5.1 Effect of annealing temperature on leakage current density 155

5.6 UV-Vis spectroscopy study on TiO_2 films 157

5.6.1 Effect of annealing temperature on transmittance of TiO_2 films 158

5.6.2 Determination of bandgap of TiO_2 films 159

CHAPTER 6 169

Electrohydrodynamic processing of Nitrogen doped TiO_2 Films 169

6.1 N-doped TiO_2 sol 170

6.1.1 Sol physical properties 171

6.2 Electrohydrodynamic processing of N-doped TiO_2 films 172

6.2.1 Mode-selection map 173

6.2.2 Operating mode and cone-shape 174

6.2.3 Effect of metal clamped needle on applied voltage and deposition area . 175

6.3 Film preparation and characterisation 178

6.4 Effect of nitrogen concentration on structural features and atomic bonding of N-doped TiO_2 films 178

6.4.1 Raman spectroscopy of N-doped TiO_2 films 179

6.4.2 XRD study of N-doped TiO_2 films 180

6.4.3 FTIR study of N-doped TiO_2 films 182

6.4.4 XPS study of N-doped TiO_2 films 183

6.5 Morphological study of N-doped TiO_2 films 184

6.5.1 Scanning electron microscopy 184

6.5.2 Atomic force microscopy 184

6.6 Optical characterisation of N-doped TiO_2 films 185

6.6.1 UV-Vis spectroscopy study on N-doped TiO_2 films 185

6.6.2 Determination of bandgap of N-doped TiO_2 films 185

6.6.3 Effect of nitrogen concentration on bandgap of N-doped TiO_2 films 186

CHAPTER 7 207

Conclusions and Future Work 207

7.1 Conclusions 207

7.2 Future work 211

REFERENCES 219

LIST OF TABLES

2.1 A comparison between different film processing methods, CVD, PVD and EHDP 69
2.2 Crystal structure data of TiO_2 72
4.1 Physical properties of TiO_2 sol and ethanol 121
5.1 Effective dielectric constant of TiO_2 films 153
5.2 The bandgap of TiO_2 films annealed at different temperatures 160
6.1 Physical properties of N-doped TiO_2 sol and ethanol 171
6.2 Deposition area and spray angle for two experimental set-ups 177
6.3 The nitrogen content in the nitrogen doped TiO_2 films 183
6.4 The bandgap and value of empirical parameter for films of different composition 187

LIST OF FIGURES

2.1 (a, b, c & d) First ever classification of different modes of electrohydrodynamic processing (Zeleny, 1917) 79
2.2 (a, b & c) Stages involved in establishing steady state cone (Taylor, 1964) 80
2.3 (a & b) Stable cone-jet mode and jet break-up (Tang and Gomez, 1996) 81
2.4 (a, b, c & d) An innovative electrostatic atomisation printing (EAP) of ceramic tracks obtained at different applied voltages (Jayasinghe and Edirisinghe, 2002) 82
2.5 Jet break-up in stable cone-jet mode (a) varicose instability (b) kink instability (Jaworek and Krupa, 1999) 83
2.6 Dripping mode of electrohydrodynamic processing (Jaworek and Krupa, 1999) 83
2.7 Micro-dripping mode of electrohydrodynamic processing (Jaworek and Krupa, 1999) 84
2.8 Spindle mode of electrohydrodynamic processing (Jaworek and Krupa, 1999)... 84
2.9 Rim-emission mode of electrohydrodynamic processing (Jaworek and Krupa, 1999) 85
2.10 Ramified mode of electrohydrodynamic processing (Jaworek and Krupa, 1999) 85
2.11 Oscillating-jet mode of electrohydrodynamic processing (Jaworek and Krupa, 1999) 86
2.12 Precession mode of electrohydrodynamic processing (Jaworek and Krupa, 1999) 86
2.13 Variation in cone shape with change in applied voltage (Jayasinghe and Edirisinghe, 2004) 87
2.14 Droplet average diameter as a function of liquid flow rate (Tang and Gomez, 1996) 87
2.15 The variation of relic sizes with flow rate (Jayasinghe and Edirisinghe, 2004) . 88
2.16 The variation of jet diameter with flow rate (Jayasinghe and Edirisinghe, 2005) 88
2.17 The variation of length of liquid column with flow rate and applied voltage (Sung and Lee, 2004) 89
2.18 The trajectory of the droplet of suspension moving from the exit of the needle to point like ground electrode (Jayasinghe and Edirisinghe, 2004) 90

2.19 The optical micrographs of relics obtained with variation in viscosity of the liquid mixtures (Jayasinghe and Edirisinghe, 2002) 91
2.20 An innovative ball cone effect obtained with the silicone oil (Jayasinghe and Edirisinghe, 2004) 92
2.21 The micro-threading effect of liquid with viscosity $>10^4$ mPa s (Jayasinghe and Edirisinghe, 2004) 93
2.22 Schematic of physical sputtering process (Seshan, 2002) 94
2.23 A typical reactive sputter deposition system (Seshan, 2002) 94
2.24 A typical CVD process set-up (www.timedomaincvd.com) 95
2.25 Different phases of TiO_2 (a) rutile (b) anatase (c) brookite 96
2.26 A relationship between bandgap and dielectric constant for simple dielectrics (Campbell et al., 1997) 97
2.27 Excitation occurs in TiO_2 when light absorption with energy equal to or greater than bandgap energy 97
3.1 Electrohydrodynamic processing set-up for TiO_2 films investigations 116
3.2 Electrohydrodynamic processing set-up for N-doped TiO_2 films investigations 117
3.3 Electrohydrodynamic processing set-up for N-doped TiO_2 films investigations 118
3.4 Heat treatment cycle for as-deposited TiO_2 and as-deposited N-doped TiO_2 films 119
4.1 TGA of titania sol 135
4.2 Mode selection map for the titania sol 136
4.3 Dripping mode at flow rate of 1×10^{-10} m^3s^{-1} and no applied voltage 137
4.4 Micro-dripping at flow rate of 1×10^{-10} m^3s^{-1} and 3.1 kV 137
4.5 Unstable cone-jet mode at flow rate of 1×10^{-10} m^3s^{-1} and 4.1 kV 138
4.6 Stable cone-jet mode at flow rate of 1×10^{-10} m^3s^{-1} and 4.5 kV 138
4.7 Multi-jet mode at flow rate of 1×10^{-10} m^3s^{-1} and 6 kV 139
4.8 Stable cone-jet mode at flow rate of 1.2×10^{-10} m^3s^{-1} and 5.5 kV 139
4.9 Stable cone-jet mode at flow rate of 1.6×10^{-10} m^3s^{-1} and 5.5 kV 140
4.10 Stable cone-jet mode at flow rate of 2×10^{-10} m^3s^{-1} and 5.5 kV 140
4.11 Stable cone-jet mode at flow rate of 2.4×10^{-10} m^3s^{-1} and 5.5 kV 141
4.12 Droplet size distribution obtained by laser spectrometry. Results of repeated experiments are shown as different coloured plots 141
4.13 Optical micrograph of droplets soon after deposition 142
4.14 Raman spectra of TiO_2 films annealed to different temperatures 142

4.15 X-ray diffraction of TiO_2 films annealed to different temperatures 143
4.17 SEM image of as-deposited TiO_2 film electrohydrodynamically processed at 1×10^{-10} m^3s^{-1} and 4.5 kV on Si substrate (magnification ×1000) 144
4.18 SEM image of as-deposited TiO_2 film electrohydrodynamically processed at 1×10^{-10} m^3s^{-1} and 4.5 kV on Si substrate (magnification ×6500) 144
4.19 SEM image of TiO_2 film electrohydrodynamically processed at 1×10^{-10} m^3s^{-1} and 4.5 kV on Si substrate annealed at 500 °C (magnification ×2700) 145
4.20 SEM image of TiO_2 film electrohydrodynamically processed at 1×10^{-10} m^3s^{-1} and 4.5 kV on Si substrate annealed at 500 °C (magnification ×6500) 145
4.21 SEM image of TiO_2 film electrohydrodynamically processed at 1×10^{-10} m^3s^{-1} and 4.5 kV on Al substrate annealed at 500 °C (magnification ×1400) 146
4.22 SEM image of TiO_2 film electrohydrodynamically processed at 1×10^{-10} m^3s^{-1} and 4.5 kV on Al substrate annealed at 500 °C (magnification ×6500) 146
4.23 SEM of TiO_2 film electrohydrodynamically processed at 1×10^{-10} m^3s^{-1} and 4.5 kV with high magnification (×230 000) 147
4.24 Cross sectional view of TiO_2 film electrohydrodynamically processed at 1×10^{-10} m^3s^{-1} and 4.5 kV (spray time 60 s) 147
5.1 FTIR studies of TiO_2 films annealed at different temperatures 163
5.2 Low frequency C-V characteristics for different annealing temperatures 164
5.3 High frequency C-V characteristics for different annealing temperatures 165
5.4 Current-Voltage characteristics for different annealing temperatures 166
5.5 Current density-Voltage characteristics for different annealing temperatures 166
5.6 Optical transmittance spectra of TiO_2 films annealed at different temperatures 167
5.7 Graph of $\alpha^{1.2}$ vs. $h\gamma$ for different annealing temperatures 168
6.1 Mode selection map for the N-doped titania sol with set-up **1** 189
6.2 Mode selection map for the N-doped titania sol with set-up **2** 190
6.3 Dripping mode at flow rate of 0.67×10^{-10} m^3s^{-1} and zero applied voltage 191
6.4 Micro-dripping at flow rate of 0.67×10^{-10} m^3s^{-1} and 2 kV 191
6.5 Unstable cone-jet mode at flow rate of 0.67×10^{-10} m^3s^{-1} and 3.3 kV 192
6.6 Stable cone-jet mode at flow rate of 0.67×10^{-10} m^3s^{-1} and 3.7 kV 192
6.7 Stable cone-jet mode at flow rate of 0.67×10^{-10} m^3s^{-1} and 4.3 kV 193
6.8 Stable cone-jet mode at flow rate of 0.67×10^{-10} m^3s^{-1} and 4.5 kV 193
6.9 Multi-jet mode at flow rate of 0.67×10^{-10} m^3s^{-1} and 4.9 kV 194
6.10 Multi-jet mode at flow rate of 0.67×10^{-10} m^3s^{-1} and 7.5 kV 194

6.11 Raman spectra of TiO_2-N1 films annealed to different temperatures 195
6.12 Raman spectra of TiO_2-N2 films annealed to different temperatures 196
6.13 Raman spectra of TiO_2-N3 films annealed to different temperatures 197
6.14 X-ray diffraction of TiO_2-N2 films annealed to different temperatures 198
6.15 Variation of crystallite size with annealing temperature for TiO_2-N2 films 198
6.16 FTIR studies of TiO_2-N1 films annealed at different temperature 199
6.17 FTIR studies of TiO_2-N2 films annealed at different temperature 199
6.18 FTIR studies of TiO_2-N3 films annealed at different temperature 200
6.19 XPS high resolution plots for TiO_2-N1 films 201
6.20 XPS high resolution plots for TiO_2-N2 films 202
6.21 XPS high resolution plots for TiO_2-N3 films 203
6.22 SEM image of TiO_2-N2 film electrohydrodynamically processed at 0.67×10^{-10} m^3s^{-1} and 3.9 kV on Si substrate annealed at 500 °C (magnification ×6500) 204
6.23 AFM image of TiO_2-N2 film electrohydrodynamically processed at 0.67×10^{-10} m^3s^{-1} and 3.9 kV on Si substrate annealed at 500 °C 204
6.24 Optical transmittance spectra of N-doped TiO_2 films annealed at 500 °C 205
6.25 Graph of $\alpha^{1/2}$ vs. $h\gamma$ for undoped TiO_2, TiO_2-N1, TiO_2-N2 and TiO_2-N3 The inset is $\ln\alpha$ vs.$h\gamma$ curves of the films 206

CHAPTER 1

Introduction

1.1 Fundamentals of electrohydrodynamic processing

Electrohydrodynamic processing is a process where a nozzle carrying liquid subjected to a high voltage, breaks up in to droplets. It is also referred as electrohydrodynamic atomisation (EHDA) or electrospraying (ES). The liquid under electric stress due to high potential difference between the nozzle and the ground electrode, emit plume of droplets which is called as spray. This spraying phenomenon was subjected to study for nearly a century.

The first systematic study of this phenomenon with a published work was dated back to 1914 by Zeleny. He further continued his research and reported on this phenomenon in the following years as well (Zeleny, 1915, and 1917). There after many people contributed to understanding this process however, Taylor (1964) was the first to calculate analytically the process by balancing the surface tension force and the electric field force acting on the droplet at the end of the nozzle. After the discovery of mass spectroscopy of large biomolecules by Fenn et al. (1989), the interest in electrohydrodynamic processing has grown in recent years as applications to material processing.

One of the most important features of electrohydrodynamic processing is the mode of spraying. The modes of spraying differ in the process of formation of the meniscus (droplet at the end of the nozzle) and the jet emerging from this meniscus (Cloupeau and Prunet-Foch, 1990; Jaworek and Krupa, 1999). The modes of spraying observed in the electrohydrodynamic processing namely dripping, micro-

dripping, spindle, stable cone-jet and multi-jet together with their numerous manifestations. Of these, the stable cone-jet mode is mostly studied by many people as it generates near mono-dispersed droplets of a few micrometers in size (Cloupeau and Prunet-Foch, 1989).

In the stable cone-jet mode, a liquid is forced through a nozzle and an electric field is applied over the nozzle and a ground electrode. This electric field induces a surface charge on the droplet formed at the exit of the nozzle. Due to this surface charge, and due to the electric field, an electric stress is created in the liquid surface. These electric stresses transform the droplet shape in to a conical shape by balancing the surface tension force acting against the electric stress. The tangential electric field accelerates the charge carriers at the liquid surface towards the cone apex. When these charge carriers collide with the surrounding liquid molecules the acceleration of the surrounding liquid take place. As a result a thin liquid jet emerges at the cone apex. This jet can break up into a number of main droplets with a narrow size distribution and a number of smaller secondary droplets and satellites (Cloupeau and Prunet-Foch, 1989; Tang and Gomez, 1994; Chen et al., 1995).

The electrohydrodynamic processing is influenced by liquid properties such as surface tension, electrical conductivity, relative permittivity, viscosity and density along with processing parameters such as liquid flow rate and applied voltage. For an example, a research work carried out by Jayasinghe and Edirisinghe (2002a) showed that, the increase in viscosity of the solution will increase the droplet size produced in a stable cone-jet mode processing.

The droplets obtained in the electrohydrodynamic processing are highly charged up to a fraction of the Rayleigh limit. The Rayleigh limit (1882) is the magnitude of charge on a drop which overcomes the surface tension force that leads to the drop fission. The charge and size of the droplets can be controlled by adjusting the liquid properties and processing parameters. The deposition of a charged spray on an object can be more effective than for uncharged spray (Jaworek et al., 2001). Some of the advantages of electrohydrodynamic processing in stable cone-jet mode are:

i. Droplets have size smaller than those available from conventional mechanical atomisers, and can be smaller than 1 μm.

ii. The size distribution of the droplets is narrow (monodispersity of droplets) and the shape of the droplets are spherical. The size distribution of the droplets could be controlled by adjusting the liquid properties and processing parameters.

iii. The charged droplets are self-dispersing in the space, which results in absence of droplet agglomeration and coagulation.

iv. The motion of charged droplets could be controlled by electric field modulation between the nozzle and the ground electrode.

v. The deposition efficiency of the charged spray on an object is much higher than for uncharged droplets.

1.2 Contents of this thesis

Chapter 1 of this thesis introduces the fundamentals of electrohydrodynamic processing. It briefly states the origin of the spraying phenomenon and the main features of the processing. The stable cone-jet mode processing and the advantages of that mode are briefly stated. This chapter also presents the overview of the thesis contents. The aims and objectives of the research carried out are clearly mentioned. This chapter further states the scope of the research under taken.

Chapter 2 includes a detailed literature study of the investigations that have been carried out previously by other people in the area of electrohydrodynamic processing. The various modes of electrohydrodynamic processing are analysed and discussed in depth. The main processing steps involved in the electrohydrodynamic processing in stable cone-jet mode are presented. This chapter also states the properties influencing the electrohydrodynamic processing including liquid physical properties and processing parameters. The fundamental concepts and theories underlying this research are discussed in the form of scaling laws derived by researchers in this field. This chapter goes on to explain the other deposition methods have been in use to prepare the films and thin films alternative to electrohydrodynamic processing. Their relative merits and demerits are tabulated along with the electrohydrodynamic processing. Finally, this chapter explains the structure and properties of TiO_2 and the applications of the TiO_2 in various fields. It concludes with doping of TiO_2 by external atoms and the reason for selection of nitrogen atom to improve the optical properties of the films.

Chapter 3 discusses the experimental details and procedures under taken in the research described in the following chapters. It describes the materials and preparations of the sols used in the research. The characterisation techniques and procedures of sols are explained in detail. The equipments used for the electrohydrodynamic processing are clearly discussed. The novel method used for the film preparations and the annealing steps followed for the prepared films are explained. The MOS capacitor fabrication for the electrical characterisation is given as well. The characterisation techniques used for the prepared films are well addressed. The basic principles behind the various characterisation techniques used for the prepared films are also summarised.

Chapter 4 explains the first investigation carried out in this thesis, the TiO_2 film preparation and the microstructural characterisation of the films. This research is the stepping stone for the research carried out in the following chapter. This chapter includes the effect of applied voltage and flow rate in preparing the TiO_2 films. The applied voltage-flow rate map (mode-selection map) was constructed with various spraying mode domains in order to select the best processing condition for the TiO_2 film preparation. The stable cone-jet and droplet characterisation is also given in this chapter. The microstructural characterisation of the prepared films was done using the Raman spectroscopy, x-ray diffraction studies and scanning electron microscope studies. The results obtained with these techniques are clearly demonstrated and discussed in this chapter.

Chapter 5 discusses the electrical and optical characterisation of electrohydrodynamically processed TiO_2 films. The Fourier transform infrared

spectroscopy studies of the prepared TiO_2 films on Si substrate are explained. The electrical characterisation of the films was done using the fabricated simple MOS structure. The capacitance-voltage and current-voltage characteristics of processed TiO_2 films are analysed in this chapter. The dielectric constant of the prepared TiO_2 film was evaluated for different annealing temperatures. The effect of annealing temperature on dielectric constant and leakage current density of the films are well discussed in this chapter. The optical properties of processed TiO_2 films were evaluated from the uv-vis spectroscopy studies of the films annealed to different temperatures. Further, the effect of annealing temperature on optical properties is discussed. Finally, the energy bandgap of TiO_2 films is determined and the effect of annealing temperature on their values is explained.

Chapter 6 describes the electrohydrodynamic processing of N-doped TiO_2 films and their characterisation. The novel method employed to process the N-doped TiO_2 films with a larger deposition area is presented. This chapter explains the effect of applied voltage and flow rate in preparing the N-doped TiO_2 films. The mode-selection map was drawn with various applied voltage and flow rate values for two set-ups used in processing the N-doped TiO_2 films. The different spraying mode domains were identified and the best processing conditions were selected in order to prepare the N-doped TiO_2 films. The effect of metal clamped needle on applied voltage and deposition area is discussed. This chapter further describes the effect of nitrogen concentration on structural features of N-doped TiO_2 films. The structural features were studied by Raman spectroscopy and x-ray diffraction. The atomic bonding was studied by Fourier transform infrared spectroscopy. The x-ray photoelectron spectroscopy was used to find out the nitrogen content in the films.

The morphological studies were carried out by scanning electron microscopy and atomic force microscopy. The optical characterisation of N-doped TiO_2 films was done using the uv-vis spectroscopy. The energy bandgap of N-doped TiO_2 films are determined and the values are tabulated for different nitrogen doping concentrations. Finally, the effect of nitrogen concentration on energy bandgap of the N-doped TiO_2 films is discussed.

Chapter 7 points out the conclusions made on the investigations carried out in **chapters 4, 5** and **6**. It also summarises the future work that should be carried out to exploit this interesting area of research.

1.3 Aims and objectives of the research

The main aim of this research is completely understanding the electrohydrodynamic processing and making use of this technique as a novel method to prepare the TiO_2 films compared to other alternative processing routes. The research aims to understand the basic principles underlying the electrohydrodynamic processing in stable cone-jet mode. There are various spraying modes have been identified in this processing which are influenced by liquid physical properties and processing parameters. Therefore, a careful study of the physical properties of liquid with processing parameters such as applied voltage and flow rate is paramount in this research. This study helps to establish the suitable processing conditions for preparing the TiO_2 films in stable cone-jet mode.

The basic understanding of principles which drive the electrohydrodynamic processing and the influencing parameters on this process should be carefully

studied before undertaking the research. Of the many modes of processing, the unique feature of stable cone-jet mode processing is to generate near mono-disperse droplets in micro and nano size range. Therefore, this research also aims to conduct a thorough literature survey to understand the various principles behind the electrohydrodynamic processing and the importance of the stable cone-jet mode over all other modes. The jet breaks up mechanism in the stable cone-jet mode and the reasons for the formation of near mono-disperse droplets are to be understood.

There are various methods available to deposit the films and coatings such as chemical vapour deposition and physical vapour deposition. A clear understanding about these techniques along with their merits and demerits is very important. The distinct advantages of electrohydrodynamic processing over these techniques are to be thoroughly understood. This research aims to carry out a detail literature study on this as well.

It is very important to understand the mechanism in which crack free crystalline TiO_2 films could be processed. The careful collection of charged droplets produced in the stable cone-jet mode processing helps to prepare the uniform films. The characterisation of films helps us to investigate the factors that dominate the formation of the microstructures. This could help us to vary the conditions or parameters in which material should be processed. The characterisation of films could be done by various methods. To compare the results of each method the films should be prepared in the same conditions.

This research also intends to show that the electrohydrodynamic processing could be utilised for preparing the TiO_2 films as an alternative to other methods. Since the stable cone-jet mode processing produce near mono-disperse droplets and have same polarity charge it could be used for preparing the uniform films with controlled thickness. The TiO_2 films are frequently found in applications related to microelectronics, photocatalysis and photoelectric. Therefore, the electrical and optical properties of TiO_2 films should be carefully studied and analysed. To completely understand the properties of TiO_2 films, the electrical and optical characterisation of the processed films are to be done and the associated properties are to be evaluated.

The TiO_2 films are efficient photocatalyst, however it absorbs ultraviolet light below 380 nm wavelengths (Shen et al., 2007). Therefore, to effectively utilise the sunlight, its absorption should be extended to visible light region. One of the ways to achieve this objective is to doping the TiO_2 by external atoms. The nitrogen doping in TiO_2 films are useful in visible light absorption (Asahi et al., 2001). This research aims to show that the N-doped TiO_2 films could be processed by electrohydrodynamic route and it could improve the visible light absorption.

The doping concentration of the nitrogen based precursors could alter the physical properties (surface tension, electrical conductivity, viscosity and density) of the sols used to prepare the N-doped TiO_2 films. This in turns influence the electrohydrodynamic processing along with processing parameters. The careful study of the physical properties of N-doped sols and then the processing parameters like applied voltage and flow rate is very important to establish the suitable

processing conditions for process the N-doped TiO_2 films in the stable cone-jet mode. This research also aims to show that the doping concentration influence the microstructural features of the N-doped TiO_2 films and the optical properties of films.

In electrohydrodynamic processing, increasing the flow rate will normally result in a larger deposition area, however, this can lead to secondary droplets and satellites (Hartman et al., 2000; Jayasinghe and Edirisinghe, 2004a). Therefore, an alternative route for depositing larger coverage area films by electrohydrodynamic route should be found. This research aims to show that the metal clamped needle could be used for preparing the larger coverage area films at low flow rate regimes.

1.4 Scope of this research

This research offers various interested parties the fundamentals and insight knowledge of electrohydrodynamic processing of TiO_2 films and N-doped TiO_2 films. It will benefit the films and coatings industries as electrohydrodynamic processing route could be capitalised to prepare the uniform and controlled thickness films. The various deposition methods including chemical vapour deposition and physical vapour deposition have their own limitations. This research offers an exciting new route for processing the TiO_2 and N-doped TiO_2 films. It has unique advantages like simple set-up and economical way to prepare the films. Depending on the applications it could be used to process the other films have different compositions as well.

The TiO_2 is a popular material with many applications in electronics and optoelectronics due to its high permittivity and refractive index (Chong et al., 2006). The electrohydrodynamically processed TiO_2 films could be used in microelectronic applications. The high permittivity of TiO_2 could pave a way to use this material as a gate oxide in complementary metal oxide semiconductor (CMOS). In addition to this, the electrohydrodynamically processed TiO_2 films could be used in anti-reflection coatings, sensors and photocatalysis.

The ecological elimination of pollutants is an issue of increasing concern in today's society. The TiO_2 is an excellent photocatalyst that permits the degradation and finally the mineralization of stable organic pollutants. However, it requires UV radiation whose energy exceeds the bandgap of TiO_2 hence ruling out the use of sunlight as an energy source for the photodegradation (Justicia et al., 2002). The electrohydrodynamically processed N-doped TiO_2 films could be useful in absorbing visible spectrum of the sunlight and hence could be lead to photodegradation of pollutants using sunlight. The electrohydrodynamically processed N-doped TiO_2 films could also very useful in photovoltaic applications to generate current.

CHAPTER 2

Literature Review

2.1 Electrohydrodynamic processing

Electrohydrodynamic processing is a process where a liquid breaks up into spray droplets under the influence of an electrical field. There are many modes of electrohydrodynamic processing, of these the stable cone-jet is attractive, in this process, liquid flowing through a capillary maintained at high potential is subjected to an electric field, which causes elongation of the meniscus to a form of jet and subsequently the jet deforms and disrupts into droplets. This basic technology, even though it deems to be simple technique to appearance, it could be more complex in understanding the exact phenomenon due to inter-relationship between the liquid properties and the dependence on liquid flow rate and applied voltage to certain extent.

The disruption of a liquid surface into a spray of charged droplets when subjected to an intense electric field has been known for more than two centuries since Bose recorded the phenomenon in 1745. This phenomenon was later explained as the action taking place on a liquid drop of electric forces opposing those of surface tension. Rayleigh (1879) found that when the charge on the drop reaches a certain value, the electric forces become stronger than those of surface tension, and the drop becomes unstable. Rayleigh made the earliest observation of instability of a droplet due to electric charge. The stability of a drop is depended upon the balance of forces, between the outward electrical stress tending to disrupt the drop and the counteracting surface tension forces which tries to hold the drop together (Rayleigh, 1882).

Rayleigh calculated the electric charge beyond which a droplet is no longer stable. This charge is given by the following equation and it is called as Rayleigh limit of the charges (Rayleigh, 1882).

$$Q_R = 2\pi(16\gamma\varepsilon_o r^3)^{1/2} \tag{2.1}$$

in which γ is the liquid surface tension, ε_o is the electric permittivity of the free space and the r is the droplet radius.

However, it is only since beginning of this century that this phenomenon has attracted considerable interest from both a fundamental and an application point of view. The pioneering work by Zeleny (Zeleny, 1914,1915, and 1917) with a nozzle carrying liquid and a ground electrode set up subjected to a high voltage that marked the important break through into this exciting field of research. The set up he used was followed by many researchers there after and it is still in use. He photographed drops held at the end of capillary tubes. He observed different modes of disruption of liquids and it is the first ever classification of modes reported. Some of the pictures showing the different modes of spraying taken from his work have been shown in **Figure 2.1**.

Although a good deal of interest in isolated electrified droplets existed for some years after but very serious effort was made on this phenomenon until Vonnegut and Neubauer (1952) noticed that mono-disperse aerosols having a particle radius of a micron or less can be formed if the capillary is positively charged and if the liquid having low electrical conductivity are used. Drozin (1955) has systematically

investigated the electrical dispersion of liquid as aerosols and evaluated the dispersion of liquid in terms of physical properties such as specific conductivity, dielectric constant and dipole moment. He found that a liquid with a negligible dielectric constant could not be dispersed and liquid dispersion could only take place only if the conductivity is below an upper limit. But the quantitative measurements regarding the limits were not explained in detail in his reporting.

The existence of steady state mode has not been satisfactorily explained on that time. Taylor (1964) was the first to derive the conditions for a meniscus to exist in equilibrium in conical form under the competing actions of electric filed and surface tension. Taylor (1964) studied the break-up of a droplet using glycerine and glycerine-water mixture when electric field is applied to the capillary tube carrying the liquid. He noticed in his investigations that when a fluid is conducting and the jet having a high viscosity the liquid does not vibrate before spraying but rather it would adopt a conical shape. He measured the conical shape to be having a sharp apex at a semi-vertical angle that was nearly equal to 49.3°. This is the angle at which a conical meniscus of a conducting liquid can exist in equilibrium under an applied electric field. The captured pictures in his research are shown in **Figure 2.2**.

Hogan and Hendricks (1965) measured the charge to mass ratio and considered the key factors influencing this, an important break through during this period. Jones and Thong (1971) found that electrical dispersion of a jet of kerosene into spray of mono-disperse droplets could only achieved within a range of applied voltage and the droplet size is almost independent of voltage however a function of flow rate.

Mutoh et al. (1979) claimed that steady state mode exist only if the conductivity of the liquid between certain limits. In the later year, Nagorynyi and Bezrukov (1980) investigated the decrease in droplet diameter at increasing applied potential, thereby suggesting the conditions necessary to produce smaller droplets.

Smith (1986) presented his experimental study on the process in terms of liquid properties such as conductivity, surface tension and viscosity. He also outlined a model for the process assuming that the meniscus is not quite an equipotential surface. In the later year Hayati et al. (1987) studied the effect of surrounding gas breakdown potential with the process. They said if that potential is lower than that required for liquid instability then electrostatic atomisation is not possible. It is only possible the gases with a higher breakdown potential than required for liquid instability. They also pointed out that the conductivity of the liquids plays a major role in the electrostatic disruption of liquids flowing through a capillary. With insulating liquids little disruption occurs since insufficient free charges are available in the bulk of the liquid. With conducting liquids very unstable streams are produced with some sparking at higher potential. Stable jets are only produced with semi conducting liquids when a sufficient voltage is applied.

The most significant work in electrohydrodynamic processing after Zeleny (1917) and Taylor (1964) was the classification of functioning modes of spraying by Cloupeau and Prunet-Foch (1990). The main modes of electrohydrodynamic processing will be discussed in detail in the following section. For constant liquid properties and flow rate electrohydrodynamic processing progresses through several visual and measurable differences with increasing applied voltage. These

differences are defined as spray modes. The particular spray mode achieved depends on the operating conditions of the experiments. Cloupeau and Prunet-Foch (1990) described the specific characteristics of each mode such as the different types of particle size distribution of aerosols emitted and the causes of irregularity in drop sizes. Followed their work Jaworek and Krupa (1999) characterised and presented the modes of electrohydrodynamic processing by two criteria: (1) The geometrical form of the liquid at the outlet of the capillary (2) The type of the jet behaviour in its disintegration into droplets. The differences between processing at positive polarity compare to negative polarity indicated in their work. At positive polarity the droplets are usually finer and the jet elongating from the meniscus is much longer.

For the larger application potential the stable cone-jet mode attracted more attention from researchers. Balachandran et al. (1992) have achieved a stable cone-jet for high flow rates (~ 10^{-9} m^3s^{-1}) and a highly conducting fluid. Rulison and Flagan (1993) generated monodisperse droplets in the order of micron and studied their electrical properties. A later work by Gomez and Tang (1996) used the capillary-plate configuration with a constant pressure source and flow rates to study the doped heptane. They investigated the cone-jet disintegration in to droplets due to electrical surface instability. Some excellent photographs of droplets during this process are presented and these are shown in **Figure 2.3**. Another significant work during 1990s was the scaling laws derived by various researchers (De la Mora and Loscertales, 1994; Ganan-Calvo et al., 1997). The relationship between the various liquid properties (liquid flow rate, electrical conductivity, surface tension, relative permittivity, density and viscosity) which are used to estimate the droplet diameter

and the current through the liquid cone are called scaling laws. This will be discussed in detail in section **2.5**.

The electrohydrodynamic processing in application point of view was well investigated by Edirisinghe and his co-workers. A lot of pioneering work marked important break through in ceramic processing industry. The most contributing and significant work was the invention of electrostatic atomization printing (EAP) for ceramic processing (Jayasinghe and Edirisinghe, 2002b). This gave a new dimension to ceramic processing field. They used a point-like ground electrode to control the trajectory of the droplets to print tracks with the aid of a stepper motor. **Figure 2.4** shows the printed track in their investigations. Jayasinghe and Edirisinghe (2002c) used the electrohydrodynamic processing to form ceramic foams which could be used in many applications namely catalyst support, fluid filters and gas diffusers. They also used this technique to prepare chitosan (Jayasinghe and Edirisinghe, 2003) and aspirin particle formation (Li et al., 2005) where they are useful in biomedical applications.

2.2 Main modes of electrohydrodynamic processing

Electrohydrodynamic processing, also called electrospraying refers to a process where a liquid breaks up into droplets under the influence of electrical forces. Depending on the strength of electric stresses in the liquid surface relative to the surface tension stress, and the kinetic energy of liquid leaving the nozzle, different spraying modes will be obtained. The mode of electrohydrodynamic processing refers to the way how the liquid is dispersed into droplets (Jaworek and Krupa, 1999). Many researchers have discussed the different modes of

electrohydrodynamic processing and have classified it according to the properties of meniscus and jet.

According to the investigations by Jaworek and Krupa (1999) the modes are discussed based on mainly two characteristic criteria;

(1) The geometrical configuration of the liquid at the end of the capillary

(2) Type of jet behaviour in the disintegration into droplets

Based on these criteria the processing modes are generally divided into two groups. The first group consists of the modes in which fragments of liquid are ejected from the capillary, such as the dripping and spindle modes. Second group includes the modes in which the liquid produces a long continuous jet which disintegrates into droplets at some distance usually a few mm from the outlet of the capillary; an example is the stable cone-jet mode. The meniscus and the jet in the second group can be stable, vibrating, or rotating spirally around the capillary axis.

Each mode has multiple characteristics and the transition between modes is not always well defined. However, for a liquid of given property the processing modes changes from one to another. This change takes place with the corresponding change in applied voltage and flow rate. This led to the work of classification of different processing modes. These modes are discussed below in detail.

2.2.1 Cone-jet mode

This is the mode that attracts most of the researchers, because of its ability to produce near monodisperse liquid droplets with a reasonable production frequency.

It also referred to as Taylor cone mode of spraying. In the cone-jet mode the liquid leaves the capillary in the form of a regular cone with a thin jet at the apex, stretching along the capillary axis. The jet is usually 100 micrometers in diameter (Hartman et al., 1999).

Electrohydrodynamic processing in the cone-jet mode has three different processes. The first process is the acceleration of the liquid in the liquid cone. This acceleration process and the shape of the liquid cone are mainly a result of the force balance of surface tension and electric stresses in the liquid surfaces. Taylor (1964) was the first to calculate analytically a conical shape, which balanced the surface tension and the electrical normal stress. However, in his assumptions there was no liquid jet at the cone apex.

The second process in electrohydrodynamic processing in the cone-jet is the break up of the jet into droplets. Each liquid has a minimum flow rate, below which a stable cone-jet mode cannot exist. At this minimum flow rate the jet breaks up due to axisymmetric instabilities. These instabilities are also called varicose instabilities. At higher flow rates, the current through the liquid cone increases due to this surface charge on the jet increases. Above a certain surface charge the jet break up will also be influenced by lateral instabilities of the jet. These instabilities are also called kink instabilities. When the influence of these kink instabilities increases, the produced size distribution of the main droplets become wider (Cloupeau and Prunet-Foch, 1989). Above a certain maximum flow rate, no stable cone-jet mode can exist.

The different forms of the cone are possible linear sides, convex or concave. The bottom part of the jet may undergo either varicose or kink instability. **Figure 2.5** shows a cone jet undergoing varicose and kink instabilities. In the case of varicose instabilities the waves are generated on the surface of the jet, but the jet does not change its linear position. The wave contracts in the nodes and the jet disintegrates into equal droplets. In the case of kink instabilities the jet moves irregularly, and breaks up into droplets due to electrical and inertial forces (Hartman et al., 2000). The space charge in the cone-jet mode is much more stable than in other spraying modes because the droplets are smaller and less mobile. The jet diameter becomes lower and its length becomes shorter with the increasing voltage.

The third process is the development of the spray after droplet production. Electrical interaction between highly charged droplets with different sizes and thus different inertia causes the size segregation effect. Small droplets will be found at the edge of the spray and the larger sizes will be found in the spray centre (Ganan-Calvo et al., 1994). If the highly charged droplets evaporate, then the Rayleigh limit for droplet charge can be reached. In that case, droplet fission can take place which changes the produced size distribution. The droplet size and droplet charge depend mainly on the liquid flow rate and on liquid properties like density, viscosity, conductivity, electrical permittivity, and surface tension. Depending on the liquid properties, the main droplet size produced ranges from nanometres with production frequencies in the order of 10^9 Hz to hundreds of micrometers with production frequencies of about 10^4 Hz. (Hartman, 1998).

2.2.2 Dripping, micro-dripping, spindle mode and intermittent cone-jet mode

A liquid is fed through a nozzle at a constant flow rate. In case of a low liquid flow rate, without an electric field applied over the droplet hanging down from the nozzle, droplets are produced at frequencies lower than 1 Hz. When an electric field is applied, which slowly increases, and then the frequency of droplet production increases. This is called dripping mode.

In the dripping mode the drops take the shape of regular spheres detaching from the capillary as the gravity force and the electric force together overcome the surface tension forces. After the detachment of the drops, the meniscus usually contracts back to form a hemispherical like meniscus before the same process take place again. The drop formation time is much longer than that of the fall of the former drop, so the drop formation is not affected by the charges carried by those previous drops.

When the voltage is increased there is an increase in electrostatic force, resulting in the elongation of the meniscus and hence smaller droplets are obtained. If the electric voltage applied is increased further, the drop is connected with the capillary by a thread, which breaks up as the drop falls, and a sibling is generated from this thread as shown in **Figure 2.6**. The sibling is usually perpendicular to the capillary axis. Also the emission of drops occurs at regular time intervals without creation of satellites; therefore all the drops can have nearly the same size, which is generally greater than the capillary diameter. The production frequency is usually low (Jaworek and Krupa, 1999) compared to other modes.

Micro-dripping occurs at the lowest liquid flow rates, and produces a narrow size distribution at a production frequency of a few kHz (Cloupeau and Prunet-Foch, 1990). **Figure 2.7** shows the occurrence of micro-dripping mode. In this mode, the electric force near the capillary exit is sufficiently high to keep a stable hemispherical or ellipsoidal meniscus. Therefore the meniscus does not need to contract back after each time when the droplet has formed at the tip of capillary which is another difference in the micro-dripping mode. The charge on the droplets approaches half of the Rayleigh limit. Even though the droplet production frequency becomes higher, the space charge formed by previously generated droplets is too weak to affect the generation process. Because the droplets are quickly removed by the electric field as well as that the size of the droplet is not sufficiently big enough (Jaworek and Krupa, 1999).

The spindle and the intermittent cone-jet mode occur at a higher liquid flow rate and at higher electric fields than micro-dipping. The spindle mode occurs when the flow rate and electric field are sufficiently increased, the liquid can elongate in the direction of the electric field, ending up with a relatively thick jet and a spindle-like fragment before a continuous jet is formed. This mode is shown in **Figure 2.8**. The spindle mode occurs at higher voltages than the dripping mode, and differs from the dripping mode in that no regular droplet is formed. After the detachment, the spindle like jet disrupts into several smaller droplets of different sizes, while the meniscus contracts to its initial shape, and a new jet starts to be formed. The intermittent cone-jet mode sometimes referred as unstable cone-jet mode is similar to spindle mode. However, there is a different observed in the size distribution of droplets formed. In the spindle mode a significant part of the liquid flow is used for

the formation of the main drops of relatively large size but in the intermittent cone-jet mode the entire flow resolves into a multitude of fine droplets (Cloupeau and Prunet-Foch, 1990).

2.2.3 Multiple-jet mode and rim-emission mode

The multi-jet mode can be developed from the cone-jet mode by increasing the electrical potential. When increase the applied potential difference, the electric field strength around the liquid cone will increases. Then the spraying mode goes from the cone-jet mode into the multiple-jet mode or into rim-emission mode.

With increasing potential difference the liquid cone of the cone-jet mode becomes smaller and smaller. At a certain moment, the liquid cone is too small for the capillary. The cone moves from the centre of the capillary toward the edge. When the potential difference increased further, then a second cone will occur. With increasing potential difference, more and more cones will be formed. For a multiple-jet mode, the bases of these cones are still attached. Together, these cones can be considered to be one droplet with multiple spraying points. In the rim-emission, a large number of very small cones are formed in a thin layer of liquid on the edge of the capillary. Which mode will occur depends mainly on the shape of the capillary, but also on the applied potential difference (Hartman, 1998). This mode is shown in **Figure 2.9**.

2.2.4 Simple-jet mode and ramified mode

In the absence of the electric field, if the liquid flow rate is relatively high, then kinetic energy of the liquid leaving the capillary can be too large to be compensated by the surface tension. In this case, a free jet is formed, which breaks up into droplets. This is the simple-jet mode. The electric forces are mainly used to control the break-up of the jet into droplets. Frequency modulation can enhance the monodispersity of the produced droplets. If the electric field around this free jet increased, the radial electric stresses in the jet can overcome the surface tension stress. In that case, small jets are emerging from the surface of the main jet. These jets break up into polydisperse spray. This mode is called the ramified-jet mode. **Figure 2.10** shows the occurrence of ramified modes.

2.2.5 Oscillating-jet mode

Oscillating-jet mode takes place at higher flow rates where the jets become continuous and are steadily connected with the capillary because of this increase in flow rate. This is shown in **Figure 2.11**. The intermittent drop generation no longer exists, but is replaced by a continuous jet which oscillates or rotates as a result of the space charge of previously formed droplets. In the oscillating jet mode the jet issues smoothly from the meniscus at the needle tip, changing its position to an oscillating one. The jet disintegrates into small but unequal droplets due to kink instabilities. The jet deflects off the capillary axis because of space charge, however when the droplets are removed to the collecting plate the jets starts to move back. Aerosol is sprayed into a cone of an elongated ellipsoidal base and an apex angle greater than 90°. The droplets are smaller than 200 μm in diameter (Jaworek and Krupa, 1999).

2.2.6 Precession mode

The precession mode is characterized by that the liquid detaches from the capillary in a skewed cone form which then smoothly changes into a thin jet (Jaworek and Krupa, 1996). **Figure 2.12** shows the precession mode of operation. Both the cone and the jet rotate regularly around the capillary axis taking the shape of a fragment of a spiral. The jet of diameter is smaller than 100 μm becomes thinner at its end, also rotates spirally. The jet disintegrates into small droplets under the influence of repulsive electrostatic forces and probably also due to the centrifugal forces, at the distance of about 5-10 mm from the tip of the capillary. With increasing voltage the jet becomes longer. This mode of spraying allows generation of fine aerosols forming uniform spatial dispersion. The droplets are finer compared to oscillating-jet mode. The droplets are of a lower mobility and take a longer time to reach the collecting electrode (Jaworek and Krupa, 1999).

2.2.7 Corona discharge

The corona discharge occurs when the electric field between the nozzle and the ground electrode becomes larger than the electrical breakdown threshold of the surface energy of liquid surrounding air interface. If they occur before the electrical field initiating the cone-jet regime is reached, they prevent the establishment of this mode. This phenomenon occurs especially with liquids having a high surface tension and requiring high fields to offset the capillary pressure (Cloupeau and Prunet-Foch, 1989). Conversely, corona discharge can favour stability by allowing a reduction in the density of the surface charge of the jet or by reducing the electric field near the outlet of the nozzle.

2.3 Processes involved in electrohydrodynamic processing in cone-jet mode

There are many physical and chemical processes involved in the electrohydrodynamic processing of layers in cone-jet mode, occurring either sequentially or simultaneously. The possible sequential steps are spray formation; droplet transport, evaporation, disruption; preferential landing of droplets, discharge, droplet spreading, penetration of droplet solution, drying; surface diffusion, reaction. All of these processes can influence the morphology of the deposited layer.

2.3.1 Spray production

In the electrohydrodynamic processing a capillary-plate configuration is usually adopted (Grace and Marijnissen, 1994). The precursor solution is placed in a syringe which is connected to a metal capillary tube. When a voltage is applied to the capillary, an electrostatic field is immediately set up across the capillary and the grounded plate. This field also penetrates the liquid surface and acts on the ions in the solution. In the case of a positive potential at the capillary, positive ions move to the surface of the solution at a rate which depends upon the electrical relaxation time constant, which in turn depends upon the electrical conductivity and the absolute permittivity of the solutions (Vellenga and Klinkenberg, 1965).

While this surface charge completely shields the bulk of the solution so that there is no free charge inside the solution. The surface charge causes an outward electrostatic pressure on the solution, which is opposite to the inward directed pressure from the surface tension. This leads to surface instabilities, which are normally called Rayleigh-Taylor instabilities (Bailey, 1988). Taylor has shown that

when the electric field is strong enough, the electrostatically stressed liquid surface can be distorted into a stable conical shape (Taylor cone) (Taylor, 1964). The applied electric field accelerates the surface charge towards the cone apex. Due to this acceleration, a jet with a high charge density occurs at the cone apex. This jet breaks up into a number of primary or main droplets and a number of secondary droplets and satellites (Cloupeau and Prunet-Foch, 1989). These primary charged particles are usually mono-dispersed.

2.3.2 Aerosol transport

An electrostatically produced charged droplet will be attracted towards a grounded substrate by a Coulomb force. To determine the state of the droplet at deposition, the position of droplet as a function of time has to be known (Rietveld et al., 2006). The motion of a charged droplet in the axial direction of the spray under influence of an electric field can be described with a gravitational force and a viscous drag force act on the droplet. The trajectory as well as the flight time taken from the nozzle to the substrate for this droplet will be determined mainly by these forces. The gravitational force may be neglected in the case of electrostatic spraying because the droplets produced in this way are very small.

2.3.3 Solvent evaporation and droplet disruption

The evaporation does not alters the droplet transport greatly after the jet break up in stable cone-jet mode, but it can drastically reduce the droplet size depending on the solvent properties, humidity, surrounding air movement and processing

temperature (Wilhelm et al., 2003). Evaporation of the solvent results in shrinkage of the droplet, keeping the total charge the same (Abbas and Latham, 1967).

Charged droplet may be disrupted into a few smaller droplets, after reaching a maximum attainable charge density. This is the so-called Rayleigh limit (Rayleigh, 1882). The disruption of a droplet ('mother droplet') usually occurs with the ejection of a few highly charged, very tiny drops ('daughter droplets').Therefore, for solutions with rather volatile solvents and/or a long nozzle-to-substrate distance and/or a high deposition temperature, the effect of droplet disruption should be taken into account. In that case, there is no longer a mono-dispersed particle size distribution. In contrast, for solutions with a relatively non-volatile solvent and/or a short nozzle-to-substrate distance and/or a low deposition temperature, the mono-sized distribution may remain during droplet flight.

2.3.4 Preferential landing of droplets on the substrate

In the strong electrostatic field, induced charges exist on the surface of the grounded substrate, with a sign opposite to that of the droplets or the nozzle. The charge distribution generally is not uniform, but depends on the position relative to the nozzle and, in particular, on the local curvature of the surface. The charges concentrate more at the places where the curvature is greater. Therefore, the electric field there is stronger than at other places. When a charged droplet approaches the surface, it will be attracted more towards these more curved areas; this is referred to as 'preferential landing'. This action will cause agglomeration of the particles, especially when the incoming droplets are small (Chen et al., 1996). Also, this means that the roughness of the substrate surface may influence the

morphology. An increase in the surface roughness will lead to more particle agglomeration.

2.3.5 Discharge, spreading and penetration of solution droplets on the surface

As soon as a charged droplet contacts with the surface of the substrate or the earlier formed layer, it starts to discharge by transferring the charge to the grounded substrate either immediately or through the layer to the substrate. This process is very fast, when the electronic conductivity of the substrate (usually a metal) and the deposited layer is relatively high. In this case, the discharge process is not expected to determine the morphology of the layer. However, in the cases of using insulating substrates or depositing insulating layers, the discharge may proceed slowly and hence, it influences the morphology. Nevertheless, when wet droplets reach the substrate surface, the discharge process could also be completed through electrical conduction in the concentrated solution on the surface. If the evaporation of all of the solvent has not been completed when a droplet reaches the surface of the heated substrate, the solution wets the surface of the substrate or the earlier deposited layer. The type and dynamics of spreading depend strongly upon the so-called spreading coefficients (S) (Davies and Rideal, 1961). The spreading rate is also influenced by the viscosity of the liquid. Qualitatively, the spreading rate decreases with increasing viscosity. However, even if $S > 0$ in an electrohydrodynamic processing, the spreading may not be complete when the simultaneous drying process proceeds rapidly.

2.3.6 Decomposition, reaction and surface diffusion of the solute(s)

The decomposition and reaction (either partial or complete) of the solute(s) may have occurred before the droplets reach the substrate, which is expected if the surrounding temperature is high enough and dried droplets have been formed. Rearrangement of these dry particles on the substrate surface by surface diffusion is not expected at moderate deposition temperatures < 500 °C used in this electrohydrodynamic processing (Chen et al., 1996). At relatively low temperatures the spreading of solution droplets on the surface and the following process, which is actually a wet chemical process of an alcohol solution of metal salt precursors, determine the layer morphology.

For the spreading process, the viscosity change of the solution droplets is important. For the wet chemical process, there are many factors which influence the morphology. Specifically, among them are the solution chemistry including the solvation state, for instance whether there is complexation of the metal ions by the alcohol, evaporation and/or reaction with ambient gas of the solvent on the heated substrate, nucleation and precipitation of the solutes, and dissociation and chemical reaction of the solutes. This may be the only way to form a relatively dense morphology except at an extremely high surrounding temperature at which the whole droplets will be vaporized before reaching the substrate surface.

2.4 Properties influencing electrohydrodynamic processing

The researchers were shown that all of the liquid properties (i.e. electrical conductivity, relative permittivity, viscosity, surface tension and density), applied voltage, liquid flow rate and configurations of equipment can affect the

electrohydrodynamic processing. Even though there is no complete theory exists that describes how the atomisation process proceeds as a function of both external (applied voltage, flow rate and experimental setup or geometry,) and internal (fluid properties) parameters, many attempted to identify the variation of operation modes with these parameters to some extent.

2.4.1 Process parameters

2.4.1.1 Effect of applied voltage

The electrical field strength between the liquid and the ground electrode is one of the main controlling parameters in the electrohydrodynamic processing. This is determined by the applied voltage and other factors such as the inter-electrode spacing (Sung and Lee, 2004) and the configuration of the ground electrode (Kim et al., 2004). The break up of the liquid takes place mainly due to electrical forces produced by this field, therefore a higher applied voltage leads to a stronger atomisation effect on the liquid. Tang and Gomez (1996) reported applied voltage to be an important variable in establishing the cone-jet mode. They observed that different modes of operation can be obtained if the applied voltage is increased gradually.

At a higher and well defined voltages the meniscus of liquid become conical and stationary. A filament issued from the apex of this cone and subsequently forming aerosol. This is called as electrohydrodynamic (EHD) mode or stable cone-jet mode. Below this voltage the spray always operate in pulsating mode (Smith, 1986). In his studies, Smith (1986) mentioned that the increase of voltage resulted in slight elongation of the cone where the potential reached for which no steady

state mode exists. These are called as unstable modes with different instabilities. Therefore the applied voltage will affect the spraying mode and thereby the process it will adopt under a specific experimental condition.

Jayasinghe and Edirisinghe (2004a) investigated the shape of the stable cone-jet in a ceramic suspension, subjecting it to different applied voltages. They observed, for a fixed flow rate the increase of voltage resulted in decrease of cone depth. These effects are shown in **Figure 2.13**. This is showing the shape of the liquid cone will be different under different electrical field strength. The applied voltage could also affect the production of droplets in this process. Therefore the droplets produced from the liquid cone will be of different sizes. A higher applied voltage induces higher electrical field strength and stronger electric forces can cause a stronger atomisation effect. This in turn will have higher droplet production frequency with smaller droplet sizes. A higher applied voltage generates smaller droplets and a reduced cone diameter. But the droplet size was reported to be virtually independent of the applied voltage for liquids of relatively high conductivity (De la Mora and Loscertales, 1994). However, Tang and Gomez (1996) observed that the droplet size decreases monotonically with the increase of applied voltage with low conductivity solutions.

The applied voltage has an effect on the current produced during the electrohydrodynamic processing with different modes. Chen et al. (1995) showed in their studies that the current produced during the processing varied with the applied voltage. There was a little current observed in the dripping mode at low voltages. When increasing the voltage the pulsating mode was produced and the

current increased gradually. Again increasing the voltage they observed the stable cone-jet mode with increasing current. These are showing that the applied voltage plays an important role in electrohydrodynamic processing.

2.4.1.2 Effect of flow rate

The flow rate is a key parameter in electrohydrodynamic processing. The flow rate could be divided into two categories: high ($> 10^{-5}$ mls^{-1}) and low ($<10^{-5}$ mls^{-1}) (Grace and Marijnissen, 1994). Usually for a specific condition there exists a flow rate range beyond which the stable droplet production cannot be achieved. At relatively high flow rate conditions achieved by Meesters et al. (1992) showed Taylor-like cone, but no visible jet. However, Balachandran et al. (1992) have achieved a stable cone-jet for high flow rates with highly conducting liquids. In the low flow rate conditions De la Mora (1992) produced spray to study their electrical properties. These sprays typically generated monodisperse droplets on the order of a micron and below.

Droplet sizes spanning more than two orders of magnitude can be easily generated from the cone-jet electrohydrodynamic processing just by varying the liquid flow rate (Tang and Gomez, 1996). The liquid flow rate like electrical field strength can affect the production of the droplets significantly. Tang and Gomez (1996) defined the onset voltage conditions, as the minimum voltage required for a cone-jet spray, which corresponds to the lower voltage boundary of the cone-jet domain. They established that the droplet size increases monotonically with the liquid flow and a power law fit their dependence with exponent equal to 0.68 for the low conductivity and 0.62 for the larger conductivity solutions. **Figure 2.14** shows a

graph in that an average diameter of the droplet increases with simultaneous increase in flow rate.

Jayasinghe and Edirisinghe (2004a) observed that the relic sizes of the alumina ceramic suspension increases with the flow rate too. Their results are shown in **Figure 2.15**. The same authors in their later work (Jayasinghe and Edirisinghe, 2005) processed alumina ceramic suspension in pico-flow rates and observed that the increase of flow rate gave increase of jet diameter of the suspension. This is shown in **Figure 2.16**. Within a stable flow rate range, electrostatic atomization at relatively low flow rates produces finer particles and this could be utilized for nano particle fabrication and mass spectrometry (Grace and Marijnissen, 1994). For higher flow rates, the particles may become bigger; the increase in flow rate can also lead to increase in polydispersity of the droplets (Higuera, 2003).

Borra et al. (1999) mentioned that, when the conductivity of the liquid increases the liquid flow rate has to be decreased. When the conductivity and voltage increase, the intensity of the electric field at the liquid surface increases, which implies that surface tension has to be increased to balance the increase of forces. In this respect, the liquid flow rate has to be decreased in order to create a smaller cone. The variation in the length of the liquid column with a variety of high voltage inputs and liquid fluid flow was observed by Sung and Lee (2004). They plotted a comparative table of the influence of applied voltage and flow rate on the droplet and on the jet length (**Figure 2.17**). For a given set of flow rate the shape of the liquid column at the exit of needle differs depending upon the applied voltage. Thus the flow rate plays an important role in the mode of spraying.

2.4.1.3 Needle size and electrode configuration

The investigations by Cloupeau and Prunet-Foch (1989) showed that the needle size has an effect on electrohydrodynamic processing. In their work, for a given liquid the range of possible flow rates varied according to their size. Tang and Gomes (1996) in their studies found that the droplet size was independent of needle size. They plotted the graph of droplet size of various needle sizes and flow rate and obtained a single curve indicating that droplet size is independent of the needle size. However, they showed that the needle size significantly affect the stable cone-jet domain of electrospray. The maximum liquid flow rate for the stable cone-jet electrospray decreases dramatically as the needle diameter increases. This is showing that in the voltage-flow rate graph the stable cone-jet domain of the electrospray becomes smaller as the needle size increases. Consequently, the larger the needle sizes the narrower the operational domain of stable cone-jet electrospray.

To test the effect of the geometric parameter of the electrode configuration, Tang and Gomez (1996) varied the electrode separation with the liquid flow rate. They found that the droplet size together with the total electric current of the spray were independent of the electrode separation for a fixed liquid flow rate as long as the spray was operated at reference onset voltage conditions. They were shown that the onset voltage of the spray increased with monotonically with the increase of the separation between the needle and ground electrode at given flow rate. These results suggesting that once the stable con-jet mode is established, the droplet size is independent of the geometric dimensions of the electrodes.

Jayasinghe and Edirisinghe (2002b) reported the droplets trajectories depend on the configuration of the ground electrode. For a point-like ground electrode, the smaller the radius of the point, the higher concentration of the droplets produced in the spraying pattern. They pioneered the use of a point-like ground electrode for their work by which they focused most of the ceramic suspension droplets. This configuration of the ground electrode was the key to their innovation of electrostatic atomization printing (EAP). The trajectory of the droplet moving towards the point shape ground electrode is shown in **Figure 2.18**. By incorporating the needle set up to a stepper motor that could move in XY direction the droplets were printed.

Princivalle et al. (2005) reported the control of porosity of films by changing the nozzle to substrate (which was functioned as a ground electrode). The amount of precursor solution arriving onto the substrate was controlled by the electrode separation. The larger the electrodes distance higher the porosity of the films. Since small quantity of precursor solution arriving to the substrate the dense and smooth films could not be obtained in larger electrodes separation.

2.4.2 Influence of liquid physical properties

2.4.2.1 Influence of electrical conductivity

This is the most important liquid physical property in controlling both the stability of the electrospray and size of the droplet produced, researchers has given much attention to this parameter. The liquid should have sufficient electrical conductivity to be processed in stable cone-jet mode. If the electrical conductivity is too low it can not be processed in the stable cone-jet mode as there is no charge build up in

the liquid. If the electrical conductivity is too high the processing is not possible unless the flow rate is lowered, which is not the possible due to equipment constraints (Hartman et al., 2000).

Jones and Thong (1971) was the first to indicate that the maximum liquid electric conductivity for a stable electrospray was 10^{-3} Sm^{-1}. Mutoh et al. (1979) claimed that a stable electrospray would be impossible to establish when the liquid electric conductivity was higher than 10^{-5} Sm^{-1}. Hayati et al. (1987) had also made a similar conclusion and they reported that a stable electrospray could be established only for semi conducting liquids, although no specific upper conductivity limit was mentioned in their paper.

However, Smith (1986) was the first to point out that no such limit exists. His suggestion is the value of liquid conductivity has influence on the morphology of the liquid issued in the stable cone-jet mode. In general, as conductivity increases, the filament width, length, droplet size and flow rate all decreases. It is believed that droplet size decreases as conductivity increases, from large droplets produced by poorly conducting liquids to the disappearance of the aerosol, owing to extremely small drop size for liquid conductivity > 10^{-1} Sm^{-1}. De la Mora and Loscertales (1994) showed that the stable electrospray can be established for liquid conductivities spanning a five order of magnitude range from 1 Sm^{-1} to 10^{-5} Sm^{-1} with the resulting sprays producing droplets in the submicron size range.

Cloupeau and Prunet-Foch (1989) reported that the electrical conductivity is the most important since a liquid with conductivity too low cannot be atomized due to

lack of tangential stress caused by the charges. This was established as the driving force responsible for producing the jet. Their observation showed that electric conductivity as the most important physical property in controlling both the stability of the electrospray and the size of the droplets. However, De la Mora (1992) mentioned that if the conductivity is too high then the electrical discharge becomes inevitable with surrounding atmosphere.

2.4.2.2 Influence of viscosity

The viscosity is another vital liquid property which plays a significant role in the jet break-up process and influence the size of the produced main and secondary droplets. According to Weber (1931) an increase in viscosity will lead to lower dominant wave numbers. The lower dominant wave numbers will lead to increase of droplet size in electrohydrodynamic processing.

Jayasinghe and Edirisinghe (2002a) studied the effect of viscosity on the size of relics produced by electrohydrodynamic processing. They found the greatest effect of increased viscosity is upon the relic size, which increases dramatically. They established that the increase in viscosity over three orders of magnitude would have a dramatic effect on the electrohydrodynamic processing of liquids and their mixtures. **Figure 2.19** shows the relics pictures of their experimental results. Jayasinghe and Edirisinghe (2004b) showed another interesting effect of high viscosity dielectric liquids in their later studies. In these studies they used family of silicone oils and produce a novel ball cone effect which is different from the fundamental stable cone-jet behaviour. Here, the jet evolves from a ball cone and increases in diameter with increasing viscosity. This behaviour is shown in **Figure**

2.20. They also pointed out the micro-threading effect of liquid with viscosity $>10^4$ mPa s. This effect is shown in **Figure 2.21**.

2.4.2.3 Influence of surface tension

In order to form a stable cone-jet mode, the surface tension has to be overcome by the electric stresses. The higher the surface tension the stronger the required electric field strength. According to the experimental results obtained by Smith (1986) the onset voltage for the stable cone-jet spray will increase with the liquid surface tension. If the liquid surface tension is large, a stable electrospray may not be established because the field required exceeds that for the electric break down in the gas surrounding the cone. Tang and Gomez (1995) used gases with higher electrical break down strength as a surrounding fluid instead of air to obtain the stable cone-jet mode for water.

2.4.2.4 Influence of dielectric constant

The dielectric constant of a material determines the polarization of this material in an electric field. The polarization reduces the electric field inside the liquid. The electric field and the liquid conductivity determine the time constant for the charge transport toward the cone surface. According to Vellenga and Klinkenberg (1965) the following relaxation time (t_e) can be used at the cone apex.

$$t_e = \frac{\beta \varepsilon_o}{K} \tag{2.2}$$

where β is the relative permittivity and K is the electrical conductivity.

Chen and Pui (1997) have studied the effect of dielectric constant on scaling laws for electrohydrodynamic processing. They studied eight different solvents with dielectric constants ranging from 12.51 to 182.4. They reported the liquids obeyed the scaling laws with a little exception.

2.4.2.5 Influence of density

Another liquid property in the scaling law is the density. It may affect the droplet production and the flow rate range for stable configuration (Hogan and Hendricks, 1965). The liquid density is of some importance since the density play a role in the acceleration process of the liquid near the cone apex. Gravity is not relevant in that area because the electrical stresses and the surface tension stress are much larger than the hydrostatic pressure. At the cone base the acceleration of the liquid is very small and does not play an important role. However, the liquid density is of some importance due to the influence of gravity on the cone shape. For large capillaries, diameters larger than 1 mm gravity influence strongly the shape of the liquid cone (Hartman, 1998).

2.5 Scaling laws

The scaling laws are established for characterising a defined electrohydrodynamic processing. It enables the produced droplet size and the emitted current to be better correlated with the factors involved in the processing. It provides better understanding of the mechanisms involved in the process. Basically, the droplet size and the emitted current are given by liquid physical properties (electrical

conductivity, density, viscosity, surface tension and dielectric constant) and liquid flow rate.

The scaling laws derived by De la Mora and Loscertales (1994) and Ganan-Calvo et al. (1997) are well correlating the liquid physical properties with the droplet size and the emitted current. Before stating these scaling laws, the conditions for classical electrohydrodynamic processing to take place is given below. This is the inequality criteria established by Ganan-Calvo et al. (1997). They established the criteria that the hydrodynamic time (t_h) should be much greater than the electrical relaxation time (t_e) as a condition that should be satisfied to have a steady state cone-jet structure.

$$t_h >> t_e \tag{2.3}$$

$$\frac{LD^2}{Q} >> \frac{\beta\varepsilon_o}{K} \tag{2.4}$$

where Q is the flow rate, D is the jet diameter and L is the axial length of the jet.

Consequently, the liquids having electrical relaxation time higher than the hydrodynamic time can not be electrohydrodynamically processed unless their electrical relaxation time is modified well below the hydrodynamic time with some additives (Ganan Calvo et al. 1997).

The scaling laws for the droplet size and the emitted current during electrohydrodynamic processing derived by De la Mora and Loscertales (1994) are given below.

$$D_d = G(\beta)\left(\frac{Q\beta\varepsilon_o}{K}\right)^{1/3} \tag{2.5}$$

$$I = f(\beta)\left(\frac{\gamma QK}{\beta}\right)^{1/2} \tag{2.6}$$

where D_d is the droplet diameter, I is the emitted current, $G(\beta)$ and $f(\beta)$ are functions of liquid relative permittivity (β).

Ganan-Calvo et al. (1997) obtained scaling laws for the spray current and the droplet size base on the theoretical model of charge transport and these are given below.

For liquids with high viscosity and conductivity: The $Q^{1/2}$ law

$$I \sim \frac{(QK\gamma)^{1/2}}{(\beta-1)^{1/4}} \tag{2.7}$$

$$d \sim \left[\frac{(\beta-1)^{1/2} Q \varepsilon_o}{K}\right]^{1/3} \tag{2.8}$$

For liquids with low viscosity and conductivity: The $Q^{1/4}$ law

$$I \sim \left[\frac{\gamma^3 \varepsilon_o K Q}{\rho}\right]^{1/4} \tag{2.9}$$

$$d \sim \left[\frac{\rho \varepsilon_o Q^3}{\gamma K}\right]^{1/6} \tag{2.10}$$

where I is the spray current, d is the droplet diameter and ρ is the liquid density.

2.6 Classification of other deposition methods

Deposition technology can well be regarded as the major key to the creation of devices such as computers, since microelectronic solid-state devices are all based on material structures created by film deposition. Another important reason for the rapid growth of deposition technology is the improved understanding of the physics and chemistry of films, surfaces, interfaces, and microstructures made possible by the remarkable advances in analytical instrumentation during the past twenty years. A better fundamental understanding of materials leads to expanded applications and new designs of devices that incorporate these materials.

There are many dozens of deposition technologies for material formation. Since the concern here is with film deposition methods for forming layers in the thickness range of a few nanometers to about ten micrometers, the task of classifying the

technologies is made simpler by limiting the number of technologies to be considered.

Basically, film deposition technologies are either purely physical, such as evaporative methods, or purely chemical, such as gas- and liquid-phase chemical processes. The following film deposition technologies such as evaporative, sputtering and chemical vapour deposition are briefly discussed below.

2.6.1 Evaporative technologies

Although one of the oldest techniques used for depositing thin films, thermal evaporation or vacuum evaporation, is still widely used in the laboratory and in industry for depositing metal and metal alloys. The following sequential basic steps take place:

(i) a vapour is generated by boiling or subliming a source material,

(ii) the vapour is transported from the source to the substrate, and

(iii) the vapour is condensed to a solid film on the substrate surface.

Although deceptively simple in principle, the skilled practitioner must be well versed in vacuum physics, material science, mechanical and electrical engineering, as well as in elements of thermodynamics, kinetic theory of gases, surface mobility, and condensation phenomena. Evaporants cover an extraordinary range of varying chemical reactivity and vapour pressures. This variety leads to a large diversity of source components including resistance-heated filaments, electron beams; crucibles heated by conduction, radiation, or rf-induction; arcs, exploding wires, and lasers.

Additional complications include source-container interactions, requirements for high vacuum, precise substrate motion (to ensure uniformity) and the need for process monitoring and control.

2.6.2 Sputtering technique

Sputtering and sputter deposition are widely used techniques for the erosion of surfaces and the deposition of films. Sputtering is usually practiced by means of plasmas which generate charged particles which can be accelerated towards a surface electrically. Sputtering is simply the process of erosion of that surface by the energetic particles, a sort of atomistic sandblasting. Sputter deposition is nothing more than the accumulation of these atoms which are blasted off the surface onto a nearby sample. Sputtering occurs whenever any particle strikes a surface with enough energy to dislodge an atom from the surface. The sputter yield is just the ratio of the number of emitted particles per incident particle:

$$Y = \text{(number of emitted particles/ number of incident particles)}$$

Sputtering can occur for virtually any incident species, including atoms, ions, electrons, photons, and neutrons as well as molecules and molecular ions. For virtually all practical cases, sputtering almost always utilizes ion bombardment, either with inert gas ions such as Ar^+ and Kr^+, or small molecular ions such as N_2^+, O_2^+, and so on. The yield for bombardment of a surface with an ion or an atom of the same energy will be virtually identical; physical sputtering relies on the transfer of physicalmomentum and kinetic energy from the incident particle to the surface atoms, and this is independent of the particle's charge (Seshan, 2002).

The sputtering process is shown generically in **Figure 2.22**. The incident particle impacts the surface or near-surface atoms of the solid with sufficient energy to break bonds and dislodge atoms. If, during this process, one or more atoms are removed from the solid, they are considered to be sputtered atoms.

The most commonly used sputtering technique is reactive sputtering, where it is used for deposition of oxides and nitride thin films. There are two approaches to reactive deposition, one where the cathode is a metal plate, and the other where the cathode is composed of the material of interest to be deposited, for example, a nitride or an oxide. The latter case is usually complicated by the nonconductive nature of many oxide and some nitride targets, requiring the use of rf power to the cathode, as well as the poor physical stability of many of these compounds. This last issue may result in cracking or shattering the compound target, or else in difficulties in bonding it to the cathode, which is usually water cooled. Reactive sputtering with a metal cathode has received the most attention because of the opportunity for high rate, controlled deposition, as well as the ability to use dc rather than rf power. Reactive sputtering is made more difficult with metallic targets, though, because of the tendency of the cathode itself to react, forming a thin film on the cathode of a nitride or oxide, which can significantly alter the sputtering process.

A reactive sputtering system is shown in **Figure 2.23**. In this system, the cathode is placed in a chamber with walls and a pumping system. The walls are important, because films will also be deposited and reacted there as well as on the sample and the cathode. Typically, a system like this would be operated with some partial

pressure of an inert gas, such as Ar, and a partial pressure of a reactive species, such as O_2 or N_2.

2.6.3 Chemical vapour deposition

Methods of film formation by purely chemical processes in the gas or vapour phases include chemical vapour deposition and thermal oxidation. Chemical vapour deposition (CVD) is a materials synthesis process whereby constituents of the vapour phase react chemically near or on a substrate surface to form a solid product (**Figure 2.24**). The deposition technology has become one of the most important means for creating thin films and coatings of a very large variety of materials essential to advanced technology, particularly solid-state electronics where some of the most sophisticated purity and composition requirements must be met.

The main feature of CVD is its versatility for synthesizing both simple and complex compounds with relative ease at generally low composition and physical structure can be tailored by control of the reaction chemistry and deposition conditions. Chemical reaction types basic to CVD include pyrolysis (thermal decomposition), oxidation, reduction, hydrolysis, nitride and carbide formation, synthesis reactions, disproportionate, and chemical transport. A sequence of several reaction types may be involved in more complex situations to create a particular end product. Deposition variables such as temperature, pressure, input concentrations, gas flow rates and reactor geometry and operating principle determine the deposition rate and the properties of the film deposit (Seshan, 2002).

Most CVD processes are chosen to be heterogeneous reactions. That is, they take place at the substrate surface rather than in the gas phase. Undesirable homogeneous reactions in the gas phase nucleate particles that may form powdery deposits and lead to particle contamination instead of clean and uniform coatings. Kinetics controls the rate of reactions and depends on temperature and factors such as substrate orientation. Considerations relating to heat, mass, and momentum transport phenomena are especially important in designing CVD reactors of maximum efficiency. Since important physical properties of a given film material are critically influenced by the structure (such as crystallinity), control of the factors governing the nucleation and structure of a growing film is necessary.

Thin film materials that can be prepared by CVD cover a tremendous range of elements and compounds. Inorganic, organometallic, and organic reactants are used as starting materials. Gases are preferred because they can be readily metered and distributed to the reactor. Liquid and solid reactants must be vaporized without decomposition at suitable temperatures and transported with a carrier gas through heated tubes to the reaction chamber, which complicates processing, especially in the case of reduced-pressure systems. Materials deposited at low temperatures (e.g. below 600 °C for silicon) are generally amorphous. Higher temperatures tend to lead to polycrystalline phases. Very high temperatures (typically 900 °C to 1100 °C in the case of silicon) are necessary for growing single crystal films. These films are oriented according to the structure of the temperatures (Seshan, 2002).

A general comparison between chemical vapour deposition (CVD), physical vapour deposition (PVD) and electrohydrodynamic processing (EHDP) and their

relative strengths and weaknesses are tabulated below (**Table 2.1**). This was extracted from Choy (2002) and modified to great extent.

Table 2.1 A comparison between different film processing methods, CVD, PVD and EHDP

CVD	PVD	EHDP
Sophisticated reactor and/or vacuum system needed.	Sophisticated reactor and vacuum system needed. Vacuum system is required to facilitate the generation of vapour species and increase the mean free path of the vapour species to reach the substrate.	No need of sophisticated reactor or vacuum system. The processing could be even carried out in open air atmosphere.
Expensive technique since sophisticated reactor and vacuum system are high cost.	Expensive technique since sophisticated reactor and vacuum system are high cost.	Relatively low cost technique.
Non line of sight process. It can coat a complex shapes and deposit coating with good conformal coverage.	Line of sight process. There is difficulty in coating a complex shapes and conformal coverage.	Non line of sight process. It can coat a complex shapes and deposit coating with good conformal coverage.
Tendency towards	Tendency for using expensive	Less volatile and more

volatile and/or toxic chemical precursors.	sintered solid targets/sources with difficulties for large area deposition and varying the composition or stoichiometry of the deposits.	environmentally friendly precursors are used.
Multi source precursors tend to produce non-stoichiometric film.	Multi targets or single targets have difficulty in controlling the stoichiometry of the films because different elements will evaporate or sputter at different rates.	Mostly single source precursors are used to avoid non-stoichiometry problems.
High deposition temperatures needed.	Low to medium deposition temperatures used.	Low to medium deposition temperatures used.

2.7 Titanium dioxide (TiO_2)

TiO_2 as a transitional metal oxide has been investigated in both industrial applications and scientific research in the last few years. Due to their unique dielectric and optical properties, TiO_2 films are used in memory cell capacitors, anti reflection coating, optical interference filtering and optical wave guides (Subramania et al., 2002). TiO_2 is a well known material having noticeable photocatalytic properties. It has been studied for air clean-up, water purification, anti-bacterial coatings and deodorant fiber and so on (Shimizu et al., 1999). More importantly it has found application in dye-sensitised solar cells (Gratzel, 2003) to increase the photoconversion efficiencies. Due to its high permittivity, high

physical and chemical stability in modern complementary metal oxide semiconductor (CMOS) fabrication, TiO_2 is largely investigated for replacement of SiO_2 in dynamic random access memory (DRAM) and micro electro mechanical system (MEMS) (Kim et al., 1996).

2.7.1 Structure and properties of TiO_2

In nature titanium dioxide crystallizes in three common polymorphs: rutile, anatase and brookite. The TiO_2 films most often consist of anatase and rutile phases. Rutile is the most stable phase. Anatase is metastable at room temperature. It transforms irreversibly into rutile upon heating above a threshold temperature. At atmospheric pressure, the transition occurs usually at about 1000 °C. However, the phase transformation temperature depends on grain size, presence of impurities, dopants, precursor materials and synthesis method (Hirano et al., 2003).

The basic unit cell structures of the three phases of TiO_2 are shown in **Figure 2.25**. The crystal parameters, the Ti-O interatomic distances and the O-Ti-O bond angles for the three phases are summarized in Table 2.2. The rutile and anatase phase show the tetragonal crystal structures containing 6 and 12 atoms per unit cell respectively. In both structures each Ti atom is co-ordinated to 6 O atoms and each O atom is co-ordinated to 3 Ti atoms. In each case, the TiO_6 octahedron is slightly distorted, with two Ti-O bonds slightly greater than the other four, and with some of the O-Ti-O bond angles deviating from 90 °. The distortion is greater in anatase than in rutile. The structure of rutile and anatase crystals has been described frequently in terms of chains of TiO_6 octahedra having common edges

(Cromer and Herrington, 1955). Two and four edges are shared in rutile and anatase respectively.

The third form of TiO_2, brookite has a more complicated structure. It has eight formula units in the orthorhombic cell. The interatomic distances and the O-Ti-O bond angles are similar to those of rutile and anatase. The essential difference is that there are six different Ti-O bonds ranging from 1.87 °A to 2.04 °A. Accordingly, there are 12 different O-Ti-O bond angles ranging from 77 ° to 105 °. In contrast, there are only two kinds of Ti-O bonds and O-Ti-O bond angles in rutile and anatase. The brookite could be envisioned by joining together the distorted TiO_6 octahedra sharing three edges (Baur, 1961).

Table 2.2 Crystal structure data of TiO_2

	Rutile [a]	**Anatase** [a]	**Brookite** [b]
Crystal structure	tetragonal	tetragonal	orthorhombic
Lattice constants ($\times 10^{-10}$ m)	a = 4.5936	a = 3.784	a = 9.184
	c = 2.9587	c = 9.515	b = 5.447
			c = 5.145
Density (kgm^{-3})	4130	3790	3990
Ti-O bond length ($\times 10^{-10}$ m)	1.949(4)	1.937(4)	1.87 ~ 2.04
	1.980(2)	1.965(2)	
O-Ti-O bond angle	81.2 °	77.7 °	77.0 ° ~ 105 °
	90.0 °	92.6 °	

[a] Reference (Cromer and Herrington, 1965)

[b] Reference (Baur, 1961)

The bulk TiO_2 has valuable properties such as high refractive index, excellent transmittance in the visible and near-infra red frequency. The bulk anatase TiO_2 has a dielectric constant to be 48 (Clark, 1968). On the other hand the bulk TiO_2 crystals in the rutile phase have a dielectric constant of 170 in the plane parallel to the c axis and 89 perpendicular to it (Lee et al., 1999). The energy bandgap of the TiO_2 is reported to be about 3.5 eV for amorphous films (Fuyuki and Matsunami, 1986), 3.2 eV for crystalline films in the anatase phase and 3 eV for the films in the rutile phase (Pascual et al., 1978).

2.7.2 TiO_2 in microelectronic applications

The dramatic improvements in microelectronics performance over the past few decades have been accompanied by a severe reduction in the size of the memory and logic devices. This scaling has required drastic decreases of the SiO_2 dielectric film thickness to achieve ever higher capacitance densities. The fundamental limits of SiO_2 as a dielectric material, imposed by electron tunnelling, will be reached as this SiO_2 film thickness approaches 2 nm (Murarka et al., 2003).

The significant parameter for scaling is not the physical thickness, but instead the capacitance per unit area (Campbell et al., 1997).

$$C_{ox} = \frac{\varepsilon}{t_{ox}} \tag{2.11}$$

where C_{ox} is the oxide capacitance, ε is the oxide permittivity and t_{ox} is the oxide thickness.

One route to continued dielectric scaling then is to employ materials with much higher permittivity than SiO_2. One of the difficulties with this approach is that when the permittivity of simple dielectric increases, the bandgap decreases. **Figure 2.26** demonstrates that effect. Thus a significant improvement of the permittivity is not practical when using simple dielectrics. Alternatively one can use lattice polarisable materials to overcome this difficulty. In these materials a high permittivity obtained by a physical displacement of one or more atoms in a response to an applied electric field. Most lattice polarisable materials are metal oxides. TiO_2 could be an alternative material with this kind could be used as an alternative material in microelectronics (Singh et al., 2005).

2.7.3 TiO_2 in photocatalytic and photoelectric applications

TiO_2 is a wide bandgap semiconductor that has been extensively investigated and applied to a wide spectrum of disciplines. The discovery (Fujishima and Honda, 1972) of photosensitization of water to yield hydrogen and oxygen by using TiO_2 electrodes leads the way to extensively research this unique material for over three decades.

As a semiconductor, TiO_2 functions by having a large bandgap which can be described as an energy threshold that electrons must obtain in order to flow through a material. The bandgap is located between the filled valence band and the higher energy conduction band. The magnitude between the electronically occupied valence band and the largely unpopulated conduction band determines both the extent of thermal population of the conduction band (i.e. the electrical conductivity of the material) and the wavelength sensitivity of the semiconductor to irradiation.

That is a material with a larger bandgap requires higher energy radiation to populate the conduction band than one with a smaller bandgap. **Figure 2.27** shows the excitation of an electron from the valence band to the conduction band initiated by light absorption with energy equal to or greater than the bandgap of the TiO_2.

The ecological elimination of pollutants is an issue of increasing concern in today's society. TiO_2 is very useful material in photocatalytic applications. In photocatalysis, it has been used for decomposition of water and degradation of organic pollutants in air as well as aqueous media. In recent years there is an increasing interest to find sustainable alternative energy sources due to the heightening cost of fossil fuels and the detrimental effect of global climate change. Photovoltaic cells have received significant attention due to limitless influx of photons from the sun (Luke et al., 2008). The TiO_2 as a semiconductor material is useful for this application. Upon illumination of the TiO_2 with light of equal or greater energy than the bandgap, charge transfer from valence band to conduction band occurs, creating a hole and a free electron. These species are useful in photovoltaic to generate current for endless needs.

This inherent property of TiO_2 curtails the overall efficiency based on the total solar radiation reaching the Earth's surface thus only absorbing a small UV fraction of solar light (Cong et al., 2007). Therefore, the most important and challenging issue is to develop efficient visible light sensitivity TiO_2. There are generally two approaches to tune the visible light sensitivity of TiO_2 one is to attach the organic dyes to surface of the TiO_2 and other is to modify the composition of TiO_2 by means of doping to alter the electronic structure of TiO_2.

2.7.4 Doping of TiO_2 and improvement its optical property

Modifying the band structure of TiO_2 to make it more responsive to visible wavelengths has been an enduring effort. A common method used to sensitize the TiO_2 in visible light is accomplished by attaching organic dyes such as ruthenium complexes to the surface of TiO_2 (O'Regen and Gratzel, 1991). Unfortunately this method is expensive and such dyes degrade in the presence of oxygen. Ruthenium dyes also detach from TiO_2 surface in aqueous medium.

The other method involves manipulating the chemical composition of the TiO_2 towards modifying its electronic structure. This could be done by doping the TiO_2 by an external atom. The doping refers to the intentional introduction of impurities to the material for the purpose of modifying electrical characteristics. The doping can be with metals and non-metals. The cationic doping of TiO_2 with transition metals has been extensively studied and there is an improvement in the optical absorption for visible wavelengths observed. However, they need expensive ion-implantation facilities; there is also an increase in thermal instability and a decrease in carrier life times which limits overall conversion efficiencies (Shankar et al., 2006).

2.7.5 Nitrogen as a dopant in TiO_2

With the above limitations in mind an ideal dopant should not impart any instability be it thermal or chemical and must improve the carrier life time to get maximum conversion efficiencies with optimally be inexpensive to apply. These demanding led to numerous anions such as C (Hsu et al., 2007), F (Huang et al.,

2006) and S (Chen and Liu, 2007) been used for doping to improve the visible light sensitivity of TiO_2.

The anion doping was proposed by Asahi et al. (2001) and they found that nitrogen doping as a substitute for oxygen in the TiO_2 lattice to be most feasible and successful approach among these anions because,

(i) Nitrogen has comparable ionic radius to oxygen

(ii) The 2*p* states of N contribute to bandgap narrowing by mixing with O 2*p* states thus capable of absorbing visible light

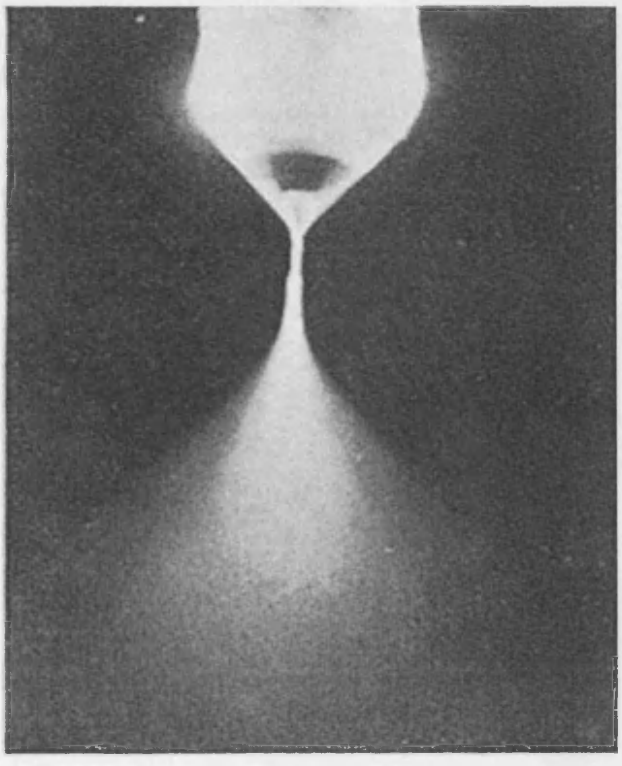

(a)

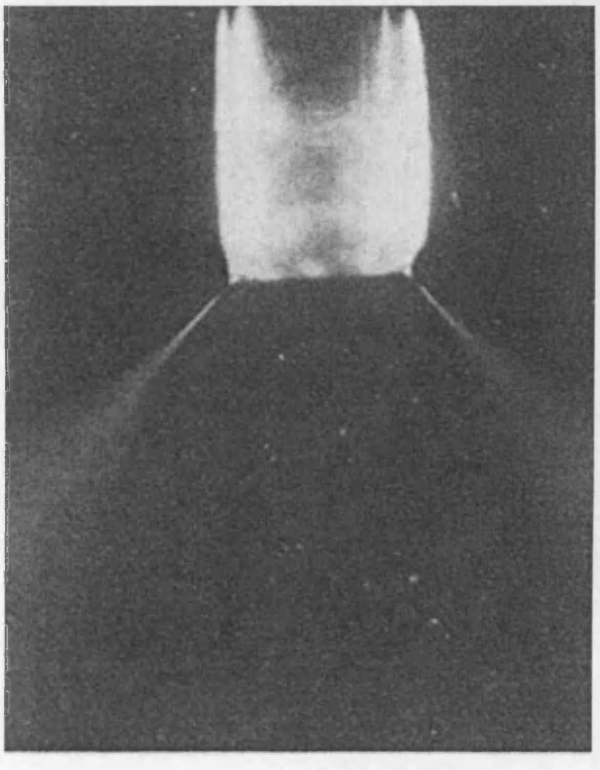

(b)

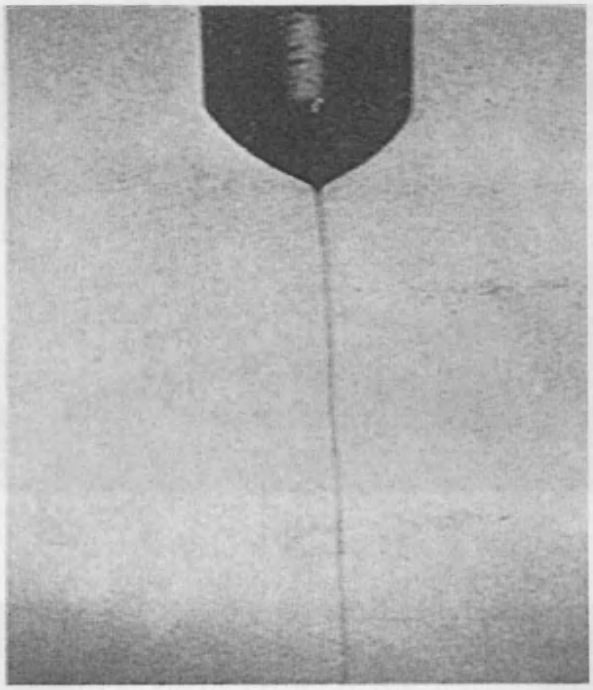

(c)

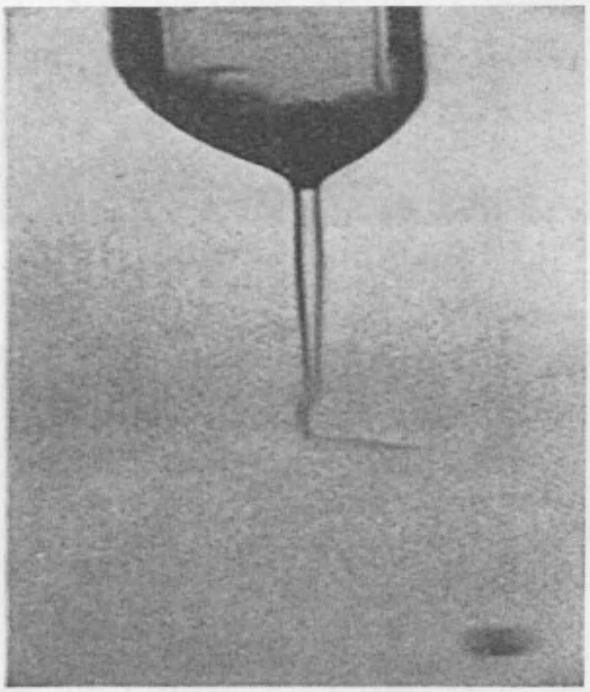

(d)

Figure 2.1 (a, b, c & d) First ever classification of different modes of electrohydrodynamic processing (Zeleny, 1917)

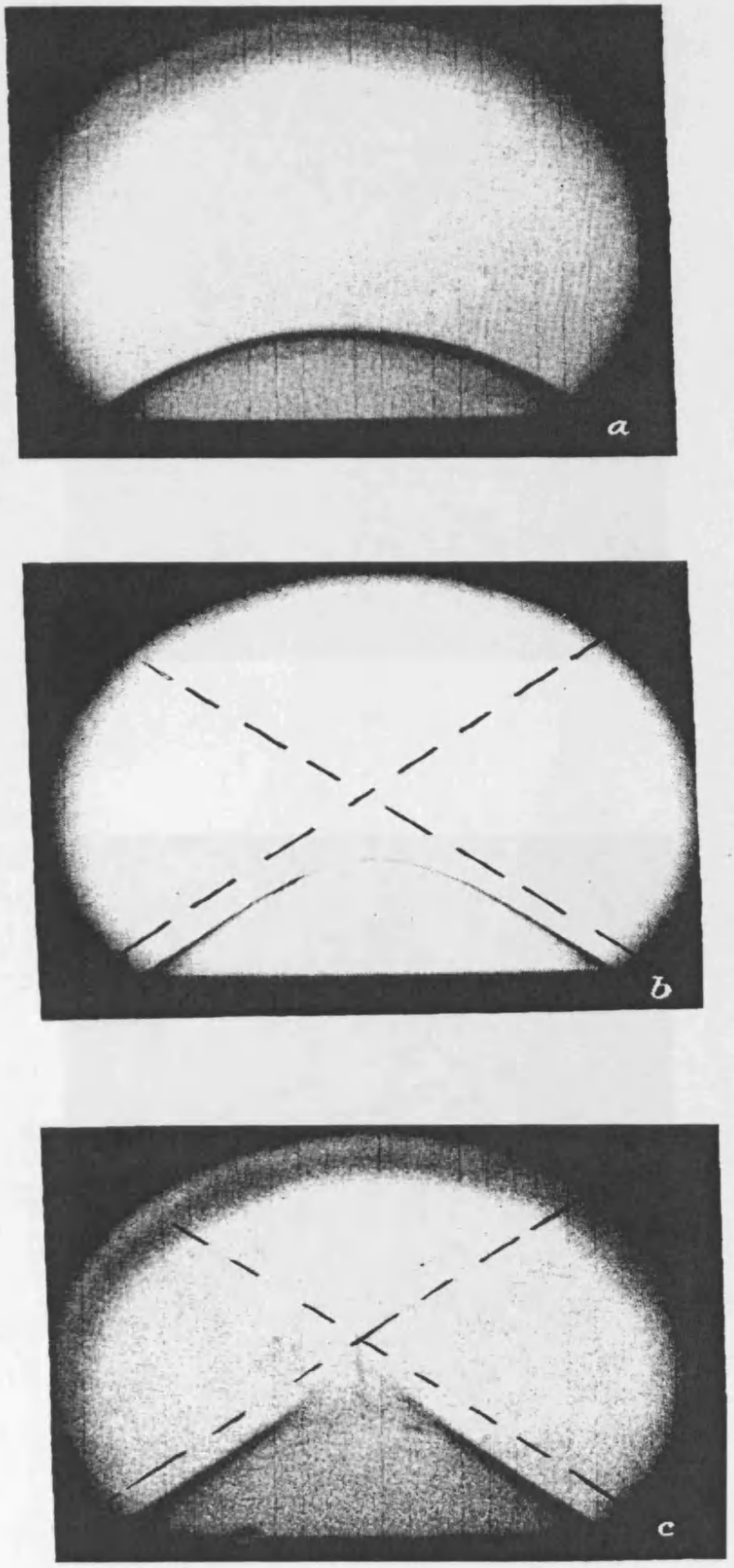

Figure 2.2 (a, b & c) Stages involved in establishing steady state cone (Taylor, 1964)

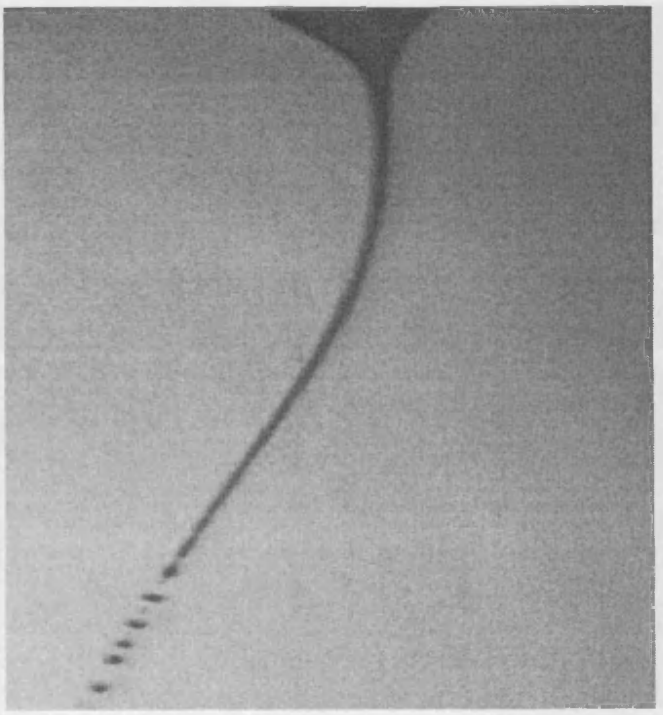

(a)

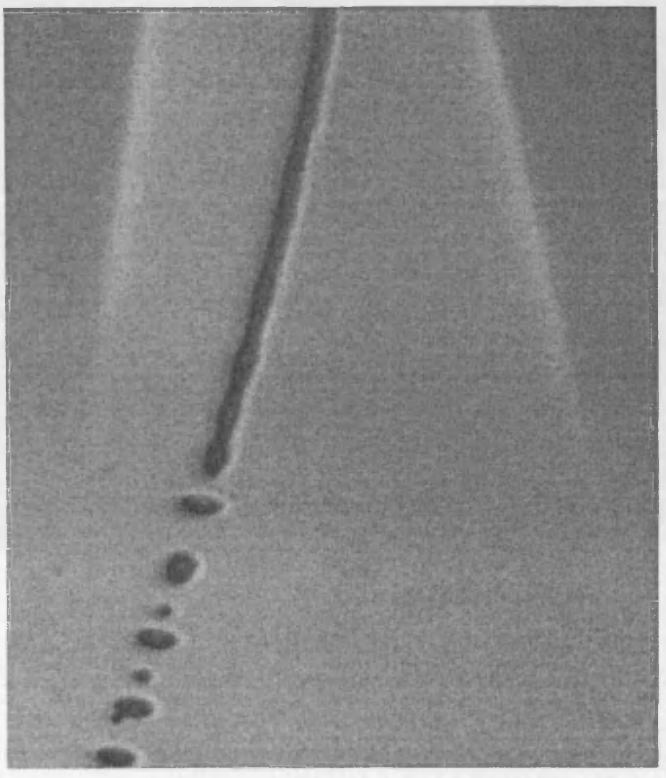

(b)

Figure 2.3 (a & b) Stable cone-jet mode and jet break-up (Tang and Gomez, 1996)

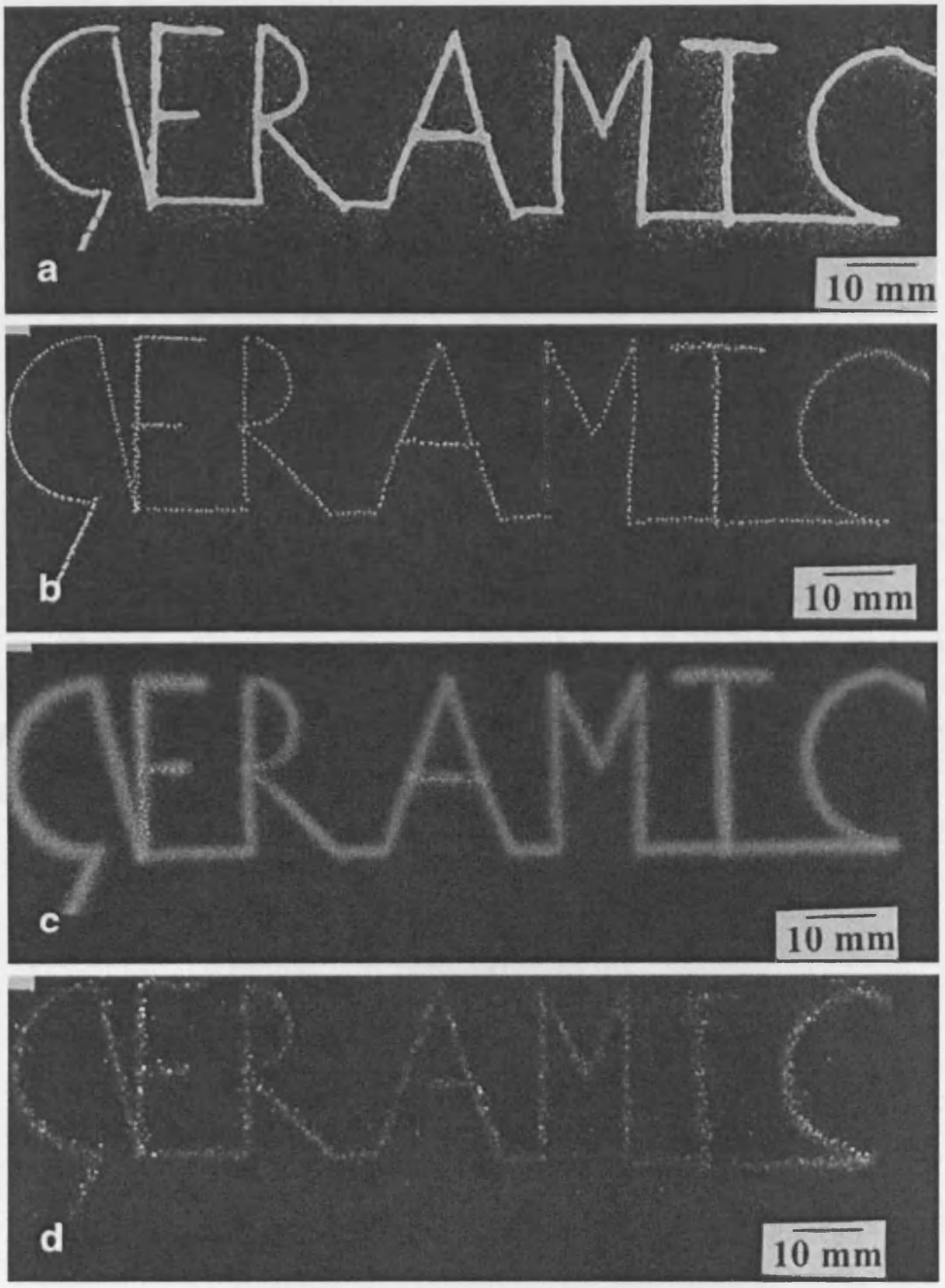

Figure 2.4 (a, b, c & d) An innovative electrostatic atomisation printing (EAP) of ceramic tracks obtained at different applied voltages (Jayasinghe and Edirisinghe, 2002)

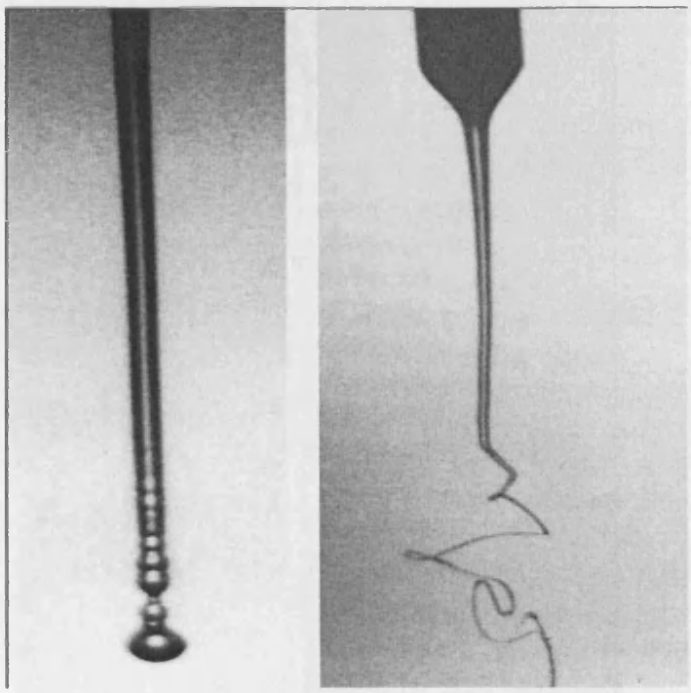

(a) (b)

Figure 2.5 Jet break-up in stable cone-jet mode (a) varicose instability (b) kink instability (Jaworek and Krupa, 1999)

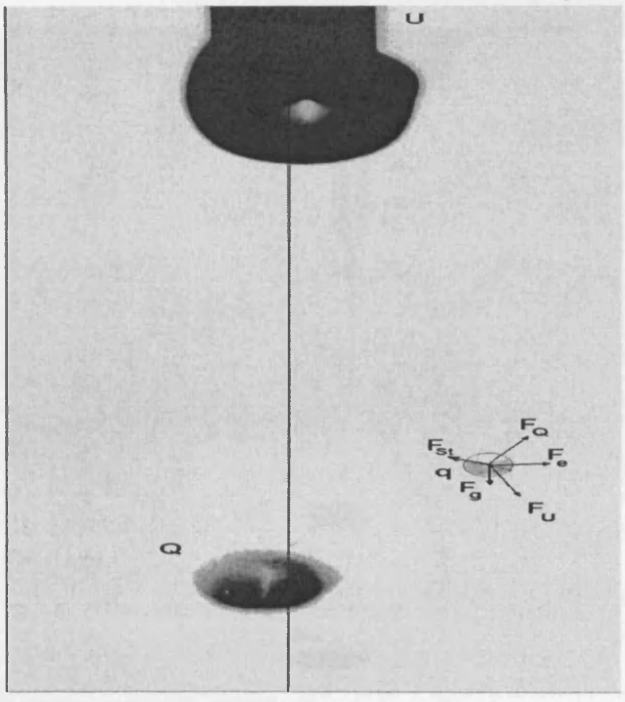

Figure 2.6 Dripping mode of electrohydrodynamic processing (Jaworek and Krupa, 1999)

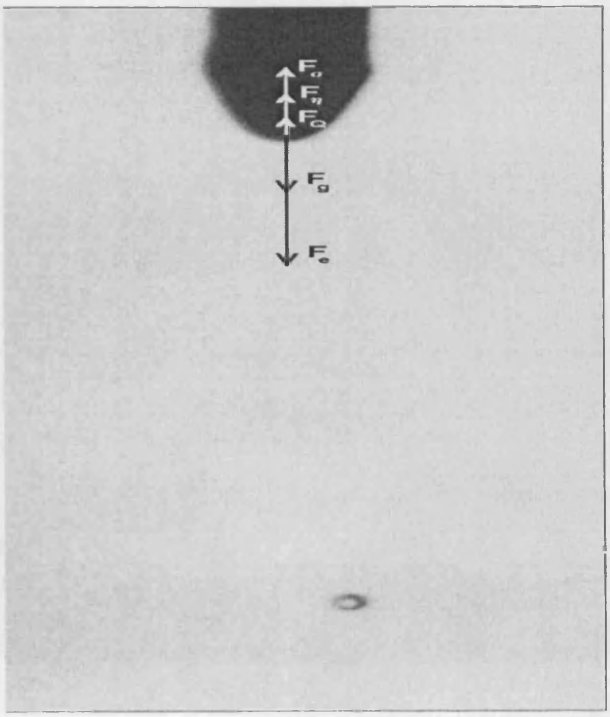

Figure 2.7 Micro-dripping mode of electrohydrodynamic processing (Jaworek and Krupa, 1999)

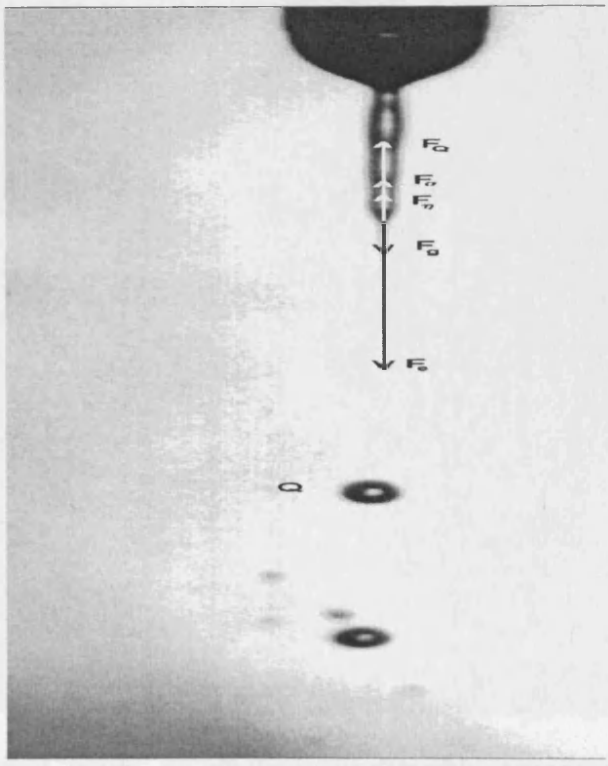

Figure 2.8 Spindle mode of electrohydrodynamic processing (Jaworek and Krupa, 1999)

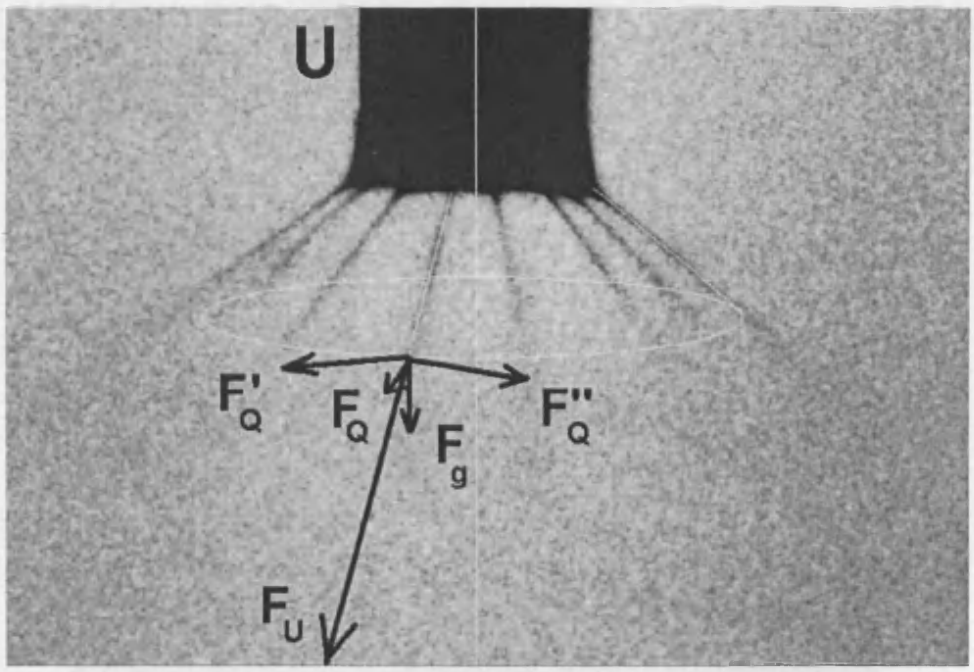

Figure 2.9 Rim-emission mode of electrohydrodynamic processing (Jaworek and Krupa, 1999)

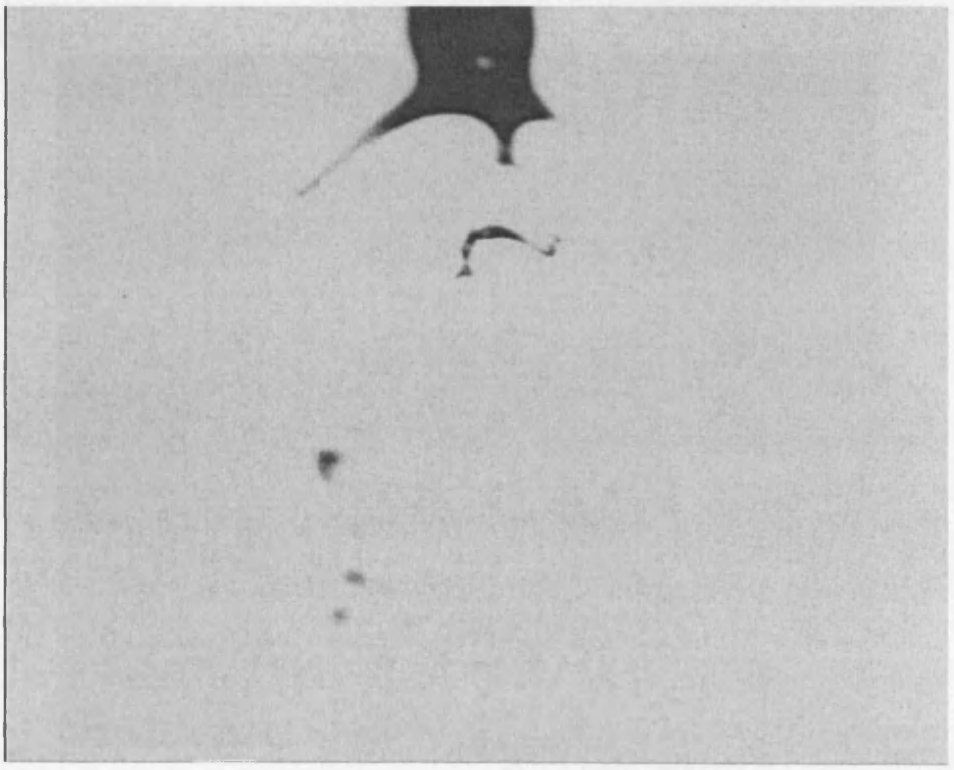

Figure 2.10 Ramified mode of electrohydrodynamic processing (Jaworek and Krupa, 1999)

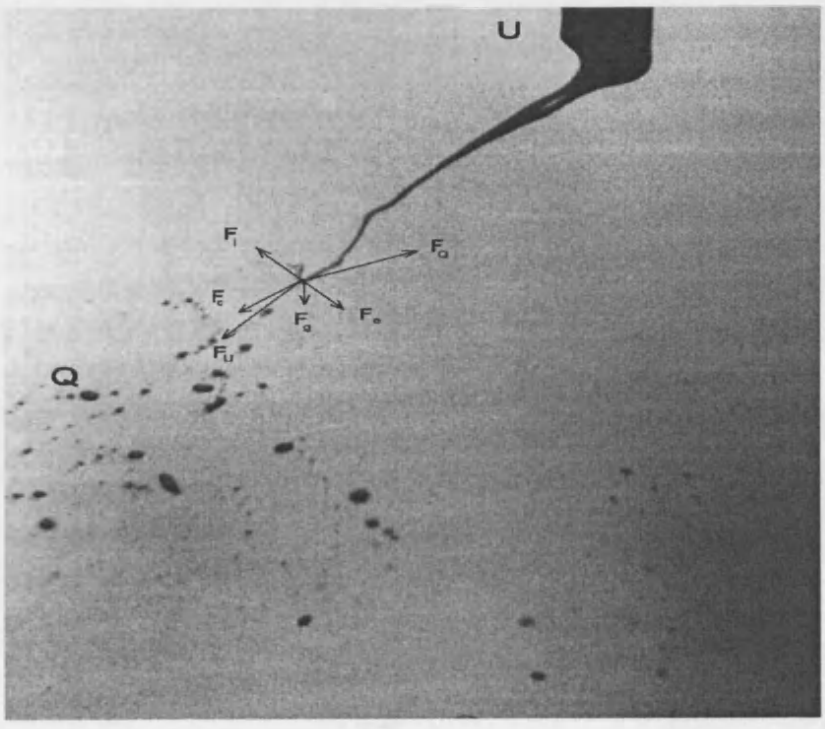

Figure 2.11 Oscillating-jet mode of electrohydrodynamic processing (Jaworek and Krupa, 1999)

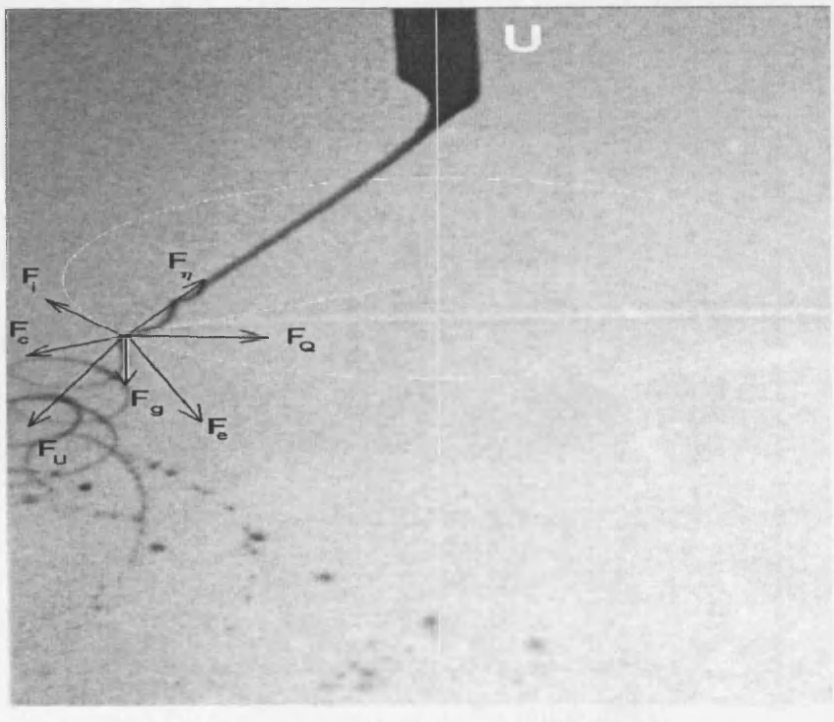

Figure 2.12 Precession mode of electrohydrodynamic processing (Jaworek and Krupa, 1999)

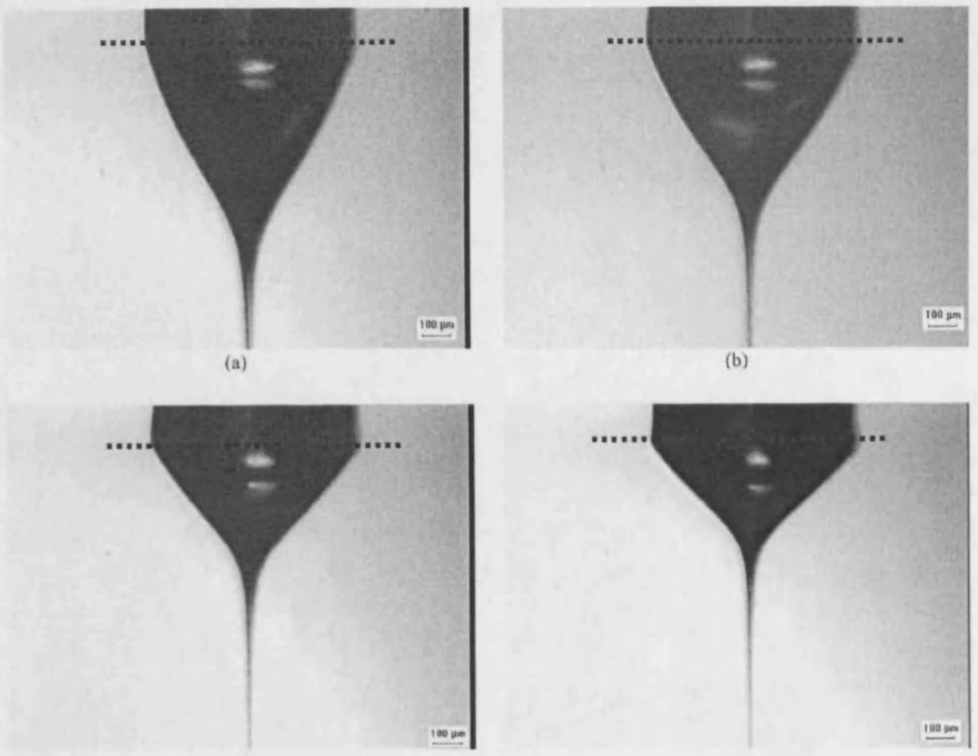

Figure 2.13 Variation in cone shape with change in applied voltage (Jayasinghe and Edirisinghe, 2004)

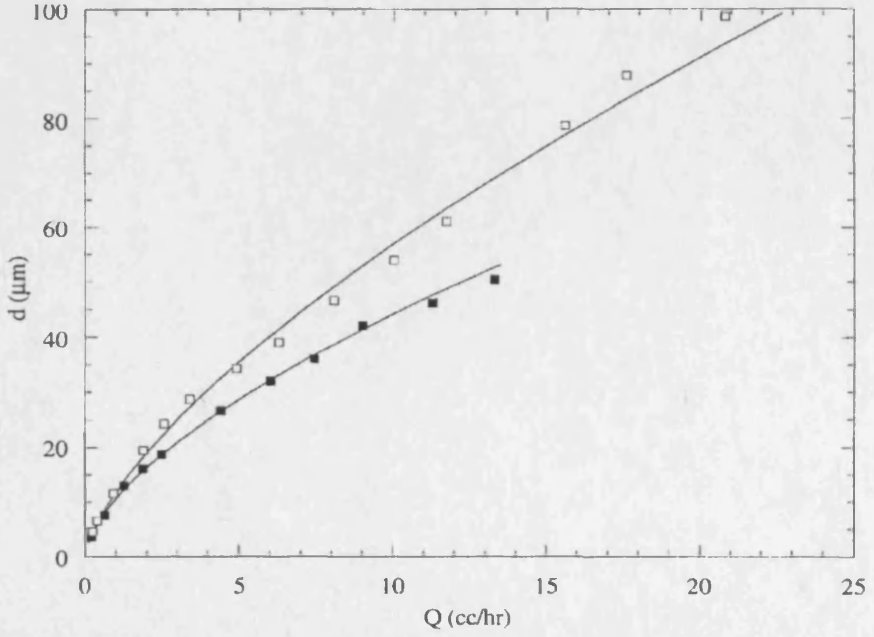

Figure 2.14 Droplet average diameter as a function of liquid flow rate (Tang and Gomez, 1996)

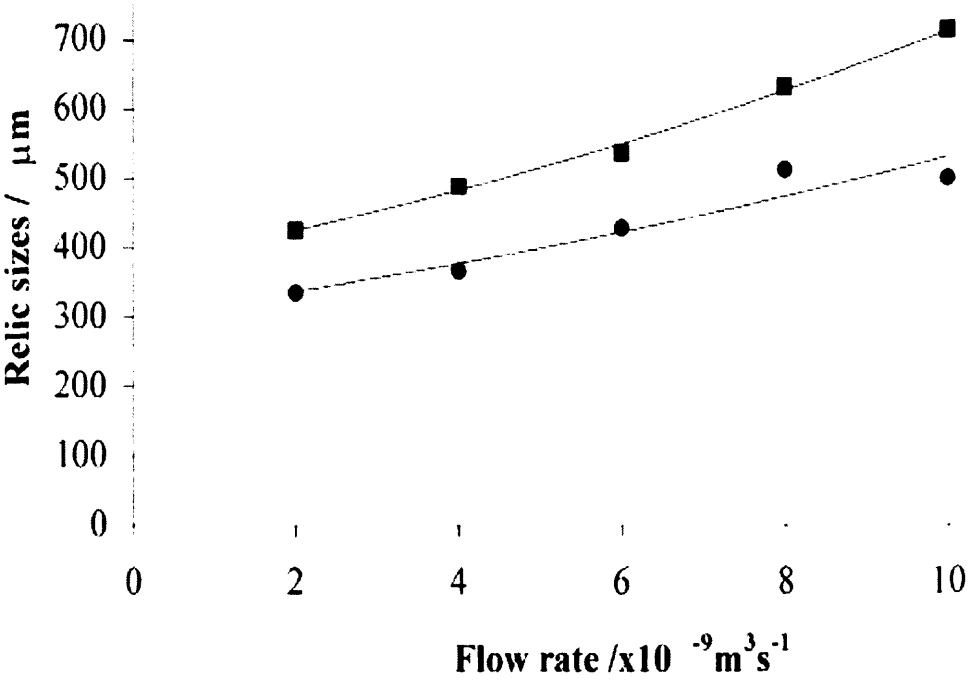

Figure 2.15 The variation of relic sizes with flow rate (Jayasinghe and Edirisinghe, 2004)

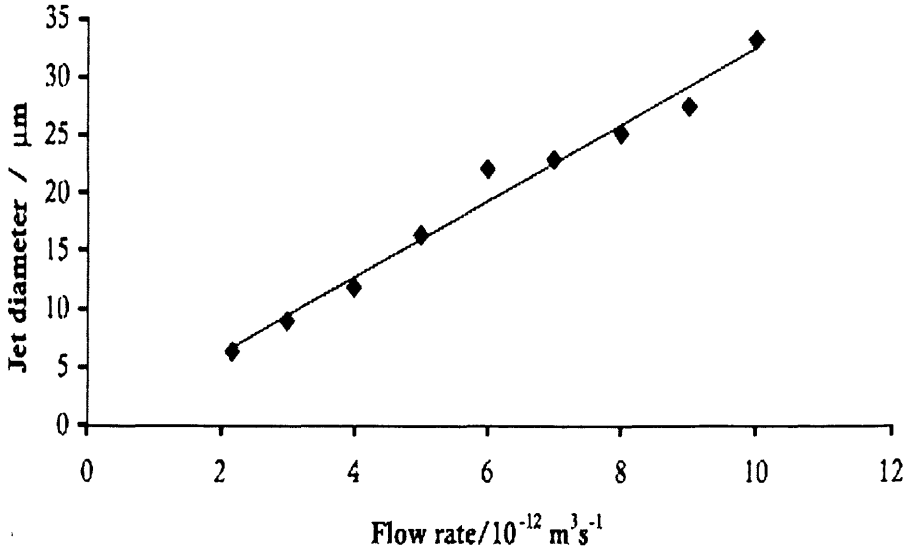

Figure 2.16 The variation of jet diameter with flow rate (Jayasinghe and Edirisinghe, 2005)

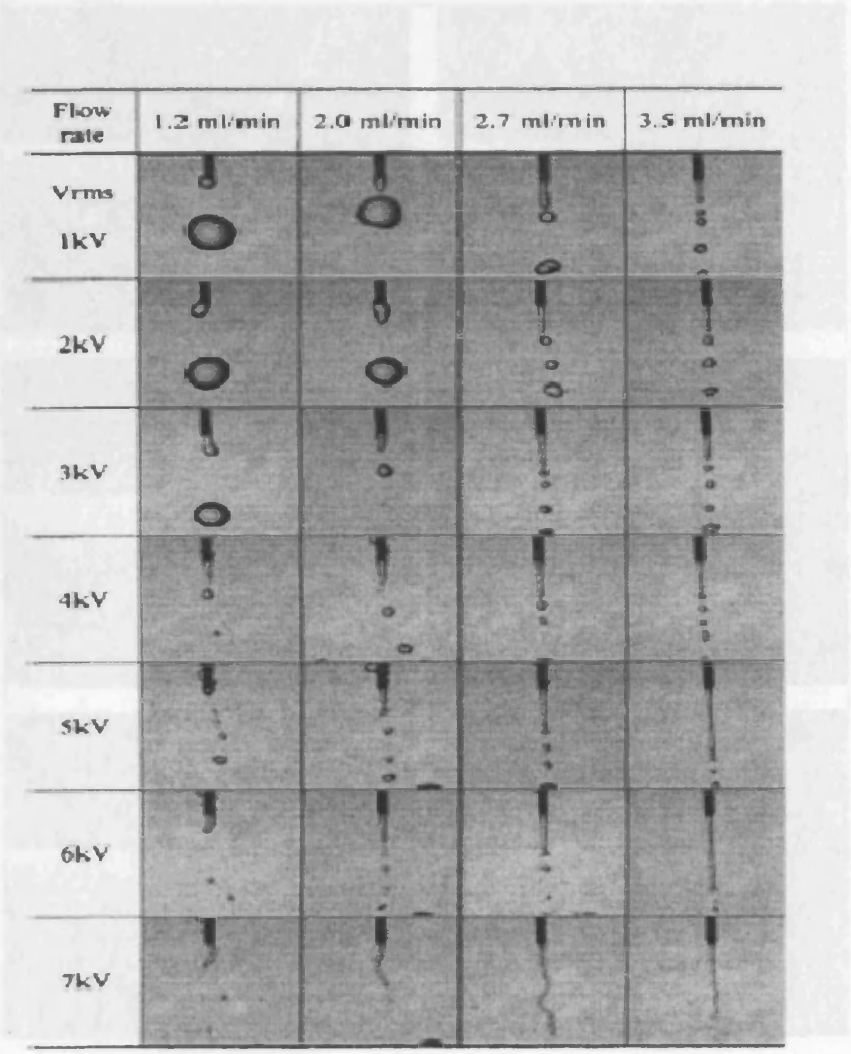

Figure 2.17 The variation of length of liquid column with flow rate and applied voltage (Sung and Lee, 2004)

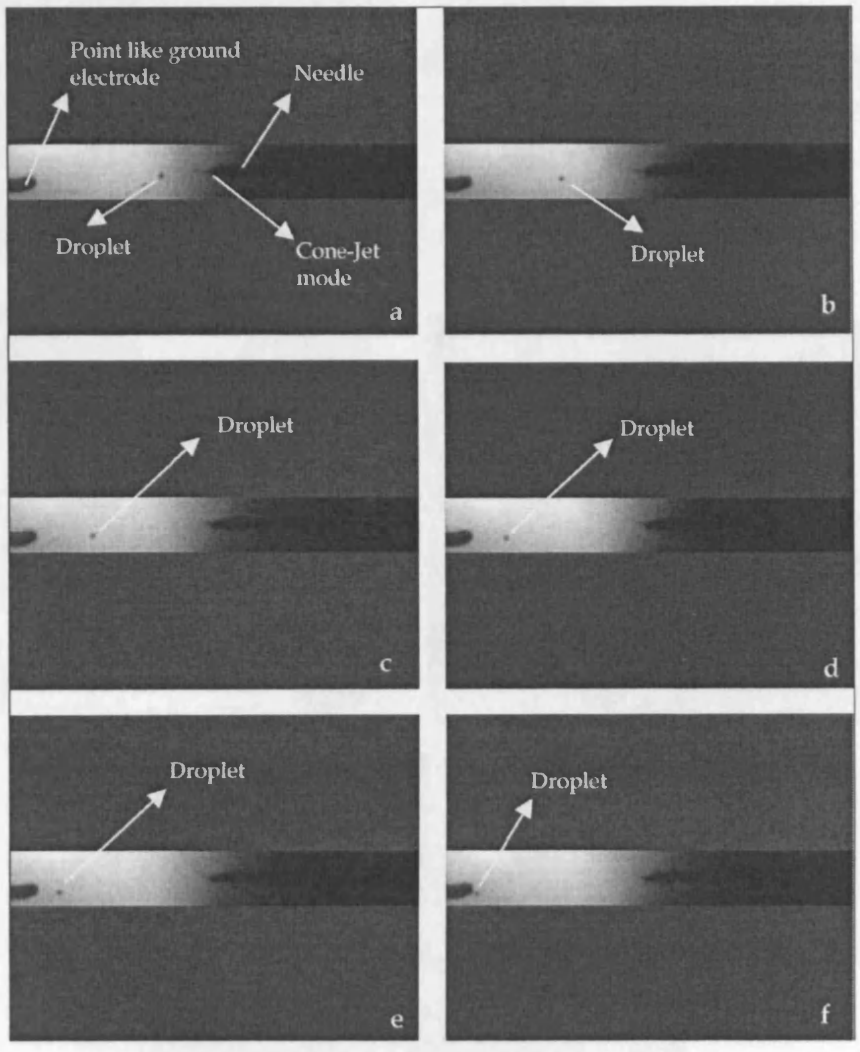

Figure 2.18 The trajectory of the droplet of suspension moving from the exit of the needle to point like ground electrode (Jayasinghe and Edirisinghe, 2004)

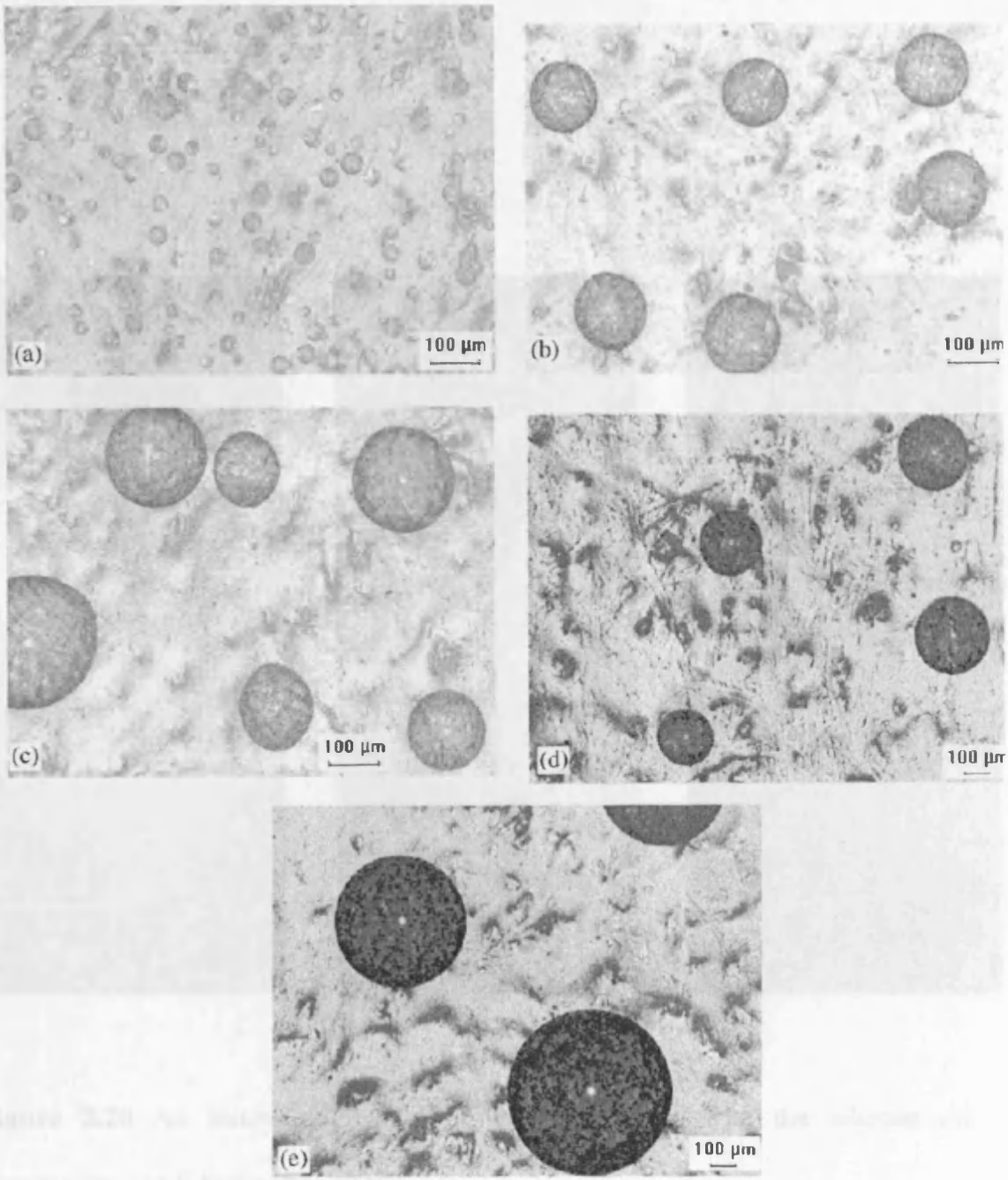

Figure 2.19 The optical micrographs of relics obtained with variation in viscosity of the liquid mixtures (Jayasinghe and Edirisinghe, 2002)

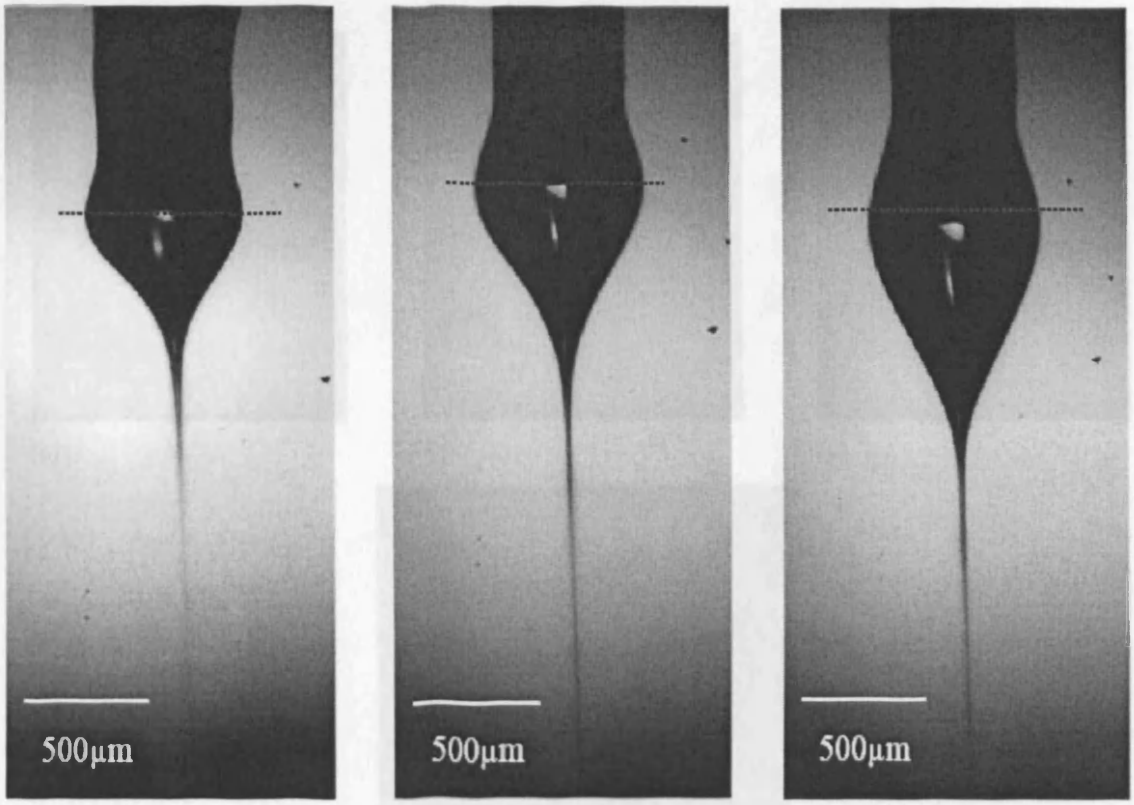

Figure 2.20 An innovative ball cone effect obtained with the silicone oil (Jayasinghe and Edirisinghe, 2004)

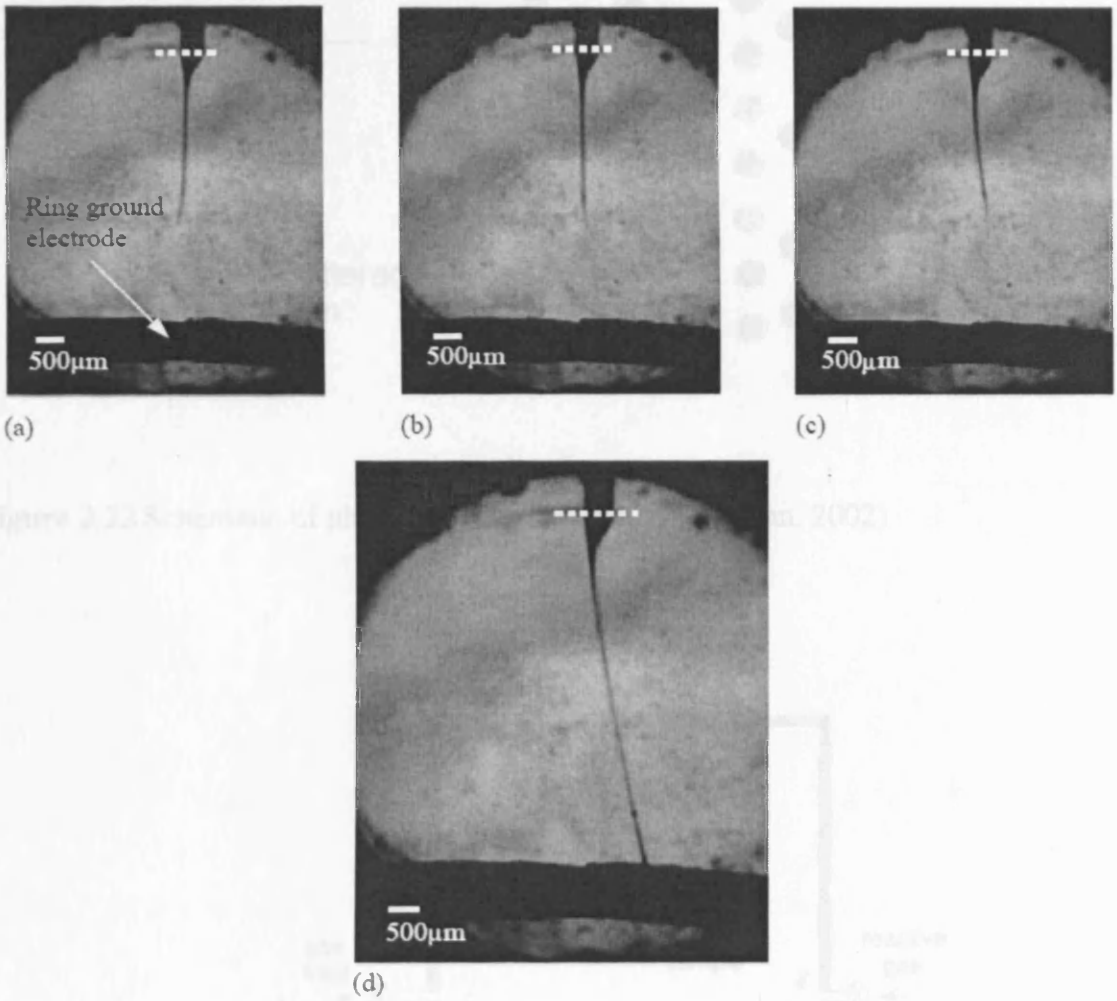

Figure 2.21 The micro-threading effect of liquid with viscosity $>10^4$ mPa s (Jayasinghe and Edirisinghe, 2004)

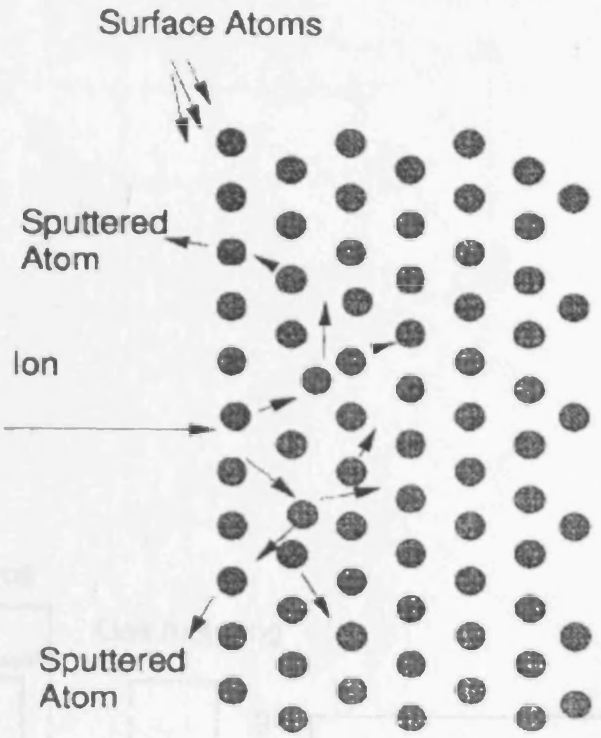

Figure 2.22 Schematic of physical sputtering process (Seshan, 2002)

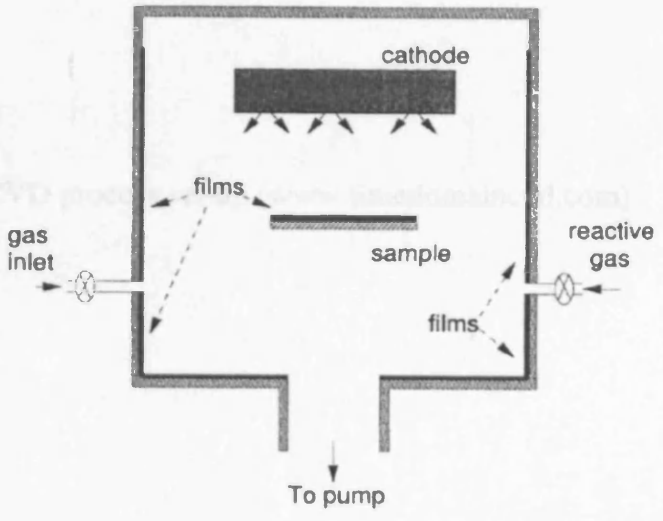

Figure 2.23 A typical reactive sputter deposition system (Seshan, 2002)

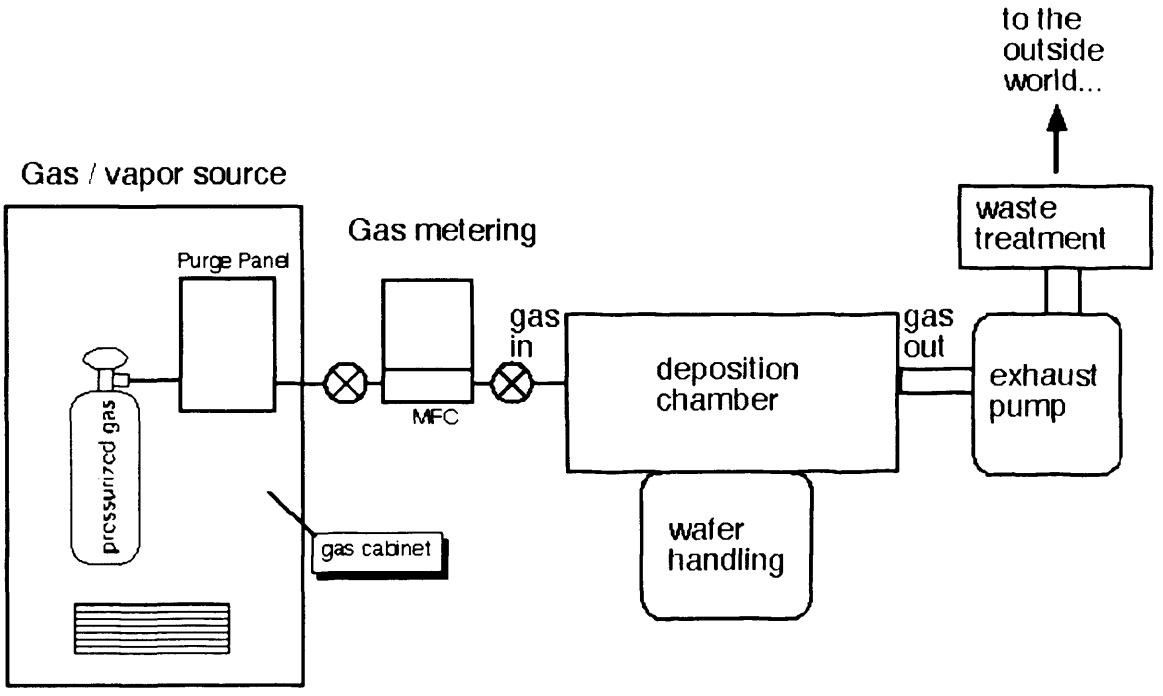

Figure 2.24 A typical CVD process set-up (www.timedomaincvd.com)

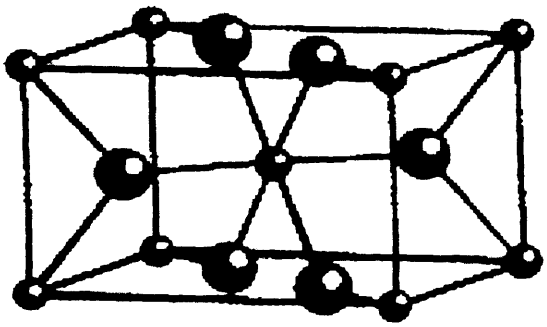

(a)

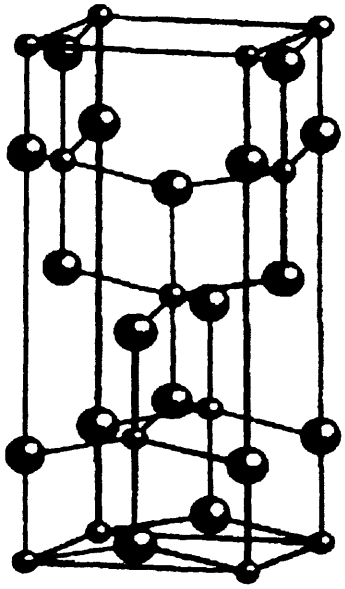

(b)

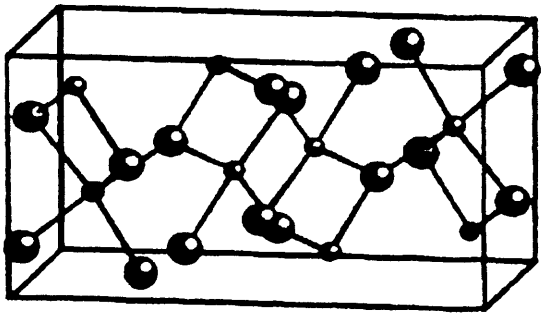

(c)

Figure 2.25 Different phases of TiO_2 (a) rutile (b) anatase (c) brookite

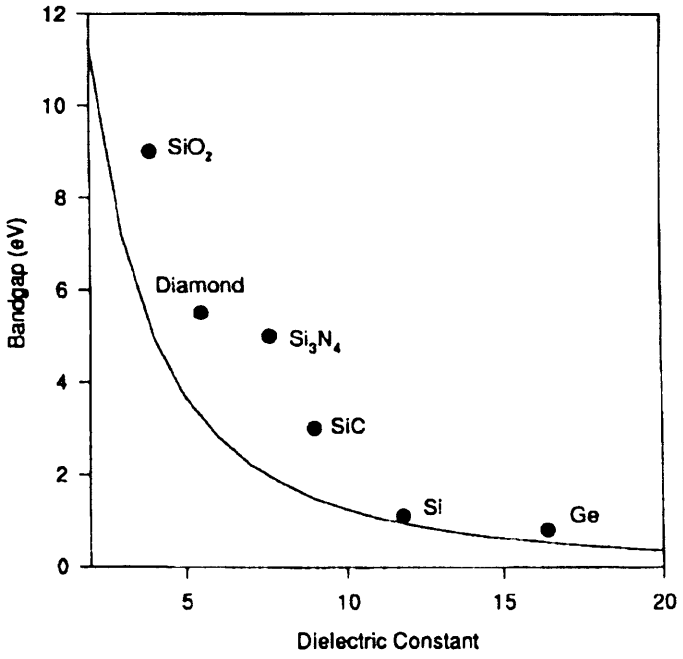

Figure 2.26 A relationship between bandgap and dielectric constant for simple dielectrics (Campbell et al., 1997)

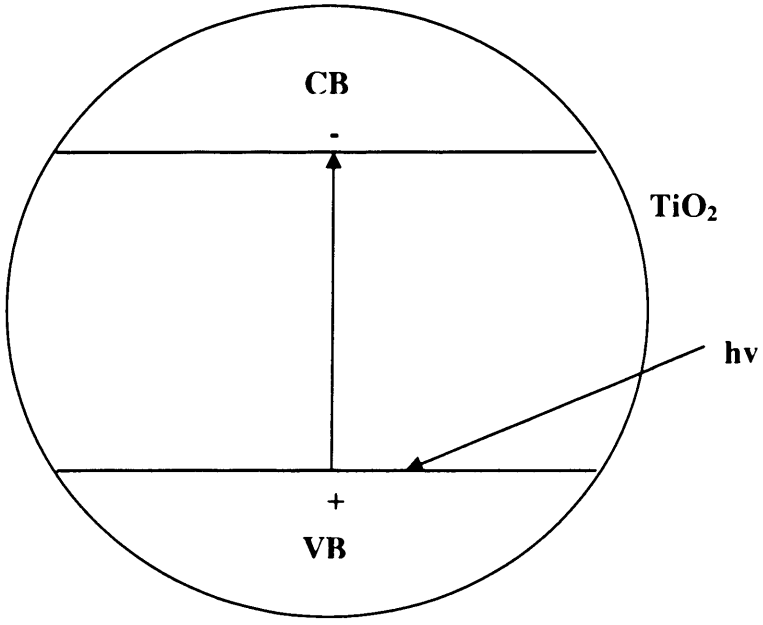

Figure 2.27 Excitation occurs in TiO_2 when light absorption with energy equal to or greater than bandgap energy

CHAPTER 3

Experimental Details

This chapter gives a detailed explanation of the experimental procedures that were followed in the investigations. The materials that were used, corresponding supplier, and product details are given. The methods followed for the preparation of titania sol, titania films, MOS capacitors, nitrogen doped titania sol, nitrogen doped titania films and the characterization techniques implemented are discussed. The detail of experimental set up that was used in electrohydrodynamic processing is also presented. All the equipments used in the experiments were calibrated against the reference data.

3.1 Materials

3.1.1 Titania sol

Titanium (IV) isopropoxide, Ti [OCH $(CH_3)_2]_4$ (Sigma-Aldrich, Poole, UK) was used as a precursor in research carried out in chapter **4**. In order to make titania sol, 99.7 % ethanol (VWR International, Lutterworth, UK) was used as a solvent. Precursor sol, which has precursor weight 2 %, had been made. The measurements for the precursor and solvent were carried out in a AND HF-1200G balance (A&D Instruments Ltd, Japan).

3.1.2 N-doped titania sol

Titanium (IV) isopropoxide, Ti [OCH $(CH_3)_2]_4$ (Sigma-Aldrich, Poole, UK) was used as a titania precursor in the experiments carried out in chapter **6**. In order to

make titania sol, 99.7 % ethanol (VWR International, Lutterworth, UK) was used as a solvent. The ammonia solution in ethanol (Sigma-Aldrich, Poole, UK) was used as a nitrogen dopant precursor in the experiments. The measurements for the precursors and solvent were carried out in a AND HF-1200G balance (A&D Instruments Ltd, Japan).

3.2 Preparation of sols

3.2.1 Preparation of titania sol

The titania precursor sol was prepared by transferring 2 wt % of precursor to an air tight bottle containing ethanol and the resulting solution was stirred using a magnetic stirrer for 3 hours at ambient conditions. The air tight bottles were used in order to prevent any evaporation or contamination until they were used. The sol obtained using ~2 wt % of precursor was very stable and no sedimentation occurred on standing indefinitely. However, it was kept on rollers for repeated use.

3.2.2 Preparation of N-doped titania sol

A 2 wt % of the precursor was added drop wise into a know weight of ethanol in an air tight bottle and stirred continuously for 3 hours to obtain a homogeneous sol. After that the ammonia solution in ethanol was added slowly drop by drop in to the aforementioned sol. Then it was subjected to vigorous stirring for 24 hours to obtain nitrogen doped colloidal solutions. The weight percentage of ammonia solution in ethanol was varied ~0.23 %, ~1 % and ~2 % to prepare three different sols and named Sol-1, Sol-2 and Sol-3.

3.3 Characterisation of sols

The important parameters governing the electrohydrodynamic processing are density, surface tension, viscosity, electrical conductivity and relative permittivity of the solution, and these physical properties were measured for the prepared sols. All the equipments used for characterisations were cleaned well and dried before each measurement and calibrated against the reference data. The characterisations were performed at ambient conditions.

3.3.1 Electrical conductivity

Electrical conductivity was measured using a HI-8733(Hanna Instrument) conductivity probe for research carried out in chapter **4** and chapter **6**. The electrode was always cleaned with distilled water and dried up before measurements. The electrical conductivity measurements were taken by using ~30 ml of sols in a beaker. The electrode was immersed in the sols up to the specified mark for a specified time and reading shown on the meter was recorded. The air bubbles residing in the sols were removed by agitating the sols slowly before the recordings. Five consecutive readings were taken and averaged for all investigations. These values are reported in this thesis.

3.3.2 Surface tension

Surface tension was measured using a Kruss Tensiometer K9 (Wilhelmy's plate method) for experiments done in chapter **4** and chapter **6**. The plate was hanged from a hook and a beaker containing the sample was placed in the stage below that. The plate was completely immersed into the sample whose surface tension is to be

measured and gradually lifted up. The reading recorded at point for which the surface of the liquid just detaches from the plate without breaking the surface gives the surface tension for the sample. Around 100 ml of the sols were used and five consecutive surface tension readings were taken to obtain the mean value of sols. The instrument was calibrated using ethanol before measuring the surface tension of the samples at every instance. The plate was cleaned and dried after each reading to minimize error.

3.3.3 Viscosity

Kinematic viscosity (ν) was determined by using a U-tube viscometer (BS/U type) in water bath at 20 °C for the research undertaken in chapter **4** and chapter **6**. This was determined by measuring the time (t) taken by samples to travel between the two marked regions in the U-tube viscometer. The time was recorded using stop watch with millisecond accuracy. Then, the kinematic viscosity was obtained by multiplying the viscometer constant (C) with the time (t).

$$\nu = Ct \tag{3.1}$$

Finally, the dynamic viscosity (η) was calculated by multiplying the kinematic viscosity with the relative density (ρ) of the sample.

$$\eta = \nu\rho \tag{3.2}$$

The de-ionised water was used to calibrate the viscometer. The average value of five readings has been reported in this thesis.

3.3.4 Relative permittivity

Relative permittivity was measured using a permittivity cell containing two copper plates of known area A mm^2 (≈491) and separated by length d mm (≈66) apart for the research described in chapter **4**. The sol was inserted between the plates and capacitance(C) across the plates was measured using the resistance-inductance-capacitance meter (RLC 100 –meter, Digimess, Korea). Taking the permittivity of free space to be ε_0 as 8.85×10^{-12} Fm^{-1}, relative permittivity(ε_r) value was calculated using equation,

$$\varepsilon_r = \frac{Cd}{\varepsilon_0 A} \tag{3.3}$$

The permittivity cell was always cleaned with distilled water and dried up before each measurement was taken.

3.3.5 Density

The densities of the samples were determined by using standard density bottle with the volume of 50 ml for the investigations mentioned in chapter **4** and chapter **5**. The standard density bottle was supplied by VWR International, Lutterworth, UK. Both the weight of the empty bottle and bottle filled with samples were measured on the chemical balance (AND HF-1200G A&D Instruments Ltd, Japan) which was capable of giving precise value up to the four decimals. All the measurements were carried out in ambient temperature and the density bottle was calibrated with ethanol. Five consecutive measurements were taken and average value of five density readings has been reported in this thesis.

3.3.6 Thermo gravimetric analysis (TGA)

The thermo gravimetric analysis (TGA) for the sol was carried out using a PEPKIN ELMER thermal gravimetric analyser for the research described in chapter **4**. The sol was placed in the sample holder and heated with the reference sample holder and the data were plotted in the computer. The thermal curves of TGA were obtained in flowing nitrogen gas at a heating rate of 10 °C min^{-1}. The temperature ranged from the room temperature to 400 °C.

3.4 Equipment used for electrohydrodynamic processing

3.4.1 Needle set-up

The equipment used for electrohydrodynamic processing of titanium dioxide films described in chapter **4**, consisted of a stainless steel needle with an internal and external diameter of ~330 μm and ~635 μm, respectively. It was held in epoxy resin, which insulates and imparts rigidity. The ring ground electrode with inner and external diameter of ~14 mm and ~16 mm respectively held below the axis of the needle was used for the droplet characterisation. The ground square shape plate (90 mm ×90 mm) attached to the rotating electric motor was used for film preparation. In the film preparation the ground plate was rotating at an off set to the axis, at 2 rpm with the help of a motor (Pareta and Edirisinghe, 2006). The needle exit to ring ground electrode or ground plate distance was kept at 40 mm. The schematic representation of the set-up is shown in **Figure 3.1**.

3.4.2 Metal clamped needle set-up

The N-doped titanium dioxide film preparation illustrated in chapter **6** was carried out using a metal clamped needle set-up. The epoxy resin holding a stainless steel needle with an internal and external diameter of ~330 μm and ~635 μm, respectively was supported by ~5 mm thick metal clamp. The ground square shape plate (90 mm ×90 mm) was held below the axis of the needle at a distance of 40 mm. The schematic representation of the set-up is shown in **Figure 3.2**. This set-up was employed to investigate the wider coverage area films at relatively low flow rate. For comparative purposes the N-doped titanium dioxide films also prepared using the same set-up with out a metal clamp (**Figure 3.3**).

3.4.3 Syringe pump

For the research carried out in chapter **4** and chapter **6**, the needle set-ups were connected to a syringe mounted on a Harvard Apparatus PHD 4400 programmable infusion pump using silicone rubber tubing. Syringes of different capacity were used for investigations and the syringe pump was calibrated for flow rate over long and short periods of time.

3.4.4 High voltage power supply

The needle and the ground electrode were connected to a high voltage power supply (Glassman Europe Ltd., Tadley, UK) using high voltage power cable which was capable of applying voltage up to 30 kV for the work mentioned in chapter **4** and chapter **6**.

3.4.5 Data recording

The images of the cone-mode and cone-shape were captured using microscopic lens in conjunction with a high speed camera (Weinberger AG, Dietikon, Switzerland) which was connected to a computer for research in chapter **4** and chapter **6**. A fibre optic light source was used for illumination.

3.5 Measurement of droplet and relic sizes

3.5.1 Sympatec laser diffraction

Droplet size distribution resulting from electrohydrodynamic processing in chapter **4** was measured using a computer controlled Sympatec Helos Model KF (helium laser optical spectrometer) sizing system (Sympatec Ltd., System Partikel-Technik, Bury, UK), which recorded and subsequently plotted the data collected. The laser system was incorporated in the electrohydrodynamic processing equipment by placing the 2.2 mm diameter laser beam approximately 15 mm below the needle exit, the same distance where manual collection of droplets took place. The sympatec system is based on the diffraction of light occurring when a laser beam impinges on the droplets of the spray. The laser beam travels perpendicular to the needle and measurements were synchronized with the appearance of the droplets in the measurement zone by monitoring the decrease in laser light transmission caused by droplet scattering. The lens used for the measurements had a droplet detection capability in the size range of 0.5 - 175 μm. The measurements were done in ambient conditions and reference background was taken prior to the measurements. The experiment was repeated 10 times, for which the 10 sets of droplet size distribution data were obtained for the sample.

3.5.2 Optical microscopy

The relics obtained from the investigation in the chapter **4** due to jet break up were collected on a microscopic glass slide approximately 15 mm below the needle exit and investigated on optical microscope (Nikon Eclipse ME 600). A joy stick connected to the table axis of microscope helps to move the table in x and y directions. The measurements were carried out by means of Acquis digital imaging software (Synoptics Ltd, Cambridge, UK).

3.6 Film and MOS capacitor preparation

The research on chapter **4** describes the titanium dioxide film preparation which was prepared using the set-up explained in section **3.4.1**. The nitrogen doped titanium dioxide film preparation which is described in chapter **6** was prepared using the set-up explained in section **3.4.2**. The description of substrates and heat treatment cycles used for the studies are given below. The MOS capacitor preparation for the research on chapter **5** also illustrated below.

3.6.1 Substrates

The silicon and glass slides were used mainly as substrates in the research carried out in chapter **4**, chapter **5** and chapter **6**. The aluminium also used as a substrate in processing of the TiO_2 films in chapter **4**. The details of the substrates are given below.

- Silicon: single crystal, (100) oriented, 500 μm thick, a specific resistivity of 0.1 Ωm, p-type doping
- Glass slides: amorphous, electrical insulator (microscope slides)

- Aluminium: 1mm thick, 10×10 mm^2 area

The silicon substrate was used for the structural and morphological studies of the films in chapter **4** and chapter **6**. This is also used in chapter **5** for the electrical characterisation of TiO_2 films. The glass substrate was used to analyse the optical properties of films described in chapter **5** and chapter **6**. The aluminium was used for the morphological studies of TiO_2 films in chapter **4**. Prior to the preparation of films, substrates were cleaned with ethanol and distilled water, finally dried carefully.

3.6.2 Heat treatment

The heat treatment was carried out on the as-deposited TiO_2 films and as-deposited N-doped TiO_2 films on silicon substrate in order to convert the films from amorphous to the crystalline structure using a furnace (Lenton Eurotherm 2216e) which can go up to the maximum temperature of 1000 °C. The as-deposited films were underwent heat treatment by ramping the temperature from the ambient temperature to 500 °C at 1 $°Cmin^{-1}$ followed by annealing at 500 °C for a further 1800 s. Finally, the films were cooled down from 500 °C to the ambient temperature at 1 $°Cmin^{-1}$ as shown in **Figure 3.4**. This procedure was followed in heat treating films to different temperatures in the investigations.

The TiO_2 films and N-doped TiO_2 films were deposited on microscope glass slides were annealed to various temperatures in the range of 400 °C to 600 °C using

similar conditions mentioned above. The TiO_2 films deposited on the aluminium substrate underwent heat treatment at 500 °C for morphological studies.

3.6.3 MOS capacitor

The metal-titanium dioxide-silicon structure was prepared before the electrical characterisation of the TiO_2 films at ambient conditions described in chapter **5**. The electrohydrodynamically processed TiO_2 films annealed to different temperatures on silicon substrate were used to prepare the MOS structure. The evaporated silver paste (Johnson Matthey Electronics, Hertfordshire, UK) was used as the top electrode in the MOS capacitor. The aluminium ohmic contact was made to the back of the silicon substrate by soldering. The active area of the structure is 3 mm^2 and 7 mm^2 for different characterisation purpose.

3.7 Characterisation of Films

Various characterisation techniques were used in all investigations mentioned in chapter **4**, chapter **5** and chapter **6**. These are explained in the following sections below.

3.7.1 Raman spectroscopy

Raman scattering measurements were done using a Renishaw Raman microscope. The Ar^+ laser with 514.5 nm incident wavelength was used to illuminate the as-deposited and annealed films. The Raman spectroscopy relies on inelastic scattering or Raman scattering of monochromatic light which is from the laser. The laser light interacts with phonons or other excitation in the system resulting in the energy of the laser photons being shifted up or down. The shift in energy gives the

information about the material. The samples were kept in the microscope slides and focused using the lens of microscope. Five different areas of the samples were selected and illuminated with the laser. The average of ten scans in the wave number range of 200-800 cm^{-1} is reported in this thesis. Before the measurements were taken, the instrument was calibrated using a standard Si substrate and during the measurements the room light was switched off to prevent the illumination from surroundings.

3.7.2 X-ray diffraction (XRD)

X-ray diffraction (XRD) was used for crystal phase identification and estimation of the crystallite size. Two x-ray diffractometers were used as per availability. The XRD measurements described in chapter **4** were made using a Siemens diffractometer D5000 using a Cu-Kα radiation source of wavelength λ=0.1540 nm. The diffracted intensity was recorded in the 2θ range 20-65° with a step of 0.02° per second. The power used for x-ray excitation was 40 kV voltage and 40 mA current. The XRD measurements described in chapter **6** were made using a Brucker D8 Discover system with a radiation source of wavelength λ=0.1540 nm. The diffracted intensity was recorded in the 2θ range 20-50° with a step of 0.02° per second. The power used for x-ray excitation was 40 kV voltage and 30 mA current.

Basically, x-ray diffraction is scattering of x-rays by crystals with accompanying variation in intensity due to interference effect. When the x-ray beam falls on crystals scattered radiation is produced by the all atoms. These scattered waves spread out spherically from all the atoms in the sample and the interference effects of the scattered radiation from the different atoms cause the intensity of the

scattered radiation to exhibit maxima and minima in various directions. This is used for identification of crystal phase and orientation of the given material. This intensity of scattered radiation could be related to the angle of the incident x-ray hitting the crystal by Bragg's law (Cullity, 1978).

$$2d \sin\theta = n\lambda \tag{3.4}$$

Where, θ is angle which the incident ray makes with the crystal plane, d is distance between the same set of planes, λ is wavelength of the x-ray and n is an integer.

The crystallite size t was estimated for the research carried out in chapter **4** and chapter **6** using the peak corresponding to orientation (101) and the Scherrer formula (Cullity, 1978), which is a generally accepted method of estimating the mean crystallite size.

$$t = \frac{0.9\lambda}{\beta \cos\theta} \tag{3.5}$$

λ is the x-ray wavelength used (0.1540 nm), β the broadening of the diffraction line measured as half of its maximum intensity (FWHM) and θ is the corresponding Bragg angle.

3.7.3 Fourier transform infrared (FTIR) spectroscopy

Fourier transform infrared (FTIR) measurements were done in transmission mode with a Perkin-Elmer system 2000. This technique is based on the interaction of

infrared radiation with the material to reveal information like the type of bonding in side the material. Molecular bonds in a material vibrate at various frequencies depending on the elements and the type of bond it has. Certain molecules absorb light at certain frequencies, which increases their vibrations. Here, the infrared radiation is absorbed by the molecules resulting in transition from ground state to an excited state. By examining the transmitted light after passing the light on to the sample how much energy is absorbed at each frequency could be determined. These could be used to find the different type of bonding in the material. The samples were placed in a sample holder and the infrared in the wave number range of 400 - 4000 cm^{-1} was directed to impinge on the samples. Ten scans were averaged at 4 cm^{-1} resolution has been reported in this thesis. Before the measurements, the background spectrum was obtained in N_2 gas flow and this was compared to the measurement with sample spectrum to determine the peaks of the spectra.

3.7.4 Scanning electron microscopy (SEM)

For the morphological characterisation of films, Jeol JSM 6300 F field emission scanning electron microscope (FE-SEM) was used. The FE-SEM uses an electron gun and capable of producing high resolution images at low as well as high keV range. The electrons are generated in a source and accelerated under influence of a strong electrical voltage gradient. With electromagnetic coils an electron gun is formed that scans the sample and secondary electrons are produced by interaction with the atoms at the surface of the sample. These electrons contain valuable information that is employed to reconstruct a very detailed image of the topography of the surface of the sample. The FE-SEM is a high resolution microscope with a

low energy input. The aluminium stub stuck with carbon sticker was used to hold the samples. Before placing the samples in the microscope they were gold coated with sputtering machine (Edwards Sputter Coater S150B) for 2 minutes.

For the as-deposited films prepared in chapter **4**, the samples were examined with the accelerating voltage of 10 kV and working distance set at 25 mm. The annealed films prepared in Si substrate were examined at accelerating voltage of 6 kV and working distance set at 25 mm. The images of annealed films prepared in Al substrate were obtained with the accelerating voltage of 10 kV and working distance of 15 mm. The cross sectional image of the film was taken by cutting the sample with diamond cutter and sticking it on an aluminium stub with an oblique surface. The image of N-doped TiO_2 film in chapter **6** was obtained with gold coating the sample on an aluminium stub for 2 minutes. The sample was examined with the accelerating voltage of 6 kV with working distance set at 25 mm.

3.7.5 Atomic force microscopy (AFM)

In chapter **6**, the atomic force microscopy (AFM) image was used to obtain the grain size of the N-doped TiO_2 film. The Si_3N_4 tips (Nanosensors) of 7 nm radius in non- contacting mode was used to obtain the image. When the tip connected to the cantilever beam travels over the surface of a sample it attracts or pushed away from the sample's surface due to forces between the tip and the surface and it deflects the cantilever beam. The laser measures the deflection with help of the photodiodes inside the machine. Before placing the sample inside the machine it was vacuum evacuated with help of a pump. The sample was placed inside the

machine and stuck with glue at backside of the sample. The scan frequency was in the range of 0.5 s^{-1}.

3.7.6 Electrical characterisation

The electrical characterisation of the films described in chapter **5** was done in room temperature, putting the samples in a light tight electrically shielded box. For reporting the effect of annealing temperature on processed films the electrical measurements were done for the films annealed at various temperatures. The capacitance-voltage (C-V) measurements for the MOS structures were conducted by measuring the capacitance as a function of bias voltage using Hewlett Packard LCR meter for different frequencies (100 kHz and 500 kHz). The bias was taken to be positive when the p-type Si substrate was held at a voltage higher than the top silver electrode deposited on the TiO_2 films. The leakage current-voltage (I-V) measurements through the structures were recorded using a Keithley electrometer.

3.7.7 UV/Vis spectroscopy

The experiments on chapter **5** and chapter **6** were carried out on an uv/vis spectrophotometer (Shimadzu UV-2401 PC). The films on glass microscope slides were used to record transmission spectra of the films in the wavelength range of 200-700 nm with an identical glass slide in the reference beam. The uv/vis spectrophotometer uses light in the visible and near ultraviolet to measure the electronic transition takes place inside the sample. It measures the intensity of light passing through a sample and compares it to the intensity of light before it passes through the sample over the range of wavelength. The produced uv-vis spectra

have broad features very useful for quantitative measurements. The light source used for the measurements was deuterium lamp for uv measurements and tungsten lamp for visible measurements. Before doing the measurements the baseline corrections were done in the spectrophotometer without placing any samples in the instruments. After that the sample and the reference sample were placed in a double-beam instrument where the light was split in to two beams. The one beam passed through the sample and the other through reference sample and analysed using the photodiode detector. The uv-vis spectra were plotted in the computer during the measurements. All the measurements were done in ambient conditions.

3.7.8 X-ray photoelectron spectroscopy (XPS)

The x-ray photoelectron spectroscopy studies described in chapter **6** was carried out using a Kratos Axis Ultra spectrometer with a monochromated Al Kα source (1486.6 eV). The measurements were performed in a high vacuum chamber with a base pressure of 10^{-8} Torr. Samples for the XPS measurements were prepared by putting the samples on the carbon tape stuck to the XPS sample support.

XPS is a surface chemical analysis technique that can be used to analyse the surface chemistry of the material. The XPS spectra are obtained by irradiating a material with a beam of x-rays while simultaneously measuring the kinetic energy (KE) and number of electrons escape from the surface of the material. A typical XPS spectrum is the plot of the number of electrons detected versus binding energy of the electrons detected. The energy of a particular x-ray wavelength equals a known quantity so the electron binding energy of each of the emitted electrons by using an equation (E Rutherford, 1914),

$$E_{binding} = E_{photon} - E_{kinetic} - \Phi \quad (3.6)$$

Where $E_{binding}$ is the energy of the electron emitted from one electron configuration within the atom, E_{photon} is the energy of the x-ray photons used, $E_{kinetic}$ is the kinetic energy of the emitted electron as measured by the instrument and Φ is the work function of the spectrometer.

The instrument used here was calibrated with the C (1s) binding energy at 284.7 eV. Multiplex XPS spectra of N (1s), O (1s) and Ti (2p) were recorded and fitted with an aid of CASA XPS software. The nitrogen content in the films was estimated from the relative area intensities of the N (1s), O (1s) and Ti (2p) peaks that were normalised using their relative sensitivity factors.

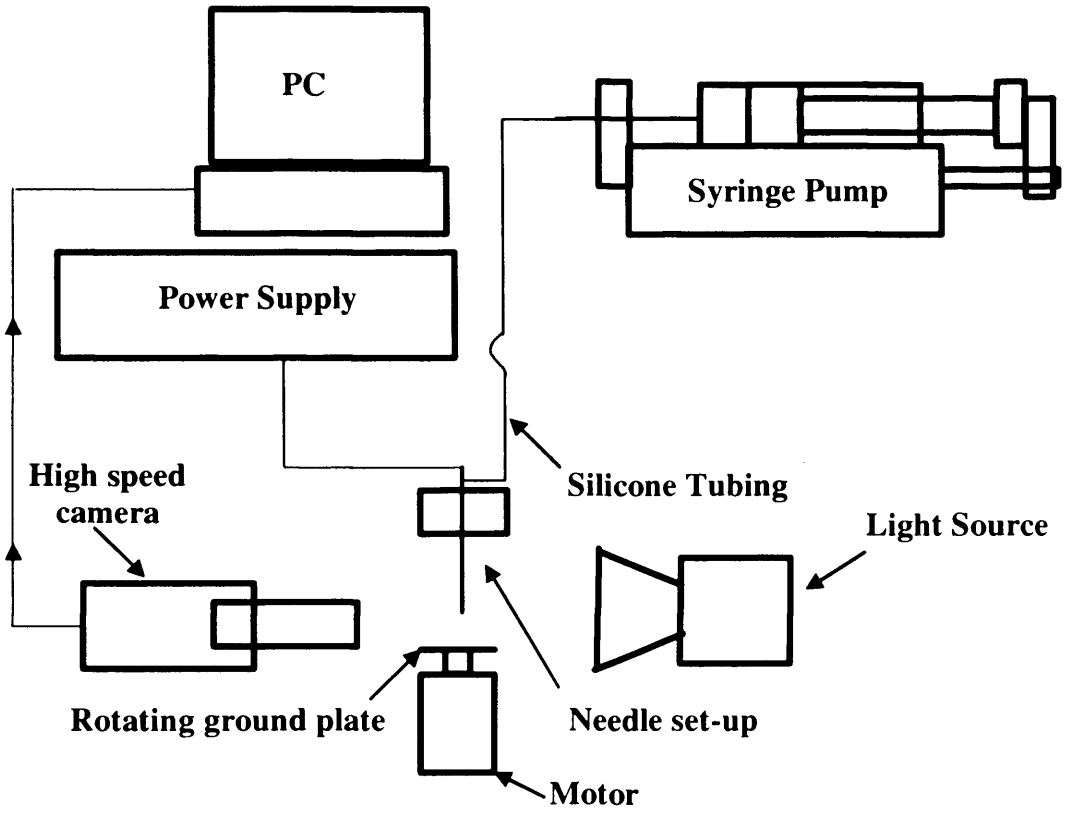

Figure 3.1 Electrohydrodynamic processing set-up for TiO_2 films investigations

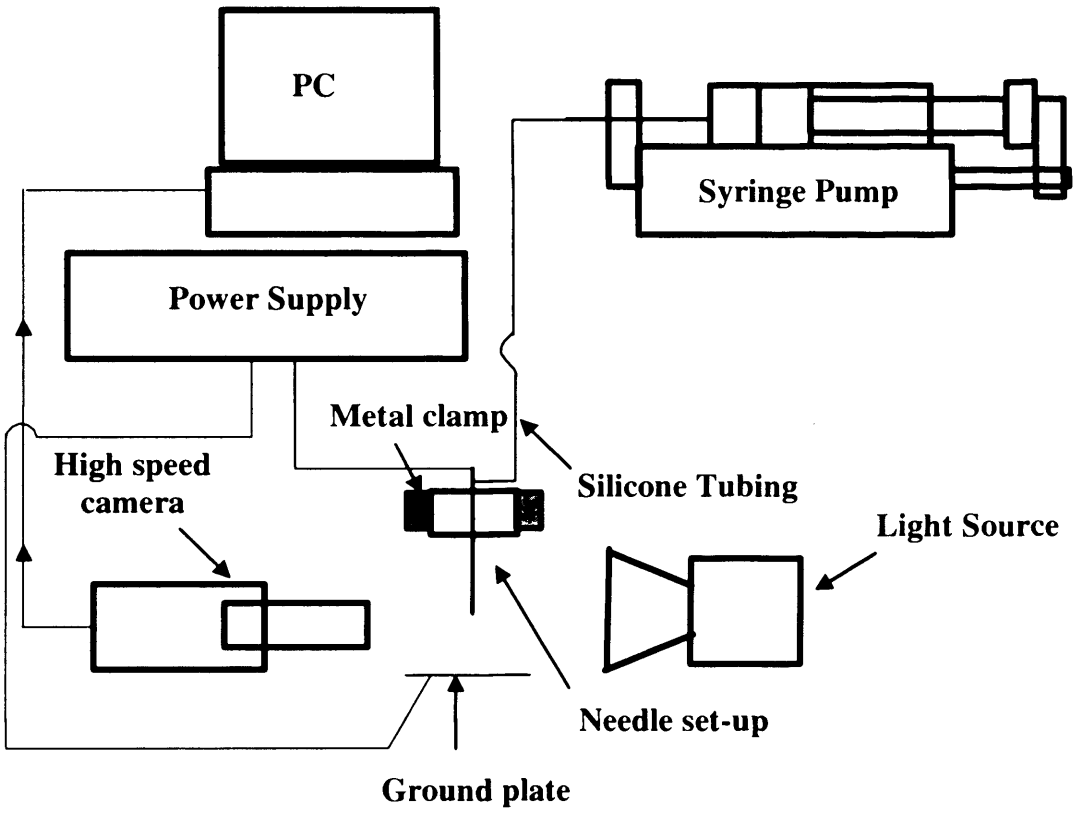

Figure 3.2 Electrohydrodynamic processing set-up for N-doped TiO_2 films investigations

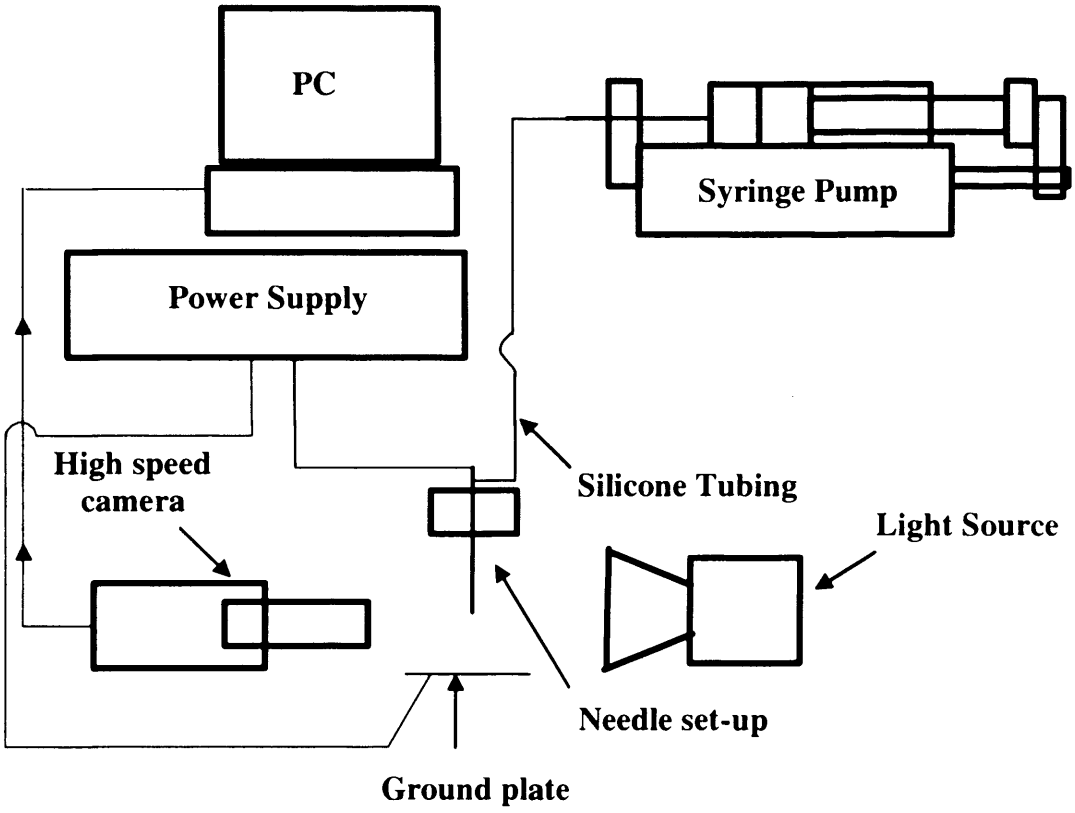

Figure 3.3 Electrohydrodynamic processing set-up for N-doped TiO_2 films investigations

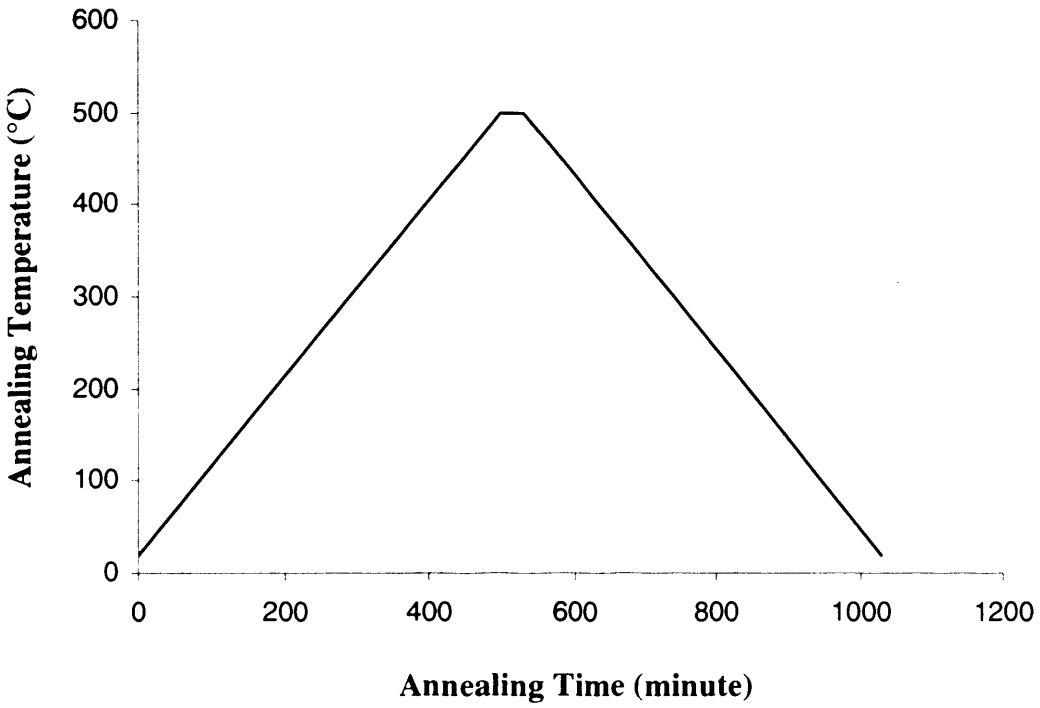

Figure 3.4 Heat treatment cycle for as-deposited TiO_2 and as-deposited N-doped TiO_2 films

CHAPTER 4

TiO_2 Film Preparation and Microstructural Characterisation

The research work on this chapter investigates the electrohydrodynamic processing viability of TiO_2 films. This route uses an electric field to generate a jet, which later breaks down to droplets, hence leading to a spray, which is a good source of material to prepare films on a substrate. The electrohydrodynamic processing has been used to form ceramic thin films due to relatively easy generation, narrow distribution of droplets in stable cone-jet mode (Watanabe et al., 2003). This chapter describes the effect of applied voltage and the flow rate employed during the electrohydrodynamic processing of titania sol to form the TiO_2 films. If the electrohydrodynamic processing method is used to prepare the TiO_2 films, it is very important to analyse the processing parameters such as applied voltage and flow rate on formation of the cone-modes. For this, the mode-selection map was drawn for various voltages and flow rates and the conditions for forming the stable cone-jet mode were established. The droplets in the stable cone-jet mode were characterised to determine the mono-dispersity.

This chapter further discusses the microstructural investigation of the electrohydrodynamically processed TiO_2 films annealed at various temperatures. The microstructural investigations were carried out using Raman spectroscopy and x-ray diffraction studies. The annealing temperature effects on microstructures of the TiO_2 films were analysed. The morphology studies of the electrohydrodynamically processed TiO_2 films were carried out using scanning electron microscopy.

4.1 Titania sol

The successful of electrohydrodynamic processing depends on stable solution for a long time. To achieve this, a low weight percentage (~2%) of precursor was used to prepare the titania sol for processing the TiO_2 films. The high weight percentage (~5%) of precursor used to obtain the titania sol was viscous and formed a sedimentation and gave a fog like appearance. The sol obtained using ~2 wt % of precursor was very stable and no sedimentation occurred on standing indefinitely, however it was kept on rollers for repeated use.

4.1.1 Sol physical properties

Since the electrohydrodynamic processing depends on physical properties of the liquids which are used in atomisation it is very important to understand and analyse the physical properties of the titania sol. The titania sol properties were determined as discussed in section **3.3**. The physical properties of the prepared TiO_2 sol and the ethanol are given in **Table 4.1**.

Table 4.1 Physical properties of TiO_2 sol and ethanol

		Sol	**Ethanol**
Electrical conductivity	Sm^{-1}	6×10^{-5}	1×10^{-5}
Surface tension	mNm^{-1}	26	23
Density	kgm^{-3}	791	790
Relative permittivity		17	26
Viscosity	mPa s	1.5	1.3

The ethanol is widely used as a liquid carrier in electrohydrodynamic processing because of its low surface tension, which enables the electric field to overcome the surface forces and generate a jet. The usage of water is avoided here in hydrolysing the metal organic precursor because it is very difficult to atomise the aqueous medium in electrohydrodynamic processing in air due to high surface tension of water, which will result in corona discharge (Smith, 1986). Since the weight percentage of the sol in ethanol is small (~2%), its density was only slightly higher than ethanol. Its electrical conductivity is greater than ethanol but not sufficiently high to make the process unstable (De la Mora and Loscertales, 1994). The surface tension and viscosity of the titania sol is also higher than the ethanol. The relative permittivity of the titania sol was considerably lower than the ethanol's relative permittivity. This parameter along with the electrical conductivity is very crucial in determining the electrohydrodynamic jetting which will be discussed later in the section **4.2.4**.

4.1.2 TGA of titania sol

Figure 4.1 shows the TGA curve for the titania sol which was used in electrohydrodynamic processing. The figure shows two break-up points, one between the room temperature and ~160 °C and another between 160 - 250 °C. The rate at which the loss of weight is higher in the first step compared to the second step. Thereafter, the weight remained constant. The first step weight loss corresponded to a loss of water and solvent molecules which were adsorbed in the titania sol. The second weight loss is associated with the loss of structural hydroxyl groups and the substances like unhydrolyzed isopropoxide/organic residues which

might left in the titania sol. The constant weight obtained above 250 °C indicating that the titania sol was independent of the dehydration.

4.2 Electrohydrodynamic processing of TiO_2 films

For ceramic thin films and coatings, the electrohydrodynamic processing in stable cone-jet mode exhibiting a very promising potential with its inherent capability of producing fine droplets in micro and sub-micrometer range with a narrow size distribution (Miao et al., 2002). The electrohydrodynamic processing of titania sol was carried out to prepare the TiO_2 films using the equipment configuration explained in section **3.4.1**. The electrohydrodynamic processing is depends on electrostatic forces to break the liquid filament in to fine charged droplets. The applied voltage was varied between 3 - 6 kV to create an appropriate electric field between the capillary and the ground electrode to overcome the surface tension forces. The flow rate was varied between 2×10^{-11} - 2×10^{-10} m^3s^{-1}. The flow rate regime was selected low as possible to minimise the current through the liquid cone and the surface charge on the jet to prevent or minimize the formation of secondary and satellites droplets (Hartman et al., 2000; Jayasinghe and Edirisinghe, 2004).

A careful selection and observation of physical properties of the processing medium and the processing parameters are essential to establish the stable electrospray for a long time to process the films. For example, the high surface tension solutions need a very high voltage for establishment of a stable electrospray, in some cases this might be higher than the surrounding atmosphere's electrical break down threshold where a stable electrospray can not be formed (Tang and Gomez, 1994). On the other hand, every liquid used in this process has a

minimum flow rate below which there is no stable cone-jet mode established (Hartman et al., 2000). In order to find out the suitable processing conditions for the titania sol to prepare the TiO_2 films the mode-selection map was drawn for various combinations of applied voltage and flow rate. The mode-selection map is very useful to identify the stable cone-jet domain and hence establish the processing conditions.

4.2.1 Mode-selection map

Figure 4.2 shows the mode-selection map for the titania sol used to process TiO_2 films as a function of flow rate and applied voltage. The map consists of different domains for each spraying modes identified in the electrohydrodynamic processing spans over the various applied voltages and flow rates. Each domain has an operating voltage window where their respective modes start and end in that particular range. By connecting the operating voltage window at different flow rates the boundaries for the each domain was developed. The stable and mono-disperse spraying could be established only within the certain ranges of applied voltages and liquid flow rates for a fixed experimental set up and a liquid medium which defines the stable cone-jet mode domain.

The stable cone-jet domain was narrower in the low flow rate ($< 8 \times 10^{-11}$ m^3s^{-1}) regime obtained within the applied voltage of 4 - 4.4 kV. At higher flow rates ($> 8 \times 10^{-11}$ m^3s^{-1}) the domain was broader and the stable cone-jet mode was obtained in the wider applied voltage window of 4.1 - 5.8 kV. However, the domain was shrunk when the flow rate was increased above 1.8×10^{-10} m^3s^{-1}. Out side the stable cone-jet mode domain dripping, micro-dripping, spindle, unstable cone-jet and

multi-jet mode domain were existed with their respective operating voltage window.

4.2.2 Effect of applied voltage

The applied voltage is an important processing parameter and affects the magnitude of electric field strength in the electrohydrodynamic processing. The different modes of operation can be observed as the applied voltage is gradually increased (Cloupeau and Prunet-Foch, 1990). The effect of applied voltage on the titania sol was studied carefully. For a fixed flow rate of 1×10^{-10} m^3s^{-1} increasing the applied voltage changed the operating modes from dripping→ micro-dripping → unstable→ stable→ multi-jet.

4.2.2.1 Operating mode and cone-shape

The mode of electrohydrodynamic processing is the way the liquid is dispersed into droplets and it could be characterised by geometrical form of the liquid at the end of the capillary (Jaworek and Krupa, 1999). **Figure 4.3** shows the dripping mode at no applied voltage. A near spherical drop was hung at the outlet of the capillary. Increasing the applied voltage changed the shape of the drop and the drop was elongated in the vertical direction. This is called micro-dripping mode and observed at the applied voltage of 3.1 kV. This has been shown in **Figure 4.4**. **Figure 4.5** shows the unstable cone-jet mode at the applied voltage of 4.1 kV where the shape of the drop changed between semi-spherical and cone shape. The stable cone-jet mode was achieved at the voltage of 4.5 kV. A very fine cone shape was observed and at the apex of the cone a fine jet was clearly seen. This is shown

in **Figure 4.6**. At this mode the electric filed strength and surface tension of the titania sol are equal. **Figure 4.7** shows the multi-jet mode. This was resulted when increasing the voltage beyond the stable cone-jet voltage window. Two attached cones with an oblique appearance were seen and at each of the cone apex the jets were ejected.

4.2.3 Effect of flow rate

The flow rate is a key variable in electrohydrodynamic processing and it influences the droplet size of the electrospray. According to Ganan-Calvo et al. (1997) the droplet size is directly proportional to the flow rate. The effect of liquid flow rate over the electrohydrodynamic processing of titania sol was investigated by keeping the applied voltage constant.

4.2.3.1 Operating mode and cone-shape

The stable cone-jet mode was obtained at a constant applied voltage of 5.5 kV as the flow rate was varied between 1.2×10^{-10} - 2.4×10^{-10} m^3s^{-1}. When the flow rate was increased the cone depth was increased notably. **Figure 4.8** shows the stable cone-jet mode obtained at a flow rate of 1.2×10^{-10} m^3s^{-1} and applied voltage of 5.5 kV. The measured cone depth was 384 μm. The cone depth obtained at a flow rate of 1.6×10^{-10} m^3s^{-1} was 408 μm. This is shown in **Figure 4.9**. **Figure 4.10** shows the cone shape at a flow rate of 2×10^{-10} m^3s^{-1} and the measured cone depth was 537 μm. The increase in cone depth was significant in this case when compared to previous case. The cone depth was even further increased when the flow rate was

increased to 2.4×10^{-10} m^3s^{-1}. This is shown in **Figure 4.11**. The cone depth obtained was 686 μm.

4.2.4 Cone-jet and droplet characterisation

The stable cone-jet diameter and the droplet size distribution of the titania sol flowing at a rate of 1×10^{-10} m^3s^{-1} determined and compared with the scaling law given by Ganan-Calvo et al. (1997).

On top of that, for a classical electrohydrodynamic stable cone-jet mode atomisation to take place, t_e, the electrical relaxation time must be much smaller than, t_h, the hydrodynamic time this establishes the inequality (Ganan-Calvo et al., 1997).

$$\frac{\beta\varepsilon_o}{K} \langle\langle \frac{LD^2}{Q} \tag{4.1}$$

as a prerequisite for film preparation, where β is the relative permittivity, K is the electrical conductivity, Q is the flow rate, D is the jet diameter and L is the axial length of the jet, ε_o is the permittivity constant (8.85×10^{-12} Fm^{-1}). In the stable cone-jet mode, the cone and jet dimensions were measured using the video recordings. The measured jet diameter (D) is 8 μm at an axial distance of 1000 μm from the exit of the needle (L). Using the values in **Table 4.1** and equation (4.1), it gives t_e 2.51×10^{-6} s and t_h 6.4×10^{-4} s. Therefore, $t_h >> t_e$ and the classical electrohydrodynamic atomisation is taking place.

4.2.4.1 Jet characterisation

Using the values in **Table 4.1**, the jet diameter (D) in the stable cone jet mode can be estimated by (Ganan-Calvo et al., 1997)

$$D \approx \sqrt[3]{\frac{(\beta - 1)^{1/2} Q \varepsilon_o}{K}} \tag{4.2}$$

Equation (4.2) gives D as ~ 4 μm; as stated before the measured jet diameter at a distance of 1000 μm from exit of the needle is ~ 8 μm. This discrepancy probably lies in the fact that equation (4.2) does not take viscosity into account.

4.2.4.2 Droplet characterisation

The electrohydrodynamic processing modes differ in the way droplets are produced and this affects the droplet size and size distribution. According to the classification of electrostatic atomisation by Jaworek and Krupa (1999), more than 10 distinct modes are found to give fine aerosols during spraying. On the other hand, only the droplets generated from the cone-jet and micro-dripping modes are near mono-disperse; while most other modes usually give polydisperse droplets although some times the size distribution can be narrow. Therefore, the cone-jet mode is considered to be the only suitable choice because it generates both fine and mono-disperse droplets.

The quality of the ceramic thin films and coatings are heavily dependent on the size and size distribution of the ceramic powder particles during deposition process (Balachandran et al., 1994), because the fine particles with narrow size distribution

have the effect of limiting the size of voids between particles, this enables coatings to be deposited with high homogeneity and without flaws.

Figure 4.12 shows the droplet size distribution measured using a laser spectroscopy. The repeated experiments showed a clear narrow unimodal droplet size distribution with a peak at ~2 μm. The average droplet size was 1.9 μm. However, the droplets collected and viewed immediately after the deposition are strikingly near mono-disperse and are ~ 1.5 μm (**Figure 4.13**). The narrowing of the size range to 1.5 μm during the flight of the droplets towards the ground electrode is most probably caused by the straying and loss of some finer droplets towards the extremities of the ground electrode and evaporation of the ethanol from the coarser droplets (Grigoriev and Edirisinghe, 2002).

4.3 Film preparation

The titania sol flowing at a rate of 1×10^{-10} m^3s^{-1} was utilised for film preparation. The films were prepared by the method proposed by Pareta and Edirisinghe (2006). The centre of the substrate was slightly off-set to the exit of the needle. Since the spraying time would influence the film thickness, it was kept as short as possible whilst not affecting the film uniformity. A film thickness of ~ 200 nm was obtained by spraying up to 60 s.

4.3.1 Characterisation of TiO_2 films

The characterisation of the processed films is quite important in order to widely apply the method to the large scale. The characterisation could be related to

determining the mechanical, electrical and optical properties of the processed films. The electrohydrodynamically processed TiO_2 films were characterised using Raman spectroscopy, XRD and SEM. The structural characterisation of the films was done to identify the phases of TiO_2 films formed in electrohydrodynamic processing. The morphological studies were carried out to assess the surface quality of the processed films.

4.3.1.1 Raman spectroscopy of TiO_2 films

A Raman spectroscopy is a very powerful tool for detecting the different crystalline phases in TiO_2 films. The results from Raman spectroscopy showed the films consisted of the anatase phase of titania and increasing the annealing temperature results in the rutile phase of titania.

The Raman spectra are shown in **Figure 4.14**. A strong peak characteristic of the Si substrate is present at 520 cm^{-1} in all the films. The as-deposited film showed no characteristic peaks other than Si substrate peak. This is indicating that the as-deposited films were amorphous in nature. The film annealed at 500 - 700 °C display three well defined peaks at 143 cm^{-1}, 396 $cm^{-1}$and 638 cm^{-1}. These are attributed to the anatase phase. It is clearly seen that the films annealed at these temperatures didn't exhibit any peaks related to the rutile phase which demonstrates that the films contain only the anatase phase. The intensity of Raman signals is well correlated with the degree of crystallinity. As the temperature is increased, progressive increases in the peak intensity accompanied by sharpening of the peaks are observed, implying an increase in the crystallinity of the anatase phase with increased temperature.

The film annealed at 800 °C shows an additional strong peak at 196 cm^{-1}, which also belongs to the anatase phase (Kelly et al., 1997). As annealing temperature increased to 900 °C a weak peak starts to appear at 439 cm^{-1} which is a feature resulting from the evolution of the rutile phase. According to Czanderna et al. (1958) the anatase phase irreversibly transforms to the rutile phase on heat treatment above 450 °C. However, the phase transition temperature depends upon the grain size, presence of impurities, dopants, precursor materials and synthesis methods (Hirano et al., 2003).

4.3.1.2 XRD study of TiO_2 films

Figure 4.15 shows the XRD studies of the electrohydrodynamically processed TiO_2 films annealed at various temperatures. It can be seen that all films show a dominant reflection at 2θ value of 25.28. This is corresponds to anatase phase with (101) direction and indicates that all films yielded this preferred orientation. In addition to this the film annealed at 500 °C showed three more distinctive peaks at 2θ values of 37.98, 48.08 and 55.07. These are related to anatase phase with (004), (200) and (211) orientations because of the closeness of their relative intensities to the standard data (JCPDS-ICDD 21-1272).

The films annealed in the range of 600 - 800 °C showed the stronger and sharper peaks compared to the film annealed at 500 °C means that increasing the annealing temperature leads to improvement in the crystallinity of the films. The films annealed in this range showed three more orientations at (103), (112) and (105). These also correspond to the anatase structure of TiO_2 films. At these temperatures there is no reflection related to the rutile phase of the TiO_2 film was observed.

However, the film annealed at 900 °C showed a peak at 2θ = 27.38 and this is attributed to the rutile phase. These results were well agreement with the results of the Raman spectroscopy results discussed in the section **4.3.1.1**.

The average crystallite size of TiO_2 films annealed at various temperatures estimated using Scherrer's formula mentioned in the section **3.7.2**. The broadening of the diffraction peaks could be related to the average crystallite size of the films. Increasing the annealing temperature resulted in less broadening of the diffraction peaks indicating that annealing temperature increases the crystallite size. The relationship between the annealing temperature and the crystallite size is shown in the **Figure 4.16**.

The growth in crystallite size was non-linear between the annealing temperatures 500 - 700 °C but the crystallite size was linearly increasing with the annealing temperature between 700 - 900 °C. The crystallite size calculated at 500 °C was ~21 nm and this result is in agreement with the grain size of ~ 30 nm observed using a scanning electron microscopy results described below (**Figure 4.23**).

4.3.1.3 Morphological study of TiO_2 films

The FE-SEM image (**Figure 4.17**) shows that the deposited film is very homogeneous and containing a reticular network of particles. The average particle size is ~ 1 μm. A high magnification investigation on one region (**Figure 4.18**) indicates that these particles are starting to become agglomerated particles, a process which can lower the total surface energy to stabilize the system. **Figures 4.19** and **4.20** shows that the films annealed at 500 °C have very dense and crack-

free surfaces. The formation of dense films could be explained by the following mechanism.

The droplets generated from the instability of the jet emerging at the tip of the cone contains particles (solutes) arriving at the substrate still "wet enough" to bond to the substrate. Once hitting the substrate the droplets start to spread and the spreading rate is influenced by surface tension forces at the substrate and viscosity of the precursor sol. It is well known that surface tension for the Si substrate is much higher than that of dielectric oxides. Therefore, the initial spreading rate must be rapid to lower the systems energy. The viscosity of the precursor sol in our case is also only slightly higher than water and helps it to increase the spreading rate considerably. For surface diffusion to take place there should be enough temperature where solute atoms migrate from one place to another to form the preferential orientation. At 500 °C particle (solute atoms) rearrangement takes place and the nature of the film becomes amorphous to crystalline.

The film annealed at 500 °C has some rough spots. This is due to the fact that particles are agglomerated and grow on the previously deposited layer of dielectric film rather than the Si substrate. The dielectric film has lower surface tension than the Si substrate and therefore spreading of droplets is reduced leaving some rough spots. Apart from this the film produced was very dense and crack free compared with those obtained on an Al substrate (**Figure 4.21** and **Figure 4.22**) where cracking in the layer is widely prevailant due to the higher different thermal expansion coefficient between the substrate and the film.

The film thickness of the TiO_2 films was measured using a scanning electron microscopy. The thickness of the films could be controlled by the spraying time. **Figure 4.24** shows the cross sectional view of the film obtained after spraying up to 60 s and the thickness was ~200 nm.

In summary, this investigation reveals crack free TiO_2 films can be processed electrohydrodynamically in the stable cone-jet mode. The effect of applied voltage and flow rate on processing TiO_2 films also investigated and analysed in this chapter. Well characteristic features of TiO_2 film were obtained by varying the annealing temperature. Surface morphology showed dense and crack free surfaces which can be useful in many applications.

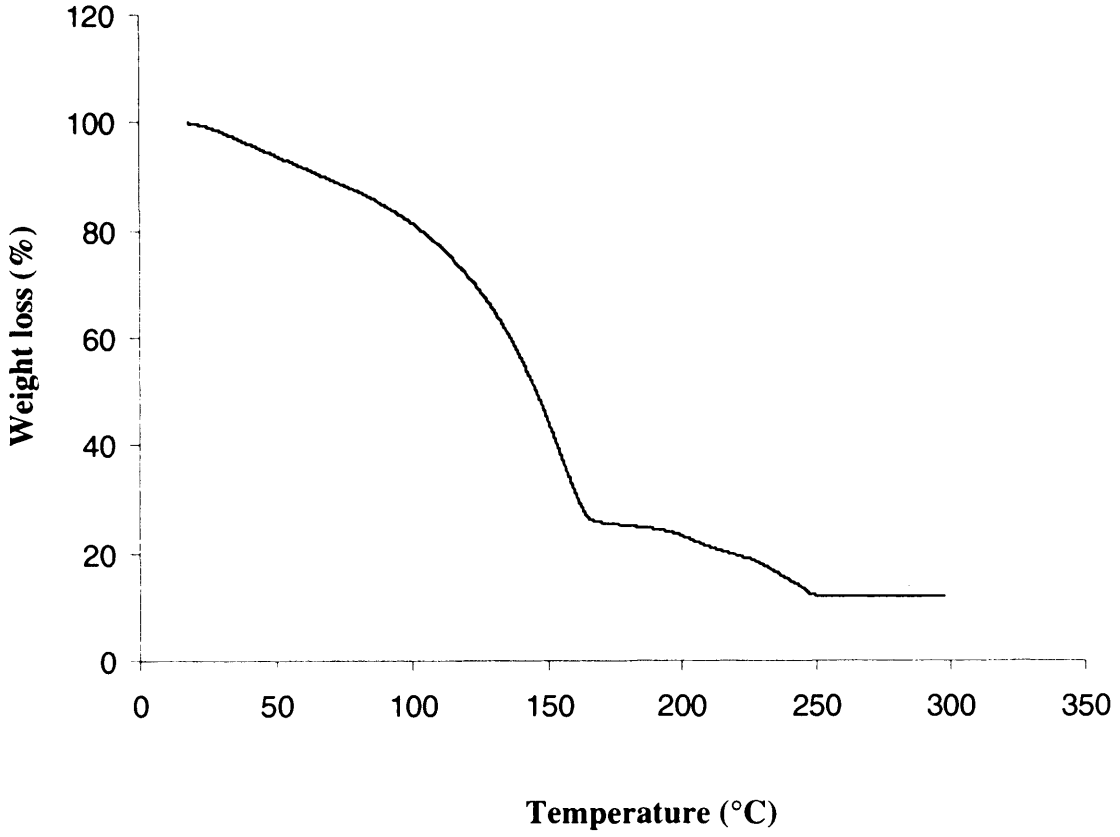

Figure 4.1 TGA of titania sol

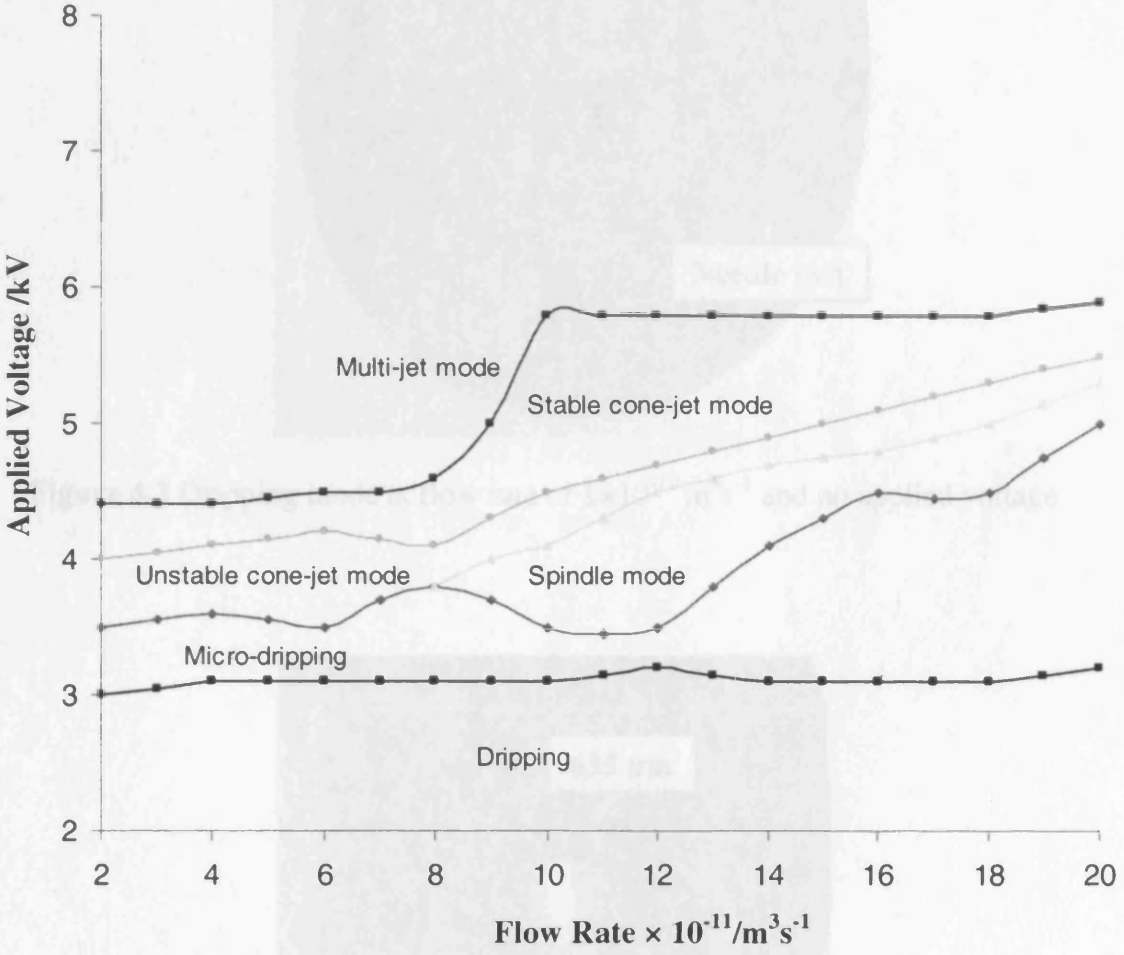

Figure 4.2 Mode selection map for the titania sol

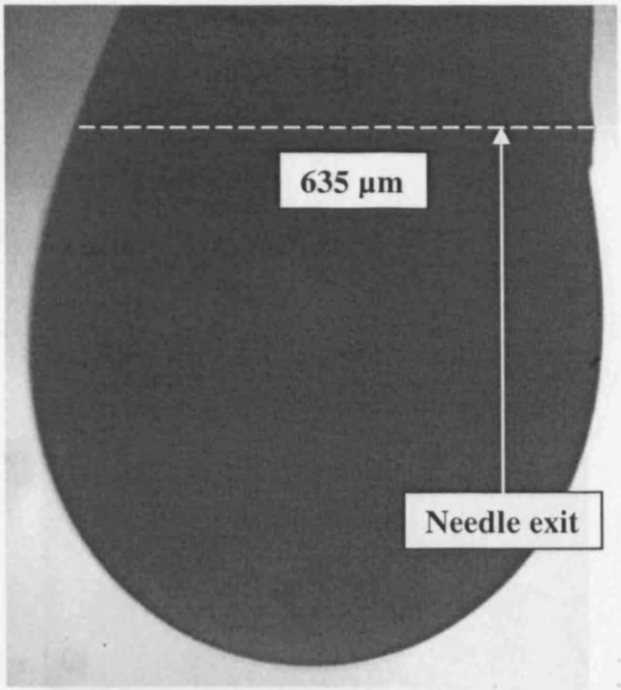

Figure 4.3 Dripping mode at flow rate of 1×10^{-10} m^3s^{-1} and no applied voltage

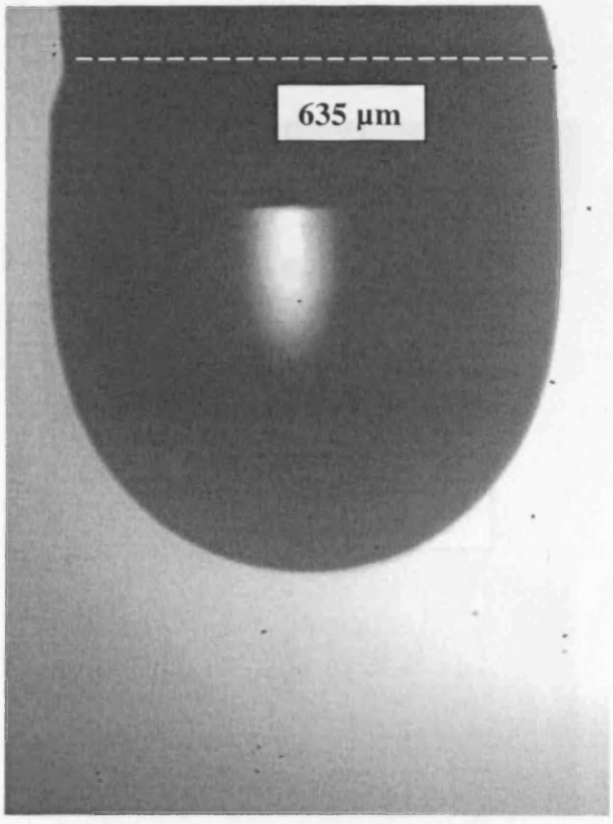

Figure 4.4 Micro-dripping at flow rate of 1×10^{-10} m^3s^{-1} and 3.1 kV

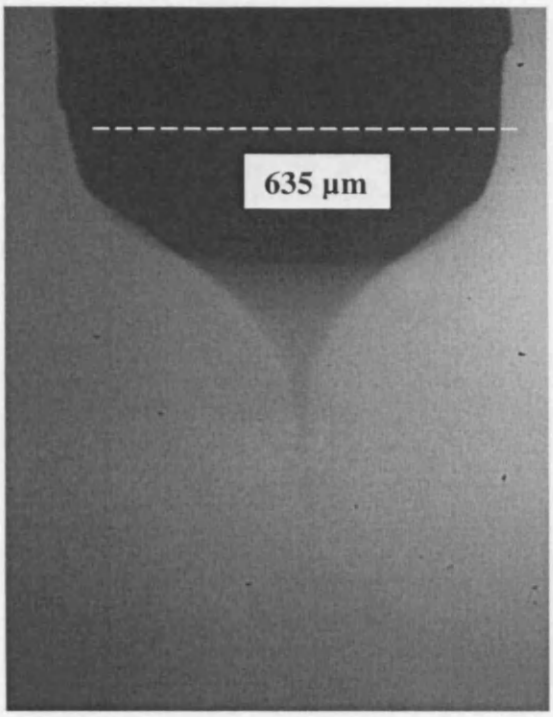

Figure 4.5 Unstable cone-jet mode at flow rate of 1×10^{-10} m^3s^{-1} and 4.1 kV

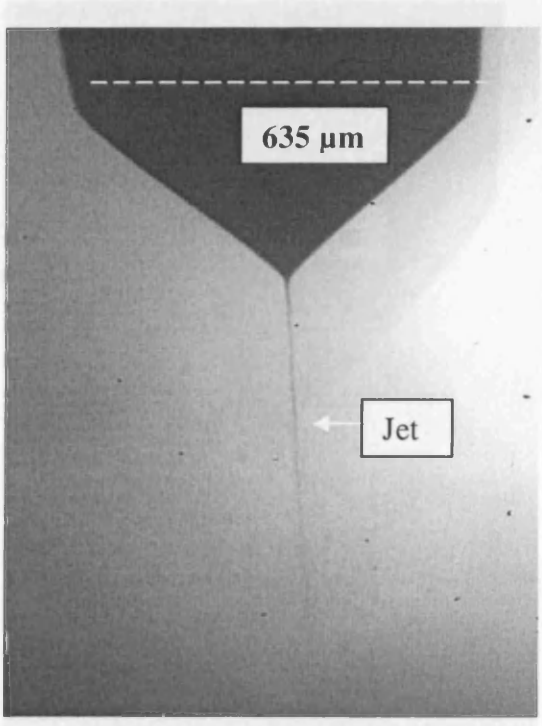

Figure 4.6 Stable cone-jet mode at flow rate of 1×10^{-10} m^3s^{-1} and 4.5 kV

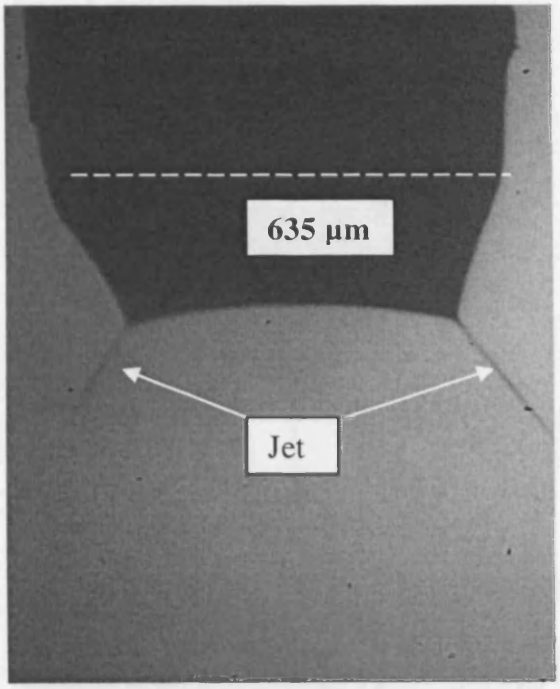

Figure 4.7 Multi-jet mode at flow rate of 1×10^{-10} m^3s^{-1} and 6 kV

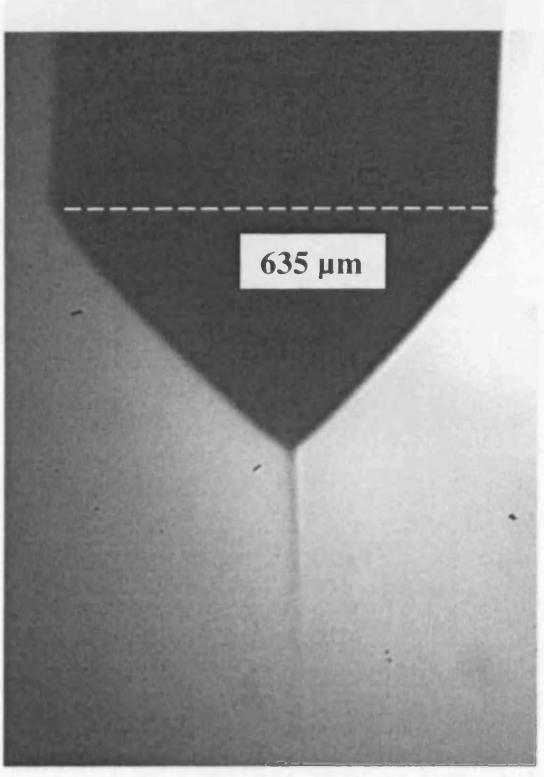

Figure 4.8 Stable cone-jet mode at flow rate of 1.2×10^{-10} m^3s^{-1} and 5.5 kV

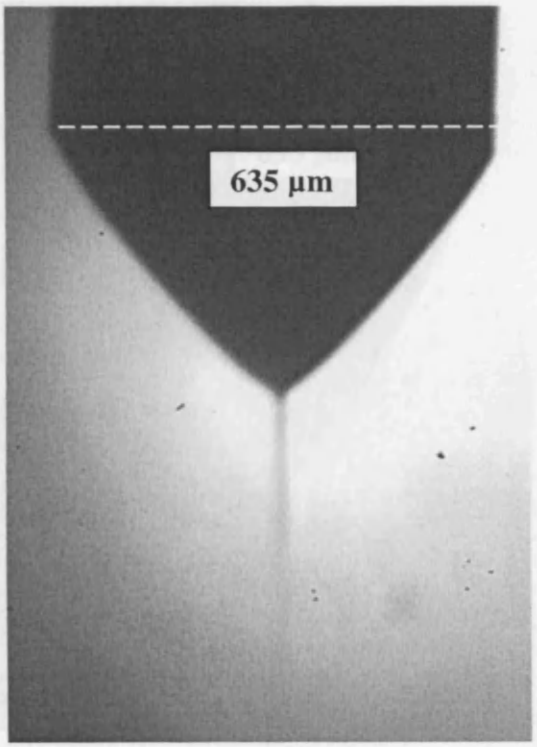

Figure 4.9 Stable cone-jet mode at flow rate of 1.6×10^{-10} m^3s^{-1} and 5.5 kV

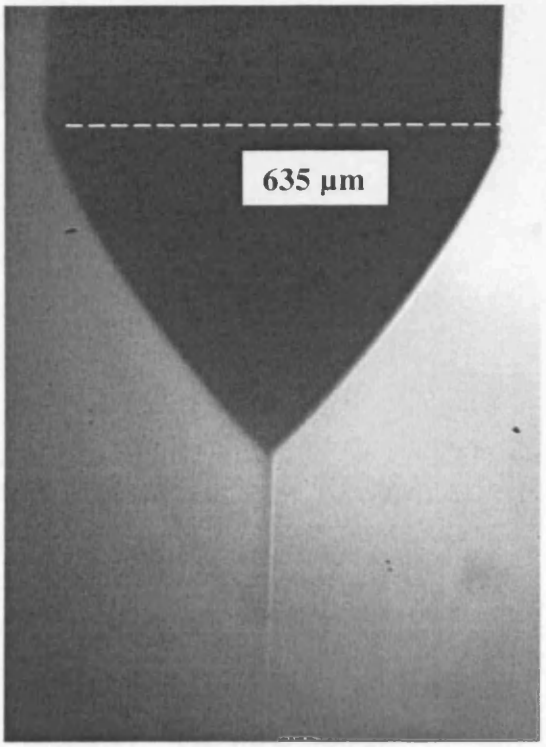

Figure 4.10 Stable cone-jet mode at flow rate of 2×10^{-10} m^3s^{-1} and 5.5 kV

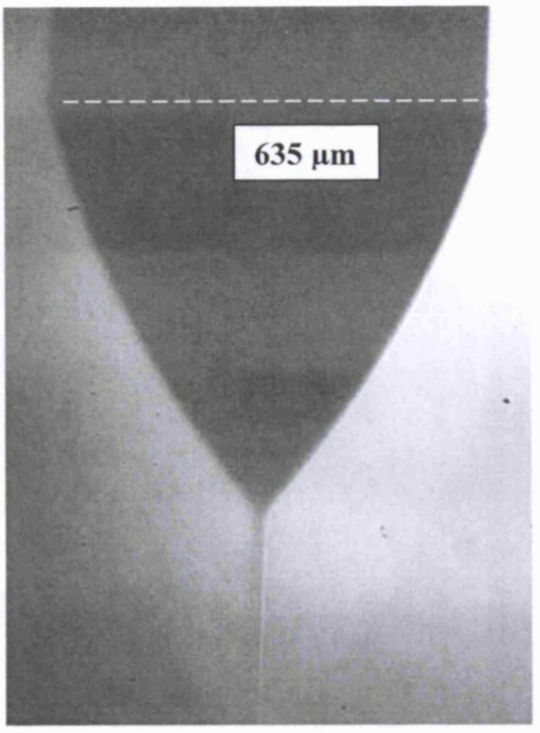

Figure 4.11 Stable cone-jet mode at flow rate of 2.4×10^{-10} m^3s^{-1} and 5.5 kV

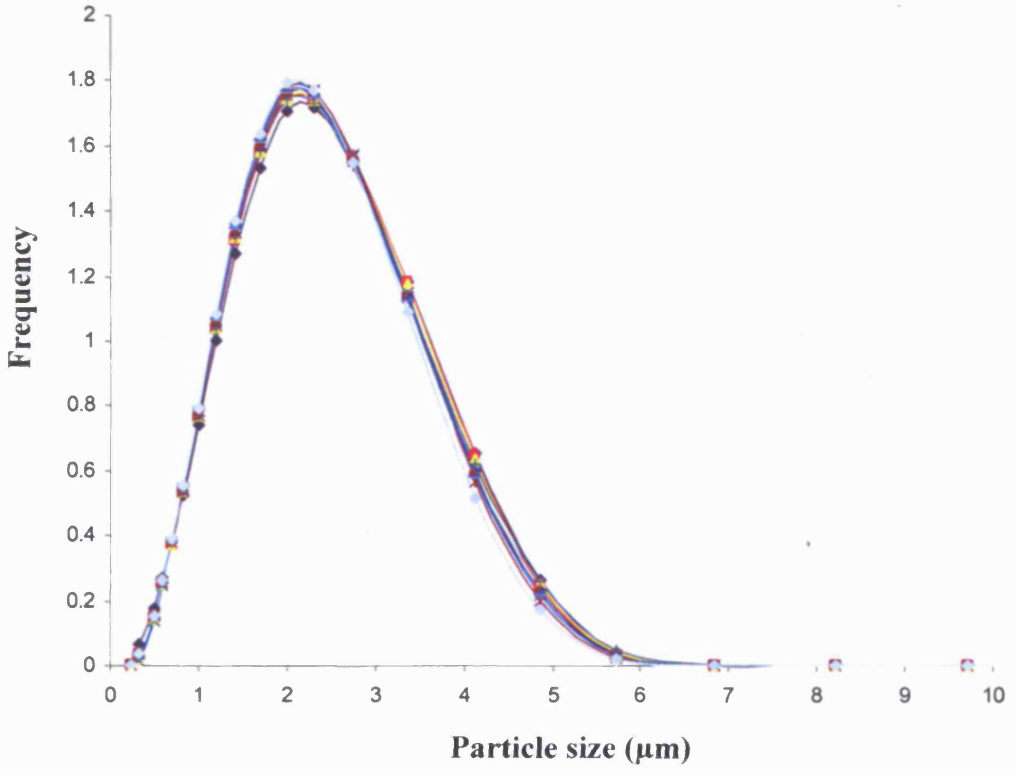

Figure 4.12 Droplet size distribution obtained by laser spectrometry. Results of repeated experiments are shown as different coloured plots

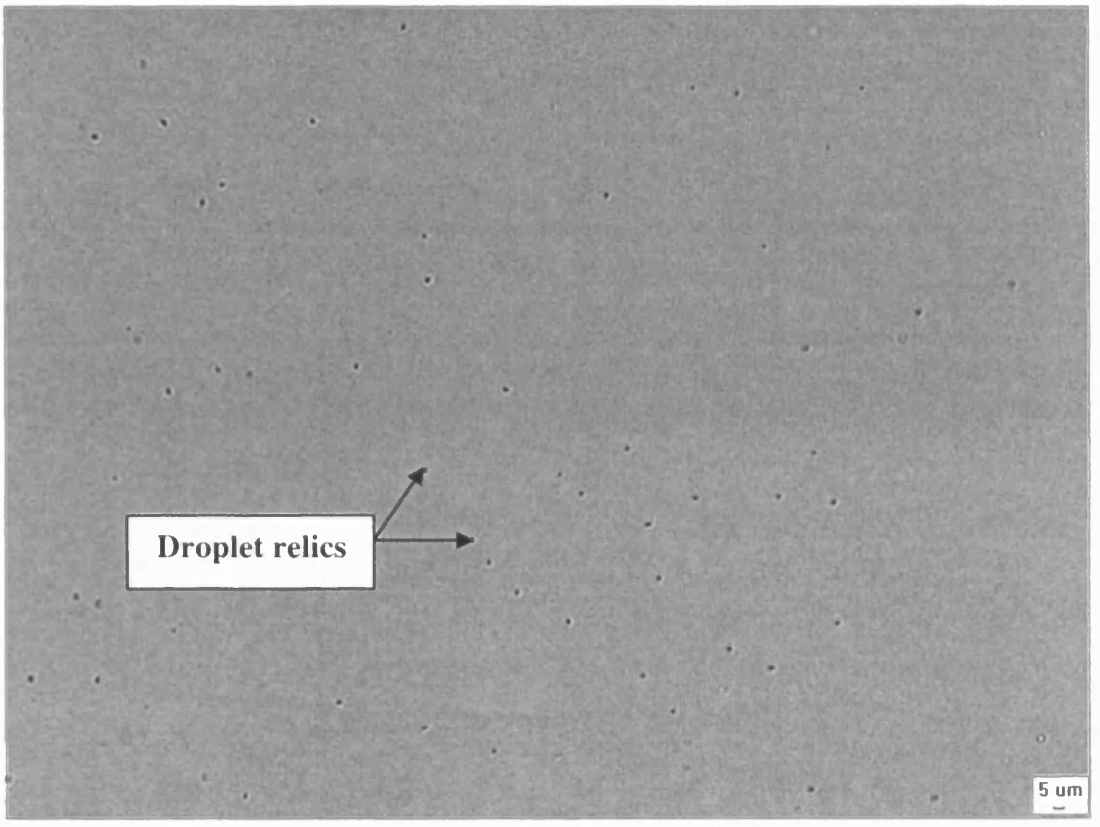

Figure 4.13 Optical micrograph of droplets soon after deposition

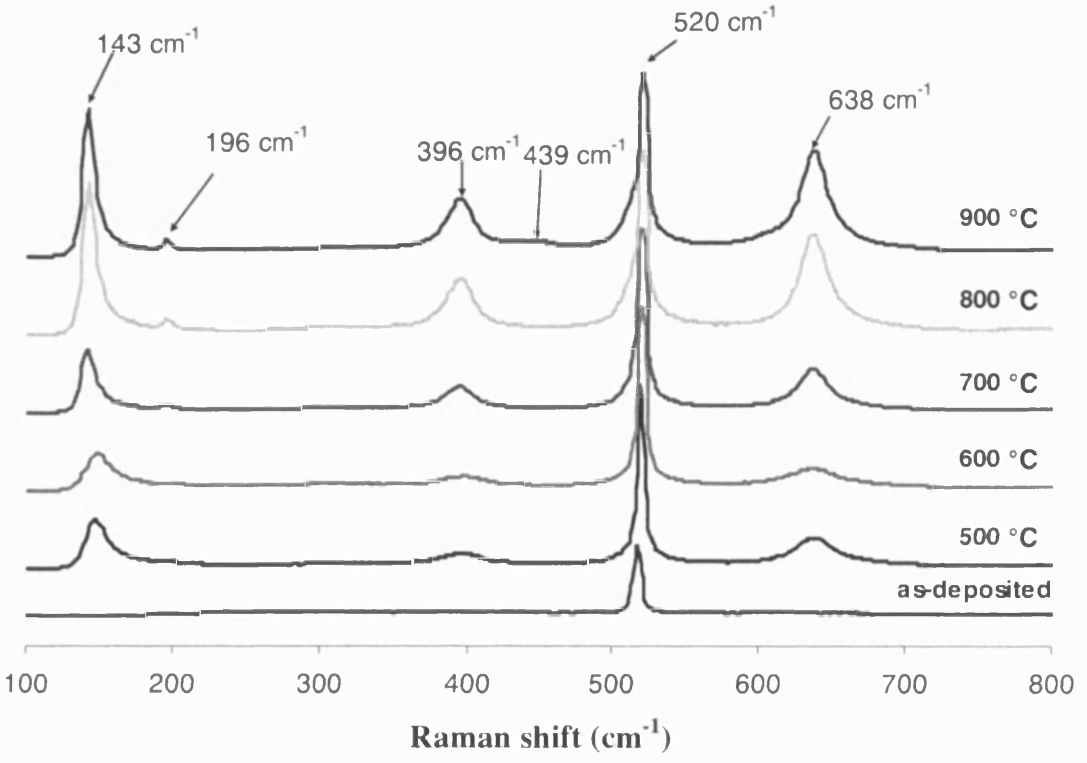

Figure 4.14 Raman spectra of TiO_2 films annealed to different temperatures

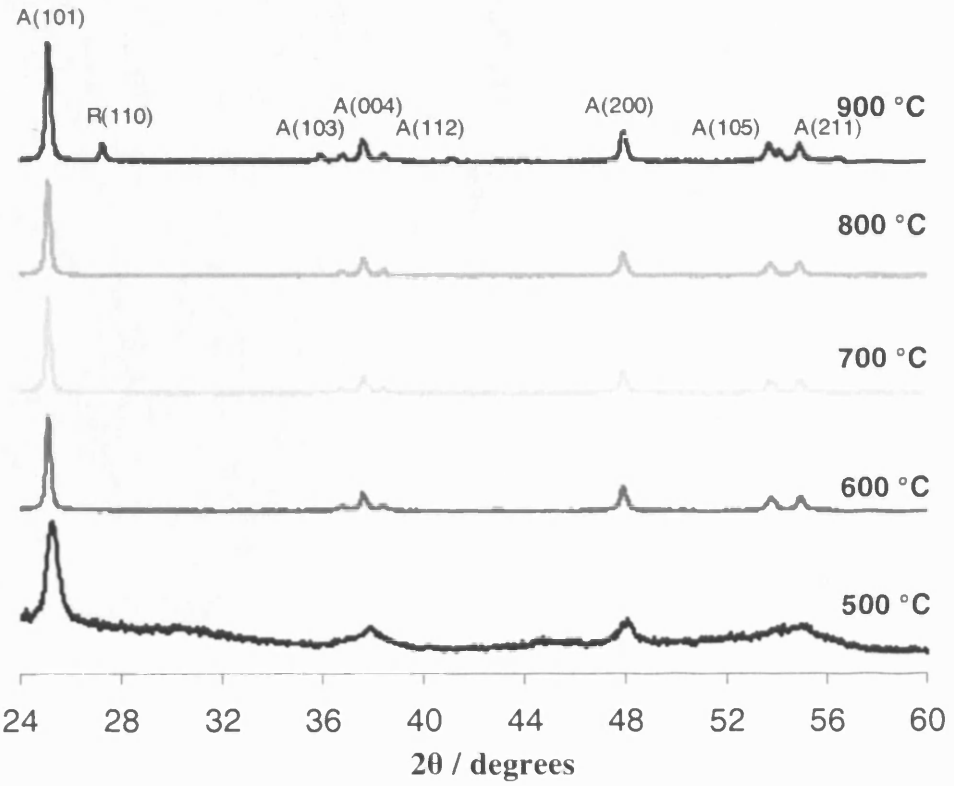

Figure 4.15 X-ray diffraction of TiO_2 films annealed to different temperatures

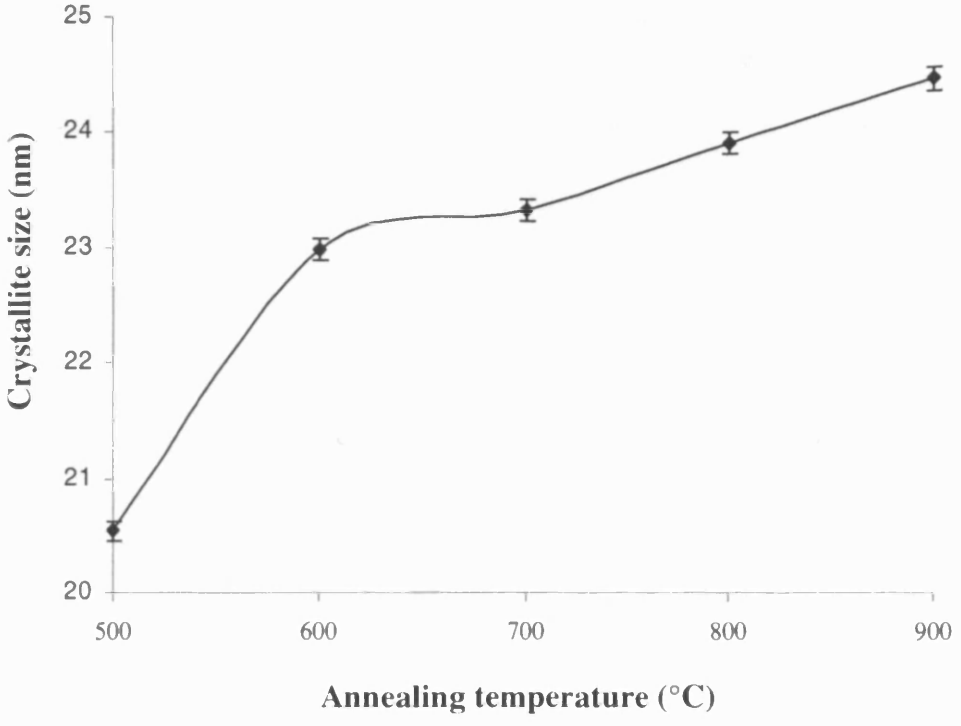

Figure 4.16 Variation of crystallite size with annealing temperature for TiO_2 films

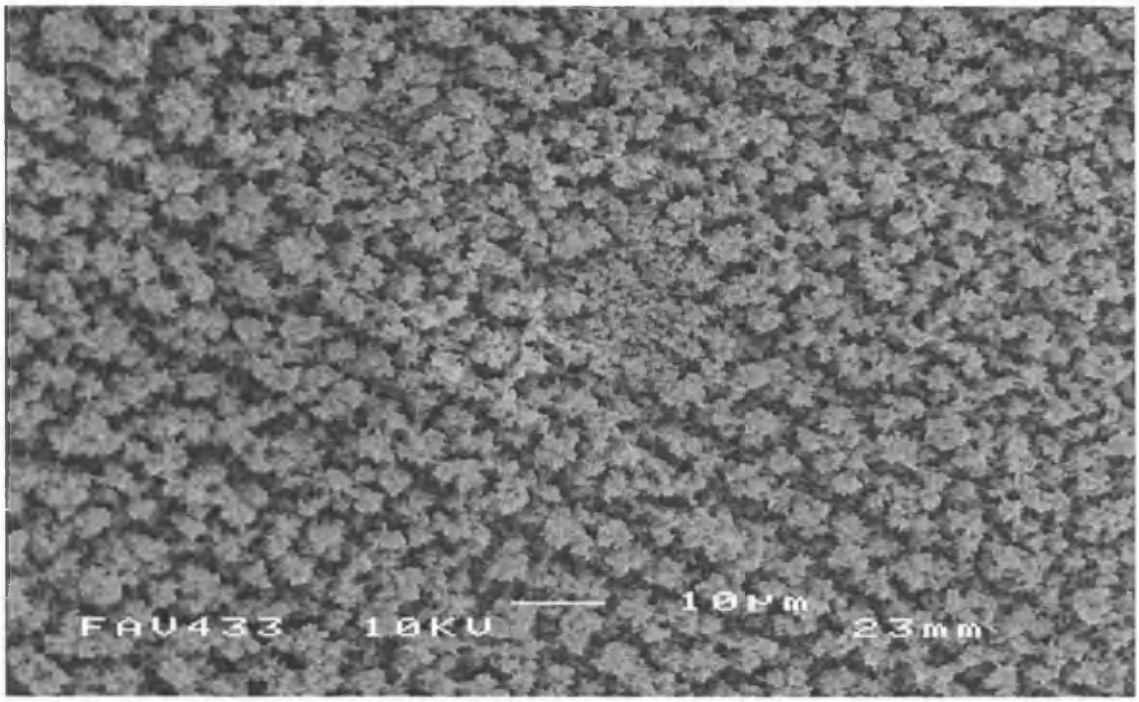

Figure 4.17 SEM image of as-deposited TiO_2 film electrohydrodynamically processed at 1×10^{-10} m^3s^{-1} and 4.5 kV on Si substrate (magnification ×1000)

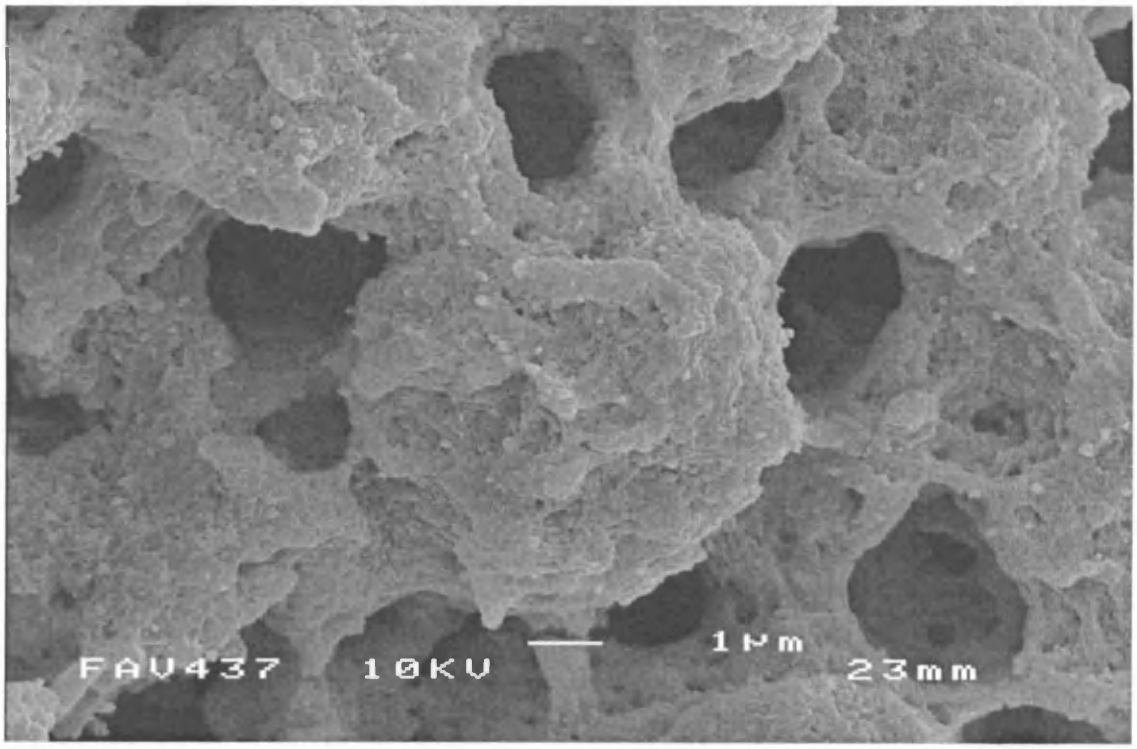

Figure 4.18 SEM image of as-deposited TiO_2 film electrohydrodynamically processed at 1×10^{-10} m^3s^{-1} and 4.5 kV on Si substrate (magnification ×6500)

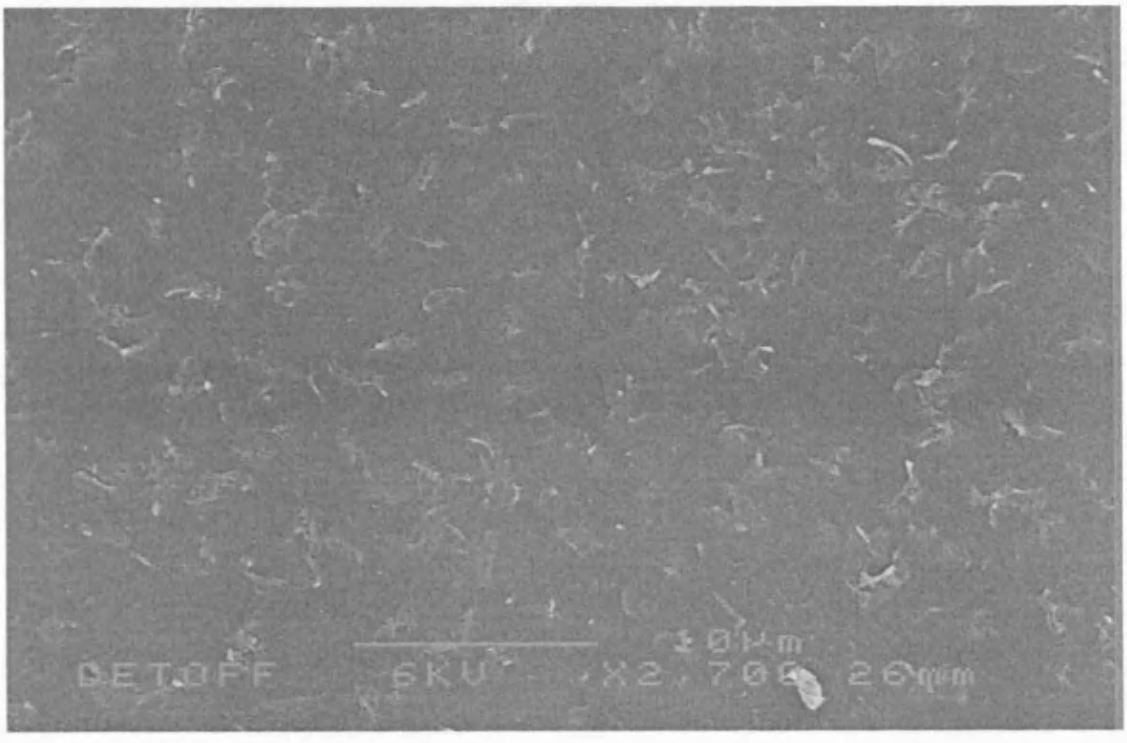

Figure 4.19 SEM image of TiO_2 film electrohydrodynamically processed at 1×10^{-10} m^3s^{-1} and 4.5 kV on Si substrate annealed at 500 °C (magnification ×2700)

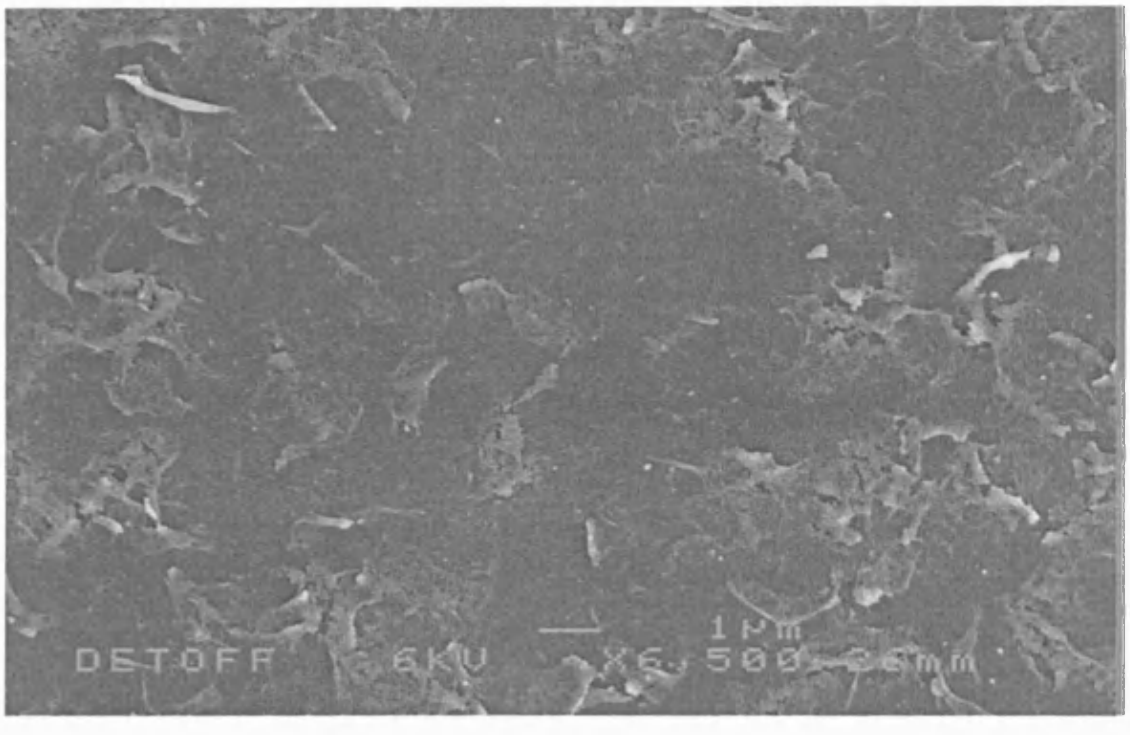

Figure 4.20 SEM image of TiO_2 film electrohydrodynamically processed at 1×10^{-10} m^3s^{-1} and 4.5 kV on Si substrate annealed at 500 °C (magnification ×6500)

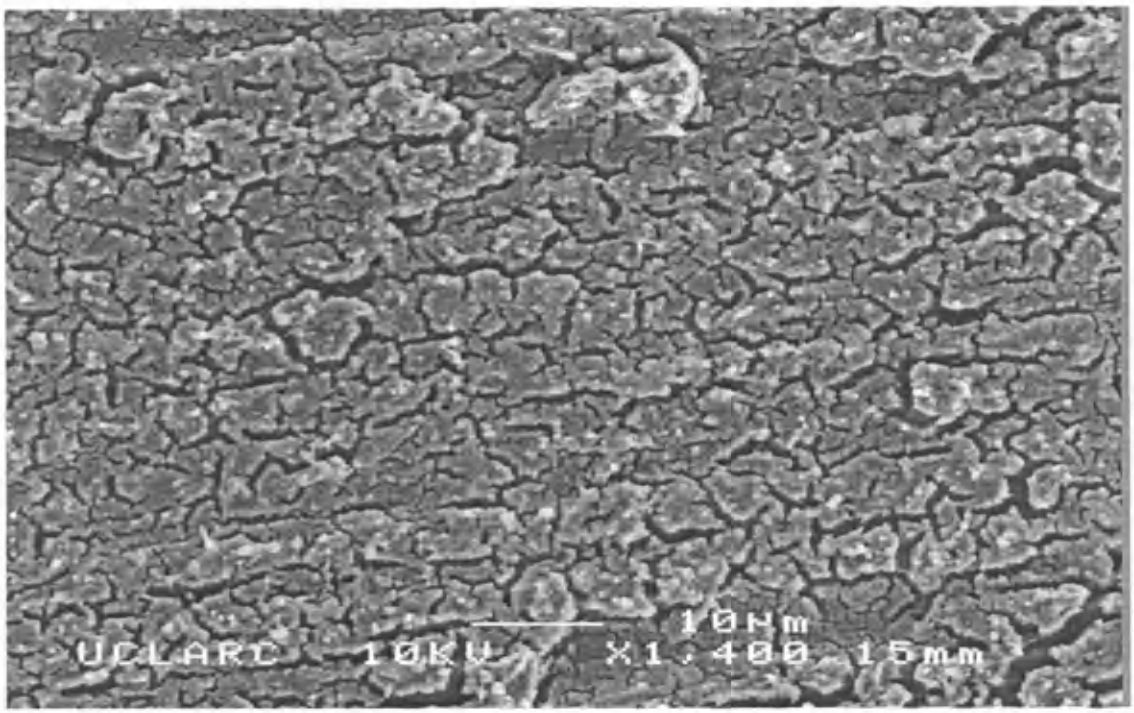

Figure 4.21 SEM image of TiO_2 film electrohydrodynamically processed at 1×10^{-10} m^3s^{-1} and 4.5 kV on Al substrate annealed at 500 °C (magnification ×1400)

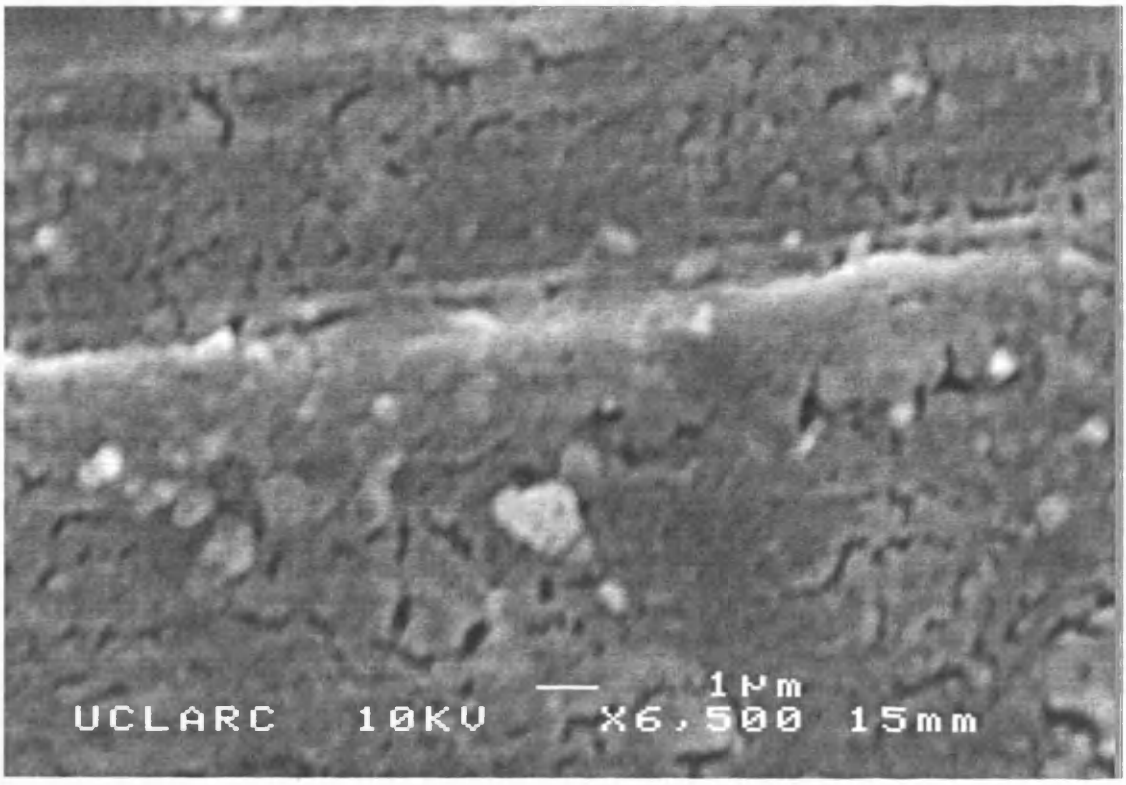

Figure 4.22 SEM image of TiO_2 film electrohydrodynamically processed at 1×10^{-10} m^3s^{-1} and 4.5 kV on Al substrate annealed at 500 °C (magnification ×6500)

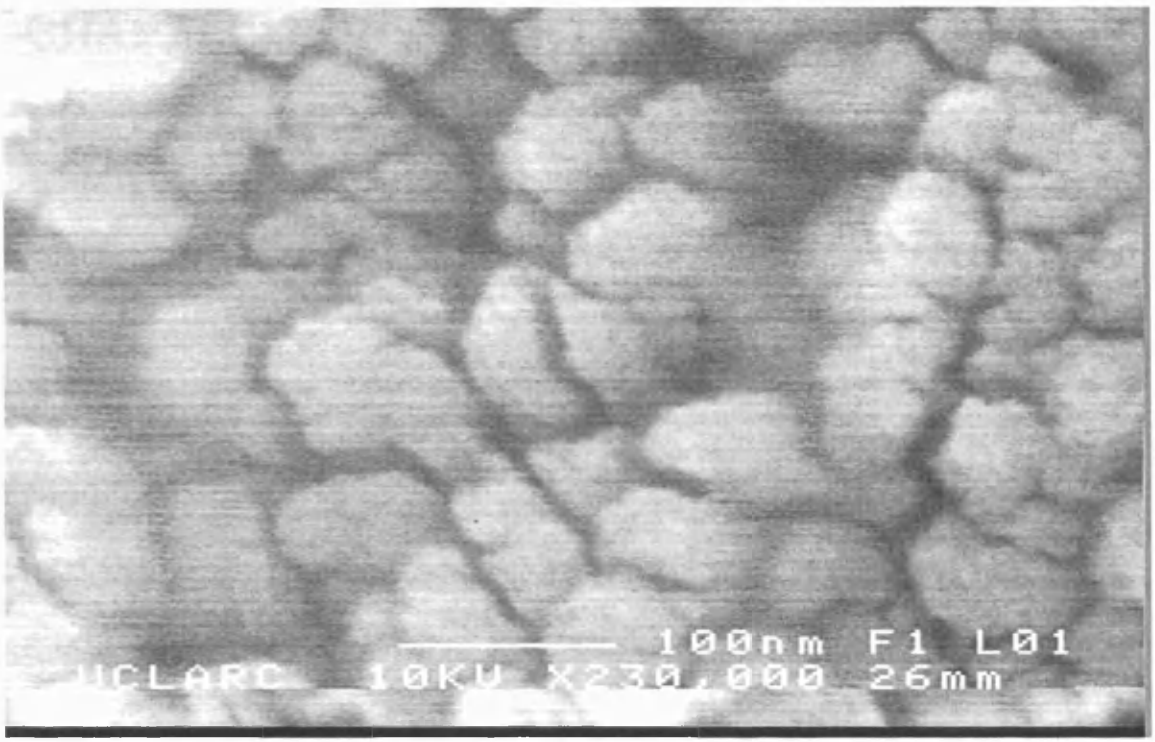

Figure 4.23 SEM of TiO_2 film electrohydrodynamically processed at 1×10^{-10} m^3s^{-1} and 4.5 kV with high magnification (×230 000)

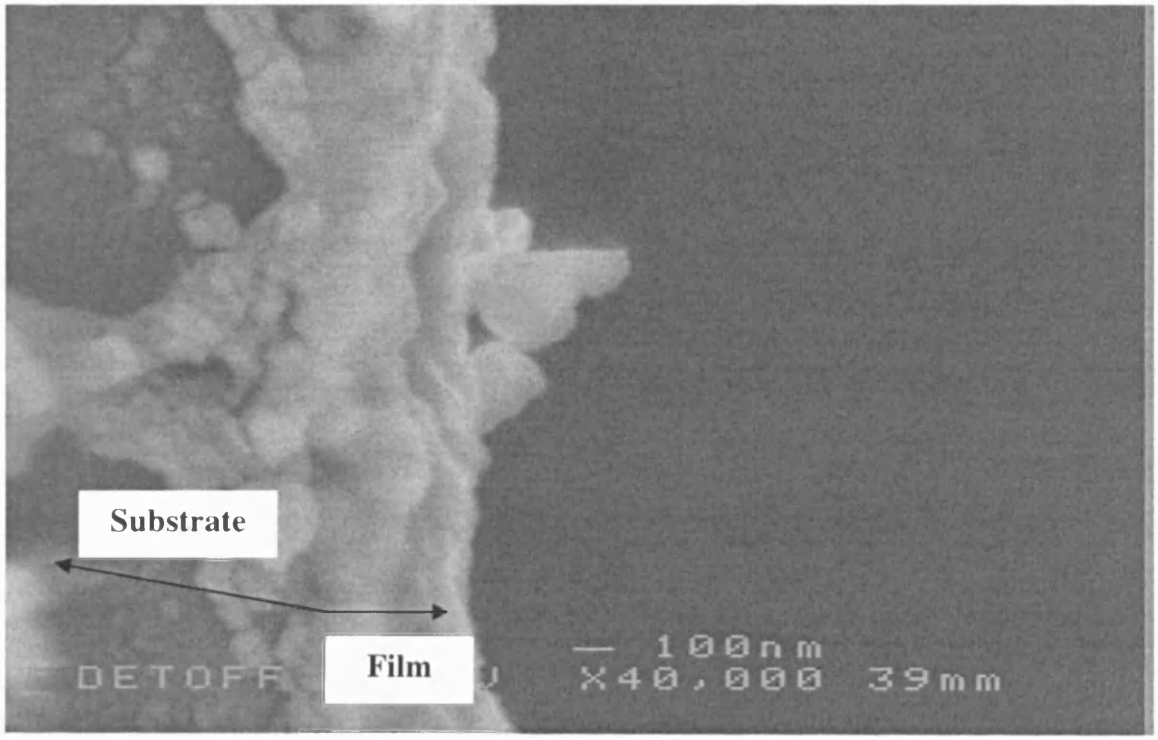

Figure 4.24 Cross sectional view of TiO_2 film electrohydrodynamically processed at 1×10^{-10} m^3s^{-1} and 4.5 kV (spray time 60 s)

CHAPTER 5

Electrical and Optical Characterisation of Electrohydrodynamically processed TiO_2 films

This chapter describes the electrical and optical characterisation of electrohydrodynamically processed TiO_2 films which were illustrated in **chapter 4**. TiO_2 has been one of the extensively studied oxides because of its remarkable optical and electrical properties. It could be used in thin film capacitors and gate dielectrics in micro electronic applications (Duenas et al., 2005). TiO_2 is also extensively used in optical thin film device applications owing to its optical properties and high thermal and chemical stabilities in hostile environments (An, 2005). Due to its potential applications in many fields it is vital to study the electrical and optical properties of the TiO_2 films. This is the first ever study of the electrical and optical properties of electrohydrodynamically processed TiO_2 and this will set the platform for the future research being carried out in this field.

The electrical properties of processed TiO_2 films were studied by fabricating a simple metal-oxide-semiconductor (MOS) structure. The electrical measurement methods used are described under experimental details (**chapter 3**). The capacitance-voltage and current-voltage characteristics of processed TiO_2 films are analysed. The effect of annealing temperature on dielectric constant and leakage current density of the films are discussed in this chapter. The optical properties of processed TiO_2 films are evaluated from the uv-vis spectroscopy studies of the films. Further, the effect of annealing temperature on optical properties is analysed.

5.1 MOS capacitors

MOS capacitor is the most powerful for investigating nearly all the electrical properties of the MOS system. The superiority of the MOS capacitor rests on its simple structure, simple fabrication and simplicity of the analysis. In this study the fabricated metal-titanium dioxide-silicon capacitor was used to analyse the capacitance-bias voltage characteristics and the leakage current-bias voltage characteristics of the system.

Before getting in to the electrical characterisation of the electrohydrodynamically processed titanium dioxide films, the FTIR studies on the films were done. The FTIR studies of the TiO_2 films prepared by electrohydrodynamic processing are useful for analysing the organic residues remaining in the films and to elucidate the nature of the bonding in the film.

5.2 FTIR study of TiO_2 films

The FTIR results of the TiO_2 films are shown in **Figure 5.1**. In the as- deposited film a broad absorption peak at 3200-3400 cm^{-1} is observed corresponding to -OH stretching region. The absorption peaks around 2700 cm^{-1} are associated with hydrocarbon groups such as -CH, $-CH_2$ in the films (Zhang et al., 2002). After annealing the films to higher temperatures these peaks are disappeared, indicating the removal of hydroxyl groups and hydrocarbons in the films. The peak located near 435 cm^{-1} in the annealed films is corresponding to the anatase phase of TiO_2. No anatase phase was found in the as-deposited films. The absorption bands near 1080 cm^{-1} and 810 cm^{-1} are characteristic features of the SiO_2 and correspond to stretching and bending vibrations of the Si-O-Si bond respectively (Mosaddeq-ur-

Rahman et al., 2000). This shows there is a growth of interfacial SiO_2 layer between the processed TiO_2 film and the silicon substrate. The diffusion of oxygen ions through the TiO_2 film covering the substrate facilitated the interfacial SiO_2 formation. The absorption peaks of the films annealed above 700 °C shifted towards the higher frequency side. This is indicating that the interfacial layer is not purely stoichiometric SiO_2. In addition to this, the film annealed at higher temperatures showed a peak around 1250 cm^{-1} is also corresponds to the SiO_2 bond (Han and Aydil, 1997).

5.3 C-V characteristics of MOS capacitors

The dependence of capacitance on bias voltage is expected for an oxide grown on silicon substrate. These features are shown in **Figure 5.2** and **Figure 5.3** for electrohydrodynamically processed films annealed at 500 °C and 600 °C for two different frequencies. **Figure 5.2** shows the low frequency C-V characteristics and **Figure 5.3** shows the high frequency C-V characteristics of the fabricated MOS capacitors. These are characterised by the presence of accumulation, depletion and inversion regions. These are shown in the figures by a, b and c.

When a negative bias was placed on the top electrode, the negative charges on the electrode attracted the holes to the silicon surface to form an accumulation region. At the very large negative bias, the hole density at the silicon surface was greatly exceeded the hole density in the bulk. The large hole charge density at the silicon surface was contributed to a large capacitance of the MOS system. When the bias voltage was made less negative, the negative charges were removed from the

electrode and the surface hole density was decreased consequently the capacitance of the MOS system was decreased.

As bias voltage was made positive, the holes repelled from the silicon surface resulted in the formation of a depletion layer of ionized acceptors. The capacitance of the MOS system was even lowered in this range. This bias range is called the depletion region. As bias voltage was made increasingly more positive, the surface hole density was decreased whereas the surface electron density was increased. When the surface electron density was exceeded the surface hole density the inversion layer of electrons was formed. This bias range is called the inversion region. However, the high frequency C-V characteristic showed the inversion region capacitance constant since the minority carrier density wasn't changed with bias voltage.

5.3.1 Low frequency (100 kHz) C-V plots

The low frequency C-V plot of MOS capacitor is shown in **Figure 5.2** for electrohydrodynamically prepared titanium dioxide films annealed at two different temperatures 500 °C and 600 °C. They showed a well characterised regions accumulation, depletion and inversion marked by a, b and c in the figure. The maximum capacitance in the accumulation region was 9.5×10^{-10} F for the film annealed at 500 °C. The film annealed at 600 °C showed a maximum capacitance of 9.2×10^{-10} F. When decreasing the negative bias voltage there was a sudden capacitance drop observed. At the bias voltage of -0.5 V the capacitance was 6×10^{-10} F for the film annealed at 500 °C and 4.9×10^{-10} F for the film annealed at 600 °C. Increasing the positive bias voltage even lowered the capacitance of the

MOS system. At the bias voltage of 0.5 V the capacitance was 2 $\times 10^{-10}$ F for the film annealed at 500 °C and 1.8 $\times 10^{-10}$ F for the film annealed at 600 °C. At the higher positive bias voltage the capacitance of the MOS system was increased. At the bias voltage of 1.5 V the capacitance was 5 $\times 10^{-10}$ F for the film annealed at 500 °C and 4.5 $\times 10^{-10}$ F for the film annealed at 600 °C. The film annealed at 600 °C showed a capacitance value lower than the film annealed at 500 °C for all bias voltages. This decrease in capacitance of the MOS system containing the film annealed at 600 °C is associated with the grown interfacial SiO_2 layer. The grown interfacial SiO_2 layer produces an in-series combination with the deposited TiO_2 layer. Therefore, there is a net reduction in the total capacitance is observed.

5.3.2 High frequency (500 kHz) C-V plots

The high frequency C-V plot of MOS capacitor is shown in **Figure 5.3** for electrohydrodynamically prepared titanium dioxide films annealed at two different temperatures 500 °C and 600 °C. The characteristic regions were same as for low frequency plots except the inversion layer region. The maximum capacitance in the accumulation region was 9.4 $\times 10^{-10}$ F for the film annealed at 500 °C. The film annealed at 600 °C showed a maximum capacitance of 9.1 $\times 10^{-10}$ F. There was a sudden drop in capacitance when the bias voltage was increased. At the bias voltage of -0.5 V the capacitance was 5.8 $\times 10^{-10}$ F for the film annealed at 500 °C and 4.8 $\times 10^{-10}$ F for the film annealed at 600 °C. When increasing the positive bias voltage the inversion region capacitance showed the constant value of 1.8 $\times 10^{-10}$ F. This is because at the high frequency there was a little time for minority charge carrier to respond with the bias voltage. Therefore, the minority charge carrier wasn't contributed to the capacitance variation in inversion region.

5.4 Dielectric constant of TiO_2 films

The dielectric constant of electrohydrodynamically processed titanium dioxide is calculated from the maximum capacitance in the accumulation region. The effective dielectric constant of the TiO_2 films could be calculated from,

$$C_{max} = \frac{\varepsilon_o \varepsilon_r A}{d} \tag{5.1}$$

Where d is the thickness of TiO_2, ε_r is the effective dielectric constant of TiO_2, ε_o is the permittivity constant and A is the device area.

By substituting the values of each variable the effective dielectric constant of the TiO_2 films are derived. These are shown in the **Table 5.1** for the films annealed at 500 °C and 600 °C.

Table 5.1 Effective dielectric constant of TiO_2 films

Annealing Temperature (°C)	Frequency	Dielectric constant
500	100 kHz	7.15
600	100 kHz	6.93
500	500 kHz	7.08
600	500 kHz	6.85

5.4.1 Effect of annealing temperature on dielectric constant

The electrohydrodynamically processed TiO_2 films annealed at 500 °C showed a higher dielectric constant compared to the TiO_2 films annealed at 600 °C. The

annealing temperature had two contrary effects on the dielectric constant of the TiO_2 films deposited in the silicon substrate. On the one hand, due to increase in the crystalline phase, in this case the anatase phase content in the films is increased when the annealing temperature is increased. This was evidenced by the Raman spectra of the annealed TiO_2 films deposited in the silicon substrate (**Figure 4.14**). The sharper peaks were obtained when increasing the annealing temperature indicating the increase in the anatase phase content. The improvement in the crystalline quality of the TiO_2 films is increased the dielectric constant of the films.

On the other hand, the interfacial SiO_2 layer is grown with the annealing temperature. This was clearly seen by the FTIR study of the TiO_2 films (**Figure 5.1**). The increase in intensity of the SiO_2 peaks was observed when increasing the annealing temperature. The growth of the interfacial SiO_2 layer is effectively reduces the total capacitance since it was in-series combination with the TiO_2 films. Consequently, the dielectric constant of the TiO_2 films is decreased when the annealing temperature is increased. This behaviour indicates that the effect of grown SiO_2 interfacial layer is greater than the structural property at high temperature. Based on the above discussion, it is obvious that the dielectric property of the electrohydrodynamically processed TiO_2 films is decreased when increasing the annealing temperature.

5.5 I-V characteristics of MOS capacitors

The leakage current behaviour of dielectric oxide is paramount need in microelectronic applications. The leakage current – bias voltage characteristics for the films annealed at 500 °C and 600 °C are shown in **Figure 5.4**.

It can be seen that the leakage current at negative bias is higher than that at positive bias. In the negative bias charge conduction is dominated by the metal/oxide interface and at the positive bias charge conduction is controlled by silicon/oxide interface (Yang et al., 2006). The charge conduction in metal/oxide interface is higher than that of silicon/oxide interface hence the leakage current is higher at negative bias.

The leakage current was increased with the applied bias voltage. For the films annealed at 600 °C (**Figure 5.4**) the leakage current was 31 μA at the bias voltage of -0.5 V. It was increased to 131 μA at -1.5 V. At the bias voltage of -2.5 V it was 256 μA. The increase in leakage current with the bias voltage is due to increase in the electric field strength across the capacitor. It was also noted that the leakage current increase between the bias voltages -0.5 V to -2 V was higher than the leakage current increase beyond -2 V. The same trend was observed for the positive bias voltages where the leakage current increase between the bias voltages 0.5 V to 2 V was higher than the bias voltage beyond 2 V. However, the leakage current found to be lower compared to the negative bias voltages. A similar trend was observed for the films annealed 500 °C.

5.5.1 Effect of annealing temperature on leakage current density

The leakage current density was obtained by dividing the leakage current by the electrode area and it shows the current passing through the film per unit area. The post deposition annealing had significantly influenced the leakage current density of the films. The as-deposited films showed a completely leakage behaviour even at lower bias voltage. However, the post deposition annealing improved the leakage

current behaviour which is shown in **Figure 5.5** for the films annealed at 500 °C and 600 °C. The films annealed at 700 °C showed again a completely leakage behaviour.

The as-deposited films were contained loosely bonded particles with a reticular structure (**Figure 4.17**). It also showed the amorphous phase in the Raman spectra characterisation (**Figure 4.14**). The FTIR studies also showed there were anhydrolysis carbon contaminants in the films (**Figure 5.1**). Therefore the as-deposited films had the high density of oxygen vacancies and high defect density due to carbon contaminants. The charges conducted easily through this microstructure. Therefore they showed a completely leakage behaviour.

The leakage current density of heat treated films also found to be sensitive to the annealing temperature. The films annealed at 500 °C showed a higher leakage current density than the films annealed at 600 °C for both negative and positive bias voltages. The leakage current density was 51 $\mu A/mm^2$ at a bias voltage of -2.5 V for the films annealed at 500 °C and 36 $\mu A/mm^2$ for the films annealed at 600 °C. This is because of annealing eliminates the structural disorders like oxygen vacancies and reduce the leakage current density. Annealing at high temperature promotes the oxygen atoms to diffuse into the film and fill the oxygen vacancies in the TiO_2 films. As the annealing temperature increases, the concentration of diffuse oxygen atoms increased, the number of vacancies decreased and the leakage current lowered. Another reason is the growth of interfacial SiO_2 layer between the Si and TiO_2 during the annealing process which also helped to reduce the leakage current (Singh et al., 2005). The growth of interfacial SiO_2 was identified in the

FTIR studies with the absorption bands near 1080 cm^{-1} and 810 cm^{-1} are confirmed the Si-O-Si bond (**Figure 5.1**).

In spite of this advantage provided by the grown SiO_2 for reducing the leakage current density, later it was found to be detrimental to the films annealed at 700 °C. The complete leakage behaviour of the films annealed at 700 °C is due to this abnormal growth of the interfacial SiO_2 where it forms a non-stoichiometric oxide leading to a defect rich interface layer facilitating the charge conduction. Therefore the optimised annealing temperature for improving the leakage current density was found to be 600 °C. This is clearly shows the annealing temperature plays a dominate role in the leakage current of electrohydrodynamically processed titanium dioxide films.

5.6 UV-Vis spectroscopy study on TiO_2 films

The optical properties of electrohydrodynamically processed TiO_2 films are evaluated using the uv-vis spectroscopy. The properties of thin films are known to differ from that of bulk materials. As the diameter of crystallites approaches the exciton Bohr diameter, the quantum size effect where splitting of the energy bands into discrete quantized energy levels occurs (Ge et al., 2006). The transmittance characteristics of the TiO_2 films in the wavelength of 200-700 nm are shown in **Figure 5.6**. The energy bandgap of the films are determined from the transmittance of the films are shown in **Figure 5.7** and **Figure 5.8**. The effects of annealing temperature on the energy bandgap of the films are tabulated in **Table 5.2**.

5.6.1 Effect of annealing temperature on transmittance of TiO_2 films

The transmittance spectra of the TiO_2 films annealed at different temperatures are presented in **Figure 5.6**. There are no oscillations observed in the spectra. Therefore, the interference effect due to reflections at the air-TiO_2 and TiO_2-glass interfaces are negligible. The transmittance in the visible light range varies between 70% to 90%. The transmittance drops almost to zero when the photon energy at shorter wavelength approaches the energy bandgap value. The optical transmission edge is not significantly affected by annealing at shorter wavelength (< 320 nm).

The film annealed at 400 °C showed higher transmission in the visible light range compared to other two. There was a drop in the transmittance for the film annealed at 500 °C. However, the film annealed at 600 °C showed higher transmission than the film annealed at 500 °C. The maximum transmittance observed ~ 90% for the film annealed at 400 °C. The change in transmittance in the visible light range for the film annealed at different temperatures may be attributed to several possibilities, primarily the anatase-rutile transformation, the film densification and the partial reduction of TiO_2 films at high temperatures (> 700 °) (Ting et al., 2000).

However, there is no anatase-rutile phase transformation observed in this case. The main reason for the increase in transmittance for the film annealed at 400 °C compared to the as deposited film was the film densification. The film densification improves the porosity of the film and reduces the scattering of the light. The decrease in transmittance for the film annealed at 500 °C compared to the film annealed at 400 °C may be due to the crystallinity. When increasing the

temperature up to 500 °C the film changes from the amorphous to polycrystalline anatase phase. The polycrystalline phase has more micro structural defects like grain boundaries and oxygen vacancies leading to more light scattering and/or absorption at these sites. However, the increase in transmittance for the film annealed at 600 °C compared to the film annealed at 500 °C could be attributed to the grain or crystallite size increased by the annealing thus reducing the scattering between the grains and hence increasing the transmittance. Another possible reason is the elimination of oxygen vacancies when annealing at 600 °C. This is well agreeing with the results of leakage current density at 600 °C mentioned in the section **5.5.1**.

5.6.2 Determination of bandgap of TiO_2 films

The bandgap energies of the films annealed at different temperatures are determined by the transmittance measurements. Firstly, for a transparent thin film, the absorption coefficient per unit length (α) is determined from its transmittance (T) neglecting any reflection effects (Garcia Sole., 2005).

$$\alpha = \frac{\ln(1/T)}{d} \tag{5.2}$$

Where d is the film thickness. Secondly, α is plotted against the photon energy hγ, from the functional relationship between α and hγ (Pancove, 1971).

$$\alpha = (h\gamma - E_g)^n \tag{5.3}$$

n = 2 for indirect transition. The bandgap energy E_g is thus obtained for indirect transition in the films annealed at different temperatures.

Figures 5.7 shows $\alpha^{1/2}$ plotted against $h\gamma$ for low photon energies for different annealing temperatures. By extrapolating the linear section of the graphs to the photon energy axis (x-axis) the bandgap energies of the films are obtained for indirect transition. These are shown in **Table 5.2** for different annealing temperatures. The absorption of the films is increased with the photon energy. The strong absorption structures start to appear between 3.5 - 4 eV. The energy band structure of TiO_2 in the bandgap region consists of O 2p states in the valence band and Ti 3d states in the conduction band (Mo and Ching, 1995). The stronger absorption implies that more electrons could be promoted from the valence band into conduction band and more separate electrons or holes could be produced.

Table 5.2 The bandgap of TiO_2 films annealed at different temperatures

Annealing temperature (°C)	***Eg(eV)*/indirect transition**
400	3.54
500	3.50
600	3.47

The film annealed at 500 °C exhibit an indirect bandgap of 3.50 ± 0.05 eV. This value is agrees well with those of Nakamura et al. (2005) for TiO_2 films. However,

this value is slightly higher than the literature data for the anatase titania film annealed at 500 °C (Karunagaran et al., 2003).

The increase in the value of the bandgap of film compared to bulk titania (E_g =3.2 eV) may be due to the nanocrystalline nature of the film where the absorption edge will shift to a shorter wavelength of the radiation with the effect of quantization. The energy bandgap of indirect transitions not significantly changed with annealing temperatures. But they were slightly decreased with the increase in annealing temperature. This change may be related to density and structural modifications. The electronic disorder induced by the presence of point defects like oxygen vacancies in the film, which is supposed to be between conduction and valence bands creating a localised field and hence changing the electronic structure of the titania film. Thus the probability of electron and hole trapping can change and this could result in a change of the measured bandgap. On the other hand increasing the annealing temperature change the structure from amorphous to crystalline, and hence lower the interatomic spacing leading to decrease in bandgaps (Vasantkumar and Mansingh, 1991).

In summary, the electrical properties of electrohydrodynamically processed TiO_2 films were investigated for the first time. The dielectric constant of TiO_2 films was ~7. The films annealed at 500 °C showed a higher dielectric constant and increasing the annealing temperature decreased the dielectric constant of the films. The leakage current density of the films was improved by post deposition annealing. The optical characterisation of the films showed a good transparency in the visible light region. The annealing temperature was influenced the

transmittance of the films. The energy bandgap of the films were ~3.50 eV for indirect transition.

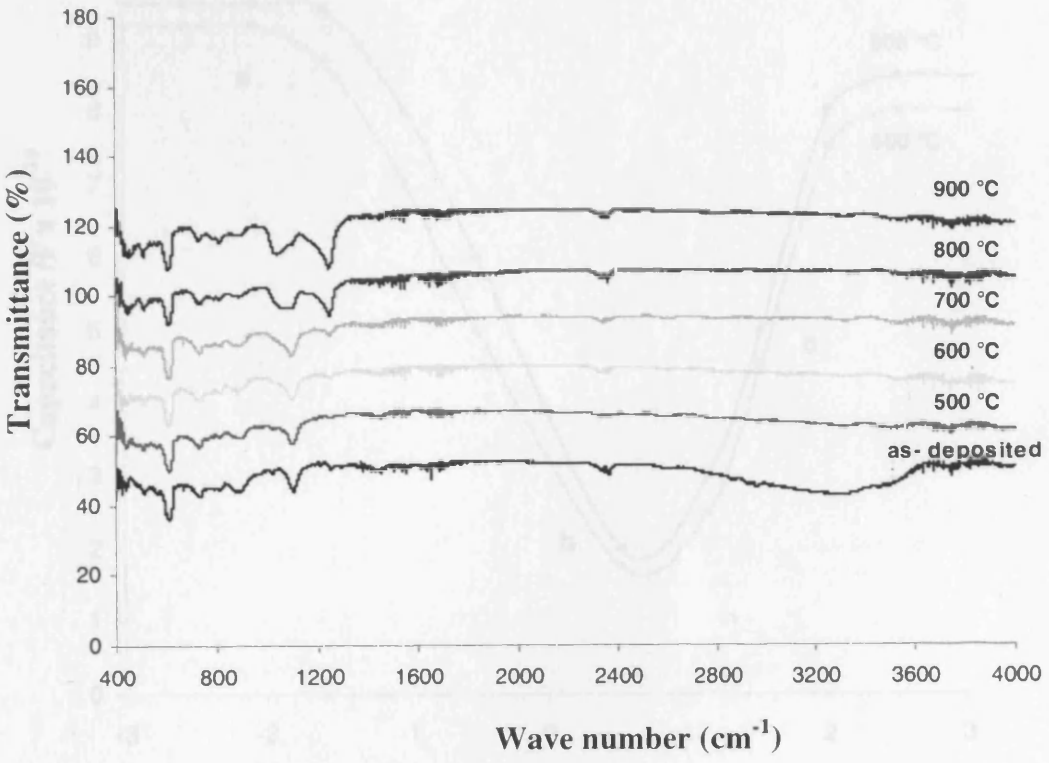

Figure 5.1 FTIR studies of TiO_2 films annealed at different temperatures

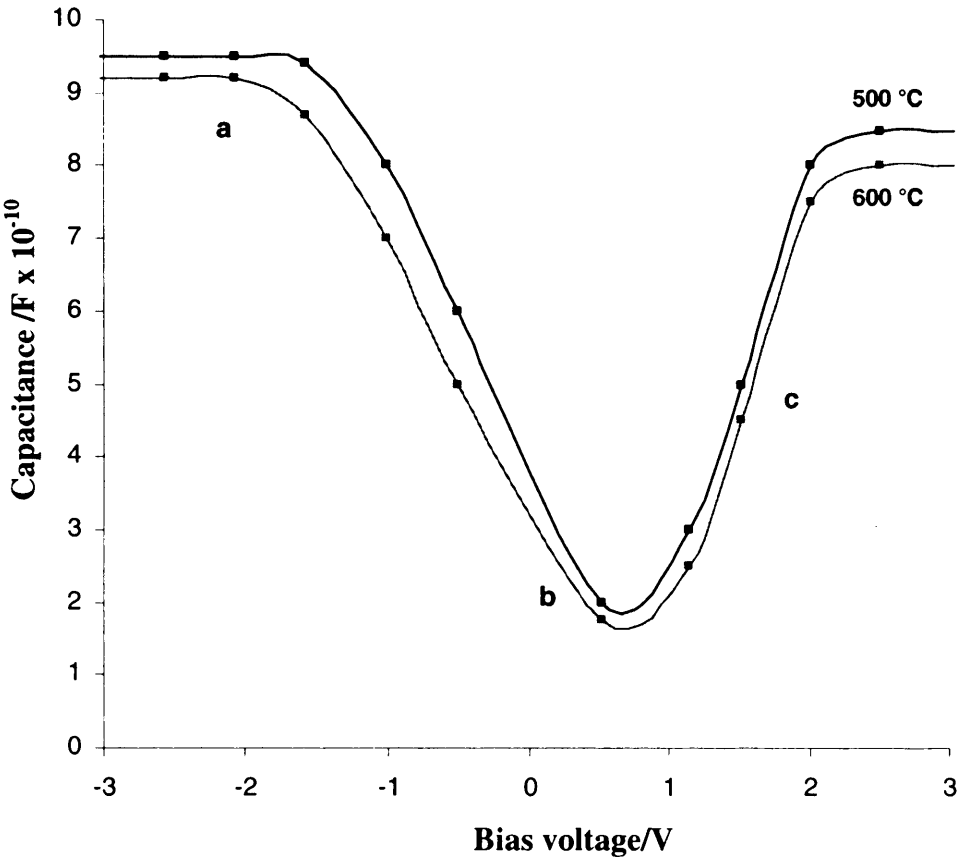

Figure 5.2 Low frequency C-V characteristics for different annealing temperatures

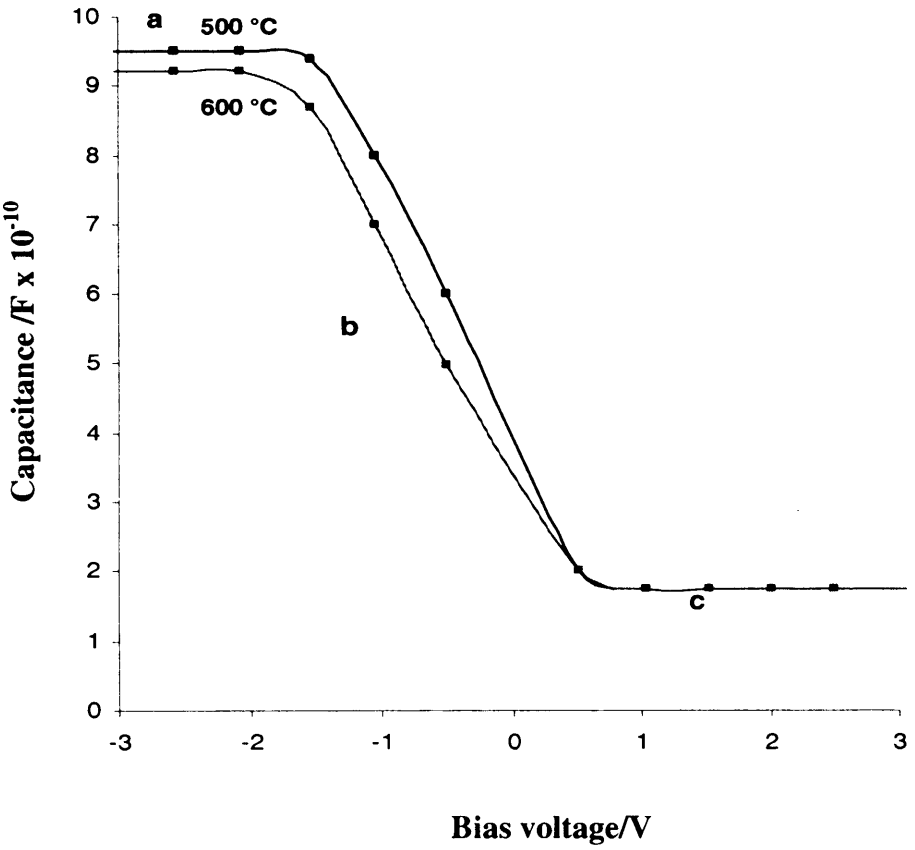

Figure 5.3 High frequency C-V characteristics for different annealing temperatures

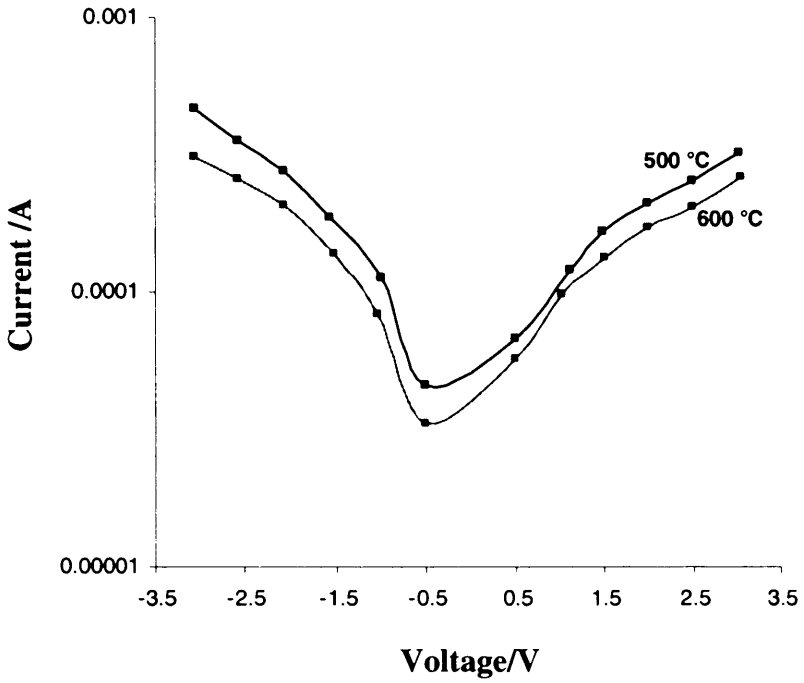

Figure 5.4 Current-Voltage characteristics for different annealing temperatures

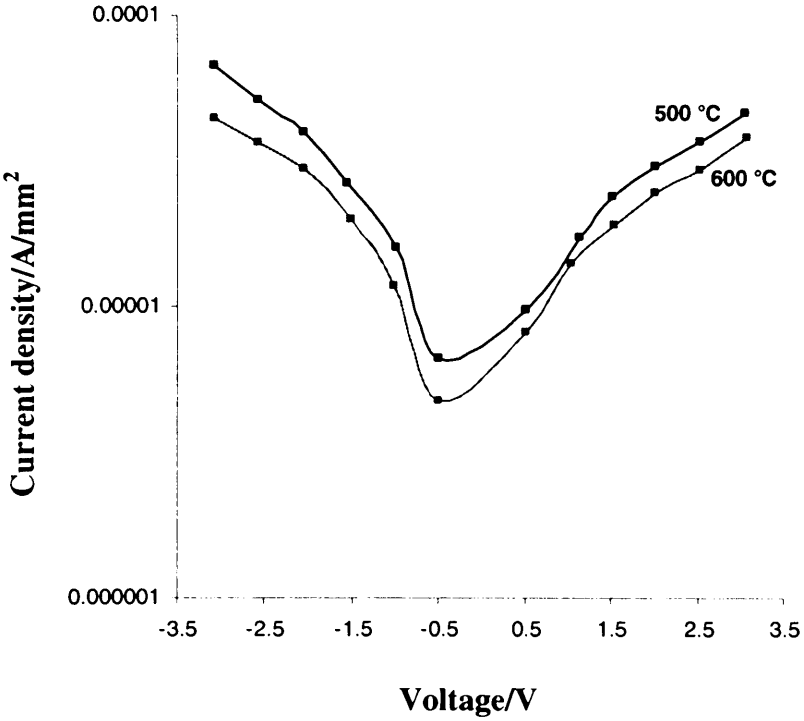

Figure 5.5 Current density-Voltage characteristics for different annealing temperatures

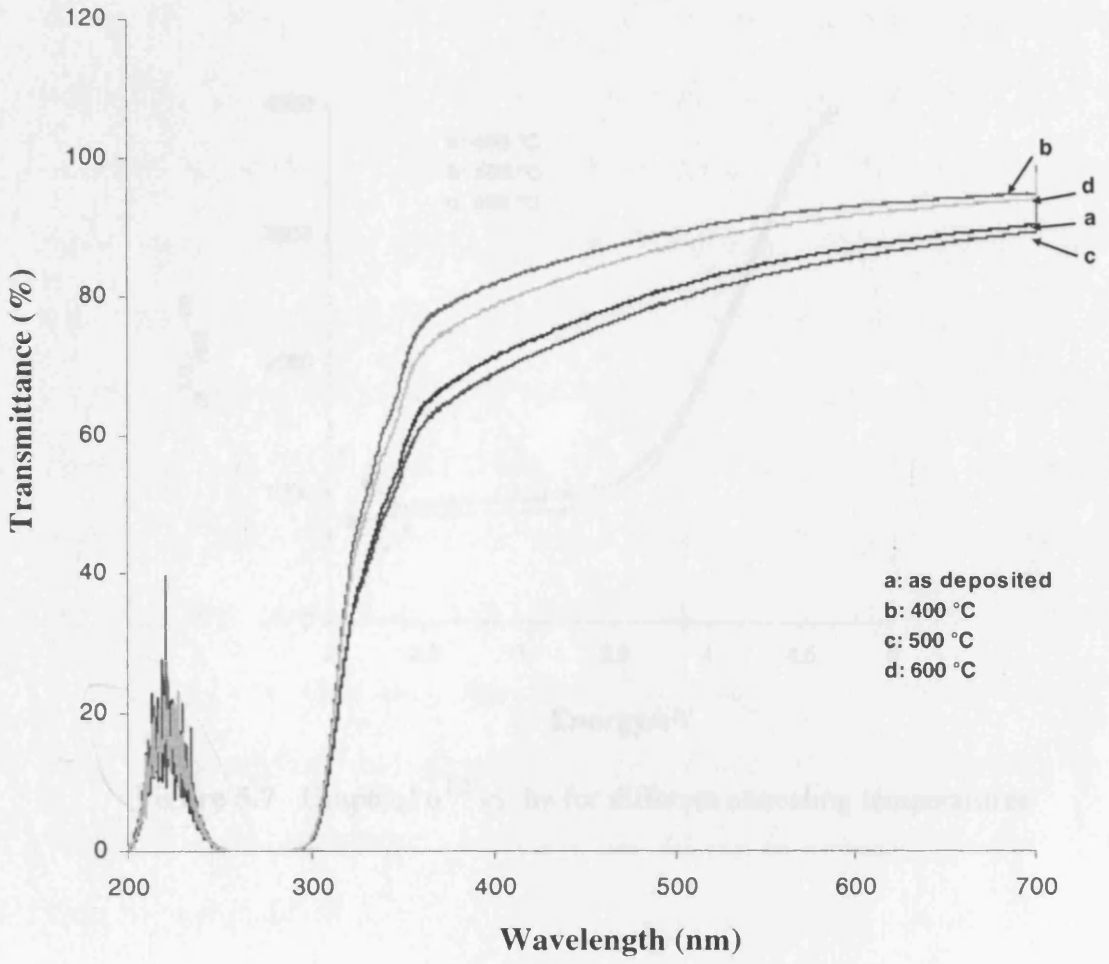

Figure 5.6 Optical transmittance spectra of TiO_2 films annealed at different temperatures

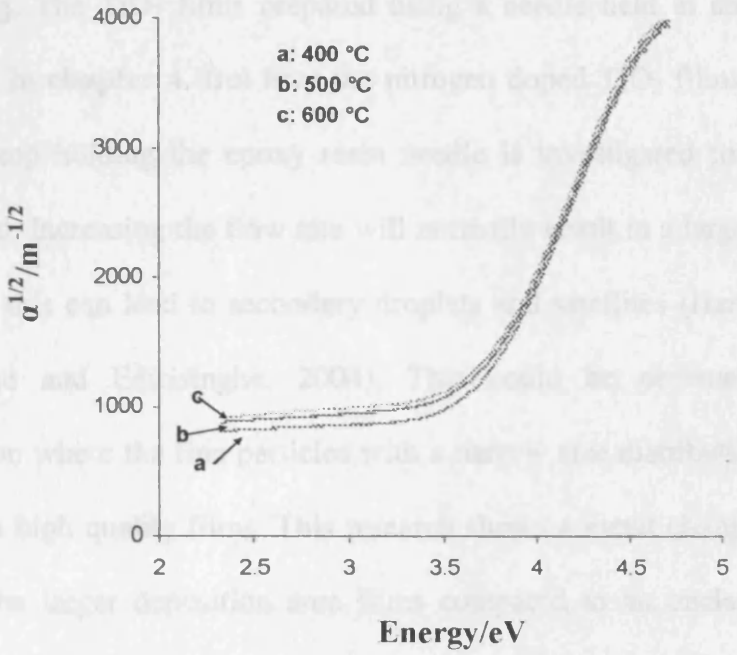

Figure 5.7 Graph of $\alpha^{1/2}$ vs. hγ for different annealing temperatures

CHAPTER 6

Electrohydrodynamic processing of Nitrogen doped TiO_2 Films

The research on this chapter describes a novel method to prepare the nitrogen doped TiO_2 films with a wider coverage area using an electrohydrodynamic processing. The TiO_2 films prepared using a needle held in an epoxy resin was described in **chapter 4**. But here the nitrogen doped TiO_2 films prepared using a metal clamp holding the epoxy resin needle is investigated for the first time is mentioned. Increasing the flow rate will normally result in a larger deposition area; however, this can lead to secondary droplets and satellites (Hartman et al., 2000; Jayasinghe and Edirisinghe, 2004). This could be detrimental to the film preparation where the fine particles with a narrow size distribution are essential in forming a high quality films. This research shows a metal clamp could be used to prepare the larger deposition area films compared to an unclamped set-up. The effect of metal clamp on processing parameters and cone-mode formation were investigated and appropriate conditions for depositing the nitrogen doped TiO_2 films were established.

The N-doped TiO_2 films have been attracting much more attention in the view of their potential application in solar energy conversion and environmental cleaning. This is a first ever study of the nitrogen doped TiO_2 films prepared by electrohydrodynamic processing. This chapter further describes the effect of nitrogen concentration on structural features of the N-doped TiO_2 films. The structural features were studied by Raman spectroscopy and x-ray diffraction. The atomic bonding was studied by Fourier transform infrared spectroscopy. The x-ray

photoelectron spectroscopy was used to find out the nitrogen content in the films. The morphological studies were carried out by scanning electron microscopy and atomic force microscopy. The optical characterisation of N-doped TiO_2 films were done by uv-vis spectroscopy and the energy bandgap of the films were evaluated. Finally, the effect of nitrogen concentration on the energy bandgap of the N-doped TiO_2 films was discussed.

6.1 N-doped TiO_2 sol

The preparation of N-doped titania sol is the key for electrohydrodynamic processing since the physical properties of the sol are main parameters in the processing. For an example the conductivity of the sol must fall in a suitable range in order to obtain the stable cone-jet (Hayati et al., 1987). The preparation method of the N-doped TiO_2 sol with various amount of nitrogen was described in section **3.2.2**. The addition of titanium tetraisopropoxide (TTIP) to ethanol solution leads to the hydrolysis of the TTIP to form reactive monomers. These reactive monomers react with each other to form the titania sol. There after the addition of ammonia precursor in the titania sol leads to the formation of N-doped titania colloidal solution which was used in electrohydrodynamic processing. The nitrogen doped titania synthesised using a wet chemical method commonly use aqueous ammonia (NH_4OH) as the nitrogen source. Here, the ammonia in ethanol used as a nitrogen source taking in to the account that it is difficult to electrohydrodynamically process the aqueous medium in air in the stable cone-jet mode due to high surface tension of water, which will result in corona discharge (Taylor, 1964; Smith, 1986).

6.1.1 Sol physical properties

The N-doped titania sol's physical properties including surface tension, density, electrical conductivity and viscosity were determined as discussed in section **3.3**. The physical properties of the sol with processing parameters, the applied voltage and flow rate governs the electrohydrodynamic processing. The sol's physical properties are compared with the solvent ethanol and given in **Table 6.1**.

Table 6.1 Physical properties of N-doped TiO_2 sol and ethanol

		Ethanol	**Sol-1**	**Sol-2**	**Sol-3**
Conductivity	Sm^{-1}	5×10^{-5}	4.9×10^{-4}	6.2×10^{-4}	8.6×10^{-4}
Surface tension	mNm^{-1}	22	21.8	21.9	21.8
Viscosity	mPa s	1.19	1.53	1.54	1.54
Density	kgm^{-3}	785	791	791	792

Comparing the properties of N-doped titania sols with ethanol reveals that the electrical conductivity increased by an order of magnitude. On the other hand comparing the sols indicate that there is a gradual increase in the electrical conductivity with increase in weight percentage of ammonia precursor in the sols. Therefore, this increase in electrical conductivity must be due to nitrogen source used to dope the titania sol. Even the increase in electrical conductivity of sols not made the electrohydrodynamic processing in stable cone-jet mode unstable.

The surfaces tension of the sols remained almost same at ~22 mNm^{-1} and inline with ethanol. The viscosity of the sols was increased considerably compared to ethanol but not made any noticeable difference between them. The density of sols also increased noticeably and remained nearly same between them.

6.2 Electrohydrodynamic processing of N-doped TiO_2 films

The titanium dioxide is a wide bandgap semiconductor could be used in many applications. The impurity doping is one of the typical approaches to tune the electronic structure and alter its optical properties. The nitrogen doping is one of the ways to achieve that goal. The electrohydrodynamic processing is a technique particularly suitable in tailoring the film morphology of a large variety of ceramic thin films and presents a good reproducibility (Kelder et al., 1994; Lintanf et al., 2007). The electrohydrodynamic processing of N-doped TiO_2 films were performed using two set-ups described in section **3.4**. The first set-up contains a needle in epoxy resin which was used in the TiO_2 film preparation in **chapter 4** while the second set-up contains a metal clamp holding epoxy resin needle was employed to increase the film deposition area.

The electrohydrodynamic processing history runs over a century and it was first systematically studied by Zeleny (Zeleny, 1914) followed by many others (Taylor, 1964; Vonnegut and Neubauer, 1952). The ceramic films prepared via electrohydrodynamic processing have been studied over a decade and no one specifically reported its deposition area. According to Chen et al. (1999) a larger deposition area could be obtained by increasing the flow rate and it was observed in normal experiments but increasing the flow rate increases the current through the

liquid cone in the stable cone-jet mode because a high flow rate requires more electric power to accelerate the liquid in the jet. Keeping this in mind, a novel method to prepare a wider coverage area N-doped TiO_2 films was established and investigated.

As already mentioned this is the first ever study of the N-doped TiO_2 films by electrohydrodynamic processing. The flow rate regime was kept low as possible and varied between 2×10^{-11} - 2×10^{-10} m^3s^{-1}. The applied voltage was tuned between 0 – 8 kV to create an electric field between needle and grounded substrate.

6.2.1 Mode-selection map

The mode selection map is very useful to identify the stable cone-jet domain and hence establish the processing conditions. The mode selection map was drawn for various combinations of applied voltage and flow rate for the two set-ups described in section **3.4** in order to find out the suitable processing conditions to prepare the N-doped TiO_2 films. The mode selection maps for the N-doped titania sol-1 are shown in **Figure 6.1** and **Figure 6.2** for the set-up **1** and the set-up **2** respectively.

For a fixed flow rate there exist two applied voltage limits within which the stable cone-jet mode is achievable. Below the lower limit the unstable cone-jet mode was obtained and above the upper limit the multi-jet mode was produced. The stable cone-jet domain was broader between the flow rates of 2×10^{-11} - 8×10^{-11} m^3s^{-1} and obtained within the applied voltage of 5 - 5.8 kV for the set-up **1** and 3.7 - 4.6 kV for the set-up **2**. There after the domain was narrowed until the flow rate of 2×10^{-10} m^3s^{-1}. However, the unstable mode domain was broader in these flow rate regimes.

The stable cone-jet domain for the N-doped titania sol was very different to the domain obtained for titania sol (**Figure 4.2**). This is indicating that the physical properties of the sols played a crucial role in determining the domains for the stable cone-jet mode.

The mode selection maps for the two set-ups showed various mode domains with different operating voltage windows and this was due to the electric field modulation between the nozzle and the grounded substrate. This will be explained in section **6.2.3**. The same operating voltage window was observed for the N-doped titania sol-2 and sol-3. There was no noticeable different in the operating voltage window for the stable cone-jet mode in the all three sols used in these flow rate regimes. Tang and Gomez (1996) studied the effect of electrical conductivity in the cone-jet domain over increasing flow rates and observed the change in position and shape of the domain. Their studies were based on the lower conductivity solutions of the order of 10^{-6} S/m. However, at lower flow rates there is no significant change in the cone-jet operating voltage window for varying electrical conductivity. The effect is prominent where the flow rates $>5\times10^{-10}$ m^3s^{-1}, especially because the top end of the cone-jet operating voltage window showed a greater variation. Even though the sols used in this work showed a higher conductivity, the cone-jet operating voltage remained almost same at low flow rate regimes and this is consistent with their results (Tang and Gomez, 1996).

6.2.2 Operating mode and cone-shape

The electrohydrodynamic processing of N-doped titania sol generated different type of operating modes and cone-shapes. For a fixed flow rate of 0.67×10^{-10} m^3s^{-1},

varying the potential difference between the needle and the ground electrode produced dripping, micro-dripping, unstable, stable and multi-jet modes. The dripping mode was obtained at zero applied voltage where the N-doped titania sol flowed drop by drop at the end of the needle. This is shown in **Figure 6.3**. Increasing the applied voltage changed the mode to micro-dripping, here the meniscus was elongated in the electric field direction and is shown in **Figure 6.4**. The unstable cone-jet mode was obtained at the applied voltage of 3.3 kV. The meniscus was pulsating and the shape was changed between the semi-spherical and cone shape. The unstable cone-jet mode is shown in **Figure 6.5**.

The stable cone-jet mode was generated at an operating voltage window of 3.7 - 4.6 kV. This mode is shown in **Figure 6.6** at the applied voltage of 3.7 kV. With an increase in voltage, the base of the cone contracted as cone angle widens and the cone height became shorter. This is shown in **Figure 6.7** and **Figure 6.8**. As the voltage was increased further the cone decreased in size and became closer to needle exit eventually formed the multi-jetting mode. This is shown in **Figure 6.9** and **Figure 6.10**.

6.2.3 Effect of metal clamped needle on applied voltage and deposition area

For the set-up **1**, for a fixed flow rate of 0.67×10^{-10} m^3s^{-1} the operating voltage window for obtaining the stable cone-jet mode was 5.1 - 5.8 kV. Increasing the voltage beyond this point generated the multi-jetting mode. The set-up **2** gave an operating voltage range of 3.7 - 4.6 kV for the stable cone-jetting at the same flow rate. This is because of the introduction of the metal clamp increased the electric

field strength near the nozzle tip. The electric field normal to the surface of the Taylor cone is given by (Taylor, 1964; Smith, 1986),

$$E = \left[\frac{2\gamma \cot\theta}{\varepsilon_o R} \right]^{\frac{1}{2}} \tag{6.1}$$

where γ is the surface tension, θ is the semi-angle of the Taylor cone, ε_o is the permittivity of vacuum and R is the local radius. Therefore, to form a cone-jet mode the electric field ≥ *E*. In the case of set-up **2**, the electric field strength near the tip of the nozzle increased due to metal clamp thus it needed a lower applied voltage to initiate the cone-jet mode. At the lower voltage the electric field near the nozzle tip is enough to overcome the surface tension stress to form a cone-jet mode.

To find out the deposition area and the spray angle by the two set-ups it was assumed that the spray is an ideal cone so the deposition area is given by:

$$A = \pi(d \tan\alpha)^2 \tag{6.2}$$

where d is the nozzle tip to collecting plate distance and α is the half spray angle.

The **Table 6.2** below shows the deposition area and the spray angle calculated from the two set-ups with their corresponding processing conditions. The spraying time was kept for 30 minutes for the two set ups.

Table 6.2 Deposition area and spray angle for two experimental set-ups

	Processing conditions	**Deposition area (cm^2)**	**Spray angle (°)**
Set-up **1**	0.67×10^{-10} m^3s^{-1}, 5.5 kV	15.91	58.72
Set-up **2**	0.67×10^{-10} m^3s^{-1}, 4.1 kV	78.57	102.68

In each case it was found that the deposition area was ~15.91 cm^2 for the set-up **1** and ~78.57 cm^2 for the set-up **2**. The spray angle for the set-up **1** was 58.72° and 102.68° for the set-up **2**, approximately 1.75 times higher than the earlier one. This is clearly shows that the metal clamped needle could be used to produce the larger deposition area films at lower flow rate regimes in electrohydrodynamic processing. The effect of metal clamp in increasing the film deposition area could be explained by the following mechanism.

The droplets trajectory is influenced by the Coulomb repulsive forces and electric field forces. By modulating the electric field strength and shape between the nozzle and the ground electrode, the spray pattern could be controlled. In the set-up **2** the focusing is weak and in the set-up **1** the focusing is strong due to strong electric field at the bottom of the spray system. In addition to this the increase in electric field strength in the radial direction of the cone in the set-up **2** results in more charge carriers in the jet, thus increasing the Coulomb forces and this results in more repulsion between the adjacent droplets (Kumbar et al., 2007). Therefore, the set-up **2** resulted in larger deposition area than the set-up **1**.

6.3 Film preparation and characterisation

The N-doped TiO_2 films were prepared using the set-up **2** (**Figure 3.2**) at a flow rate of 0.67×10^{-10} m^3s^{-1} and in the operating voltage window of 3.7 - 4.6 kV. The films were marked as TiO_2-N1, TiO_2-N2 and TiO_2-N3, respectively, corresponding to sols 1, 2 & 3 used to prepare them. The characterisation of processed films annealed at different temperatures is done by various techniques. The structural evaluation and atomic bonding in the N-doped TiO_2 films were performed using Raman spectroscopy, x-ray diffraction and Fourier transform infrared spectroscopy. The morphological studies were carried out by scanning electron microscope and atomic force microscope. The uv-vis spectroscopy was used to study the optical properties of the films.

6.4 Effect of nitrogen concentration on structural features and atomic bonding of N-doped TiO_2 films

The nitrogen concentration of nitrogen doped TiO_2 films were controlled by varying the nitrogen precursor concentration of the prepared sol (section **3.2.2**). The identification of structural features of the N-doped TiO_2 films is quite important since the properties of the films depend on its structural features. The effect of nitrogen concentration on formation of different phases of the TiO_2 was carefully studied for the TiO_2-N1, TiO_2-N2 and TiO_2-N3 films annealed at various temperatures.

6.4.1 Raman spectroscopy of N-doped TiO_2 films

The Raman spectroscopy permits a detail analysis of various phases of titanium dioxide. There are six fundamental Raman active modes for the anatase phase titanium dioxide including A_{1g} (519 cm^{-1}), B_{1g} (399 and 519 cm^{-1}), and E_g (144, 197, and 639 cm^{-1}) (Cong et al., 2007). The Raman spectra of nitrogen doped titanium dioxide films TiO_2-N1, TiO_2-N2 and TiO_2-N3 annealed from 500 °C to 1000 °C are shown in **Figure 6.11**, **Figure 6.12** and **Figure 6.13**.

A strong peak characteristic of the Si substrate is present at 520 cm^{-1} in all the films. The as-deposited films show no peaks other than those of the Si substrate, so the films are amorphous. Increasing the temperature from the ambient temperature (~ 22 °C) to 500 °C changes the phase of the film from the amorphous to crystalline. The peaks observed at 143 cm^{-1}, 196 cm^{-1}, 396 cm^{-1} and 638 cm^{-1} can be attributed to the anatase phase. The results indicate that the films retained the anatase phase of titanium dioxide even for the films prepared with higher doping concentration of nitrogen precursor. However it can be clearly seen that increasing the doping concentration depresses the phase formation. The TiO_2-N2 and TiO_2-N3 films only show two prominent peaks of the anatase compared to TiO_2-N1 films where five peaks are seen.

The rutile TiO_2 shows four Raman active modes at B_{1g} (144 cm^{-1}), E_g (448 cm^{-1}), A_{1g} (613 cm^{-1}) and B_{2g} (827 cm^{-1}) (Chen et al., 2005). There are no Raman features observed at these frequencies even in the films annealed at 1000 °C indicating no rutile phase is present in the films. In the previous work (**chapter 4**) where the undoped titanium dioxide films were prepared by electrohydrodynamic processing,

a peak for the rutile phase was observed in the film annealed at 900 °C. This comparison shows that the nitrogen doping retards the phase transformation. The introduction of nitrogen atom in to the TiO_2 structure made obstacle for diffusion of atoms to form the rutile phase.

According to Mwabora et al. (2004) the presence of small amount of nitrogen facilitates the rutile to anatase phase transformation. However, they prepared the N doped TiO_2 films using a sputtering technique. Okato et al. (2005) observed higher N concentration resulted in more rutile phase. They used a pulsed laser deposition to prepare their films. These contradictions clearly show that the processing method strongly influences the structure of prepared films. For the non-stoichiometric titanium nitride films the Raman bands appear at 200 cm^{-1}, 330 cm^{-1}, and 550 cm^{-1} (Gyorgy et al., 2002). There is no such peak in the prepared films ruling out the possibility of formation of a TiN structure. The peaks of the anatase phase notably shift towards the lower wave numbers, for an example the peak obtained at 391 cm^{-1} for TiO_2-N3 film and that at 396 cm^{-1} for TiO_2-N1 film with increasing nitrogen precursor concentration might be due to the increase of residual stresses created by nitrogen in the crystal lattice which leads to a peak shift in the films.

6.4.2 XRD study of N-doped TiO_2 films

The XRD patterns of TiO_2-N2 films at different annealing temperatures are shown in **Figure 6.14**. The dominant feature is the peak at $2\theta = 25.4°$ observed in all films, corresponding to the anatase (101) phase, which is the preferential orientation of the prepared films. The intensity variation of the peaks normally

relate to either changes in crystallinity or film thickness. In this case there is no change in film thickness because all films were prepared under identical conditions. Therefore, a variation in intensity is mainly due to crystallinity. The peaks get sharper and stronger when increasing the temperature, indicating improved crystallinity. However, at 1000 °C the peak intensity diminishes but there is no sign of any peaks relating to TiN or the rutile phase. Additional peaks relating to the anatase phase observed at $2\theta \sim 38°$ and $2\theta \sim 48°$ correspond to (004) plane and (200) plane respectively. These results are in quite good agreement with the Raman spectra results shown in the previous section **6.4.1** because it shows only the anatase phase and no other phases.

The average crystallite size of TiO_2 films annealed at various temperatures estimated using Scherrer's formula mentioned in the section **3.7.2**. The variation of crystallite size with annealing temperature is shown in **Figure 6.15**. The average crystallite size was increased with the annealing temperature. However, it was not increased to the extent where titania crystals could be observed in the micro-structure, probably due to the dopant N hindering their growth.

The lattice parameters a and c were estimated from the following equation by substituting for the interplanar distance d.

$$\frac{1}{d^2} = \frac{h^2 + k^2}{a^2} + \frac{l^2}{c^2} \qquad (6.3)$$

The estimated values are 0.380±0.002 nm and 0.952±0.004 nm for a and c, respectively. The values are close to the standard values of 0.378 nm and 0.951 nm

(JCPDS-ICDD 21-1272). A slight variation in parameters may be associated with the doping effect of N in crystals. The ionic radius of Ti^{4+} (0.68 °A), O^{2-} (1.40 °A) and N^{3-} (1.46 °A) indicate that nitrogen ions are bigger than the other two, so interstitial doping of N may create stress in the lattice leading to variation in the lattice constant.

6.4.3 FTIR study of N-doped TiO_2 films

The FTIR studies of the N-doped TiO_2 films prepared by electrohydrodynamic processing are useful for analysing the surface functional groups and elucidate the nature of bonding in the film. The FTIR results of the TiO_2-N1, TiO_2-N2 and TiO_2-N3 films are shown in **Figure 6.16**, **Figure 6.17** and **Figure 6.18** respectively. In the as- deposited films a broad absorption peak at 3200-3400 cm^{-1} is observed corresponding to adsorbed water and hydroxyl groups. After annealing the film to higher temperatures these peaks disappeared indicating the removal of hydroxyl groups in the films. The peak located near 435 cm^{-1} in the annealed films corresponding to the anatase phase of TiO_2 (Duenas et al., 2005). The absorption bands near 1080 cm^{-1} and 810 cm^{-1} are characteristic features of the SiO_2 and correspond to stretching and bending vibrations of the Si-O-Si bond respectively (Mosaddeq-ur-Rahman et al., 2000). In addition to this, the peak around 1250 cm^{-1} is also corresponds to the SiO_2 bond (Han and Aydil, 1997).

According to Chen et al. (2005) the amine residues display a peak at 2950 cm^{-1}. This peak has been detected in all as-deposited films however, the annealed films didn't display it. Chen et al. (2005) mentioned that the infrared bands of NO_2 occur at 1618 cm^{-1}, 1318 cm^{-1} and 750 cm^{-1}. There are no peaks related to these wave

numbers in the films prepared in the present work, ruling out the chances of formation and/or physisorption of NO_2 species on the surface of the films.

6.4.4 XPS study of N-doped TiO_2 films

The presence of nitrogen in the films was confirmed by XPS measurements. **Figures 6.19**, **6.20** and **6.21** show the high resolution Ti (2p), O (1s) and N (1s) XPS spectra of the TiO_2-N1, TiO_2-N2 and TiO_2-N3 films annealed at 500 °C respectively. The films showed two peaks for Ti (2p) associated with Ti $2p_{3/2}$ and Ti $2p_{1/2}$ core levels at the binding energy of 458.2 eV and 464.1 eV respectively. The O (1s) core level peak was obtained between 530 - 532 eV for the films. A broad N (1s) core level peak was observed between 398 - 403 eV.

The XPS quantification was performed to find out the N content in the films. The estimated N content was 0.11 with respect to Ti for the TiO_2-N1 film. Similarly, the N content in the TiO_2-N2 and TiO_2-N3 films were found which are given in the **Table 6.3**. The estimated N content in the films were low compared to which in the initial sol this is probably due to some of the N related species may be removed during annealing process.

Table 6.3 The nitrogen content in the nitrogen doped TiO_2 films

Film	N/Ti ratio
TiO_2-N1	0.11
TiO_2-N2	0.17
TiO_2-N3	0.26

6.5 Morphological study of N-doped TiO_2 films

The surface morphology study was done to determine the quality of the processed films. The morphology studies of electrohydrodynamically processed N-doped TiO_2 films were carried out using scanning electron microscopy and atomic force microscopy.

6.5.1 Scanning electron microscopy

The FE-SEM micrograph of the N-doped TiO_2 film processed at a flow rate of 0.67×10^{-10} m^3s^{-1} and the operating voltage range of 3.7 - 4.6 kV is shown in **Figure 6.22**. The film was annealed to 500 °C. The morphology of N-doped TiO_2 film shows a relatively flat surface with some rough areas. The films were dense and no cracks observed in the processed films. In electrohydrodynamic processing, the droplets contain solutes arriving to substrate spread to form layers. Spreading of droplets is restricted in the already formed previous layer. This might be the reason for rough areas in the processed films.

6.5.2 Atomic force microscopy

The AFM image for the N-doped TiO_2 film is shown in **Figure 6.23**. The AFM image shows that the film consists of granular features. A substantial difference observed between the AFM grain size and XRD measurements. It may be due to the aggregation of small particles lead to an increase in the grain size in the AFM image.

6.6 Optical characterisation of N-doped TiO_2 films

The optical characterisation of the TiO_2-N1, TiO_2-N2 and TiO_2-N3 films were done by uv-vis spectroscopy. The spectroscopy measurements were used to evaluate the energy bandgap of the processed films.

6.6.1 UV-Vis spectroscopy study on N-doped TiO_2 films

The transmittance characteristics of the TiO_2-N1, TiO_2-N2 and TiO_2-N3 films along with the undoped TiO_2 film annealed at 500 °C measured in the wavelength range of 200 - 800 nm are shown in **Figure 6.24**. Their transmittance decreased with decreasing wavelength and the films with nitrogen doping showed a greater drop in transmittance compared with the undoped film in the wavelength between 400 - 500 nm. The transmittance of the N-doped TiO_2 films decreased with increase in doping concentration in the films. This indicates that there is a pronounced effect due to nitrogen doping in visible light range. The transmission drops almost to zero when the photon energy at shorter wavelength approaches the energy bandgap value. The optical transmission edge is not significantly affected by doping concentration at shorter wavelengths.

6.6.2 Determination of bandgap of N-doped TiO_2 films

The fundamental absorption edge of the films corresponds to electron transitions from the valence band to the conduction band and this edge could be used to calculate the bandgap for indirect transition (Pancove, 1971) using:

$$\alpha = (h\gamma - E_g)^2 \tag{6.4}$$

where α is the absorption coefficient, $h\gamma$ is the photon energy and E_g is the bandgap of the films.

Figure 6.25 shows the plots of $\alpha^{1/2}$ vs. $h\gamma$ for all films. The extrapolation of absorption edge to α=0 will yield the bandgap of the films, which were estimated and tabulated in **Table 6.4**. These values are agrees well with those of Nakamura et al. (2005) for TiO_2 films and there is no noticeable different in the bandgaps of the doped films. This is indicating that there is no bandgap narrowing due to doping and contradict the results of Asahi et al. (2001) where they claims that the N dopant occupies the substitutional site and its 2*p* states contributing to bandgap narrowing by mixing with O 2*p* states.

6.6.3 Effect of nitrogen concentration on bandgap of N-doped TiO_2 films

To investigate the dopant effect and absorption in the visible range in the N-doped TiO_2 films the low energy tail known as the Urbach tail (Urbach, 1953) was analysed. This provides overall disorder in the films. The absorption coefficient just below the band edge should vary exponentially with absorbed photon energy (Dutta et al., 2007) according to:

$$\alpha = \alpha_o \exp\left(\frac{h\gamma}{E_o}\right) \tag{6.5}$$

where α_o is a constant and E_o is an empirical parameter representative of the width of the band tail states. E_o could be estimated by the reciprocal of the slope of

the linear plot of $\ln(\alpha)$ vs. $h\gamma$ curve which is shown in inset of **Figure 6.25**. The E_o value obtained for the films are shown in **Table 6.4**. The value of E_o increased when nitrogen was introduced in the structure. This is indicating that the localised states created by nitrogen increased in the structure. The value of E_o increased with nitrogen concentration in the TiO_2 films. The increase in the width of band tail states is the reason behind the optical transition in the visible light range. The occupied states in the valence band tail will pump the electrons to unoccupied states of the conduction band edge. The localised states should be created by interstitial nitrogen rather than the substitutional nitrogen. If nitrogen is substituted in the lattice an abrupt change in transmission could have been observed in the nitrogen doped films. So in these nitrogen doped films, nitrogen occupies the interstitial sites rather than the substitutional site. This interstitial site nitrogen occupancy is consistent with the structural characterisation results (section **6.4**).

Table 6.4 The bandgap and value of empirical parameter for films of different composition

Film	E_g **(eV)/indirect transition**	E_o **(eV)**
TiO_2	3.50	1.65
TiO_2-N1	3.52	1.87
TiO_2-N2	3.52	1.92
TiO_2-N3	3.51	1.95

In summary, the preparation of nitrogen doped TiO_2 films by electrohydrodynamic processing was investigated for the first time. The effect of applied voltage and flow rate on processing N-doped TiO_2 films also investigated and analysed in this chapter. A new method to increase the film coverage area is proposed; metal

clamping the nozzle lowered the stable cone-jet operating voltage window and increased the spray angle leading to wider area coverage. The nitrogen doping was retarding the phase formation of TiO_2 films. The absorption in visible light region was increased by nitrogen doping and could be used in many applications including photocatalysis and photoelectric.

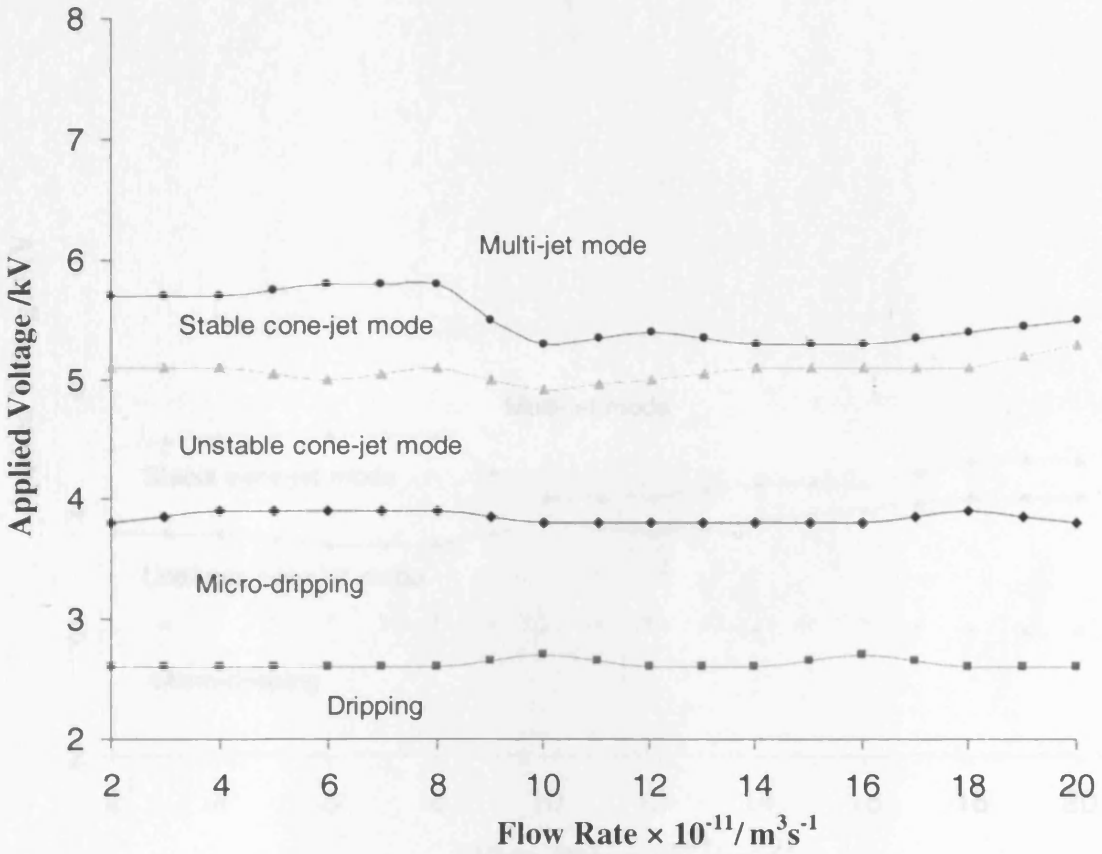

Figure 6.1 Mode selection map for the N-doped titania sol with set-up **1**

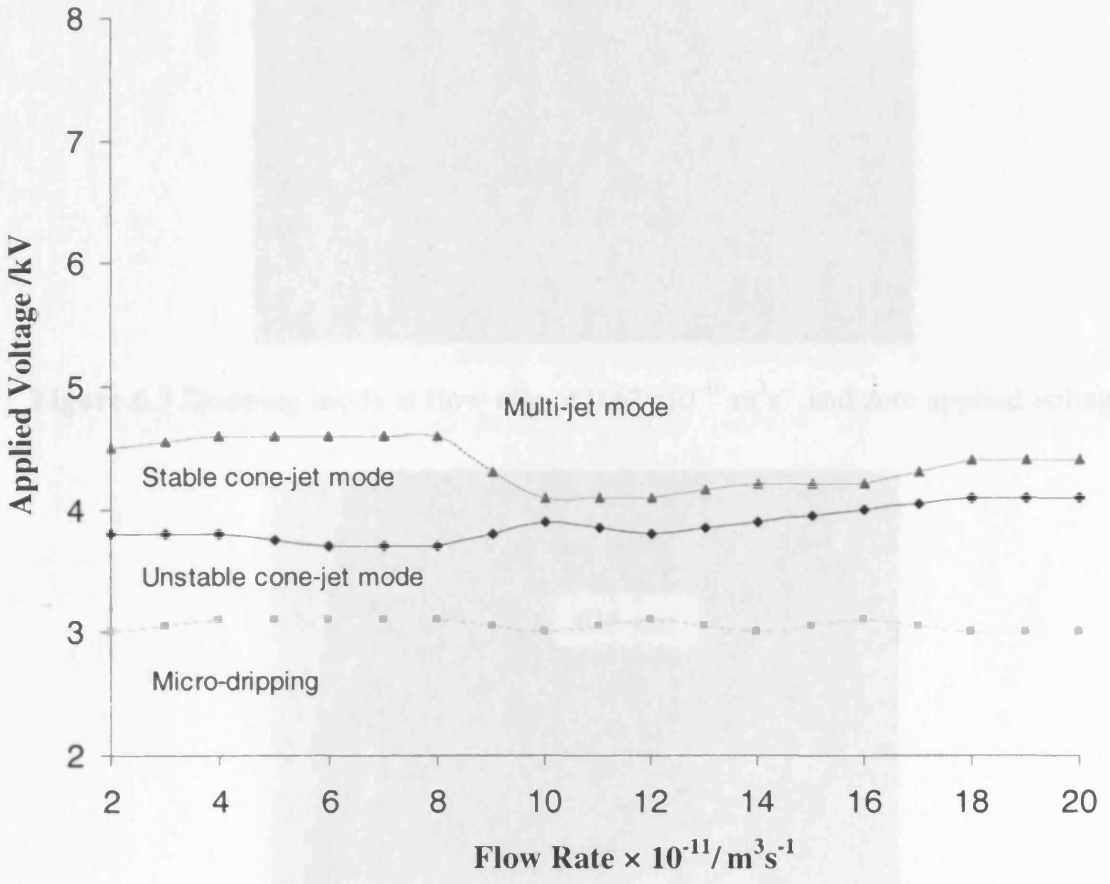

Figure 6.2 Mode selection map for the N-doped titania sol with set-up **2**

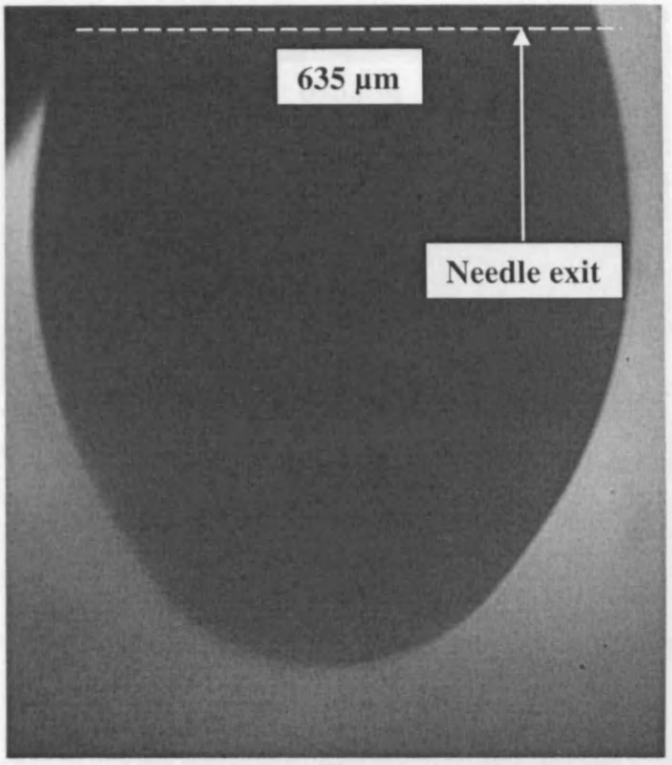

Figure 6.3 Dripping mode at flow rate of 0.67×10^{-10} m^3s^{-1} and zero applied voltage

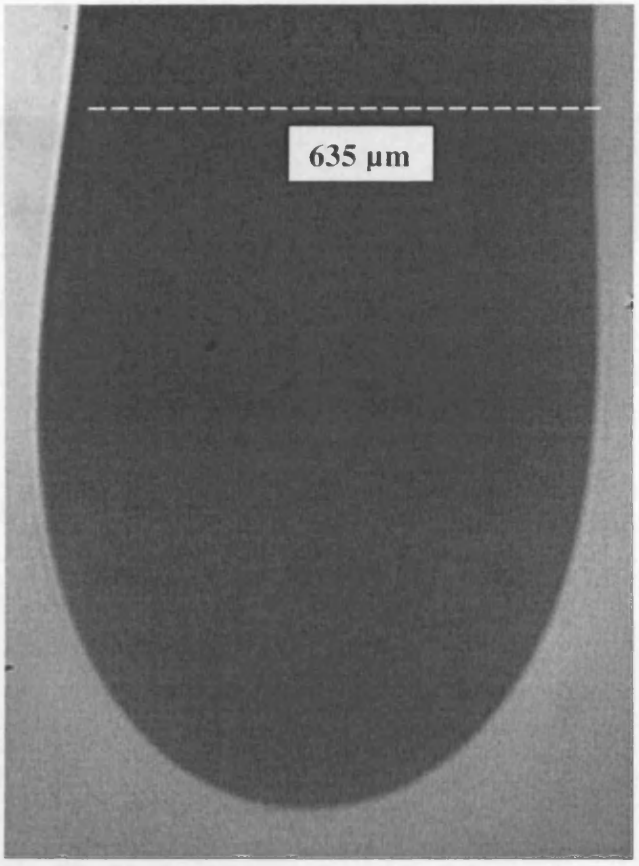

Figure 6.4 Micro-dripping at flow rate of 0.67×10^{-10} m^3s^{-1} and 2 kV

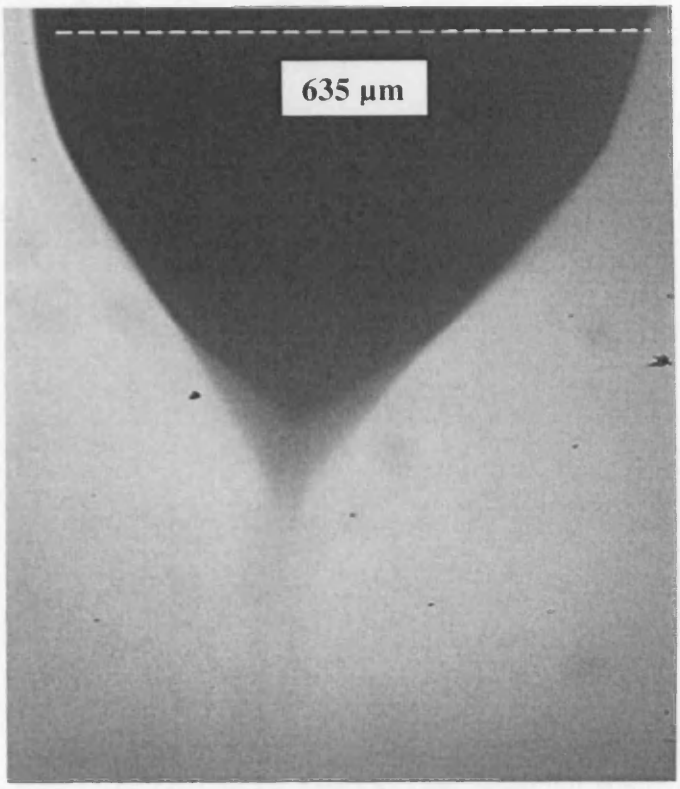

Figure 6.5 Unstable cone-jet mode at flow rate of 0.67×10^{-10} m^3s^{-1} and 3.3 kV

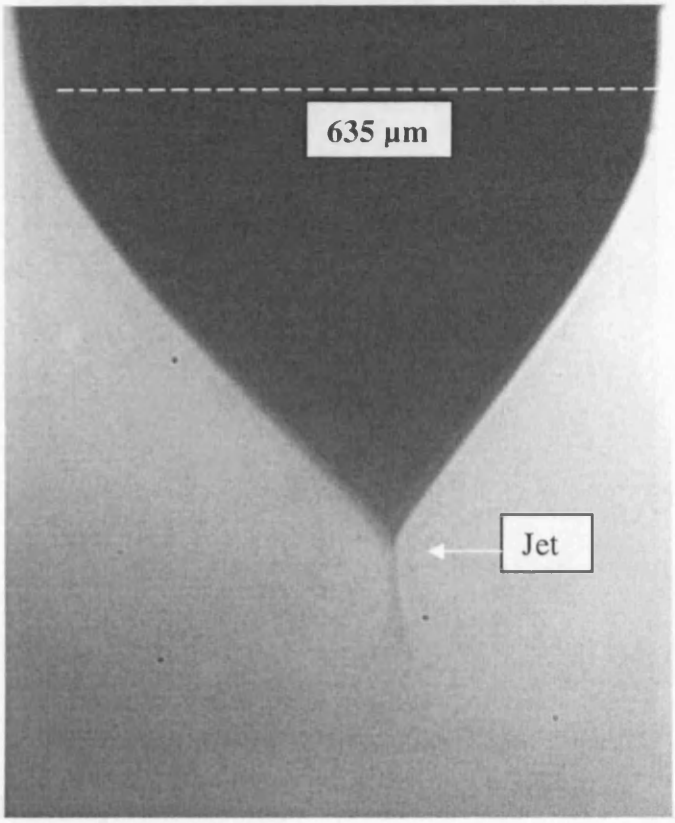

Figure 6.6 Stable cone-jet mode at flow rate of 0.67×10^{-10} m^3s^{-1} and 3.7 kV

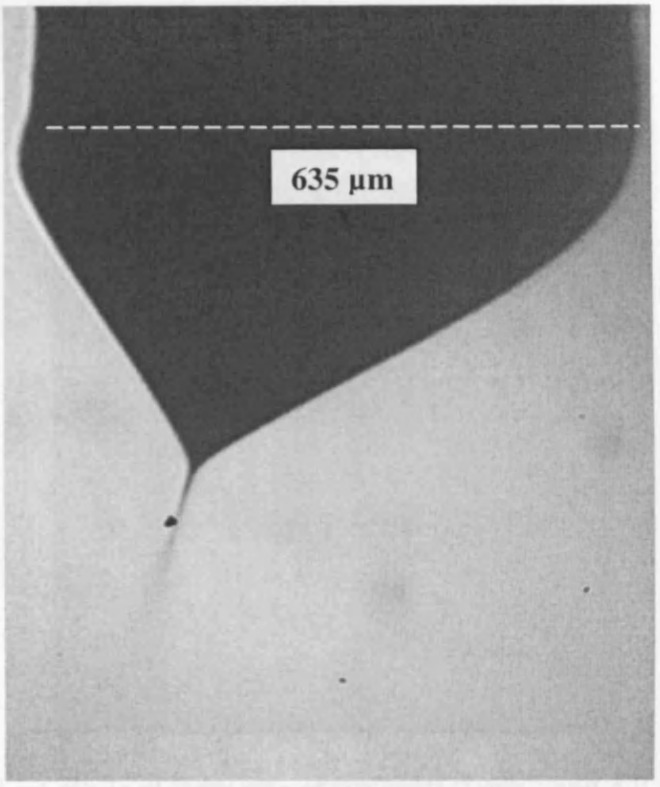

Figure 6.7 Stable cone-jet mode at flow rate of 0.67×10^{-10} m^3s^{-1} and 4.3 kV

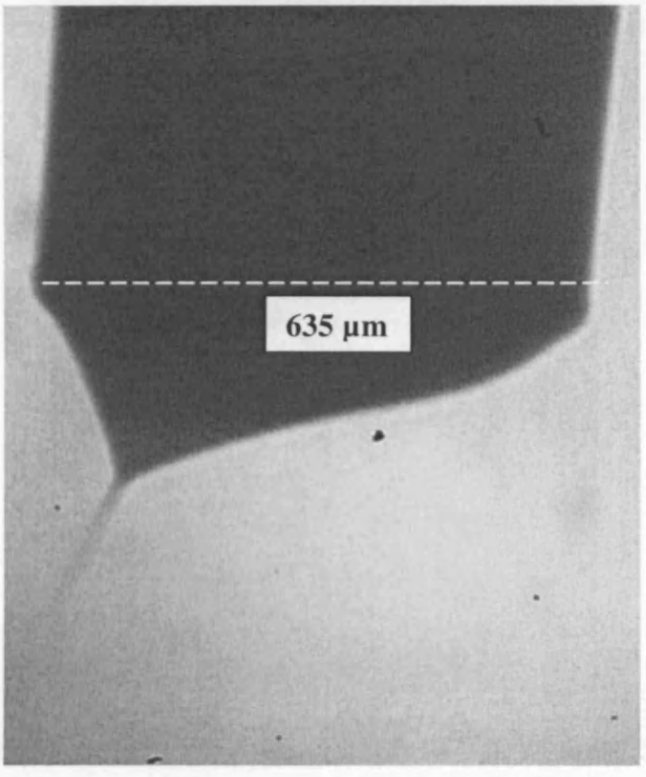

Figure 6.8 Stable cone-jet mode at flow rate of 0.67×10^{-10} m^3s^{-1} and 4.5 kV

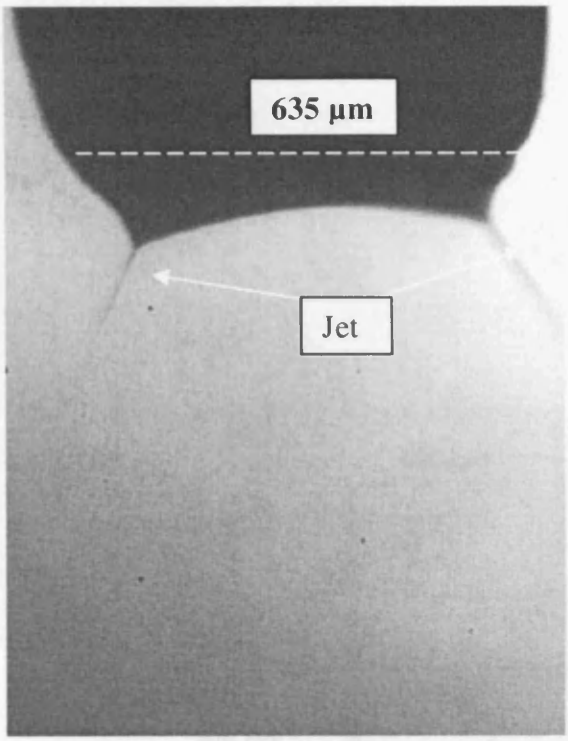

Figure 6.9 Multi-jet mode at flow rate of 0.67×10^{-10} m^3s^{-1} and 4.9 kV

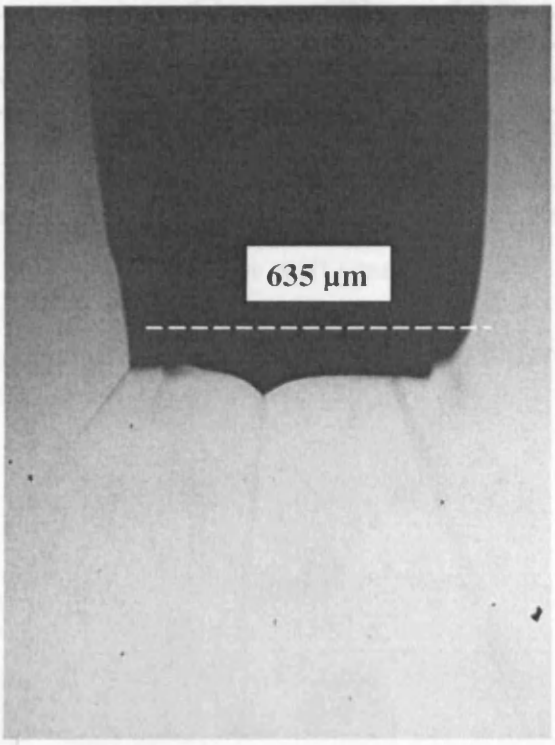

Figure 6.10 Multi-jet mode at flow rate of 0.67×10^{-10} m^3s^{-1} and 7.5 kV

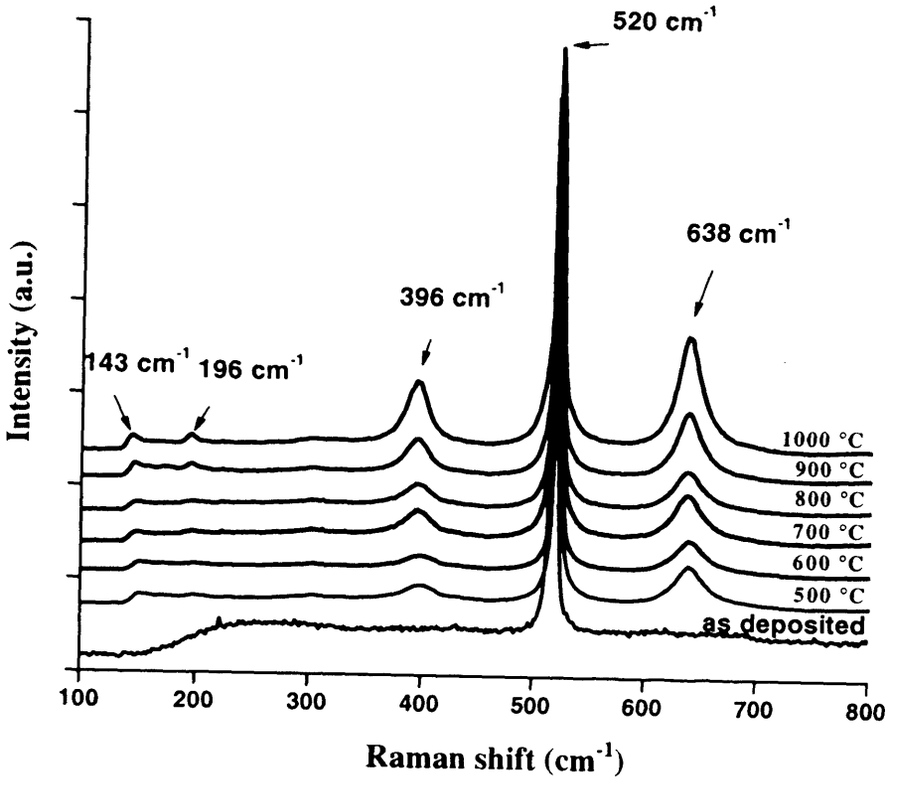

Figure 6.11 Raman spectra of TiO_2-N1 films annealed to different temperatures

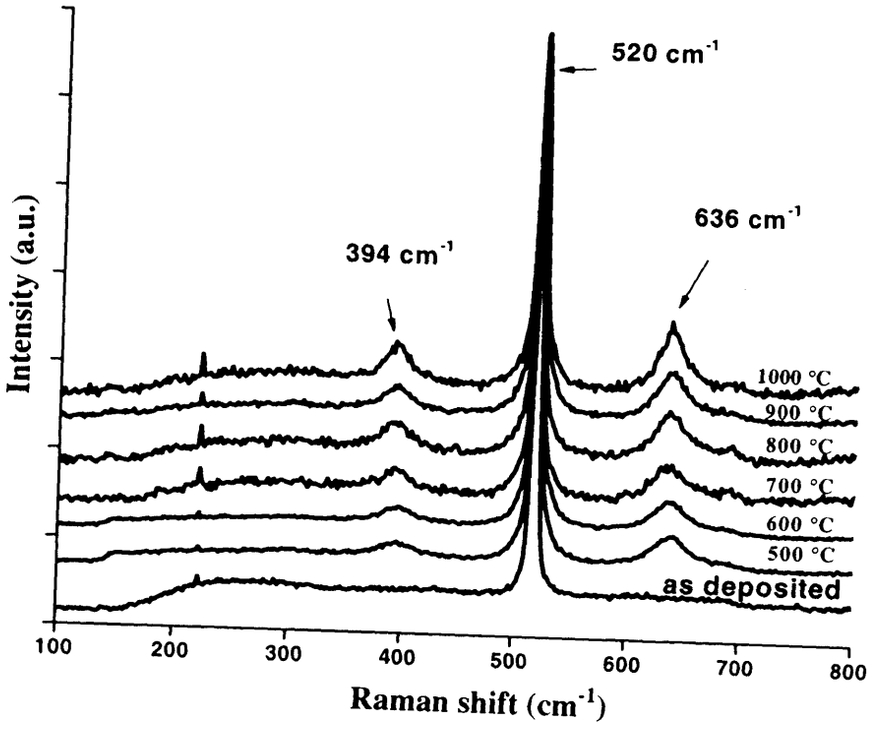

Figure 6.12 Raman spectra of TiO_2-N2 films annealed to different temperatures

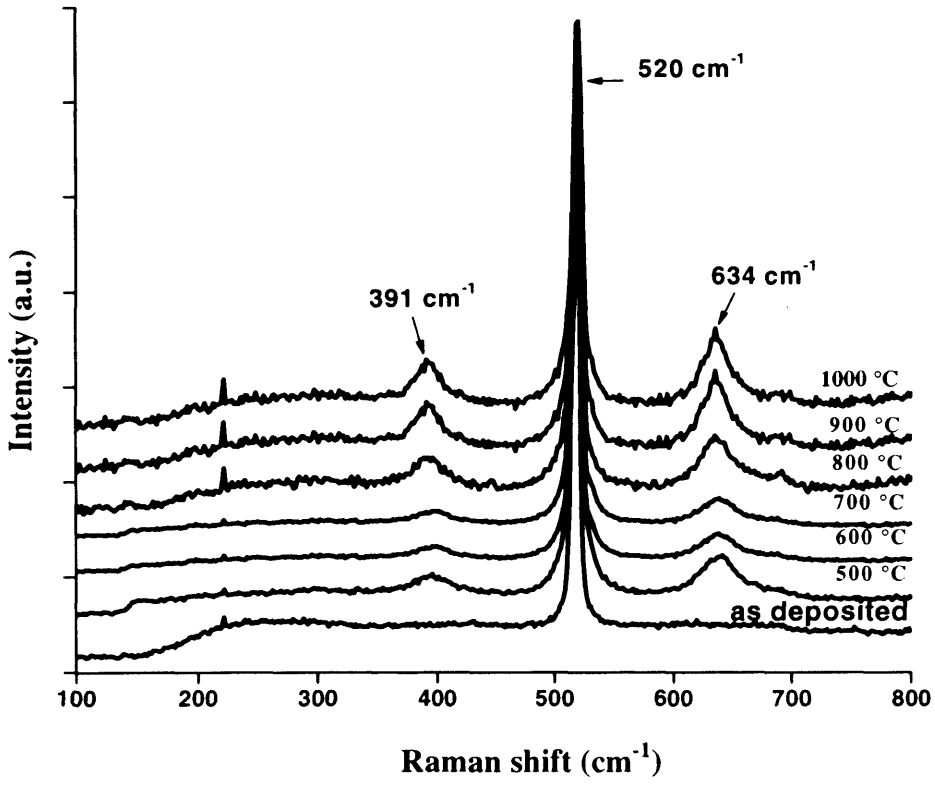

Figure 6.13 Raman spectra of TiO_2-N3 films annealed to different temperatures

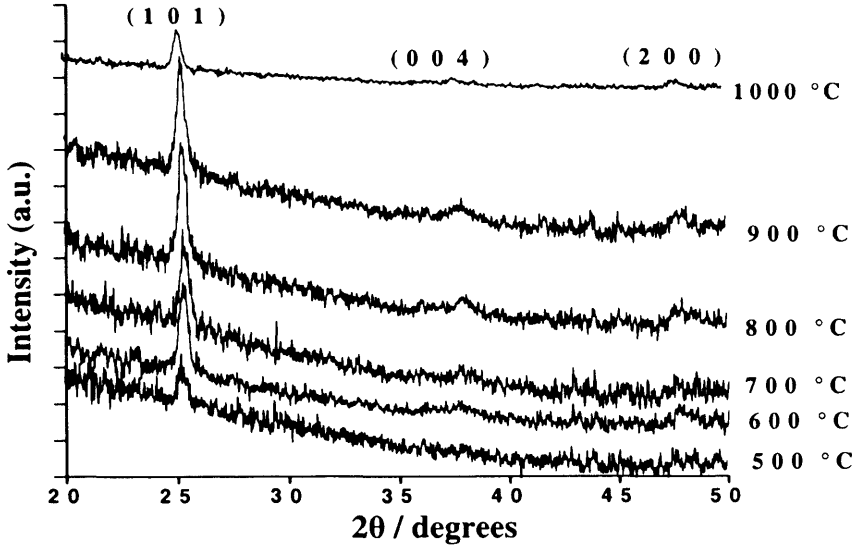

Figure 6.14 X-ray diffraction of TiO_2-N2 films annealed to different temperatures

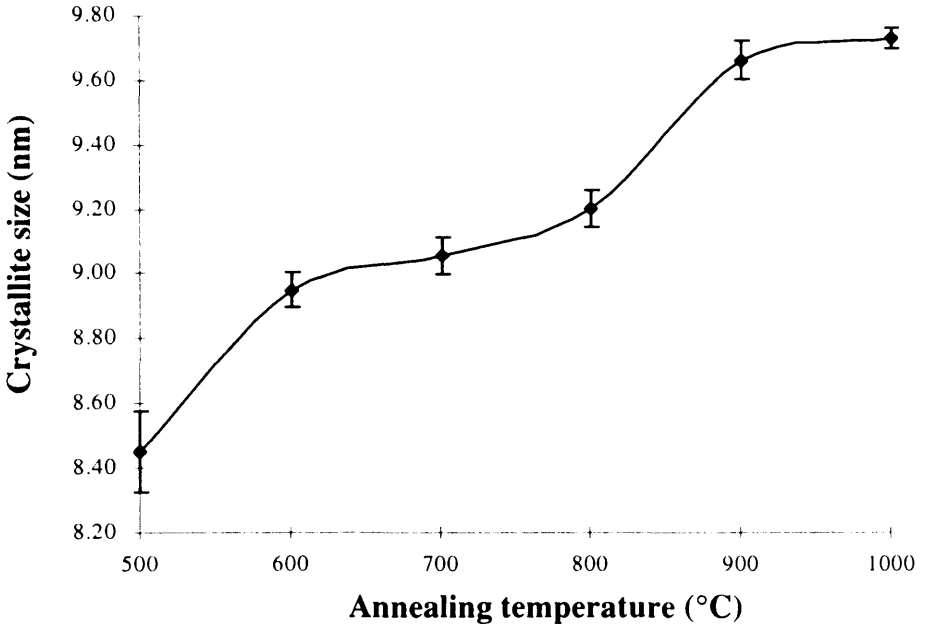

Figure 6.15 Variation of crystallite size with annealing temperature for TiO_2-N2 films

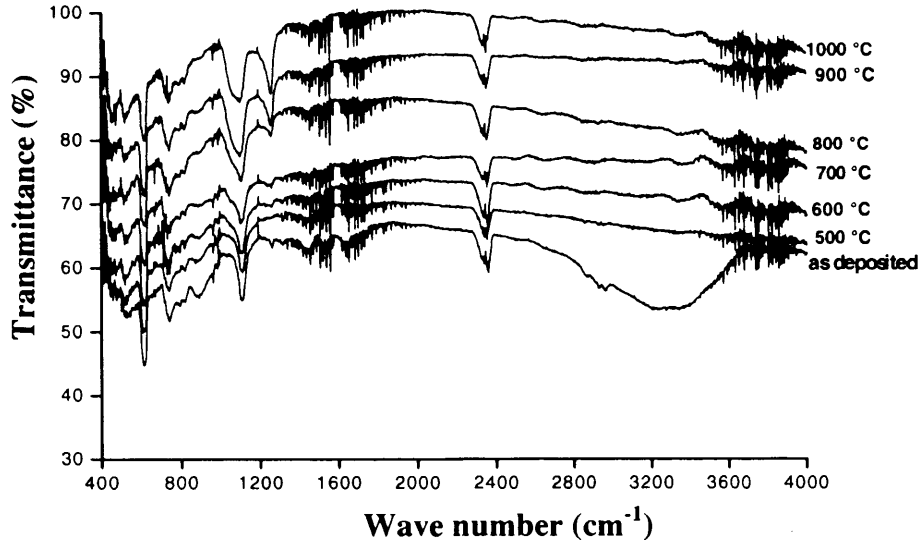

Figure 6.16 FTIR studies of TiO_2-N1 films annealed at different temperature

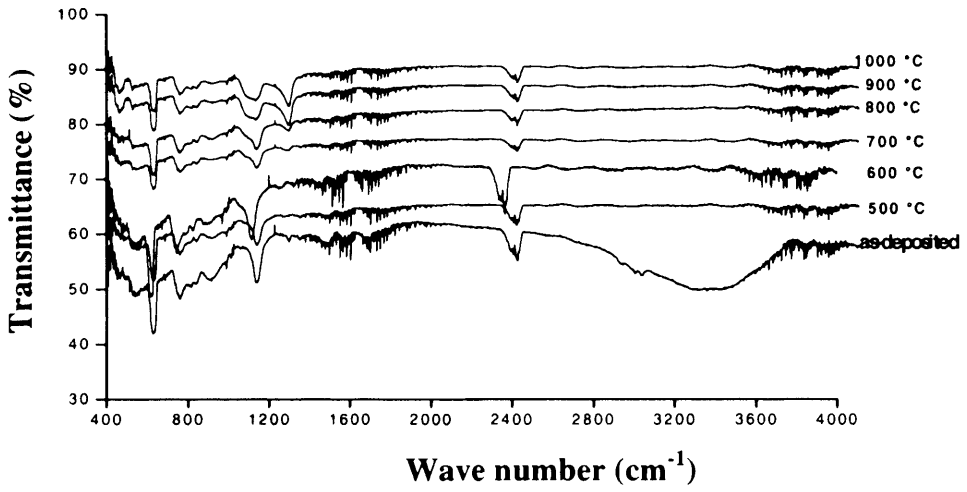

Figure 6.17 FTIR studies of TiO_2-N2 films annealed at different temperature

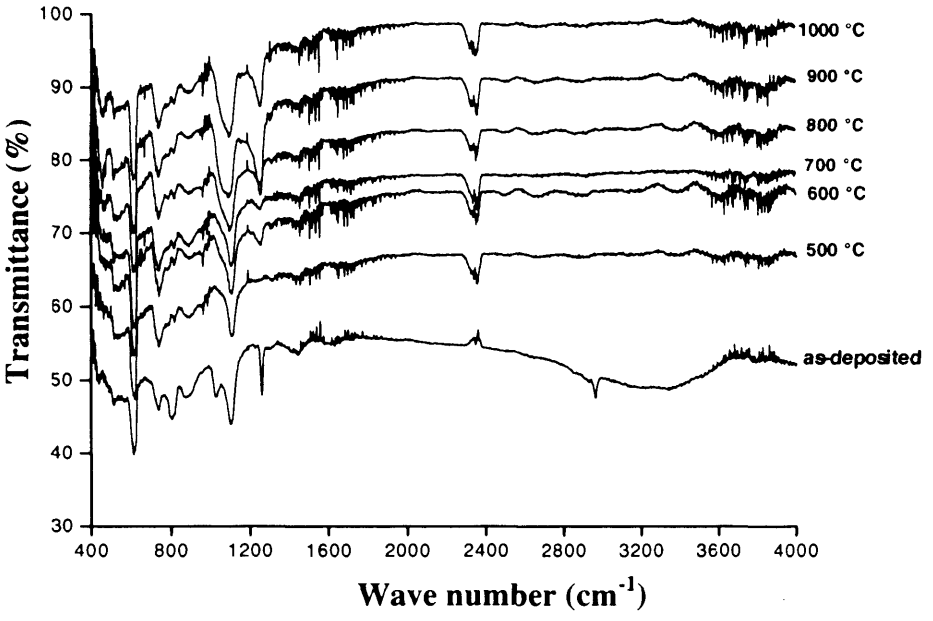

Figure 6.18 FTIR studies of TiO_2-N3 films annealed at different temperature

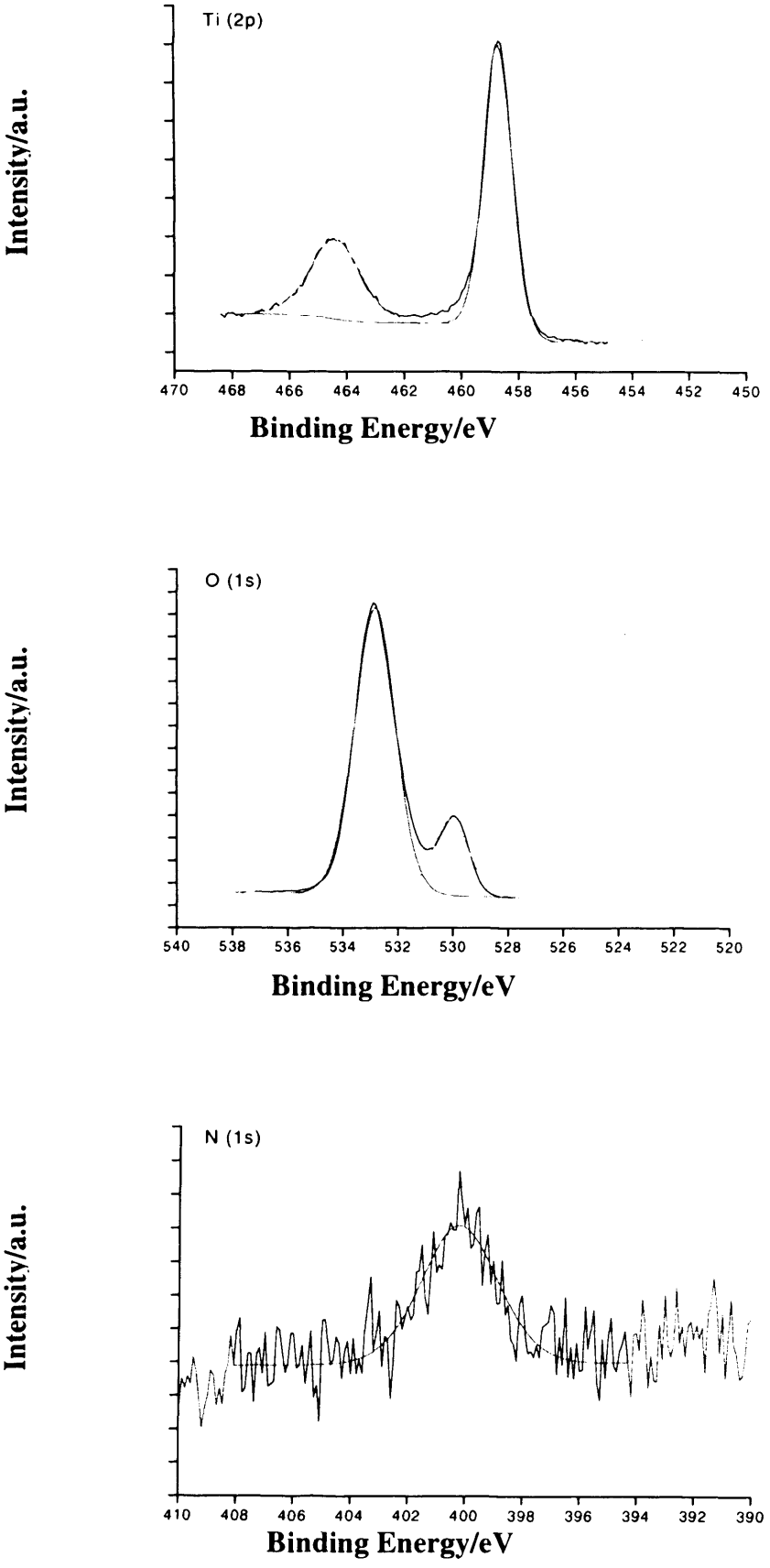

Figure 6.19 XPS high resolution plots for TiO_2-N1 films

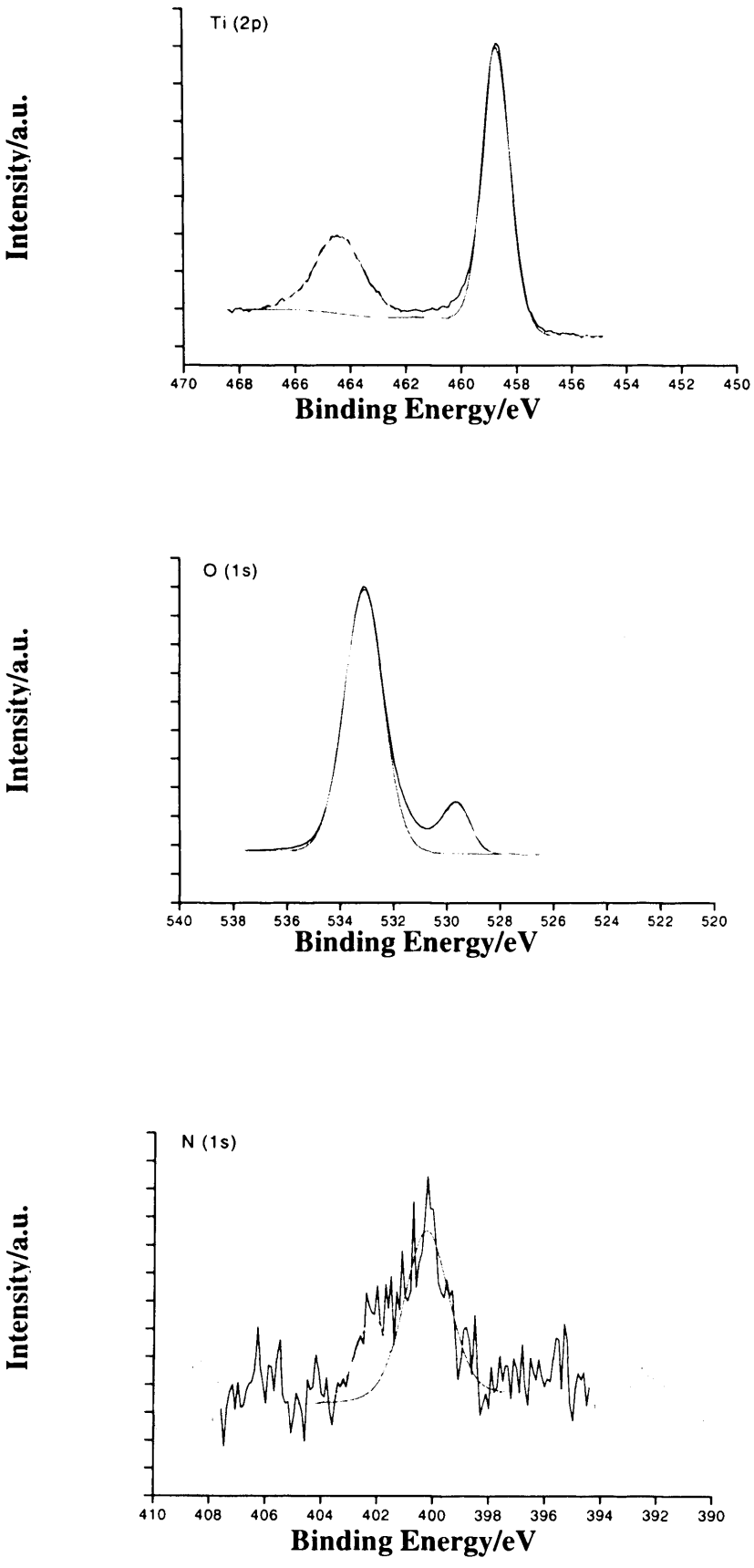

Figure 6.20 XPS high resolution plots for TiO_2-N2 films

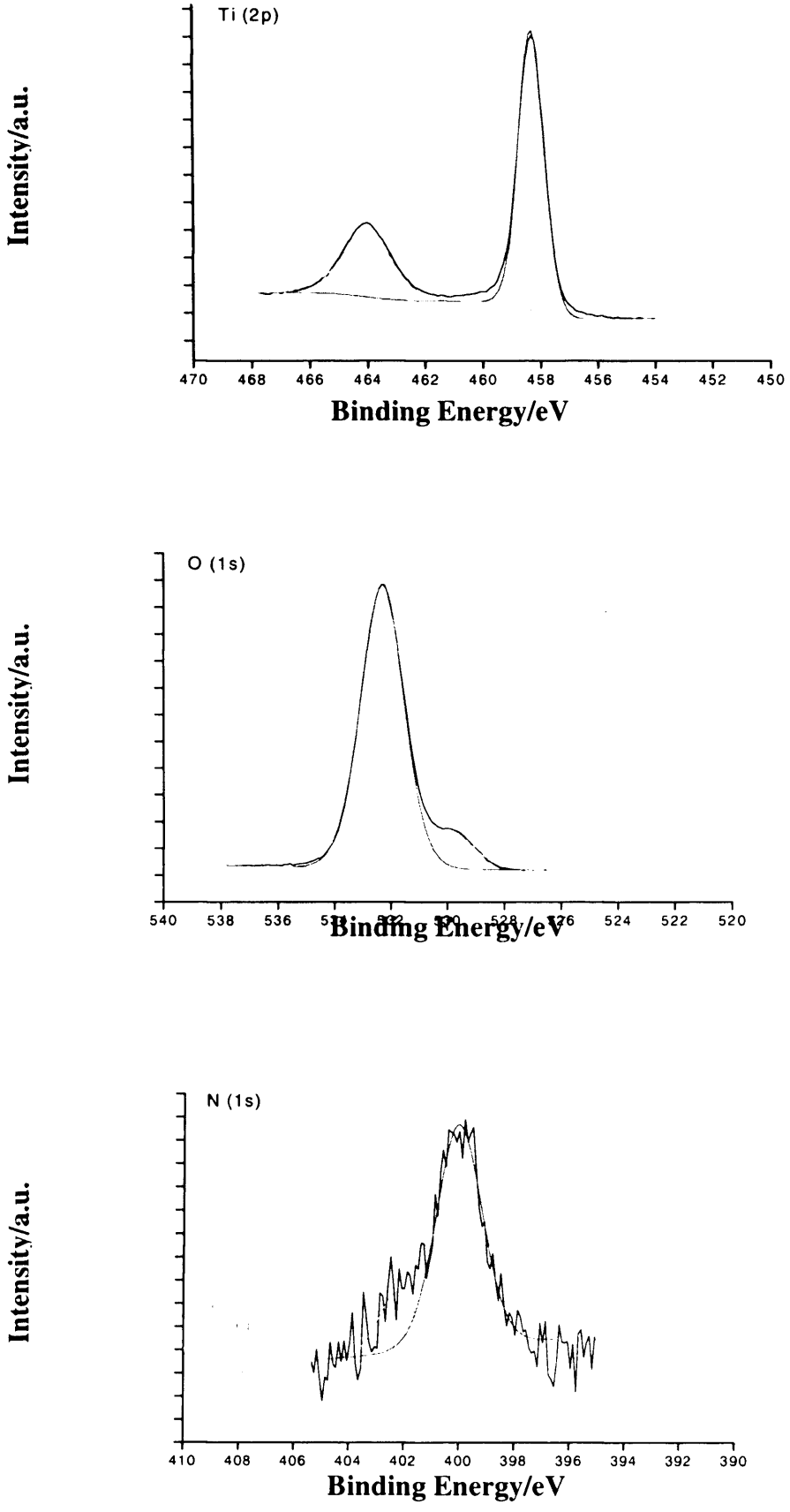

Figure 6.21 XPS high resolution plots for TiO_2-N3 films

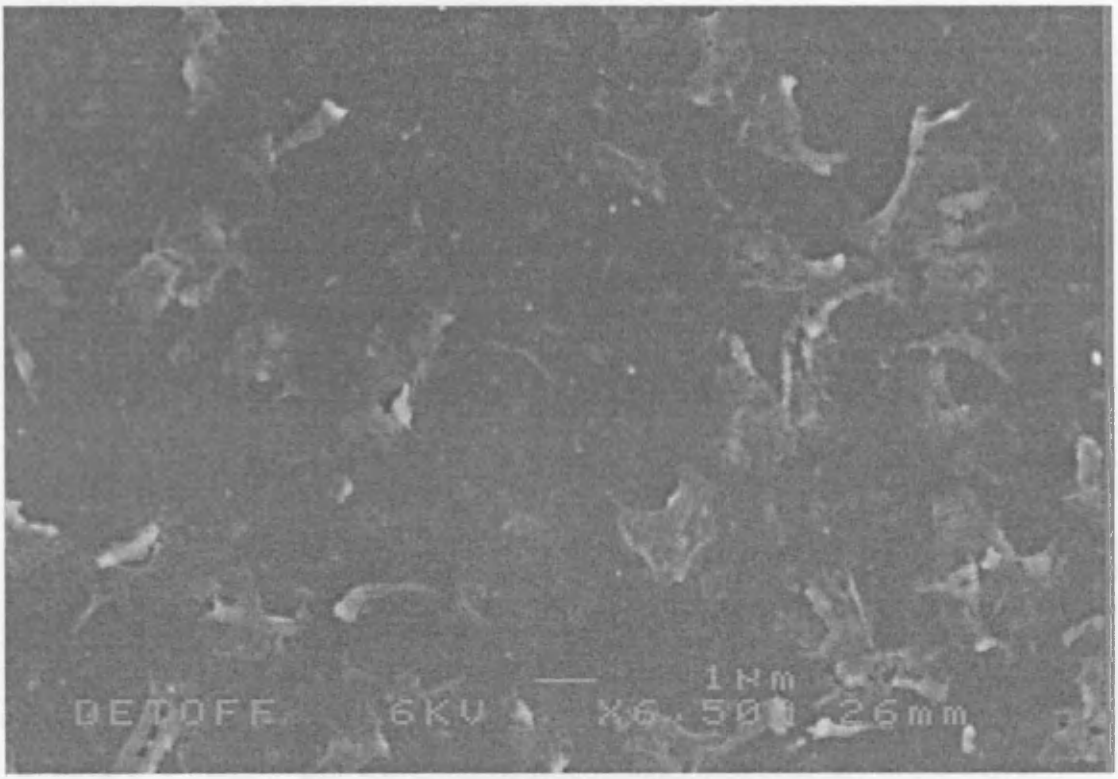

Figure 6.22 SEM image of TiO_2-N2 film electrohydrodynamically processed at 0.67×10^{-10} m^3s^{-1} and 3.9 kV on Si substrate annealed at 500 °C (magnification ×6500)

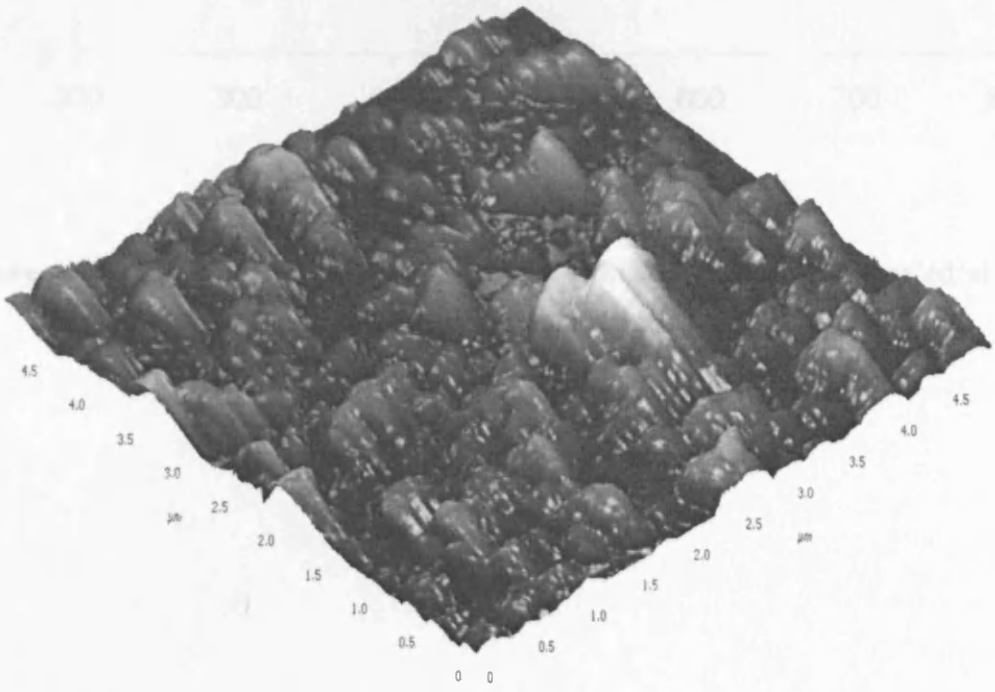

Figure 6.23 AFM image of TiO_2-N2 film electrohydrodynamically processed at 0.67×10^{-10} m^3s^{-1} and 3.9 kV on Si substrate annealed at 500 °C

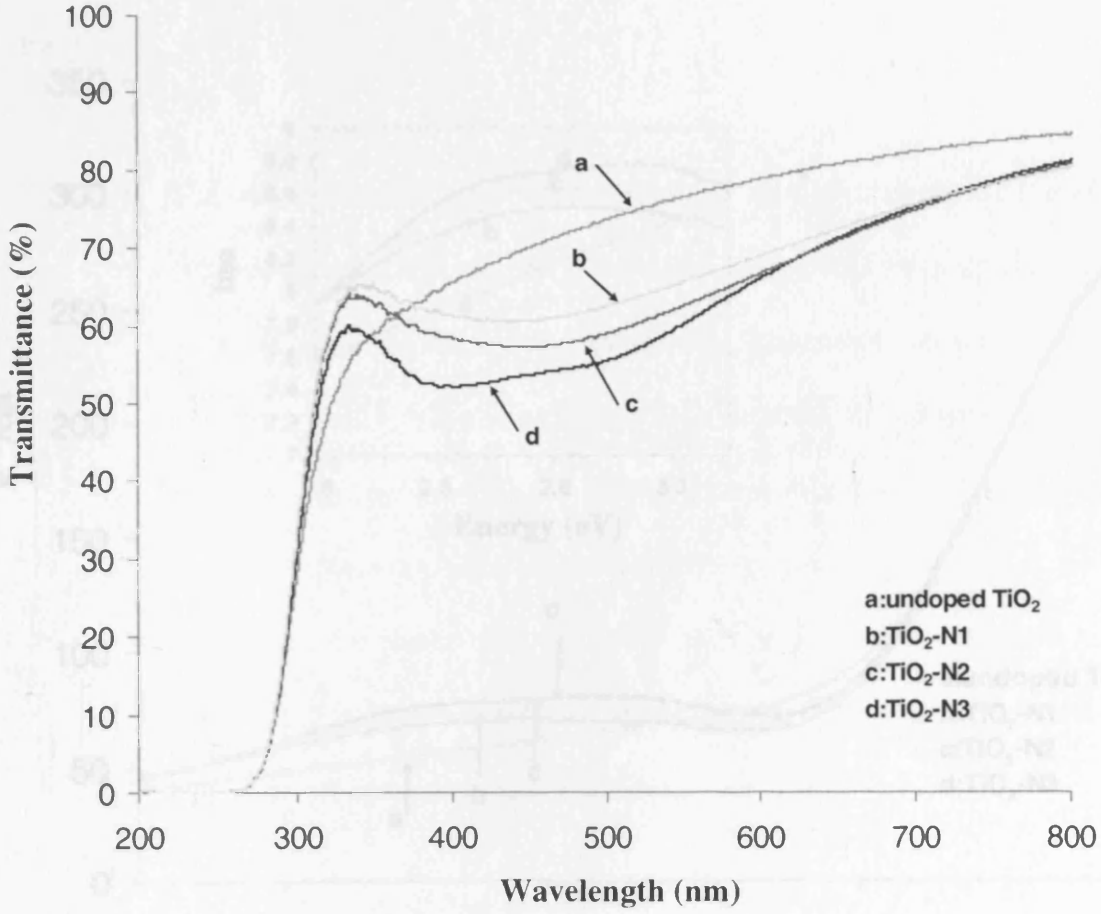

Figure 6.24 Optical transmittance spectra of N-doped TiO_2 films annealed at 500 °C

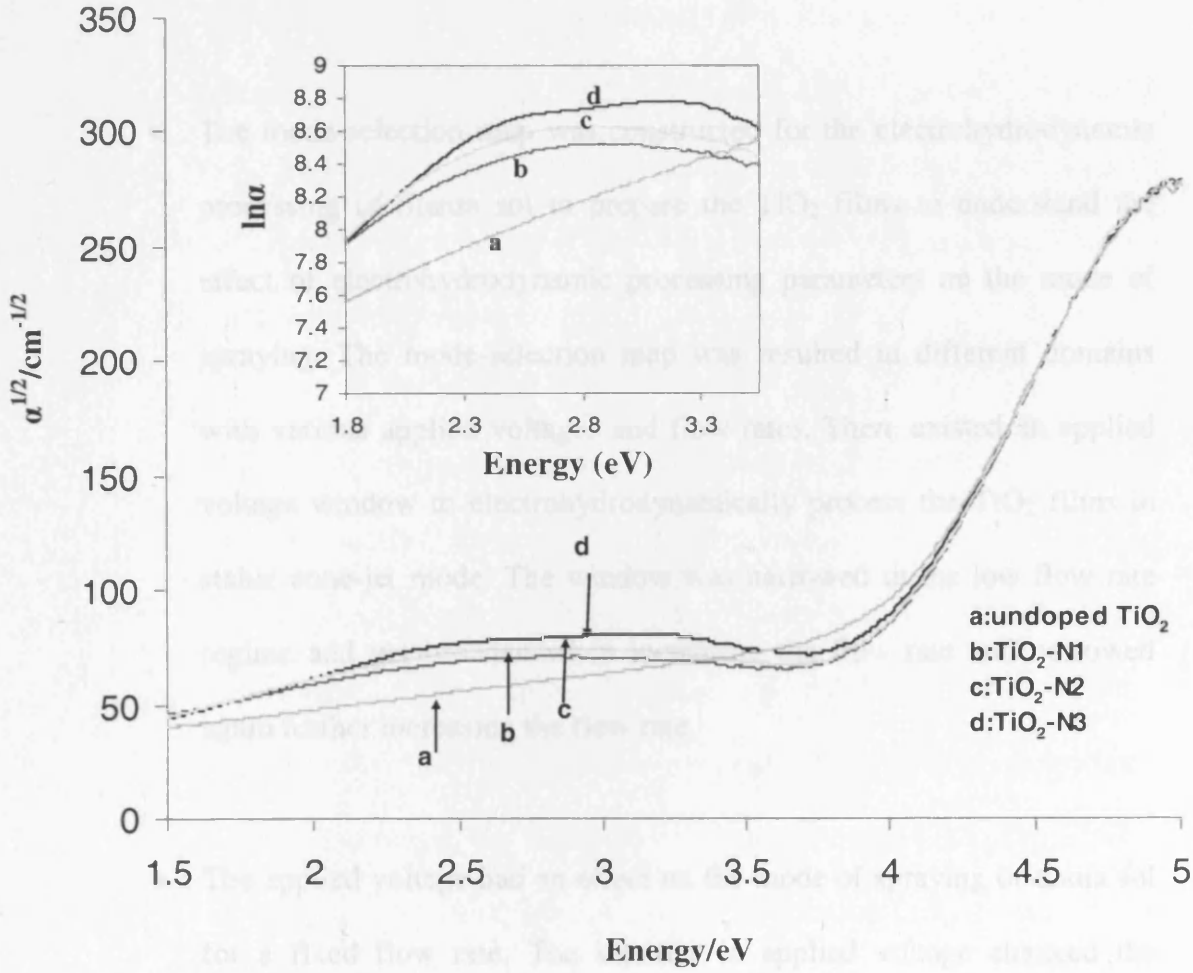

Figure 6.25 Graph of $\alpha^{1/2}$ vs. hγ for undoped TiO_2, TiO_2-N1, TiO_2-N2 and TiO_2-N3 The inset is lnα vs.hγ curves of the films

CHAPTER 7

Conclusions and Future Work

7.1 Conclusions

The following conclusions are drawn from the investigations carried out in this research.

- The mode-selection map was constructed for the electrohydrodynamic processing of titania sol to prepare the TiO_2 films to understand the effect of electrohydrodynamic processing parameters on the mode of spraying. The mode-selection map was resulted in different domains with various applied voltages and flow rates. There existed an applied voltage window to electrohydrodynamically process the TiO_2 films in stable cone-jet mode. The window was narrowed in the low flow rate regime and get broaden when increasing the flow rate and narrowed again further increasing the flow rate.

- The applied voltage had an effect on the mode of spraying of tiania sol for a fixed flow rate. The increase in applied voltage changed the operating modes from dripping, micro-dripping, unstable, stable and multi-jet for a fixed flow rate. The flow rate had an effect on the shape of the stable cone obtained at a fixed applied voltage. The increase in flow rate resulted in increase in depth of the cone at a fixed applied voltage. The droplets and relics obtained in stable cone-jet mode spraying showed a near mono-disperse characteristics with the mean droplet size of 1.9 μm.

- The structural characterisation of electrohydrodynamically processed TiO_2 films revealed the well defined phases of nanocrystalline TiO_2 films. The annealing temperature played a role in the phases obtained in the TiO_2 films. Increasing the annealing temperature changed the phase from the anatase to rutile. The surface morphology studies showed dense, crack free surface and nanocrystalline grains could be obtained in electrohydrodynamic processing. These are showing that the electrohydrodynamic processing in stable cone-jet mode could be used in preparing the nanocrystalline TiO_2 films with the good structural and surface textural features.

- The electrical characterisation of electrohydrodynamically processed TiO_2 films was reported in this research. The capacitance-voltage graphs of the prepared MOS capacitor showed three distinct regions named the accumulation, depletion and inversion. The dielectric constant was obtained from the maximum accumulation capacitance was ~7. The annealing temperature had an effect on dielectric constant of the films. Increasing the annealing temperature decreased the dielectric constant of the films due to the growth of interfacial SiO_2 layer between the substrate and the TiO_2 film. The leakage current-bias voltage characterisation showed a leaky behaviour for the as-deposited films and improved for the annealed films. The annealing temperature had an effect on leakage current density of the films. The films annealed at 600 °C showed a lower leakage current density compared to the films annealed 500 °C.

- The optical characterisation of the processed TiO_2 films showed good transmittance features in the visible light region. The transmittance was dropped when reducing the wavelength of the light. The annealing temperature had an effect on transmittance of the TiO_2 films. These were due to macro and micro structural changes in the films during annealing. The calculated energy bandgap of the processed TiO_2 films was ~3.5 eV for indirect transition. The energy bandgap of the films were not changed significantly with the annealing temperature, however a slight decrease in the bandgap was observed with the increase in annealing temperature.

- A novel electrohydrodynamic processing of N-doped TiO_2 films was demonstrated in this research. The N-doped TiO_2 films were prepared in electrohydrodynamic processing route for the first time. The electrohydrodynamic processing was achieved for all three sols with various nitrogen concentrations. The mode-selection map was drawn to choose the right processing conditions for the stable cone-jet mode processing. The mode-selection maps were constructed for the electrohydrodynamic processing in the metal clamped needle set-up and the normal set-up with various applied voltages and flow rates.

- The mode-selection map for the two set-ups resulted in the various mode of spraying domains with defined boundaries. The operating voltage windows for the metal clamped set-up showed a significant change compared to the normal set-up due to electric field modulation

between the needle and the ground plate. The applied voltage had an effect on mode of spraying for a fixed flow rate. The increase in applied voltage resulted in dripping, micro-dripping, unstable, stable and multi-jet modes.

- It was shown in this research that the metal clamping the needle would increase the coverage area of the films. This is very useful for preparing the films with a wider coverage area in the electrohydrodynamic processing route even at low flow rate regimes. The stable cone-jet spray angle for the metal clamped needle was increased by 1.75 times than the normal set-up needle.

- The structural characterisation of the processed N-doped films revealed the films consisted of the anatase phase. The nitrogen doping concentration had an effect on structural features of the prepared TiO_2 films. The increase in doping concentration retarded the phase formation of TiO_2 films. There was no rutile phase or TiN observed in all processed films even at higher annealing temperatures. The morphological studies showed the N-doped TiO_2 films contained dense and crack free surfaces.

- The optical characterisation of N-doped TiO_2 films showed a drop in transmittance in the visible light region. The nitrogen doping concentration had an effect on transmittance of the prepared films. The increase in doping concentration lowered the transmittance in the visible

light region. The calculated energy bandgap of the films was ~3.50 eV for indirect transition. The analysis of Urbach's tail effect showed the nitrogen doping created the localised states within the energy bandgap and this was the reason behind the absorption of visible light of the N-doped TiO_2 films.

- The novel electrohydrodynamically processed N-doped TiO_2 films could be used in many applications including the following.

  1) They could be applied to hospital floor and wall tiles to reduce the surface and airborne bacteria with the use of interior lighting.

  2) They could be deposited in self-cleaning glasses used in structural and decorative applications where cleaning is difficult.

  3) They could be also used in interior of the vehicles such as cars and vans to reduce the odour caused by cigarette smoke.

7.2 Future work

The research carried out in this thesis produced some exceptional results and offering the electrohydrodynamic processing route could be used for preparing films with very good properties. To further exploit this interesting and exciting area of research the following recommendations for the future work are given below.

- The mechanical properties of electrohydrodynamically processed TiO_2 films should be evaluated like the electrical and optical properties since the TiO_2 films could be used in biomedical implants due to its biocompatibility, chemical inertness and non-toxic nature. It is a promising material to use as a wear resistant with good tribological properties. Therefore, the nanoindentation and the scratch test should be done to find out the hardness and the adhesion property of the deposited TiO_2 films.

- The rapid thermal annealing in O_2 atmosphere should be carried out instead of conventional annealing to the electrohydrodynamically processed TiO_2 films to further improve the electrical properties of the films particularly the dielectric constant of the prepared films. The conventional annealing exposed the prepared films to longer time and promoted the growth of SiO_2 interfacial layer during the annealing. The rapid thermal annealing can help to reduce the interaction at the interface.

- The electrohydrodynamic processing route should be used to produce the TiO_2 and the N-doped TiO_2 particles in the future. Since the flow rate is proportional to the droplet size of the produced spray, the particle size could be controlled and produced in the range of micron to nano-meter. The particle size could be also varied by changing the sol concentration that is being electrohydrodynamically processed. A slight modification in the set-up used in this research by incorporating a heater near to the collection point of the droplets or surrounding the droplet formation zone these particles could be produced. These particles are very useful for

photocatalysis especially in the textile industries for the degradation of used dyes and the waste water treatment.

- The porous TiO_2 films with excellent pore size control could be processed in the electrohydrodynamic route. The use of templating agent (eg: polymeric binder) with the titania sol can aid the preparation of micro, meso and macro porous TiO_2 films. The uniform porous TiO_2 films could be prepared because of near mono-disperse droplets produced in the stable cone-jet mode of processing. This research will be challenging and fascinating as polymeric binder will alter the physical properties of the sol particularly the viscosity come in to play the dominant role. The careful study of this could lead to prepare the uniform porous TiO_2 films. These films are very useful in gas sensors and capturing CO_2 gas which are crucial to the next generation technologies. The same method should be employed to prepare the porous TiO_2 particles by slightly modifying the processing conditions mentioned above.

- The electrohydrodynamic processing of TiO_2 and mixed oxides like alumina, silica and zirconia should be investigated. This mixed oxide composite can improve the mechanical strength, thermal stability and surface area of doped titania. The high hardness alumina mixed with titania is very useful for thermal shock resistance, micro-hardness and wear resistance. Therefore, the textural and structural property variations in titania with varying amounts of other oxides should be carefully studied.

- The feasibility study should be conducted to process the TiO_2 and N-doped TiO_2 incorporated textile materials like silk and wool. The silk and wool are textile materials valued for their strength, warmth, water resistance and texture. But they are lack in stain resistance. To improve the stain resistance TiO_2 and N-doped TiO_2 could be included in these materials and should be tested for their stain degradation ability under solar light. This is very useful for the textile industries.

- The electrohydrodynamically processed TiO_2 and N-doped TiO_2 films should be deposited in various substrates and studied for the photocatalytic degradation of dyes under the visible and uv light. The influence of crystal structure, particle size, surface area and porosity of the films on various substrates should be investigated in detail and the comparison between them should be made to evaluate the maximum photocatalytic efficiency. The film -substrate coupled system could also be tested for their reaction efficiency.

- The TiO_2 fibers with controllable size and shape could be processed by adjusting the sol properties. When the applied electric field overcomes the surface tension of the liquid a continuous jet is ejected which upon subsequent solvent evaporation and bending produces the fibers. Here, the technique is referred as electrospinning. The fibers could be produced by increasing the viscosity of the sol either by increasing the precursor concentration or increasing the polymeric binder concentration. The fibers with core-sheath, hollow and porous structures also processed by varying

the composition of the sol. These fibers with high surface area to volume ratio have a great potential and play a vital role in photonics, nanoelectronics and data storage.

- Another possible and interesting area of research might arise introducing an UV lamp in to the electrohydrodynamic processing set-up. There is a possibility to process new polymeric materials using the electrohydrodynamic route and induce a polymerisation simultaneously by using the UV light. Here, the idea is to start the photochemical and chemical reactions in the organic materials while processing. The solvent evaporation could also be facilitated by the UV light. This new technique will give a new dimension to the electrohydrodynamic processing and offer some significant contributions to a wide variety of industries.

- The electrohydrodynamic processing route should be incorporated with a three dimensional printing to print and pattern the quantum dots using the stable cone-jet mode. This could be achieved by keeping the substrates above the jet break up point where the stable jet will impinge on the substrates to form well defined structures. The printable patterns could be extended to printing conducting tracks, nano-wires, nano-ribbons and nano-rods. These are the emerging technologies and have a great potential in photonic and electronic applications.

- The composite materials could be processed by the electrohydrodynamic route through employing two needle set-ups. The usage of two needles positioned one inside the other and a set of immiscible liquids pumped into each needle could be help to form the composite materials. For a certain range of values of the electrical potential and flow rates, a stable cone forms at the exit of individual needles will result in atomisation of each materials. This set-up could be extended to process the fiber composite materials by pumping the viscous liquid in the outer needle. A wide variety of composites including metal-ceramic, metal-polymer, polymer-polymer and ceramic-ceramic composites could be processed by carefully studying the processing conditions. As an example the carbon nanotubes on the polymer matrices could be processed and it has a potential being used as a structural materials due to its higher mechanical strength arising from the carbon nanotubes.

- The two needle set-up should also be investigated to process the encapsulated drugs for controlled release. The controlled drug delivery is very important in curing certain diseases and eliminating the chances of under and over dosing the patients. It could be processed by encapsulating the specific drug by a biocompatible material in a way that the drug is released from the material in an appropriate manner. More detail study must be done to assess the processing viability of encapsulated drugs for controlled release.

- The two needle set-up has to be further modified to incorporate several needles of small size within a larger size needle. This could result in encapsulating a different variety of materials inside a microstructure. These are very useful in protecting the core from the pollution, decreasing the adverse effects on environment from poison, shielding smells, and controlling the release of the substance.

- More studies should be carried out to deposit metal, semiconductor, biological and organic nanoparticles by electrohydrodynamic processing route. The nanoparticles are very fine particles with high surface area and their physical properties are intermediate between those of the bulk solid and molecules. The physical properties of the various systems will determine their viability to be processed in the electrohydrodynamic route. For an example the conductivity of the metals are commonly high and their processing may be challenging therefore careful studies should be done.

- The future investigation should also be done in reducing the spray angle of the produced electrospray in stable cone-jet mode. For certain applications like coating a complex component or hidden areas of a component, the narrower spray would be an advantage. The produced electrospray could be narrowed by attaching a non conducting plate to the needle and might reduce the electric field effect surrounding the needle. A thorough investigation should be carried out to find out the spraying conditions in terms of the applied voltage and the flow rate.

- The electrohydrodynamic processing of multilayer films should be investigated. These multilayer films could be processed by employing the multi nozzles with a rotating ground plate set-up. A systematic study should be done in using the multi nozzle set-up since droplet trajectory, the recombination of droplets, and other interactions between the charged droplets might result when processing the different materials. The electric field effect is high when using the multi nozzle set-up compared to single nozzle set-up. The processing of multi layer film could be challenging because depositing one layer by other may reduce the electric field effect between the nozzle and the ground plate. This research might lead to a new way to produce multi layer thin films and these multilayer films are promising in controlled drug delivery applications. The multi nozzle set-up also very useful in scaling up of the electrohydrodynamic processing route.

REFERENCES

Abbas, M.A., and Latham, J. (1967): The instability of evaporating charged drops. *Journal of Fluid Mechanics* **30** 663-670.

An, M.H. (2005): Composition, structural, and electrical investigations on DC-magnetron-sputtered TiO_2 thin films. *Journal of the Korean Physical Society* **47** 853-857.

Asahi, R., Morikawa, T., Ohwaki, T., Aoki, K., and Taga, Y. (2001): Visible-light photocatalysis in nitrogen-doped titanium oxide. *Science* **293** 269-271.

Bailey, A.G. (1988): Electrostatic spraying of liquids. John Wiley & Sons, New York.

Balachandran, W., Machowski, W., and Ahmad, C.N. (1994): Electrostatic atomization of conducting liquids using AC superimposed on DC fields. *IEEE Transactions on Industry Applications* **30** 850-855.

Balachandran, W., Ahmad, C.N., and Machowski, W. (1992): Electrostatic atomization of conducting liquids using AC superimposed on DC field. *Conference record of the 1992 IEEE industry applications society annual meeting* **2** 1369-1373.

Baur, W.H. (1961): Atomabstande und Bindungswinkel im Brookit, TiO_2. *Acta Crystallographica* **14** 214-216.

Borra, J.P., Tombette, Y., and Ehouarn, P. (1999): Influence of electric field profile and polarity on the mode of EHDA related to electric discharge regime. *Journal of Aerosol science* **30** 913-925.

Bose, G. M. (1745): Recherches sur la Cause et sur la veritable Theorie de l'Electricite. *Wittenberg*.

Campbell, S.A., Gilmer, D.C., Wang, X.C., Hsieh, M.T., Kim, H.S., Gladfelter, W.L., and Yan, J.H. (1997): MOSFET transistors fabricated with high permittivity TiO_2 dielectrics. *IEEE Transactions on Electron Devices* **44** 104-109.

Capan, R., Chaure, N.B., Hassan, A.K., and Ray, A.K. (2004): Optical dispersion in spun nanocrystalline titania thin films. *Semiconductor Science and Technology* **19** 198-202.

Chen, C.H., Emond, M.H.J., Kelder, E.M., Meester, B., and Schoonman, J. (1999): Electrostatic sol-spray deposition of nanostructured ceramic thin films. *Journal of Aerosol Science* **30** 959-967.

Chen, C.H., Kelder, E.M., van der Put, P.J.J.M., and Schoonman, J. (1996): Morphology control of thin $LiCoO_2$ films fabricated using the electrostatic spray deposition (ESD) technique. *Journal of Materials Chemistry* **6** 765-771.

Chen, D. R., Pui, D. Y. H., and Kaufman, S. L. (1995): Electrospraying of conducting liquids for monodisperse aerosol generation in the 4 nm to 1.8 μm

diameter range. *Journal of Aerosol Science* **26** 963-977.

Chen, D.R., and Pui, D.Y.H. (1997): Experimental investigation of scaling laws for electrospraying: Dielectric constant effect. *Aerosol Science and Technology* **27** 367-380.

Chen, X.B., Lou, Y.B., Samia, A.C.S., Burda, C., and Gole, G.L. (2005): Formation of oxynitride as the photocatalytic enhancing site in nitrogen-doped titania nanocatalysts: Comparison to a commercial nanopowder. *Advanced Functional Materials* **15** 41-49.

Chen, X.Y., and Liu, S.X. (2007): Preparation and characterization of S-doped Ti1-xSyO2 photocatalyst with wide range light response. *Acta Physio-Chimica Sinica* **23** 701-708.

Chong, L.H., Mallik, K., Groot, C.H., Kersting, R. (2006): The structural and electrical properties of thermally grown TiO_2 thin films. *Journal of Physics: Condensed Matter* **18** 645-657.

Choy, K.L. (2002): Innovative processing of films and nanocrystalline powders. Imperial College Press, London.

Clark, R.J.H. (1968): The chemistry of titanium and vanadium: An introduction to the chemistry of the early transition elements. Elsevier, Amsterdam.

Cloupeau, M., and Prunet-Foch, B. (1989): Electrostatic spraying of liquids in cone-jet mode. *Journal of Electrostatics* **22** 135-159.

Cloupeau, M., and Prunet-Foch, B. (1990): Electrostatic spraying of liquids: Main functioning modes. *Journal of Electrostatics* **25** 165-184.

Cong, Y., Zhang, J.L., Chen, F., and Anpo, M. (2007): Synthesis and characterisation of nitrogen-doped TiO_2 nanophotocatalysts with high visible light activity. *Journal of Physical Chemistry C* **111** 6976-6982.

Cromer, D.T., and Herrington, K. (1955): The structures of anatase and rutile. *Journal of the American Chemical Society* **77** 4708-4709.

Cullity, B.D. (1978): Elements of x-ray diffraction. Adison-Wesley, Reading.

Czanderna, A.W., Rao, C.N.R., and Honig, J.M. (1958): The anatase-rutile transition .1. Kinetics of the transformation of pure anatase. *Transactions of the Faraday Society* **54** 1069-1073.

Davies, J.T., and Rideal, E.K. (1961): Interfacial Phenomena, Academic, New York.

De la Mora, J.F. (1992): The effect of charge emission from electrified liquid cone. *Journal of Fluid Mechanics* **243** 561-574.

De la Mora, J.F., and Loscertales, I.G. (1994): The current emitted by highly conducting Taylor cones. *Journal of Fluid Mechanics* **260** 155-184.

Drozin, V. G. (1955): The electrical dispersion of liquids as aerosols. *Journal of Colloidal Science* **10** 158-164.

Duenas, S., Castan, H., Garcia, H., San Andres, E., Toledano-Luque, M., Martil, I., Gonzalez-Diaz, G., Kukli, K., Uustare, T., and Aarik, J (2005): A comparative study of the electrical properties of TiO_2 films grown by high-pressure reactive sputtering and atomic layer deposition. *Semiconductor Science and Technology* **20** 1044-1051.

Dutta, S., Chattopadhyay, S., Sutradhar, M., Sarkar, A., Chakrabarti, M., Sanyal, D., and Jana, D. (2007): Defects and the optical absorption in nanocrystalline ZnO. *Journal of Physics-Condensed Matter* **19** 236218.

Fenn, J. B., Mann, M., Meng, C. K., Wong, S. F. and Whitehouse, C. M. (1989): Electrospray ionization for mass spectrometry of large biomolecules. *Science* **246** 64 – 71.

Fujishima, A., and Honda, K. (1972): Electrochemical photolysis of water at a semiconductor electrode. *Nature* **238** 37-38.

Fuyuki, T., and Matsunami, H. (1986): Electronic properties of the interface between Si and TiO_2 deposited at very low temperatures. *Japanese Journal of Applied Physics* **25** 1288-1291.

Ganan-Calvo, A.M., Lasheras, J.C., Davila, J., and Barrero, A. (1994): The electrostatic spray emitted from an electrified meniscus. *Journal of Aerosol Science* **25** 1121-1142.

Garcia Sole, J., Bausa, L.E., and Jaque, D. (2005): An introduction to the optical spectroscopy of inorganic solids. John Wiley & Sons, New York.

Ge, L., Xu, M.X., Sun, M., and Fang, H.B. (2006): Low-temperature synthesis of photocatalytic TiO_2 thin film from aqueous anatase precursor sol. *Journal of Sol-Gel Science and Technology* **38** 47-53.

Grace, J.M., and Marijnissen, J.C.M. (1994): A review of liquid atomization by electrical means. *Journal of Aerosol Science* **25** 1005-1019.

Gratzel, M. (2003): Dye-sensitized solar cells. *Journal of Photochemistry and Photobiology* **4** 145-153.

Grigoriev, D.A., and Edirisinghe, M.J. (2002): Evaporation of liquid during cone-jet mode electrospraying. *Journal of Applied Physics* **91** 437-439.

Gyorgy, E., Del Pino, A.P., Serra, P., and Morenza, J.L. (2002): Surface nitridation of titanium by pulsed Nd:YAG laser irradiation. *Applied Surface Science* **186** 130-134.

Han, S.M., and Aydil, E.S. (1997): Detection of combinative infrared absorption bands in thin silicon dioxide films. *Applied Physics Letters* **70** 3269-3271.

Hartman, R. P. A. (1998): Electrohydrodynamic atomization in the cone-jet mode: from physical modeling to powder production. Netherlands organization for scientific research.

Hartman, R.P.A., Brunner, D.J., Camelot, D.M.A., Marijnissen, J.C.M., and Scarlett, B. (1999): Electrohydrodynamic atomization in the cone-jet mode physical modeling of the liquid cone and jet. *Journal of Aerosol Science* **30** 823-849.

Hartman, R.P.A., Brunner, D.J., Camelot, D.M.A., Marijnissen, J.C.M., and Scarlett, B. (2000): Jet break-up in electrohydrodynamic atomization in the cone-jet mode. *Journal of Aerosol Science* **31** 65-95.

Hayati, I., Bailey, A. I., and Tadros, T. F. (1987): Investigations into the mechanisms of electrohydrodynamic spraying of liquids. *Journal of Colloidal Interface and Science* **117** 205-221.

Higuera, F.J. (2003): Flow rates and electric current emitted by a Taylor cone. *Journal of Fluid Mechanics* **484** 303-327.

Hirano, M., Nakahara, C., Ota, K., Tanaike, O., Inagaki, M. (2003): Photoactivity and phase stability of ZrO_2-doped anatase type TiO_2 directly formed as nanometer-sized particles by hydrolysis under hydrothermal conditions. *Journal of Solid State Chemistry* (2003) **170** 39-47.

Hogan, J. J., and Hendricks, C. D. (1965): Investigation of the charge-to-mass ratio of electrically sprayed liquid particles. *AIAA Journal* **3** 296-301.

Hsu, S.W., Yang, T.S., Chen, T.K., and Wong, M.S. (2007): Ion-assisted electron-beam evaporation of carbon doped titanium dioxide films as visible-light photocatalyst. *Thin Solid Films* **515** 3521-3526.

Huang, D.G., Liao, S.J., and Dang, Z. (2006): Preparation, characterization and photocatalytic performance of anatase F doped TiO_2 sol. *Acta Chimica Sinica* **64** 1805-1811.

Jaworek, A., and Krupa, A. (1996): Generation and characteristics of the precession mode EHD spraying. *Journal of Aerosol Science* **27** 75-77.

Jaworek, A., and Krupa, A. (1999): Classification of the modes of EHD spraying. *Journal of Aerosol Science* **30** 873-893.

Jaworek, A., Adamiak, K., Krupa, A., and Castle G.S.P. (2003): Trajectories of charged aerosol particles near a spherical collector. *Journal of Electrostatics* **51-52** 603-609.

Jayasinghe, S. N., and Edirisinghe, M. J. (2002a): Effect of viscosity on the size of relics produced by electrostatic atomization. *Journal of Aerosol Science* **33** 1379-1388.

Jayasinghe, S.N., Edirisinghe, M.J., and Wilde, T.D. (2002b): A novel ceramic printing technique based on electrostatic atomization of a suspension. *Materials Research Innovations* **6** 92-95.

Jayasinghe, S.N., and Edirisinghe, M.J. (2002c): A novel method of forming open cell ceramic foam. *Journal of Porous Materials* **9** 265-273.

Jayasinghe, S.N., and Edirisinghe, M.J. (2004a): Electrostatic atomisation of a ceramic suspension. *Journal of the European Ceramic Society* **24** 2203-2213.

Jayasinghe, S.N., and Edirisinghe, M.J. (2004b): Electrically forced jets and microthreads of high viscosity dielectric liquids. *Journal of Aerosol Science* **35** 233-243.

Jayasinghe, S.N., and Edirisinghe, M.J. (2005): Electrostatic atomization of a ceramic suspension at pico-flow rates. *Applied Physics A: Materials science & Processing* **80** 399-404.

JCPDS-ICDD 21-1272 database.

Jones, A. R., and Thong, K. C. (1971): The production of charged monodisperse fuel droplets by electrical dispersion. *Journal of Physics D: Applied Physics* **4** 1159-1166.

Justicia, I., Ordejon, P., Canto, G., Mozos, J.F., Fraxedas, J., Battiston, G.A., Gerbasi, R., and Figueras, A. (2002): Designed self-doped titanium oxide thin films for efficient visible-light photocatalysis. *Advanced Materials* **14** 1399-1402.

Karunagaran, B., Kumar, R.T.R., Viswanathan, C., Mangalaraj, D., Narayandass, S. K., and Rao, G.M. (2003): Optical constants of DC magnetron sputtered titanium dioxide thin films measured by spectroscopic ellipsometry. *Crystal Research and Technology* **38** 773-778.

Kelder, E.M., Nijs, O.C.J., and Schoonman, J. (1994): Low temperature synthesis of thin films of YSZ and $BaCeO_3$ using electrostatic spray pyrolysis (ESP). *Solid State Ionics* **68** 5-7.

Kelly, S., Pollak, F.H., and Tomkiewicz, M. (1997): Raman spectroscopy as a morphological probe for TiO_2 aerogels. *Journal of Physical Chemistry B* **101** 2730-2734.

Kim, H.S., Gilmer, D.C., Campbell, S.A., and Polla, D.L. (1996): Leakage current and electrical breakdown in metal-organic chemical vapor deposited TiO_2 dielectrics on silicon substrates. *Applied Physics Letters* **69** 3860-3862.

Kim, M.C., Lee, S.K. and Balachandran, W. (2004): Change of atomization performance with selection of nozzle materials in electrohydrodynamic spraying. *Atomization and Sprays* **14** 175-190.

Kumbar, S.G., Bhattacharyya, S., Senthuraman, S., and Laurencin, C.T. (2007): A preliminary report on a novel electrospray technique for nanoparticle based biomedical implants coatings: Precession electrospraying. *Journal of Biomedical Materials Research Part B-Applied Biomaterials* **81B** 91-103.

Lee, B.H., Jeon, Y., Zawadzki, K., Qi, W.J., and Lee, J. (1999): Effects of interfacial layer growth on the electrical characteristics of thin titanium oxide films on silicon. *Applied Physics Letters* **74** 3143-3145.

Li, S.W., Jayasinghe, S.N., and Edirisinghe, M.J. (2006): Aspirin particle formation by electric-field-assisted release of droplets. *Chemical Engineering Science* **61** 3091-3097.

Lintanf, A., Neagu, R., and Djurado, E. (2007): Nanocrystalline Pt thin films prepared by electrostatic spray deposition for automotive exhaust gas treatment. *Solid State Ionics* **177** 3491-3499.

Luke, T.L., Wolcott, A., Xu, L., Chen, S., Wen, Z., Li, J., De la Rosa, E., Zhang, J.Z. (2008): Nitrogen-doped and CdSe quantum dot sensitized nanocrystalline TiO_2 films for solar energy conversion applications. *Journal of Physical Chemistry C* **112** 1282-1292.

Meesters, G.M.H., Vercoulen, P.H.W., Marijnissen, J.C.M., and Scarlett, B. (1992): Generation of micron-sized droplets from the Taylor cone. *Journal of Aerosol Science* **23** 37-49.

Miao, P., Balachandran, W., and Xiao, P. (2002): Formation of ceramic thin films using electrospray in cone-jet mode. *IEEE Transactions on Industry Applications* **38** 50-56.

Mo, S.D., and Ching, S.W. (1995): Electronic and optical properties of three phases of titanium dioxide. *Physical Review B* **51** 13023-13032.

Mosaddeq-ur-Rahman, M., Yu, G.L., Soga, T., Jimbo, T., and Ebisu, H., Umeno, M. (2000): Refractive index and degree of inhomogeneity of nanocrystalline TiO_2 thin films: Effects of substrate and annealing temperature. *Journal of Applied Physics* **88** 4634-4641.

Murarka, S.P., Eizenberg, M., and Sinha, A.K. (2003): Interlayer dielectrics for semiconductor technologies. Elsevier, Amsterdam.

Mutoh, M., Kaieda, S., and Kamimura, K. (1979): Convergence and disintegration

of liquid jets induced by an electrostatic field. *Journal of Applied Physics* **50** 3174-3179.

Mwabora, J.M., Lindgren, T., Avendano, E., Jaramillo, T.F., Lu, J., Lindquist, S.E., and Granqvist, C.G. (2004): Structure, composition, and morphology of photoelectrochemically active $TiO_{2-x}N_x$ thin films deposited by reactive DC magnetron sputtering. *Journal of Physical Chemistry B* **108** 20193-20198.

Nagorynyi, V. S., and Bezrukov, V. I. (1980): Droplet emission in an electrostatic field. *Magn Gidrodin USSR* **16** 111.

Nakamura, T., Ichitsubo, T., Matsubara, E., Muramatsu, A., Sato, N., and Takahashi, H. (2005): Preferential formation of anatase in laser ablated titanium dioxide films. *Acta Materialia* **53** 323-329.

Okato, T., Sakano, T., and Obara, M. (2005): Suppression of photocatalytic efficiency in highly N-doped anatase films. *Physical Review B* **72** 115124.

O'Regan, B., and Gratzel, M. (1991): A low cost, high-efficiency solar cell based on dye-sensitized colloidal TiO_2 films. *Nature* **353** 737-740.

Pancove, J. (1971): Optical processes in semiconductors. Dover Publications, Inc. New York.

Pareta, R., and Edirisinghe, M.J. (2006): A novel method for the preparation of the

starch films and coatings. *Carbohydrate Polymers* **63** 425-431.

Pascual, J., Camassel, J., and Mathieu, H. (1978): Fine structure in the intrinsic absorption edge of TiO_2. *Physical Review B* **18** 5606-5614.

Princivalle, A., Perednis, D., Neagu, R., and Djurado, E. (2005): Porosity control of LSM/YSZ cathode coating deposited by electrospraying. *Chemistry of Materials* **17** 1220-1227.

Rayleigh, L. (1879): On the stability or instability of certain fluid motions. *Proceedings of the London Mathematical Society* **1-11** 57-72.

Rayleigh, L. (1882): On the equilibrium of liquid conducting masses charged with electricity. *Philosophical Magazine* **14** 184-186.

Rietveld, I.B., Kobayashi, K., Yamada, H., and Matsushige, K. (2006): Electrospray deposition, model, and experiment: Toward general control of film morphology. *Journal of Physical Chemistry B* **110** 23351-23364.

Rulison, A.J., and Flagan, R.C. (1993): Scale-up of electrospray atomization using linear arrays of Taylor cones. *Review of Scientific Instruments* **64** 683-686.

Seshan, K. (2002): Handbook of thin film deposition. Noyes, New York.

Shankar, K., Tep, K.C., Mor, G.K., and Grimes, C.A. (2006): An electrochemical strategy to incorporate nitrogen in nanostructured TiO_2 thin films: modification of bandgap and photoelectrochemical properties. *Journal of Physics D: Applied Physics* **39** 2361-2366.

Shen, H., Mi, L., Xu, P., Shen, W.D., and Wang P.N. (2007): Visible-light photocatalysis of nitrogen-doped TiO_2 nanoparticulate films prepared by low-energy ion implantation. *Applied Surface Science* **253** 7024-7028.

Shimizu, K., Imai, H., Hirashima, H., and Tsukuma, K. (1999): Low- temperature synthesis of anatase thin films on glass and organic substrates by direct deposition from aqueous solutions. *Thin Solid Films* **351** 220-224.

Singh, R., Paily, R., DasGupta, A., DasGupta, N., Misra, P., and Kukreja, L.M. (2005): Optimized dual temperature pulse laser deposition of TiO_2 to realize MTOS (metal-TiO_2-SiO_2-Si) capacitors with ultrathin gate dielectrics. *Semiconductor Science and Technology* **20** 38-43.

Smith, D. P. H. (1986): The electrohydrodynamic atomization of liquids. *IEEE transactions on industry applications* **IA-22** 527-535.

Subramania, G., Constant, K., Biswas, R., Sigalas, M. M., and Ho, K.M. (2002): Visible frequency thin film photonic crystals from colloidal systems of nanocrystalline titania and polystyrene microspheres. *Journal of the American Ceramic Society* **85** 1383-1386.

Sung, K., and Lee, C. S. (2004): Factors influencing liquid breakup in electro hydrodynamic atomization. *Journal of Applied Physics* **96** 3956-3961.

Tang, K., and Gomez, A. (1994): On the structure of an electrostatic spray of monodisperse droplets. *Physics of Fluids* **6** 2317-2332.

Tang, K., and Gomez, A. (1994): Generation by electrospray of monodisperse water droplets for targeted drug-delivery by inhalation. *Journal of Aerosol Science* **25** 1237-1249.

Tang, K., and Gomez, A. (1995): Generation of monodisperse water droplets from electrosprays in a corona assisted cone-jet mode. *Journal of Colloid and Interface Science* **175** 326-332.

Tang, K., and Gomez, A. (1996): Monodisperse electrosprays of low electric conductivity liquids in the cone-jet mode. *Journal of Colloidal Interface and Science* **184** 500-511.

Taylor, G. (1964): Disintegration of water drops in an electric Field. *Proceedings of the Royal Society of the London. Series A, Mathematical and Physical Science* **280**, 383-397.

Ting, C.C., Chen, S.Y., and Liu, D.M. (2000): Structural evolution and optical properties of TiO_2 thin films prepared by thermal oxidation of sputtered Ti films. *Journal of Applied Physics* **88** 4628-4633.

Urbach, F (1953): The long-wavelength edge of photographic sensitivity and of the electronic absorption of solids. *Physical Review* **92** 1324.

Vasantkumar, C.V.R., and Mansingh, A. (1991): Properties of RF sputtered tetragonal and hexagonal barium titanate films. *IEEE 7th Symposium on Applications of Ferroelectrics* 713-716.

Vellenga, S. J., and Klinkenberg, A. (1965): On the rate of discharge of electrically charged hydrocarbon liquids. *Chemical Engineering Science* **20** 923-930.

Vonnegut, B., and Neubauer, R. L. (1952): Production of monodisperse liquid particles by electrical atomization. *Journal of Colloidal Science* **7** 616-620.

Watanabe, H., Matsuyama, T., and Yamamoto, H. (2003): Experimental study on electrostatic atomisation of highly viscous liquids. *Journal of Electrostatics* **57** 183-197.

Wilhelm, O., Madler, L., Pratsinis, S.E. (2003): Electrospray evaporation and deposition. *Journal of Aerosol Science* **34** 815-836.

Weber, C. (1931): On the breakdown of a fluid jet. *Journal of Mechanics and Applied Mathematics* **11**, 136-159.

Yang, W., Marino, J., Monson, A., and Wolden, C.A. (2006): An investigation of annealing on the dielectric performance of TiO_2 thin films. *Semiconductor Science and Technology* **21** 1573-1579.

Zeleny, J. (1914): The electrical discharge from liquid points and a hydrostatic method of measuring the electric intensity at their surfaces. *The Physical Review* **3**, 69-91.

Zeleny, J. (1915): On the conditions of instability of electrified drops, with applications to the electric discharge from liquid points. *Proceedings of the Cambridge Philosophical Society* **18**, 17-24.

Zeleny, J. (1917): Instability of electrified liquid surfaces. *The Physical Review* **17**, 1-8.

Zhang, J.Y., Boyd, I.W., O'Sullivan, Hurley, P.K., Kelly, P.V., and Senateur, J.P. (2002): Nanocrystalline TiO_2 films studied by optical, XRD, FTIR spectroscopy. *Journal of Non-Crystalline Solids* **303** 134-138.